NASA Conference Publication 2029

THIRD NATIONAL AERONAUTICS AND SPACE ADMINISTRATION WEATHE AND CLIMATE PROGRAM SCIENCE REVIEW

The proceedings of a review held November 29-30, 1977
at the NASA Goddard Space Flight Center,
Greenbelt, Maryland

Edited by
Earl R. Kreins
Sponsored by
The National Aeronautics and Space Administration
Office of Space and Terrestrial Applications

Prepared at Goddard Space Flight Center

National Aeronautics and
Space Administration

Goddard Space Flight Center
Greenbelt, Maryland 20771

NASA Conference Publication 2029

THIRD NATIONAL AERONAUTICS AND SPACE ADMINISTRATION WEATHER AND CLIMATE PROGRAM SCIENCE REVIEW

The proceedings of a review held November 29-30, 1977
at the NASA Goddard Space Flight Center,
Greenbelt, Maryland

Edited by
Earl R. Kreins
Sponsored by
The National Aeronautics and Space Administration
Office of Space and Terrestrial Applications

Prepared at Goddard Space Flight Center

National Aeronautics and
Space Administration

Goddard Space Flight Center
Greenbelt, Maryland 20771

FOREWORD

This document summarizes the proceedings of the third in a series of annual reviews of the principal meteorological research results conducted under the Weather and Climate Program of the NASA Office of Space and Terrestrial Applications. The previous reviews were for the primary purpose of evaluating program progress and to provide a basis for justifying future activities. The third review was expanded in scope to promote information exchange with the meteorological community. To aid in this exchange, representatives from the National Oceanic and Atmospheric Administration, National Science Foundation, and Department of Defense were invited to attend the science review which was held at the NASA Goddard Space Flight Center, Greenbelt, Maryland, on November 29-30, 1977.

The NASA Weather and Climate Program has two major thrusts; the first involves the development of experimental and prototype operational satellite systems, sensors, and space facilities for monitoring and understanding the atmosphere, the second involves basic scientific investigations aimed at studying the physical and chemical processes which control weather and climate. These major aspects of the program focus on exploiting the capabilities of space technology for: (1) the detection, monitoring, and prediction of severe storms, (2) the improvement of global weather forecasting; and (3) the monitoring and prediction of climate change. The third science review concentrated on the scientific research rather than the hardware development aspect of the program.

Thirty-six scientific papers were presented covering these three general areas. Session moderators were E. R. Kreins, R. C. Herfurth, and C. R. Laughlin, NASA Meteorology Program Office, Goddard Space Flight Center. The papers published in these proceedings are separated into two sections. The first section contains those papers presented orally at the science review (papers numbered 1-36). The second section contains additional research results which were not presented in the review due to time limitations (papers numbered 37-59). To expedite the publication of these proceedings, papers were submitted in camera ready format. Each author assumed full responsibility for the content of his paper.

Earl R. Kreins
Science Review Coordinator
NASA Meteorology Program Office
Goddard Space Flight Center

 PAGE 11 INTENTIONALLY BLANK

TABLE OF CONTENTS

SESSION 1
SEVERE STORMS AND LOCAL WEATHER RESEARCH

Session Moderator – Earl Kreins

SESSION 2
GLOBAL WEATHER RESEARCH

Session Moderator – Richard Herfurth

SESSION 3
CLIMATE RESEARCH

Session Moderator – Charles Laughlin

ADDITIONAL FY 1977 ACHIEVEMENTS IN SEVERE STORMS AND LOCAL WEATHER RESEARCH

ADDITIONAL FY 1977 ACHIEVEMENTS IN GLOBAL WEATHER RESEARCH

N79-20576

Paper No. 1

DRY AIR ENTRAINMENT INTO CONVECTIVE CLOUDS

Dr. J. Telford, President, *Effective Concepts Inc.*

ABSTRACT

A systematic approach to the study of turbulent motion must be undertaken if we are to achieve adequate successes in weather modification. The most urgent problem relates to effects on the cloud particles of the variable evaporative cycles as dry air is mixed into clouds. Such studies have a broad applicability to all atmospheric and climatic studies. A zero-g study is proposed to enable the basic experimental data to be collected so that theory may be developed to generalize such results for practical quantitative applications.

INTRODUCTION

The obvious societal need to utilize every possible means to adjust one's environment for the greatest benefit for everyone is nowhere better illustrated than in the case of weather modification. Weather modification has become the first real confrontation between atmospheric science and the atmosphere itself where the need justifies continued efforts in the face of formidable problems, and effectiveness can easily be judged by the average citizen.

The science of atmospheric clouds presently falls far short of completeness. Hypotheses and theories abound but most are acceptable contributions only because the variability in the measurements is tacitly taken to support a view which allows that actual observed cases should provide no realistic limits on models, the observations being inherently "inconsistent" or "unreliable". This is the core of the problem. The reality of statistical variability, originating in the fundementally turbulent nature of the atmosphere, is somehow avoided. Ideal tools have not been found for dealing with it in theory. The results of standard statistical data analyses are disappointingly vague when met in weather modification experiments. We tend to have the scientific effort divided into two groups; those who make only vague attempts to understand the phenomena in detail and rely on the black box type of empirical studies, measuring of stimulus and response, and those who attempt to synthesize from fundamental principles the more complex behavior met with in the real world.

There is some justification for the feeling that the synthetic approach has produced solid gains which will be part of the science when all the statistically based experiments which did not quite succeed are forgotten. However, these studies can not much longer be justified unless a direct attack is made on the way turbulence is to be included in cloud models. It has been possible to publish very simplified models ignoring turbulence (or over simplifying it) because observations in cloud are extremely expensive and difficult, so permitting inadequate theories to evade the crunch of meeting inescapable facts; up until now. The author (Telford, 1975) has drawn attention to these conflicts between many models and the most reliable observations, and none of these conflicts is more relevant than those arising from the usual model formulation ignoring vertical mixing of dry overlying air down into the cloud.

Cloud Physics Background

Perhaps the most fundamental problem related directly to the rain formation process in the microphysics of warm clouds is in the exact consequences of the mixing of dry air into the cloud. Warm rain formation involves a process whereby the cloud drops collide and coalesce, the bigger drops falling faster and overtaking and gathering up the smaller ones in their path. There has always been a well recognised problem as to how drops of sufficient size difference were formed during the initial condensation process. The author (Telford, 1955) showed how, once a few percent of the drops developed to twice the average size, the random statistics of successive drop collisions resulted in a sufficient proportion growing faster than the rest to account for the drop numbers found in rain. These grew in perhaps 20% of the time which would have been needed at the average growth rate.

This stochastic theory has been elaborated over the last ten years, so that every detail has been included. In addition the dynamics of the collisions between two drops for each of the possible collision sizes has been calculated theoretically. However, despite the lack of irrefutable experimental checks the general conclusion is that it is difficult to form drizzle sized drops in the cloud lifetime as actually observed, if the drops perform as current theory would predict.

The basic problem appears to be that, in order to make the calculations feasible, the cloud model is simplified by omitting the random turbulent motions. However, the most noticeable feature of cumulus clouds, which are usually selected for study because of their simplicity relative to other cloud systems, is the enormous variability in external form. In-cloud measurements show that their internal form is equally variable, with, however, some regularities of great significance. (Telford, 1975, Telford and Wagner, 1976, Wagner & Telford, 1976)

The problem of cloud formation condensation was studied from earliest work (Howell, 1949, Squires, 1952A, 1952B) on the scientific treatment of clouds. It was clear that the drops in the cloud depended on the size and number of the particles capable of starting the condensation process, and that the rate of adiabatic water release was also important. It was also clear that the bigger nuclei completely dominated the process. Thus the source of nuclei found over the oceans usually lead to fewer cloud drops in maritime clouds than in continental clouds. This difference leads to the deduction that small, more numerous drops in continental clouds are less likely to coalesce and so form rain by this mechanism and thus the freezing rain mechanism must become more important. Recent work (Hallett and Mossop, 1974) also shows the importance of the initially available cloud drop sizes in initiating ice crystal multiplication processes.

The Mixing Process

The evidence that mixing is fundamental to cloud dynamics is now well established. The theories regarding the details of mixing and turbulence appear to have glossed over what is perhaps the most fundamental property of real clouds, the variability on scales of the turbulent eddies. The importance of this role is now beyond dispute in the study of cloud dynamics.

Mixing is sometimes incorporated into cloud models on the basis of very simple assumptions which simulate some of the consequences of mixing. Thus in the single model of cumulus cloud growth the whole cloud is instantaneously diluted with outside air at a rate describing the transfer of air through its outside envelope. Each infinitesimal volume of cloud dilutes the same as any other volume within the cloud, instantly, as soon as the outside air is entrained into the cloud through its surface. This has been applied in a model where mixing occurs only across a constant height layer within the cloud with account being taken of the condensation nuclei so introduced. The artificiality of these assumptions is a reflection of the difficulty in achieving a better description of the turbulent processes actually in action.

When studying turbulence, the approximation to turbulent diffusion by postulating an eddy diffusivity has lead to contradictions with observations. The eddy diffusivity implies that the rate of transfer of moisture, heat or monentum is proportional to the gradient in these properties. This is certainly untrue for atmospheric convective plumes where extremely sharp transitions are maintained on the upstream side of the plumes where diffusion considerations would ensure a smooth profile.

In cloud dynamics recent work has been done based on the inertial platform supported measurement of air motion around cumulus clouds. Consideration of the liquid water distribution measured in these clouds, from previous data, and this new

information has emphasized the contradictory nature of cloud mixing when viewed as an eddy diffusion phenomenon. Indeed the horizontal uniformity is shown to be a result of extremely rapid vertical mixing and insignificant horizontal transfer; contrary to expectations based on eddy diffusion. Typical models of condensation and convection in uniform updrafts, justified by eddy diffusivity dynamics, do not warrant our confidence.

The Next Step

The most urgent problems to be solved, if cloud physics is to provide a useful model for improving weather modification attempts, are all related to turbulent entrainment and mixing. Of particular importance is the effect on the drop size spectrum of the statistical variation in the final stages of the turbulent mixing of dry and cloudy air. It appears likely from recent simple experiments that this effect is large and if so, it will go a long way towards explaining why the current theory is so inadequate. A systematic study including theoretical analyses of the turbulence process and laboratory experiments should be undertaken.

The experimental examination of this problem is particularly suited to a zero-g approach because in zero-g we will not have continual generation of turbulence throughout the measurement. This arises under gravity because droplet evaporation cools the air and increases its density differentially as the mixing proceeds. The fundamental mixing process needs to be verified under conditions where the key assumptions can be studied separately. The carryover to cloud physics of a well established theoretical and experimentally verified description of turbulent mixing could be convincingly accomplished with a relatively simple theoretical extension to allow for the energy released into the turbulent motion from interaction with gravity. On the other hand if the basic mixing theory is at all vague, because of the problem of interpreting ground based experiments with all the complicated swirling that evaporation introduces, acceptance will be slow and the traditional view will prevail that accounting for turbulence is an unnecessary overelaboration.

A zero-g experiment in which a systematic study is made of the motion and cloud drop sizes resulting when a small chamber half filled with cloud, with the remainder dry air, is mixed by carefully metered turbulent motion needs to be accomplished. This experiment which appears to have insurmountable problems if attempted in the laboratory, will shed much light on both the nature of real cloud processes and turbulence in general.

This experiment offers a fundamental advance in the oldest and most studied branch of cloud physics, cloud droplet growth. It could well revolutionize the subject and has a potential

Pay-off in societal needs greater than the most elaborate and costly weather modification experiment so far contemplated.

References:

Hallett, J and S. C. Mossop, 1974: Production of Secondary Ice Particles During the Riming Process. Nature, 249, 4542,26-28.

Howell, W. E., 1949: J. Met. 6,134-49

Squires, P., 1952A: The Growth of Cloud Drops by Condensation: I. General Characteristics. Aust. J. of Scientific Research, 5,59-86.

Squires, P., 1952B:II. The Formation of Large Cloud Drops. Aust. J. of Scientific Research, 5,473-499.

Telford, J. W., 1955: A New Aspect of Coalescence Theory. Jour. Met., 12,436-444.

Telford, J. W., 1975: Turbulence Entrainment and Mixing in Cloud Dynamics. Pageof, 113,1067-1084.

Telford, J. W. and P. B. Wagner, 1976: The Interaction of Small Cumuli with their Environments. Preprints, International Conference on Cloud Physics, July 26-30, Boulder, Colorado.

Wagner, P. B. and J. W. Telford, 1976: The Measurement of Air Motion in and Near Clouds. Preprints, Internation Conference on Cloud Physics, July 26-30, Boulder, Colorado.

Paper No. 2

N79-20577

THREE DIMENSIONAL CLOUD TOP CHANGES RELATED TO THUNDERSTORM SEVERITY

Robert F. Adler, *Goddard Space Flight Center, Greenbelt, Maryland*

ABSTRACT

Digital infrared data from a geostationary satellite are used to study thunderstorm top growth rates and other parameters in relation to the occurrence of severe weather on the ground. Both the rate of upward growth of the thunderstorm top and the maximum height reached are shown to be useful parameters in the detection of severe thunderstorms.

1. OBJECTIVE AND APPROACH OF STUDY

The rationale behind this study is simple. The occurrence of thunderstorm-related severe weather (tornadoes, hail, high winds) is highly correlated with the intensity of convection. Using SMS IR data one should be able to observe or calculate parameters related to convection intensity, such as cloud top temperature and its rate of change.

Limited-scan (5 minute interval) SMS-2 digital IR data from the period 1803–2208 GMT on May 6, 1975 are used in this study. The calculations presented are performed on the Atmospheric and Oceanic Information Processing System (AOIPS), an interactive image processing system. With this system, an irregularly-shaped area can be outlined on a color enhanced television image and a histogram of the digital counts inside the area obtained.

From this histogram a cumulative histogram is compiled starting from the cold end of the temperature distribution. That is, the number of points, N_i, with blackbody temperature $T_{BB} \leq T_i$ is obtained, with T_i ranging from the coldest temperature in the area to the warmest valid temperature, T_o. The technique was first outlined by Adler and Fenn (1976) and is also described in Adler and Fenn (1977).

The thunderstorms analyzed in this study lie along a generally north-south oriented cold front running from Nebraska southward through Texas. This area contains all the reported tornadoes for this day during this time, other severe thunderstorms, and thunderstorms with no reported severe weather.

2. RESULTS FROM TORNADO-BEARING STORMS

Five clouds or elements in the area examined had tornadoes associated with them, with the total number of tornadoes being nine. An example of a growth rate diagram for a tornado cloud is shown in Figure 1 for cloud 4. The diagram indicates the relation between N_i and time, where N_i is the number of data points in the element with blackbody temperature, T_{BB}, less than or equal to T_i. For example, the curve in Figure 1 for T_i = 218K exhibits an increase

PAGE 6 INTENTIONALLY BLANK

from N = 14 at 1808 GMT to N = 60 at 1823 GMT. The location in time of the severe weather events is shown across the top of the diagram.

Cloud 4 in Figure 1 shows a rapid decrease in minimum blackbody temperature, or T_{min} and a rapid expansion of areas within isotherms. The decrease in temperature can be calculated by moving horizontally across the diagram at, for example, N = 10. The 218K line and the 212K line are separated by 40 minutes, indicating a rate of decrease of 0.15K min^{-1}. The values of 1/N dN/dt are of order of magnitude 10^{-3} s^{-1}. The decrease in temperature and expansion of isotherms, of course, implies ascent.

Three tornadoes are associated with Cloud 4 (Fig. 1). The Pierce, Nebraska tornado, the strongest of the three, was first reported at 1905 GMT. At that time and immediately preceding it, during the tornado formation period, the element exhibits cold area expansion and decreasing temperature, indicating ascent. The same pattern also is associated with the weaker Knox County tornado.

During the time period examined, nine tornadoes were reported, eight of which could be clearly linked with a small, cold area in the IR data. Of the remaining eight cases, all but one occurred during, or just after, a rapid increase in cold area, indicating cloud top ascent. Therefore, it appears that the formation of tornadoes in a large majority of cases occurred during an increase in thunderstorm top height. This vertical velocity applies on a spatial scale of approximately 15km and does not indicate growth of individual overshooting tops.

3. SUMMARY OF RESULTS FOR ALL STORMS

Thirty-nine elements are identified and monitored. Fifteen of these have severe weather reports associated with them, with five having tornadoes. All these elements are active thunderstorms or thunderstorm clusters.

Two satellite-based parameters are found to be correlated with the occurrence of severe weather. These parameters are the maximum rate of expansion of blackbody temperature isotherms and the minimum blackbody temperature attained by the element. The isotherm expansion is, of course, an indicator of the upper level divergence and therefore the rate of vertical growth of the thunderstorm top. The minimum temperature is an indicator of maximum thunderstorm height.

The scatter diagram of maximum rate of expansion, 1/N dN/dt, and minimum cloud top temperature is shown in Figure 2. Elements having tornadoes or hail are noted by T's or H's, respectively. The dots represent non-severe cases. The severe weather elements tend to have minimum cloud top temperatures less than 213K and rates of cold area expansion greater than 3 x 10^{-3} s^{-1}.

A series of discriminant analyses were carried out with the two variables individually, and with the two combined. The diagonal line in Figure 2 is the result of the two-variable discriminant analysis. The results are summarized in Figure 3. For cloud top minimum temperature the dividing point is determined to be 212.8K, for the rate of expansion the value is 3.5 x 10^{-3} s^{-1}. The combined or two variable discriminant shows perhaps the best capability. Less than 20% of the cases below the line have severe weather, while two-thirds of elements above the line have hail or tornadoes. The ratios in parentheses indicate the distribution of the 5 elements having tornadoes. It is obvious that, at least for the dependent data sample in this case, the satellite data can be used to discriminate severe and non-severe thunderstorms.

The potential for warning in terms of lead time is also examined. Based on the criteria shown in Figure 3 the time between when the criterion was met and the time of the first severe weather report was calculated. The results

indicate that a potenti warning time interval of 20 minutes is a reasonable estimate.

.. SUMMARY AND ONCLUSIONS

A tech.nique ·ing digital infrared data from a geostationary satellite (SMS-2) have been shown to have skill in differentiating between severe and non-severe thunderstorms. The severe thunderstorms tend to have large rates of expansion of blackbody temperature isotherms, which is indicative of rapid ascent, and low minimum blackbody temperatures, indicating relatively high thunderstorm tops.

An examinatio· of five cloud elements having eight tornadoes shows that in seven of the eight cases the first report of the tornado took place during, or just after, a rapid expansion of cold areas; this indicates rapid ascent of the thunderstorm top on the scale observed by the satellite.

REFERENCES

Adler, R. F. and D. D. Fenn, 1976: Thunderstorm monitoring from a geosynchronous satellite. In Preprints of 7th Conference on Aerospace and Aeronautical Meteorology, 307–311.

_____ and _____, 1977: Satellite-based thunderstorm intensity parameters. In Preprint Volume of 10th Conference on Severe Local Storms, 8–15.

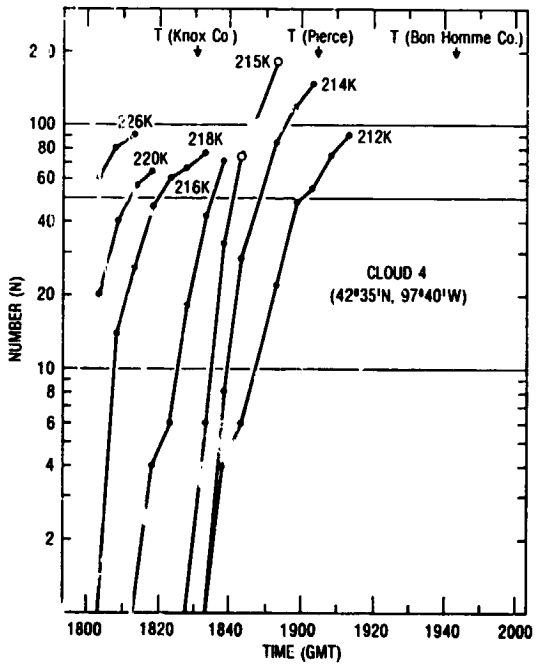

Fig. 1–Thunderstorm growth rate diagram for cloud 4

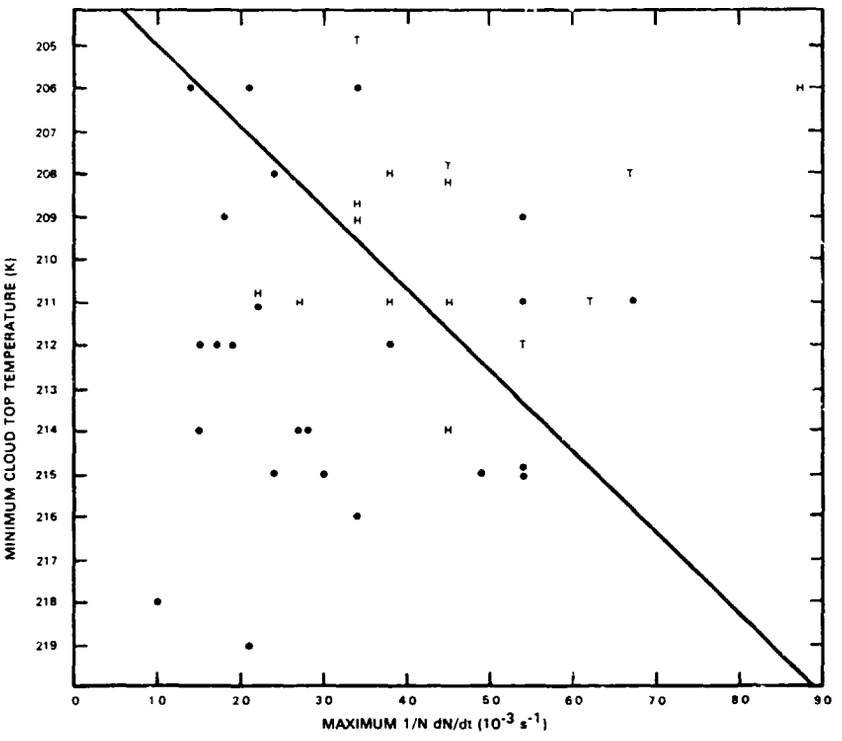

Fig. 2–Occurrence of severe weather as a function of rate of expansion and minimum cloud top temperature

DISCRIMINANT ANALYSIS

VARIABLE(S)	VALUE FOR $L = 0$	FRACTION OF ELEMENTS WITH SEVERE WEATHER	
		FOR $L < 0$	FOR $L > 0$
CLOUD TOP MINIMUM TEMPERATURE (T_{MIN})	212.8K	$\frac{1}{12}\left(\frac{0}{12}\right)$	$\frac{14}{27}\left(\frac{5}{27}\right)$
MAXIMUM RATE OF GROWTH $\left(\frac{1}{N}\frac{dN}{dt}\right)$	$3.5 \times 10^{-3} s^{-1}$	$\frac{5}{22}\left(\frac{1}{22}\right)$	$\frac{10}{17}\left(\frac{4}{17}\right)$
COMBINED T_{MIN} AND $\frac{1}{N}\frac{dN}{dt}$	$L = 9.75 + 91\left(\frac{1}{N}\frac{dN}{dt}\right) - .048\, T_{MIN}$	$\frac{4}{23}\left(\frac{0}{23}\right)$	$\frac{11}{16}\left(\frac{5}{16}\right)$

( ) INDICATES TORNADO CASES

Fig. 3–Discriminant analysis summary

N79-20578

Paper No. 3

DETECTION OF SEVERE STORMS THROUGH A TROPOSPHERIC-IONOSPHERIC COUPLING MECHANISM

R. J. Hung, *The University of Alabama in Huntsville, Alabama*
R. E. Smith, *Marshall Space Flight Center, Alabama*

ABSTRACT

Acoustic-gravity waves have been detected by a ground-based ionospheric sounding array, and the location of the wave generation source has been determined by a reverse group ray path computation. Computed sources of these waves were located near locations where tornadoes touched down from 2 to 4 hours later. It is suggested that the overshooting and ensuing collapse of convective turrets may be responsible for generating the acoustic-gravity waves observed.

INTRODUCTION

The correlation between acoustic-gravity waves and severe storms has been investigated during the past twenty years. Tepper (1950), Matsumoto and Akiyama (1969), and Uccellini (1975) all contend that acoustic-gravity waves influence severe convective storms.

Along the same line, Hung and Smith (1977), Hung et al. (1978) and Hung and Smith (1978) have shown that acoustic-gravity waves associated with severe storm systems are observed 2 hours ahead of the touchdown of tornadoes. Acoustic-gravity waves are detected by a high frequency radio wave Doppler sounder array located in the Tennessee Valley area, and the location of severe storms responsible for the wave generation is determined by group ray path computations.

It is believed that acoustic-gravity waves observed at ionospheric heights are generated by intense convection associated with severe thunderstorms and tornadoes when intense updrafts impinge upon and sometimes penetrate the tropopause; thereby perturbing the stable stratosphere. When results of Shenk's (1974) analysis of the overshooting and ensuing collapse of convective turrets are used in a turbulent flow model of wave excitation proposed by Lighthill (1952), waves with the same period as those apparently associated with severe thunderstorm activity observed in the ionosphere can be generated.

IONOSPHERIC OBSERVATIONS OF ACOUSTIC-GRAVITY WAVES

A detailed description of the experimental facility used in extensive studies of thunderstorms, tornadoes and hurricanes has been given by Hung et al. (1978). The propagation characteristics of atmospheric acoustic-gravity waves can be determined from observed electron density fluctuations in the ionosphere.

Figure 1 shows the result of the power spectral density analysis of the data observed at 4.0125 MHz between 1800-1900 UT on April 3, 1974 on the transmission between Ft. McClellan, Alabama and Huntsville, Alabama. The average period of the observed waves was 13 minutes.

Cross-correlation analysis was used to establish the coherency of the signals as well as the horizontal phase velocity of the disturbances. Figure 2 depicts the results of the cross-correlation analysis of the data used in the power spectral density analysis whose results are shown in Figure 1. The notation F-N denotes the time delay of the arrival of the signal between Ft. McClellan, Alabama and Nickajack Dam, Tennessee; M-N, the time delay between Muscle Shoals, Alabama and Nickajack Dam, Tennessee; and M-F, the time delay between Muscle Shoals, Alabama and Ft. McClellan, Alabama. The horizontal phase velocity of the waves was 217 m/sec.

Theoretical discussions of group rays of atmospheric gravity waves indicate that the geometrical optics approximation is valid. The wave propagated is assumed to be locally plane so that a local dispersion relation of atmospheric gravity waves is satisfied. Ray tracing, thus, can be carried out by following the group velocity direction through a wind-stratified model atmosphere.

The propagation of wave energy in a lossless transparent medium follows the direction of the group velocity which in general, in an anisotropic medium, is different from that of the wave vector. The reverse ray tracing computation is the integration of group velocity with respect to time domain from the ionospheric reflection point

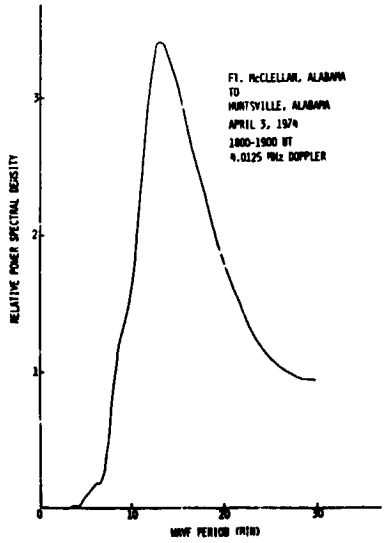

Figure 1. Power spectral density of ionospheric disturbances from Ft. McClellan, Alabama to Huntsville, Alabama at 1800-1900 UT, April 3, 1974, at operating frequency 4.0125 MHz.

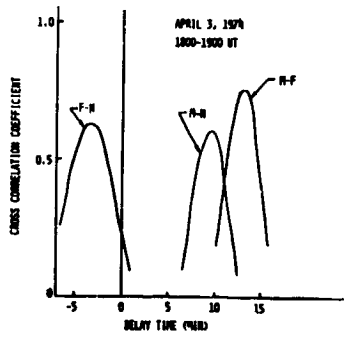

Figure 2. Cross-correlograms from Nickajack Dam (N), Muscle Shoals (M), and Ft. McClellan (F) at time period 1800-1900 UT, April 3, 1974.

back down to the tropopause using the wave period, wavelength, and azimuthal direction of wave propagation obtained from the observational data, the initial vertical wave vector computed from the dispersion relation, and appropriate atmospheric parameters. The effect of wind is taken into account by considering the time space transformation given by the Galilean transformations of the displacement vector, time, Doppler-shift of the wave frequency, and wave vector. (See Hung et al., 1978, for details).

In this study, the neutral wind is treated as a constant in each slab of the atmosphere considered. The values of atmospheric parameters for each altitude are calculated from the U.S. Standard Atmosphere (1962) and profiles of the neutral wind are established by fairing in winds computed from the Kohl and King (1967) model above 100 Km altitude, with meteorological rocketsonde data from Cape Kennedy, Florida below 90 Km.

An example of the computed group ray path of waves observed during the time period 2000-2200 UT, April 3, 1974, and the locations and times of actual tornado touchdowns is given in Figure 3 where actual data are provided by the National Severe Storms Forecast Center. The wave traveling time from the computed wave source to receivers at Huntsville, Alabama was 1 hour and 52 minutes; therefore, the signal was excited roughly 2-3 hours ahead of the touchdown of the tornadoes. Figure 4 is a radar summary, provided by the National Weather Service, for the time 1935 UT, April 3, 1974, which corresponds to the time when the ionospheric disturbances observed during 2000-2200 UT, at Huntsville, Alabama were excited. It clearly indicates that the tops of thunderstorms are significantly above the tropopause in the Indiana area.

ANALYSIS OF CONVECTIVE OVERSHOOTING TURRETS BASED ON SATELLITE PHOTOGRAPHS

It is known that tornadoes are closely associated with severe thunderstorms (Davies-Jones and Kessler, 1974). Our observations indicate that waves are observed 2 hours ahead of the touchdown of the tornadoes. These results are apparently similar to the conclusion drawn by Uccellini (1975) that acoustic-gravity waves are a precursor to thunderstorms.

Recent studies (Smith and Hung, 1975; Prasad et al., 1975; Jones and Georges, 1976) reveal that quasisinusoidal oscillations, with two harmonics of wave periods, 3 to 5 minutes and 6 to 9 minutes, are observed when severe thunderstorms with tops (radar heights) in excess of about 12 Km occur within a radius of several hundred kilometers of the observation point. During tornado activity, another two harmonics of wave periods, 13 to 15 minutes and 27 to 30 minutes, are observed. Since these acoustic-gravity waves are only present when tops are above about 12 Km, it is possible that penetration of updrafts through the tropopause could be the mechanism generating the waves. The relationship between the dynamics of the penetration of intense convection and waves with wave period τ based on the turbulent flow model proposed by Lighthill (1952) is given by

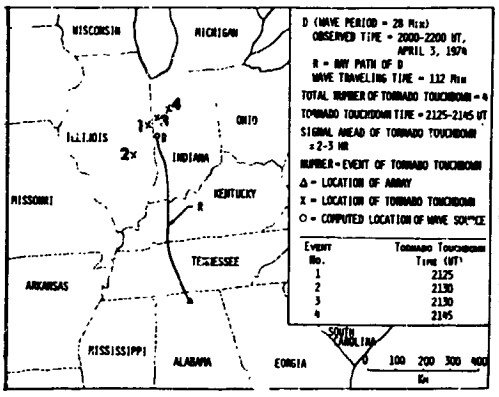

Figure 3. Geographical map of the trajectory of the computed group ray path of waves during the time period 2000-2200 UT, April 3, 1974, and the locations and times of the actual tornado touchdown.

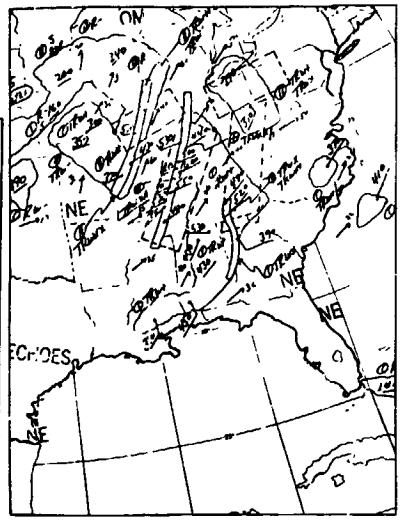

Figure 4. Radar weather summary of the Eastern United States at 1935 UT, April 3, 1974.

$$\tau = \frac{h}{u} \qquad (1)$$

where h is the height of the penetration of the turrets above the tropopause, and u is the growth (or collapse) rate of the turrets. Recently, Shenk (1974) made extensive observations of strong convective cells from geosynchronous satellite and airplane photographs. By using the data observed by Shenk (1974) and Equation (1), wave periods of acoustic-gravity waves which could have been generated by the observed growth and collapse of convective turrets are:

	Height of Turret (Km)	Vertical Growth Rate (m/sec)	Possible Wave Period (Min)
0000 UT May 13, 1972	2.26	11.4	3.3
Average (based on 21 cases)	1.4	4	6
Data Based on Freq. of Occurrance	0.9	4	3.75
Data Based on Freq. of Occurrance	0.6	3	3.3

The computed possible wave periods are in exact agreement with the wave periods of the acoustic-gravity waves observed by the Doppler sounder array.

DISCUSSION

Results indicate that severe storm systems are responsible for the excitation of acoustic-gravity waves with some particular ranges of wave periods and phase velocities which can be detected at F-region ionospheric heights. It is suggested in this study that the overshooting and ensuing collapse of the convective turrets may be directly responsible for the generation of these acoustic-gravity waves and, therefore, the analysis of Doppler sounder observations of acoustic-gravity waves together with the study of the growth and collapse of convective overshooting turrets from satellite photographs can contribute greatly to the understanding of the life cycle of severe storms. The more than 2 hours lead time for the excitation of acoustic-gravity waves associated with tornadic storms may be utilized to develop tornado warning systems.

REFERENCES

Davies-Jones, R., and E. Kessler, Tornadoes, in Weather and Climate Modification, ed. by W. N. Ness, pp. 552-595, Wiley Interscience, New York, 1974.

Hung, R. J., and R. E. Smith, Space Research, XVII, 211, 1977.

Hung, R. J., T. Phan and R. E. Smith, Observation of Gravity Waves During the Extreme Tornado Outbreak of April 3, 1974, J. Atmos. Terr. Phys., 1978 (in press).

Hung, R. J., and R. E. Smith, Ray Tracing of Gravity Waves as a Possible Warning System for Tornadic Storms and Hurricanes, J. Appl. Meteor., 1978 (in press).

Jones, R. M., and T. M. Georges, J. Acoustic Soc. America, 59, 765, 1976.

Kohl, H., and J. W. King, J. Atmos. Terr. Phys., 29, 1045, 1967.

Lighthill, M. J., Proc. Roy. Soc. A, 211, 564, 1952.

Matsumoto, S., and T. Akiyama, J. Meteor. Soc. Japan, 47, 255, 1969.

Prasad, S. S., L. J. Schnack, and K. Davies, J. Atmos. Terr. Phys., 37, 1357, 1975.

Shenk, W. E., J. Appl. Meteor., 13, 917, 1974.

Smith, R. E., and R. J. Hung, J. Appl. Meteor., 14, 1611, 1975.

Tepper, M., J. Meteor., 7, 21, 1950.

Uccellini, L. W., Mon. Wea. Rev., 103, 497, 1975.

United States Committee on Extension to the Standard Atmosphere, U. S. Standard Atmosphere 1962, U. S. Government Printing Office, Washington, D. C., pp. 278, 1962.

Paper No. 4

N79-20579

MESOANALYSIS OF RECORD CHICAGO RAINSTORM USING RADAR, SATELLITE, AND RAIN-GAGE DATA

T. Theodore Fujita, *The University of Chicago, Chicago, Illinois*

ABSTRACT

Comparison of cloud-top topography and rainfall rates at the surface revealed that the areas of heavy rain are located where there are depressions at the anvil top. It was also found that the Z-R relationships show a large scatter when vertical and/or horizontal air currents are strong. Results of this research led to Project NIMROD proposed to begin in May 1978.

1. INTRODUCTION

On June 13, 1976 the Chicago area was hit by an F4 tornado followed by an up to 7-inch rainfall which paralyzed the entire city for hours.

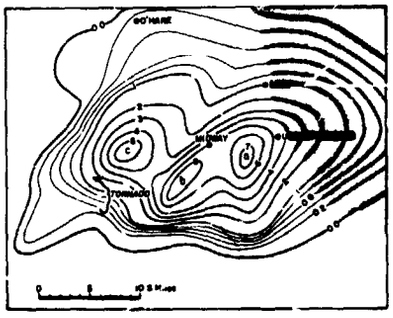

Figure 1. Isohyets of precipitation in inches during the 5-hour period between 2030Z and 0130Z, June 13-14 1976. Stranded motorists who escaped from flooded expressways met street gangs who stoned or stopped their cars. One driver with his family in the car was shot to death.

Since the Rapid City flood, the Big Thompson flash flood in 1976 killed 139 people and more recently, a dam burst in Georgia killed over 40 persons. It is extremely important to develop techniques of precipitation estimates based on satellite data as well as radar data in order to protect people who live in canyons, below dams, and in large cities.

PAGE 16 INTENTIONALLY BLANK

2. RAINFALL RATES AND CLOUD-TOP FEATURES

Cloud photography from a Lear Jet conducted during past years has revealed that the tops of thunderstorms overshooting into the lowermost stratosphere undergo overshooting-collapsing cycles.

Figure 2. Isohyets superimposed upon three SMS pictures at 2230, 2330 and 0030 GMT on June 13-14, 1976. Isohyets are 0, 1, 2, ...inches per hour. It is seen that the areas of rain are much smaller than those of anvil areas. Furthermore, heavy rain is occurring often beneath depressions characterized by dark shadows.

3. VERTICAL MOTIONS AND Z-R RELATIONSHIPS

In an attempt to estimate the effects of vertical motions of air in which raindrops fall, an analytic function in Figure 3 was used. Then

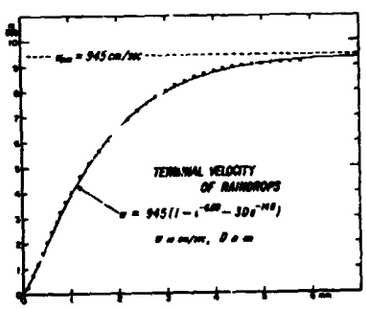

Figure 3. An analytic function of terminal velocity of various sized rain drops. This function was combined with Marshall-Palmer type drop size distribution to obtain Figure 4.

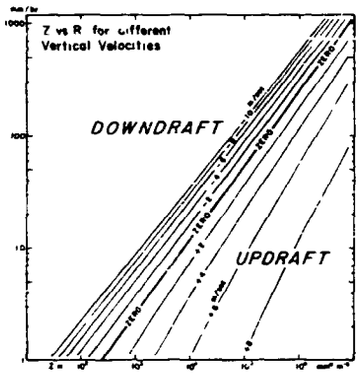

Figure 4. Variation of Z-R relationships as a function of vertical velocities. No raindrops reach the ground when updraft exceeds 9.45 m/sec, the largest terminal velocity. Downdraft increases rainfall rate, but its effect above 10 m/sec is relatively small.

the Z-R relationships in Figure 4 were computed.

4. LARGE SCATTER OF Z-R

Scatter of Z-R was found to be extremely large. Data points were divided into those with hail and without hail. But the scatter remained practically unchanged.

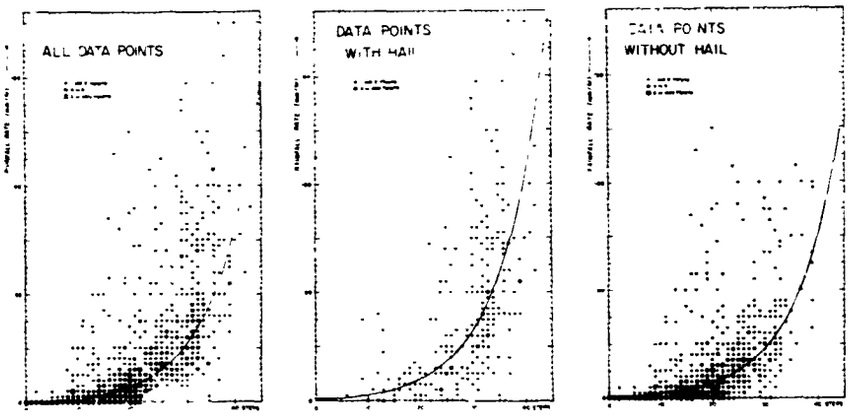

Figure 5. Z-Gain Step relationship with large scatter.

5. EFFECTS OF HORIZONTAL MOTION

Data points in Figure 2 away from the mean curve toward the left cannot be explained by introducing the downdraft in Figure 4. To overcome this difficulty, it was assumed that raindrops are carried by horizontal winds from high to low reflectivity region of echoes.

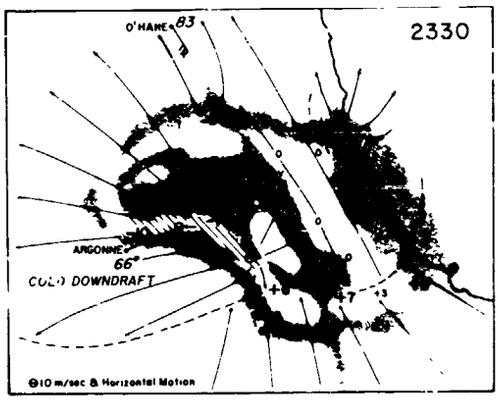

Figure 6. Vertical velocities at 2330Z June 13, 1976 estimated from Z-R relationships in Fig. 4. Velocities are in m/sec. When estimated downdraft exceeded 10 m/sec, horizontal motions were added.

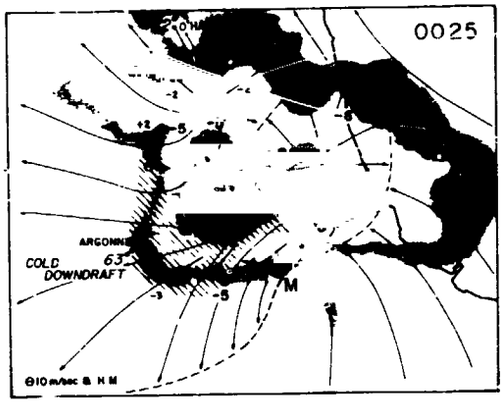

Figure 7. Vertical velocities at 0025Z June 13, 1976. The region of large horizontal flow extends from Midway Airport toward Argonne National Laboratory.

Precipitation maps were analyzed at 5-min intervals between 2100 Z through 0100 Z, June 13-14, 1976. Examples at 2330 and 0025 Z are presented in Figures 6 and 7.

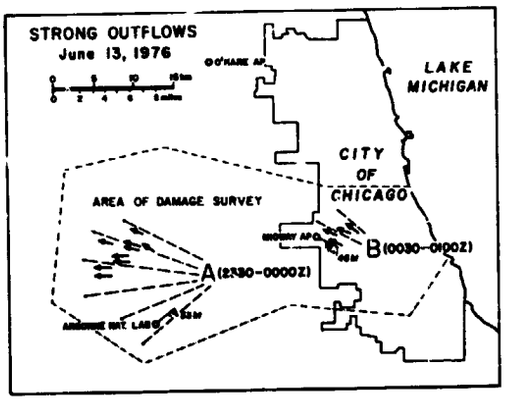

Figure 8. Areas of two strong outflows "A" and "B" mapped by an aerial survey on June 14.
"A" occurred at the time of Figure 6 and "B", that of Figure 7. Trees were uprooted or pushed over by diverging winds up to 80 mph from easterly direction.

6. PROJECT NIMROD

Analysis of the Chicago rainstorm led to a conclusion that an observational network to combine satellite, radar, aircraft, balloon, and surface data are required for further understanding of rain and downburst thunderstorms. The NIMROD network shown below is now being established.

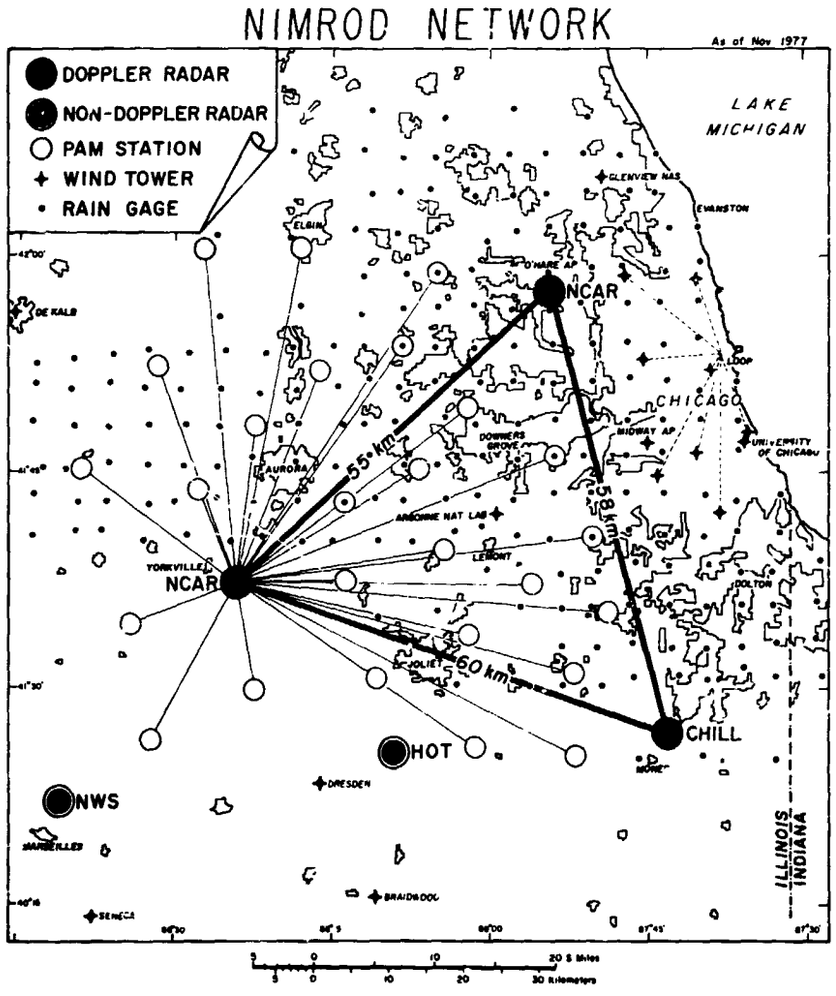

Figure 9. NIMROD (Northern Illinois Meteorological Research On Downburst) NETWORK to be operated in May and June, 1978. The network was designed by Fujita and Srivastava assisted by NCAR.

Paper No. 5

SEVERE STORMS AND THEIR INTERACTION WITH THE ENVIRONMENT

James R. Scoggins, *Texas A&M University, College Station, Texas*

ABSTRACT

A brief description is given of significant research accomplishments and of planned research on atmospheric variability and the interaction of severe storms with their environment using AVE data. Use of the results for the assessment of satellite capabilities are described briefly.

INTRODUCTION: Meteorological systems whose scales are smaller than synoptic are not well understood, yet they are responsible for much of the observed weather including thunderstorms, tornadoes, showers, floods, and numerous other weather elements on a local or regional scale. Before these systems can be predicted they must not only be understood but their relationship with the larger scale atmospheric systems must be understood also. With the usual synoptic-scale data these relationships must be inferred to a large degree rather than determined from the analysis of data. Improvements in both the temporal and spatial resolutions of measurements are required in order to determine the interaction between severe storms and their environment. The atmospheric variability experiments conducted by NASA have improved the temporal resolution and have contributed greatly to the knowledge of environmental processes in the vicinity of severe storms. There have been a total of six atmospheric variability experiments (AVE) and two atmospheric variability and severe storm experiments (AVSSE) conducted (Hill and Turner, 1977). All of these experiments, except the first, were conducted since May 1974. These experiments consist of rawinsonde soundings made at 3- and 6-h intervals during periods ranging from one to four days. A wide variety of atmospheric conditions existed during these experiments, although severe storms was the central focus and extensive convective activity was present in all but one experiment which was conducted in February for comparison with non-convective conditions.

DATA PROCESSING: Extreme care was taken in the processing of the AVE soundings. They were checked for errors at several stages during the data reduction process by computer programs prepared for that purpose. Azimuth and elevation angle data were obtained at 30-sec intervals and ordinate data for every pressure contact. This gives the maximum resolution possible for the thermodynamic

data and provides more accurate wind data than provided by soundings processed in the usual manner (Fuelberg, 1974). The data are processed for each pressure contact and at 25-mb intervals from the surface to 25 mb. These data were put on magnetic tapes and data reports prepared which contain the 25-mb data (Scoggins and Smith, 1973 a and b; Scoggins and Turner, 1975; Fuelberg and Turner, 1975; Fucik and Turner, 1976 a, b and c; Humbert and Hill, 1977).

GRADIENTS: Horizontal gradients of geopotential height, temperature, wind speed, and mixing ratio were computed on selected constant-pressure surfaces ranging from 850 to 200 mb for AVE II and AVE IV (McCown and Scoggins, 1977). The objective of this study was to determine the distribution of gradients in convective and nonconvective areas and how these gradients differed between areas. Gradients were determined by computer from gridded fields of the AVE data, convective storm areas determined from manually digitized radar data provided by the National Weather Service, and various statistics of the gradients computed for convective and nonconvective regions. The results show large variability in the gradient patterns over periods of three hours; that frequency distributions of the gradients for the two AVEs analyzed, as well as over convective and nonconvective areas, were similar in shape but not necessarily in magnitude; that the largest mixing ratio gradients occur near convective areas although in general no particular gradient pattern or combination of patterns appear to be related to air mass severe storms; and that typical gradient patterns and trends are associated with squall lines.

VORTICITY AND STABILITY IN RELATION TO CONVECTIVE ACTIVITY: This was a study designed to investigate the synoptic-scale kinematic and thermodynamic properties of the atmosphere preceding and accompanying severe thunderstorms (Read and Scoggins, 1977). The complete vorticity equation was evaluated, convective instability determined, and time changes in these parameters investigated in relation to the occurrence of thunderstorms. All computations were performed from AVE IV gridded data. It was found that the development of circulation systems determined from the vorticity budget was related to the formation of severe thunderstorms; low level production of vorticity exists in areas of thunderstorm development six hours prior to initial formation; low level vorticity production is large prior to and during initial development of thunderstorms then decreases as convective systems interact with the low-level synoptic scale wind field; synoptic-scale production of vorticity was associated with severe storm regions; convective instability was observed in areas where thunderstorms developed; and, changes in circulation systems and instability sufficient to produce severe storms occur on a time scale considerably less than 12 h.

ENERGY TRANSFORMATIONS: Synoptic-scale budgets of kinetic and total potential energy for the AVE IV period were determined

for regions enclosing intense storms (Fuelberg, 1976; Fuelberg and Scoggins, 1977). All computations were performed objectively from gridded fields of the AVE data. Volumes enclosing severe thunderstorms were found to have large values of cross contour conversion of potential to kinetic energy and large horizontal export of kinetic energy. Transfer of kinetic energy from grid to subgrid scales of motion occurred in the volumes and latent heat release was large in the middle and upper troposphere. Total potential energy was found to be imported horizontally in the lower half of the atmosphere, transported aloft, and then exported horizontally. Local changes of kinetic and total potential energy were observed to be small although the interaction between the volumes enclosing severe storms and the surrounding atmosphere was quite large as indicated by boundary fluxes.

MOISTURE BUDGET: The objective of this study (Scott and Scoggins, 1977) was to examine the moisture budget in areas of severe storms to determine the energy source for the storms and how the ambient moisture conditions related to severe storm areas. The moisture balance was evaluated objectively from gridded data during the AVE IV period. It was found that the net horizontal and vertical boundary fluxes accounted for most of the moisture that was concentrated in convective regions, and that the largest values of moisture accumulations were located slightly downwind of the most intense storms. The best relationship between synoptic-scale moisture processes and severe storms occurred when the moisture processes preceded the severe storms by a period of 3 h. This suggests that a redistribution of moisture in space may be required well in advance of severe storms and that it may be possible to detect these processes. The residual of moisture which represents all sources and sinks of moisture in the budget equation was largely accounted for by precipitation.

SHORT-PERIOD FORECASTING: A method was developed for forecasting thunderstorms over periods of 2-6 h (Zak, 1977). The forecasting method was developed by use of screening regression techniques. More than 60 variables were considered in the analysis with 17 surviving as significant predictors. Of these only four were found to be highly significant in all cases. These variables are surface mixing ratio, occurrence of precipitation during the morning, moisture convergence, and a stability measure. When applied to independent data, the forecasting model accounted for a relatively large fraction of the total variance, the amount depending upon the number of variables used. The study demonstrated that the method can be used with routinely available synoptic-scale data.

TRAJECTORY ANALYSIS: This study (Wilson, 1977) considers relationships between convective storms and their environment in AVE IV determined from three-dimensional air trajectories. Net vertical displacements of air parcels and spatial fields of buoyant energy were found to be highly correlated with convective

activity. By combining the net vertical displacements with buoyant energy using multiple linear regression, it was found that convective activity of various intensities can be spatially determined. Convective and nonconvective areas can be delineated with about 80% accuracy which demonstrates a high degree of scale interaction between synoptic- and convective-scale systems.

INFLUENCE OF CLOUDS ON THE RETRIEVAL OF TEMPERATURE PROFILES FROM SATELLITE RADIANCE DATA: A single field-of-view method for retrieving tropospheric temperature profiles from cloud-contaminated radiance data was developed (Hodges 1976). The radiative transfer equation was applied to a partly cloudy atmosphere with the use of observed shelter temperature and estimated cloud top heights. The results show that the single field-of-view method improves the accuracy of the guess profiles when the retrieval process includes cloud information. The method shows an improvement in the guess temperature profile under cloud layers. Also, it potentially can provide useful data for mesometeorological research in the form of accurate relative temperature profiles over a relatively small horizontal area. However, the absolute accuracy of the retrieved profile is a function of the a priori knowledge of the state of the atmosphere. The method can be used to estimate average tops of a thick overcast layer when there are no thick clouds present above the overcast layer. It was found that observed cloud parameters do not possess sufficient precision for use directly in the retrieval process.

FUTURE PLANS: It is not possible to capture all aspects of the atmosphere and the complicated interactions with severe storms in a few experiments, each of which covers a limited period of time. Additional experiments are needed covering a wide range of synoptic-scale conditions. One additional experiment is planned for the spring of 1978, and it is hoped that additional experiments can be conducted in the future so we can better understand severe storm processes.

Analyses of the types briefly described above will continue in the immediate future with the analysis being extended to encompass an investigation of the information content in 3- versus 12-h rawinsonde data, the development of conditions that lead to severe storms, and an extension of the trajectory analysis. These research efforts continue to be aimed at a better understanding of severe convective storms and the applicability of space technology, especially satellite measurements, to improving this understanding.

CONCLUDING REMARKS: Results from the analysis of the AVE data not only continue to provide a better understanding of the interaction between severe storms and their environment, but also a basis for an assessment of satellite capabilities and potential. Part of the ongoing research is to determine the characteristics of such parameters as vorticity, advection of temperature, thickness, and other parameters, and gradients of various parameters.

The results will also be used as the basis for establishing the optimum distance between satellite sounding points and times, and from these analyses what improvements are needed in satellite data so that the above parameters may be evaluated with accuracies now possible with rawinsonde data. Initial results are available (Arnold, et al., 1976) and additional results, made possible by the AVE data, are expected to be available in 1978.

REFERENCES

Arnold, J.E., J.R. Scoggins, and H.E. Fuelberg, 1976: A Comparison Between Nimbus 5 ... AVE II Experiment. NASA CR-2757.

Fucik, N.F. and R. E. Turner, 1976a: Data for NASA's AVE IV Experiment. NASA TN D-8161.

_____ and _____, 1976b: Data for NASA's AVSSE I Experiment. NASA TN D-8155.

_____ and _____, 1976c: Data for NASA's AVSSE II Experiment. NASA TN D-8154.

Fuelberg, H.E., 1974: Reduction and Error Analysis of the AVE II Pilot Experiment Data. NASA CR-120496.

_____, 1976: Atmospheric Energetics in Regions of Intense Convective Activity. PhD Dissertation, Texas A&M University.

_____ and R.E. Turner, 1975: Data for NASA's AVE III Experiment. NASA TM X-64938.

_____ and J.R. Scoggins, 1977: Relationship between ... Convection. Preprints, 10th Conf. on Severe Local Storms.

Hill, Kelly and R.E. Turner, 1977: NASA's AVEs. BAMS 58 (2).

Hodges, D.B., 1976: A Single Field ... Radiance Data. NASA CR-2726.

Humbert, M.E. and Kelly Hill, 1977: Data for NASA's AVE V Experiment. NASA TM X-73370.

McCown, M.S. and J.R. Scoggins, 1977: Gradients of Meteorological Parameters ... Areas. NASA CR-2818.

Read, W.L. and J.R. Scoggins, 1977: Vorticity Imbalance and Stability in Relation to Convection. NASA CR-2819.

Scoggins, J.R. and O.E. Smith, 1973a: Data for First ... Experiment (AVE I), Part I. NASA TM X-2938.

_____ and _____, 1973b: Data for First ... Experiment (AVE I), Part II. NASA TM X-2948.

_____ and R.E. Turner, 1975: 25-mb Sounding Data ... AVE II Experiment. NASA TN D-7832.

Scott, R.W. and J.R. Scoggins, 1977: The Moisture Budget in Relation to Convection. NASA CR-2817.

Wilson, G.S., 1977: Relationships Between ... Model. Preprints, 10th Conf. on Severe Local Storms.

Zak, J.A., 1977: Forecasting Thunderstorms Over a 2- to 5-h Period by Statistical Methods. PhD Dissertation, Texas A&M University.

Paper No. 6

A REAL-TIME SUBSYNOPTIC, MESO, AND MICROSCALE SEVERE STORM FORECAST SYSTEM

M. L. Kaplan, *The George Washington University, Langley Research Center, Hampton, Virginia*

ABSTRACT

A system of differential equations is integrated numerically in space and time over several different matrices in an effort to simulate the atmospheric wave structures which organize severe local storms. Preliminary results with case studies indicate that dynamical fields produced by the numerical simulations can be translated into very fine scale space and time zones where severe storm forecast indices can be developed. These fine scale indices are now available in real-time when run on Langley's STAR 100 computer system.

INTRODUCTION

Presently, operational severe storm forecasting done by the National Weather Service and the US Air Force, involve explicit time integration of the equations of atmospheric motion at only the largest or synoptic scales. Typically, these synoptic scale results are then refined by using them in statistical models or empirical indices. This further increases their effectiveness for synoptic scale periods in time and areas in space in the forecasting of preferred zones of severe weather development. Thus with only the explicit simulation of large scale motions to guide them, enhanced refinement of the short period motions which organize severe local storm systems is only possible by radar, satellite, and surface reporting stations, i.e., NOW casting. However, these sources give forecasters very little local lead time in disseminating severe storm warnings. The system to be described in this paper differs from the aforementioned one because it is designed to explicitly simulate the short period instabilities at the subsynoptic, meso, and microscales which explicitly organize the severe thunderstorm itself. By so doing, it is anticipated that, the lead time given forecasters for the position, time and intensity of severe convective storm development can be increased from minutes to hours.

Numerical Models - The numerical model now utilized for the simulation of the subsynoptic, meso, and submesoscale motions is a hydrostatic, incompressible, adiabatic primitive equation system. The differential equations which are integrated in space and time are conservation equations for mixing ratio, potential temperature,

u and v velocity components and low-level pressure. Typical diagnostic relationships among pressure, specific volume, potential temperature and mixing ratio are employed to maintain hydrostatic equilibrium. The continuity equation is integrated vertically to get the vertical velocity. The numerical space differencing is fourth-order and the time-marching scheme is the Euler forward-backward technique. Spatial diffusion is simulated with a space smoother-desmoother. There are 12 vertical levels in a z vertical coordinate system. The x and y-space mesh lengths are, for the subsynoptic, meso, and submesoscales, respectively, 38.1, 19.05 and 9.025 km (1/10, 1/20 and 1/40 times the National Weather Service coarse mesh of 381.0 km) for a 60 x 48 x,y-space matrix of grid points. A second numerical model was developed for the simulation of explicit convective and subconvective scale motions. This model is an 18-level nonhydrostatic compressible primitive equation system. It is presently not utilized in the real-time system because of computer time limitations. When it is implemented in the future, it will be run with an x,y,z-space mesh length of 1 km and less.

Data Acquisition, Nesting Procedures, and Forecasting Procedures - The fundamental flow of information on any given forecast day starts with the National Weather Service's limited fine mesh analysis data base. This data is regularly sent to the Bureau of Reclamation data base in Denver, Colorado and is valid at 1200 Greenwich mean time. A program is executed daily from Langley which selects a "window" of this data, based upon its synoptiscale potential for severe storm generation. The window is relocatable to anywhere in the continental US and covers an area of approximately 2400 x 2000 km. The data is available at 1440 Greenwich mean time. Once this select window of information is sent to Langley it is reduced and interpolated and serves as the initial state for a 16-hour forecast performed at the 38.1 km grid mesh length. During the course of this forecast, at 30 minute intervals, a sophisticated dynamical index is evaluated which indicates areas of intensifying subsynoptic scale hydrodynamical instabilities. If the index reaches a preset threshold value, the coordinates of this developing feature will serve as the center point of a reduced scale and reduced time period forecast window. It should be noted that the threshold can only be achieved if the column's vertical temperature and moisture variations indicate conditional instability. A maximum of two windows within the 16-hour forecast window may be selected. Each of these windows is approximately 1200 x 1000 km in dimension. For each window, 3-hour forecasts are made from each interpolated data base which was "frozen" at the time and space of the aforementioned hydrodynamical instability amplification. This same downward extrapolation concept is employed for each 3-hour forecast performed at the 19.05 km grid mesh length. Thus 4 windows are then made available for the 9.025 km scale by evaluating the 19.05 km forecasts at 15 minute intervals and saving 2 maximum values each from 2 different forecasts. Each of the 4 (9.025) km mesh length windows of 60 x 48

x,y-space points is integrated for approximately 32 minutes of real-time and evaluated for maximum index threshold values at 4 minute intervals. Thus we have a sequence of instability setting up instability which leads to the preferred positioning in space of very finescale severe weather potential zones. It takes approximately 30 minutes of real-time to make all of these forecasts making the final "product" available typically by data time + 4 hours or approximately 1600 Greenwich mean time.

Omaha Tornado Case Study - On May 6, 1975, a major tornado outbreak occurred in eastern Nebraska, southeastern South Dakota and southwestern Iowa. The most damage occurred in Omaha, Nebraska. This case will be examined in terms of the multiscale forecast index and the potential guidance it could render in the real-time forecast environment. Figures 1a-1c are representative of what may be termed forecast clusters. Each triangle, rectangle, or square on any one of these 3 figures is representative of a cluster of maximum values of the forecast index. Each cluster is also indicative of a series of maximum values in time. Thus, a cluster is made up of more than 1 maximum value of the forecast index which are in proximity in space and sequence in time.

On the morning of May 6, 1975, a major storm system was centered over southwestern South Dakota. Pivoting about this synoptic-scale vortex were more than 1 well-organized trough systems extending from the lower through the middle troposphere. As the synopticscale trough moved along the southern side of the large vortex the potential for developing smaller scale hydrodynamical instabilities increased dramatically. Coupled with the emerging imbalance of forces, was a well-organized zone of significant low-level moisture spreading northwestwards from the Gulf of Mexico to northeastern South Dakota insuring a large region of potential or conditional instability.

If one observes figures 1a-1c, it is evident that as the scale of each model is reduced there is a refining in space and time of the zone of predicted high index potential. Figure 1a, for the 1/10 scale index, indicates 2 dominant areas of high potential, namely east central and northeastern Nebraska as well as south central and southwestern Missouri. Since most of the very severe activity occurs in the northern region we will concentrate on it. Note that the clusters in figure 1a numbered 1-3 are numbered sequentially in time indicating that during the early to middle forecast period, i.e. 3-9 hours, the most intense growth of the subsynopticscale hydrodynamical instability is in eastern Nebraska. However, this area is still large when compared to the narrow zone of activity indicated in figure 2. A further refining of the index may be seen, however, in figure 1b where the first nested window is automatically initialized from a threshold-exceeding index value and run between 1800 and 2100 Greenwich mean time, or 6-9 hours relative to the initial time of the 1/10 scale model. This 1/20 scale northern window forecast indicates that the maximum growth of the hydrodynamical instability is clustered along a line from the Iowa, Nebraska, and South Dakota borders southeastwards

to near the Nebraska, Missouri, and Iowa borders which is consistent with the bulk of the tornadic activity, as designated in figure 2. During the period from 2000 to 2100 G.M.W., activity in the form of tornadic windstorms develop and spread southeastwards from Yankton, South Dakota to southwest of Omaha, Nebraska. If one extrapolates this concept to figure 1c one will note 4 windows initialized from the two 1/20 mesh forecasts. The time periods between maximum index value calculation have been reduced from 30 minutes at 1/10 scale to 15 minutes and 4 minutes for 1/20 and 1/40 scale reflecting the enhanced sensitivity of the index as space and time scales are reduced. As far as the northern area is concerned, the 1/40 scale index reflects a general concentrated maximum of clusters between Omaha and Norfolk, Nebraska and Sioux City, Iowa. While many of the largest and most devastating tornadoes were in proximity to this region, the 1/40 scale index appeared to be somewhat too early in timing the outbreak. This may possibly be due to the inability to simulate with this system of equations explicit convective scale motions. One will note, however, that when the northern portion of the index clusters at the 1/40 scale are encircled and compared with the activity, i.e., tornado, severe thunderstorm, and hail reports, there is good mesoscale agreement with 23 of 28 reports between 1700 and 2300 G.M.T. within the encircled forecast index zone. The timing of the activity probably could be greatly improved by explicit simulations of convective scale motions. It should also be pointed out that activity does intensify later, as is inferred from figures 1a-1c, in the evening mostly after 0000 G.M.T. May 7, in southwestern Missouri and northwestern Arkansas. The tornado and damaging wind reports are less numerous in this area.

Summary and Conclusions

A real-time subsynoptic, meso, and submesoscale numerical modeling system is now being tested at the Langley Research Center. It is anticipated that this system will be improved to the point where significant increases in the forecasting in the amplitude and spatial-temporal evaluation of severe local storm systems will be possible over present-day systems. The most significant aspect of forecast products available from this system may be the increased lead-time it will give to the people responsible for making severe local storm forecasts.

ACKNOWLEDGEMENT

The author would like to acknowledge Arthur L. Gooden of the Langley Research Center for the invaluable aid he has given in developing software for this system.

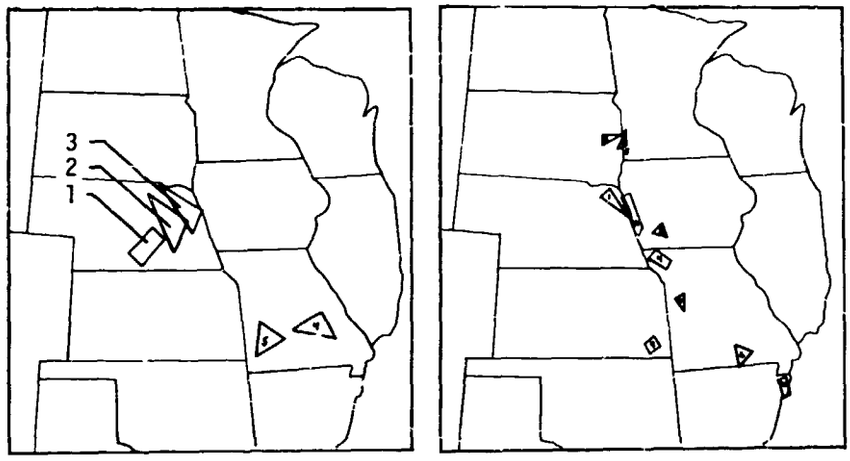

(a) 1/10 scale.

(b) 1/20 scale.

Figure 1.- Forecast index clusters for various length scales.

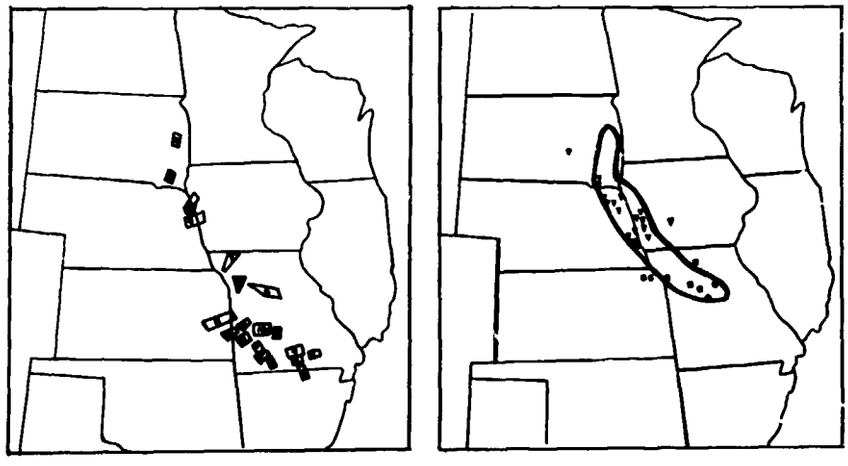

(c) 1/40 scale.

Figure 1.- Concluded.

Figure 2.- Observed northern activity versus 1/40 scale forecast index clusters.

Paper No. 7

N79-20582

LATENT HEAT CALCULATIONS AND THEIR RELATIONSHIP TO TROPICAL CYCLONE INTENSITY

Robert F. Adler, Edward B. Rodgers, *NASA/Goddard Space Flight Center, Greenbelt, Maryland 20771*

ABSTRACT

Data from the Nimbus-5 Electrically Scanning Microwave Radiometer (ESMR) have been used to calculate total storm latent heat release (LHR) and other precipitation parameters for over 100 satellite observations of Pacific Ocean tropical cyclones. The data have shown to be useful in determining the rainfall characteristics of these storms and appear to be potentially useful in the monitoring of them.

1. INTRODUCTION

The estimation of precipitation and latent heat release (LHR) in tropical cyclones is important for understanding the dynamics and energetics of such systems, for the development of techniques useful in tropical analysis and forecasting, and for possible initialization of tropical cyclone numerical models.

This paper presents results from the calculation of the magnitude and distribution of rainfall using data from the Nimbus-5 Electrically Scanning Microwave Radiometer (ESMR) for one Western Pacific tropical cyclone and gives a summery of results for the approximately 100 satellite observations of Eastern and Western Pacific storms in various stages of development. All observations were for cyclones that reached hurricane or typhoon intensity during their lifetimes.

2. DESCRIPTION OF DATA AND METHOD

The Nimbus-5 ESMR is a passive microwave instrument measuring emi Hed radiation in the 19.35 GHz (1.55 cm) region with a resolution of 25 km at nadir. The instrument is described by Wilheit (1972), and the physical basis for rain estimations over water is detailed by Wilheit (1977). Over water radiation emitted by the earth and atmosphere (expressed as brightness temperature T_B) is affected primarily by the state of the sea surface, and by atmospheric water vapor and atmospheric liquid water. Liquid water, in the form of drops of the size associated with rain, is the dominating factor in the variation of T_B over water.

After a small adjustment to the ESMR T_B as described by Adler and Rodgers (1977), rainfall rate for each data point can be determined through a rainfall rate-T_B relation derived empirically from calibrated radar data and adjusted theoretically to 5 km tropical cyclone freezing level height (Wilheit et al. 1977).

3. CASE STUDY RESULTS

The one Western Pacific tropical cyclone that will be presented in this paper is Irma (November, 1974). Figure 1 displays the storms LHR as a function of time for circular areas whose radius is 2° and 4° latitude from the storm center. Also displayed is the fraction of precipitation contributed by rainfall rates greater than 5 mmh^{-1}, hereafter called the precipitation intensity parameter (PIP) (the number in parentheses). The maximum surface wind and estimated central surface pressure is also displayed in the figure.

From November 17 to November 21, before the system intensified, the storm LHR ($< 2 \times 10^{14}$ W) and PIP are small. The observation on November 21 shows what can be interpreted as evidence of intensification. The storm's LHR on the 21st has more than doubled from the two previous satellite passes. In addition, the PIP magnitude is 0.27, much larger than the earlier values.

The next available ESMR observation of Irma is on the 23 November, when the storm is about to reach typhoon intensity. The LHR within 4° latitude of the center increases to 6.5×10^{14} W while the PIP rises only slightly. Over the next two days the storm intensity continues to increase as does the LHR (maximum of 7.9×10^{14} W) and the PIP (maximum .55). The LHR for the area whose radius is 2° latitude from the center increases more rapidly indicating a concentration of rainfall towards the center.

Before Irma hit land (27 November) the satellite derived precipitation parameters indicate little further intensification. This is consistent with the independent in situ measurements.

4. RESULTS FOR WESTERN PACIFIC STORMS

In order to obtain a better understanding of the relation of storm intensity to ESMR derived precipitation parameters, the Western Pacific tropical cyclones were examined. To eliminate storms which had recurved or crossed the Philippine Islands, only the tropical cyclones located south of 25°N and east of 125°E were used.

The scatter diagram between LHR and storm intensity is shown in Figure 2. This diagram indicates a positive correlation between storm LHR over a circular area of radius 4° latitude and storm intensity. The median LHR for disturbances and depressions (< 17 ms^{-1}) is 1.1×10^{14} W, for storms (18 to 32 ms^{-1}) is 4.7×10^{14} W, and for typhoons

(33-65 ms^{-1}) is 6.6×10^{14} W. These values are comparable to other estimates of LHR measurements (Adler and Rodgers, 1977).

The fraction of LHR within 2° latitude was examined next. A weak positive correlation is found between the increase LHR and storm intensity for tropical cyclones above disturbance stage. Most tropical depressions, storms, and weak typhoons have from 0.4 to 0.6 of their LHR within 2° latitude of the center. The more intense typhoons show a value of approximately 0.7. Thus, among the more organized tropical cyclones examined, there is a general indication of the concentration of rainfall towards the storm center with increasing intensity.

A weak positive correlation is also found between storm intensity and the precipitation intensity parameter (PIP). The mean PIP for weak tropical cyclones (< 25 ms^{-1}) is .12, for storms and weak typhoons (25 to 45 ms^{-1}) is .34, and for intense typhoons (>45 ms^{-1}) is .47. Thus, as the tropical cyclone intensifies so does the rainfall intensity.

The azmuthal distribution of rainfall is also examined for tropical storms and typhoons. The rainfall distribution is rotated to a common axis based on the storm motion. The results indicate a slight preference for higher rainfall rates in the right half of the storm. Frank (1977) indicates a slight preference for the right-rear quadrant based on co mpositing conventional measurements.

5. COMPARISON OF WESTERN PACIFIC TYPHOONS AND EASTERN PACIFIC HURRICANES

Analysis of the ESMR-5 derived rainfall-rate estimates reveals that there are significant differences between tropical cyclones in eastern and western portions of the Pacific Ocean. The comparison of results for hurricanes and typhoon stage cyclones are shown in Table 1. A large disparity is seen in table for LHR between mature systems in the Western and Eastern Pacific. The numbers in the parentheses are the sample size. There are a greater number of observations at 2° latitude

Table 1 Mean rainfall-rate characteristics of Western Pacific typhoons and Eastern Pacific hurricanes.

	Western Pacific Typhoons	Eastern Pacific Hurricanes
LHR (2° latitude)	2.7×10^{14} W (34)	1.3×10^{14} W (11)
LHR (4° latitude)	5.0×10^{14} W (20)	1.6×10^{14} W (11)
Fraction of LHR (2° latitude from center)	0.54	0.81
PIP	0.38 (20)	0.25 (11)

for Western Pacific storm because of land contamination in the outer portions of some observations.

The LHR values for the Eastern Pacific hurricanes may be somewhat underestimated relative to the Western Pacific typhoons. This is because a freezing level height of 5 km is assumed in both cases and there appears to be a slight difference in the climatological freezing level, with the freezing level being lower in Eastern Pacific. However, the potential error due to this factor is small relative to the large difference noted in the table.

The fraction of LHR contained within the inner 2° latitude is calculated for a "mean" storm by simply computing the ratio 2° latitude LHR and the 4° latitude LHR in the table. The hurricanes of the Eastern Pacific are obviously, in the mean, more compact than their western counterparts. The PIP calculation shows that the Eastern Pacific storms have a smaller contribution from the heavier rain rates.

Thus, the results from this comparison indicate that the Eastern Pacific hurricanes have less LHR, less intense rainfall rates and rainfall more concentrated toward the center than do the Western Pacific typhoons. The reason for these differences are not clear, although the less favorable environmental conditions (less available moisture and cooler sea surface temperature) prevalent in the Eastern Pacific outside the Intertropical Convergence Zone (ITCZ) are probably producing a different type of tropical cyclone.

6. SUMMARY

The case study as well as the sub-sample of Western Pacific tropical cyclones indicate that the ESMR derived LHR and PIP increase with storm intensification and there is a tendency for rainfall to concentrate closer towards the center as the storm intensifies. ESMR derived rainfall rate also indicated in the mean heavier precipitation rates in the right half of the storm.

A comparison of Eastern Pacific hurricanes and Western Pacific typhoons shows that the Eastern Pacific storms have less LHR, have less intense rainfall rates, and have rainfall more concentrated towards the center. The difference in storm LHR is striking, with the Eastern Pacific storms having a mean value less than one half that of Western Pacific storms.

REFERENCES

Adler, R. F., and E. B. Rodgers, 1977: Satellite-observed latent heat release in a tropical cyclone. Mon. Wea. Rev., 105, 956-963.

Frank, W. M., 1977: The structure and energetics of the tropical cyclone, Part 1: Storm structure. Mon. Wea. Rev., 105, 1119-1135.

Wilheit, T. T., 1972: The electrically scanning microwave radiometer (ESMR) experiment. Nimbus 5 User's Guide, NASA Goddard Space Flight Center, 55-105.

_____, T. C. Chang, M. S. V. Rao, E. B. Rodgers and J. S. Theon, 1977: A satellite technique for quantitatively mapping rainfall rates over the oceans. J. Appl. Meteor., 16, 551-560.

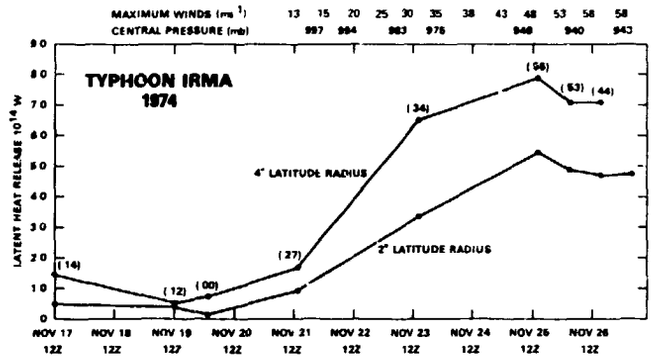

Fig. 1-LHR as a function of time at 2° and 4° latitude radius for tropical cyclone Irma. Numbers in parentheses are fractions of rainfall contributed by rainfall rates greater than 5 mmh^{-1}.

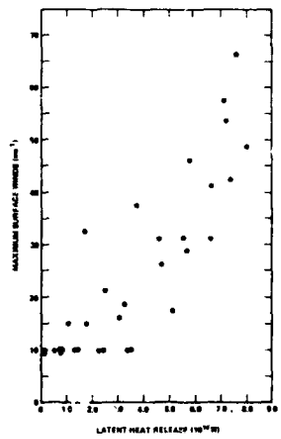

Fig. 2-Scatter diagram of storm intensity versus LHR for Western Pacific cyclones.

Paper No. 8

N79-20583

CLOUD TEMPERATURES AND PREDICTION OF HURRICANE INTENSITY

R. Cecil Gentry and Joseph Steranka, *General Electric Space Division, Beltsville, Maryland*
Edward Rodgers and William E. Shenk, *Goddard Space Flight Center, Greenbelt, Maryland*

ABSTRACT

Equivalent black body temperatures of clouds around tropical cyclones are used in a statistical technique to forecast changes in maximum winds for 24 hours in advance.

INTRODUCTION

Hurricane caused damages in the United States average over $600 million per year, and these damages vary exponentially with the maximum wind speeds. Historical surveys suggest that the damage varies with a power of the wind speed which is greater than 3. (Howard, et al 1972). This relationship emphasizes the importance of observing and forecasting the intensity of a tropical cyclone.

Reductions in aircraft reconnaissance of tropical cyclones in recent years to economize have motivated expanded efforts to use satellite data to observe and predict tropical cyclones. Results have been encouraging and efforts increase as each new satellite series makes improved data more readily available. The purpose of this paper is to present techniques which utilize satellite measured temperatures to forecast tropical cyclone intensity.

The hurricane is a heat engine with most of the fuel driving its winds coming ultimately from the latent heat released by the warm tropical air ascending in the cumulus towers prominent in the convective cloud system of the hurricane (Dunn and Miller, 1960). The intensity of this convection can be considered an index of the latent heat released and possibly of the storm intensity. Dvorak and earlier investigators (1973) have used the size of the dense overcast surrounding the center of the storm and the degree of organization of the spiral bands of convective clouds associated with the storm to identify the current intensity and to estimate the future intensity. Both of these parameters are by-products of the convection. Objective measurements of the cloud expanse and organization might then be not only crude indices of the organized convective activity, but also be expected to furnish information about the storm intensity and expected changes. The theoretical-numerical model experiments of Rosenthal (1977) suggest that maximum intensity of the vertical motion or convec-

tion should precede the time of maximum storm intensity by one or two days.

THE DATA

The equivalent black body temperatures for a number of storms were analyzed using the scheme illustrated in Figure 1 to get a measure of the expanse and organization of the storm. The rings concentric about the storm center are 111 km apart. The mean temperature for each ring was used in this study. The hypothesis is that the colder the mean temperatures of the cloud tops over a moderate sized area, the stronger and more persistent are the convection and maximum winds in the storm.

A test was made using 1970 Western Pacific Tropical Cyclones to determine if the colder temperatures occurred in intensifying storms. In Figure 2 the data for 1970 storms south of 30°N are stratified according to the change of intensity during the succeeding 24 hours. The four categories are: intensifying (maximum winds increasing at least 10 knots--12 cases), weakening (maximum winds decreasing at least 10 knots--4 cases), little change (wind change less than 10 knots--6 cases) and tropical storms which never intensified to the typhoon stage (5 cases). Graphs are plotted for the last 3 categories with the mean temperature for each ring plotted as the departure from the corresponding mean temperature for the itensifying storms. It is interesting that the greater the rate of intensification the colder the mean temperatures in all rings through 9. The intensifying storms are 15-20°C colder in rings 2-4 than the storms that never reached typhoon intensity, about 10°C colder in rings 1-8 than the weakening storms, and 4-10°C colder in rings 1-9 than the storms changing slowly in intensity.

Figure 3 illustrates the time-lag between the changes of equivalent black body temperatures of the cloud tops and the changes of the maximum winds in two typhoons. The temperature scale is inverted and for interpretation one might consider the temperature graph as a crude index of the convective activity. Note that the minimum temperature (or maximum of the convection index) for Typhoon Billie occurred more than 2 days earlier than the maximum winds. For Typhoon Hope the wind graph maximum lags by more than one day (missing data make it impractical to determine the exact time of the temperature minimum). These types of data have been examined for many storms and results suggest that changes in the maximum winds lag changes in the temperatures by 24 to 36 hours. This suggests the temperatures have predictive value. It is interesting that the time lag is about the same as the lag Rosenthal found with the model experiments.

Analyses of the data and reasoning suggest that the equivalent black body temperatures will vary with at least the: tropical cyclone intensity, rate of change of storm intensity,

latitude, month, and mean temperatures of the troposphere. Because of these and other factors, the data used in preparing the graphs in Figure 2 showed considerable scatter. It was necessary, therefore to consider parameters other than the temperatures when developing an objective technique. Even a cursory examination of the data reveals, for example, that the relationship between temperature and future storm intensity is different between storms that have been intensifying and those that have been weakening. Black body temperatures are also indicators of both the current and future intensities of the storm. These two effects need to be separated.

FORECASTS AND RESULTS

Two regression equations were developed using 61 cases from 1970 Western Pacific Tropical Cyclones as dependent data:

$$Y_W = 131.2 - 0.545\ X_1 + 0.436\ X_2$$

$$Y_S = 205.57 + 0.555X_2 - 0.634X_3 - 0.534X_4$$

where Y_W is the predicted 24-hour change in maximum winds (knots) for storms whose current maximum winds $\leq$ 65 knots, Y_S is the same for storms whose maximum winds exceed 65 knots, X_1 is mean equivalent black body temperature for area between 110 and 330 km radii about the storm center, X_2 is the change in maximum winds (knots) of the storm during the preceding 24 hours, X_3 is the mean temperature for area between 110 and 550 km radii, and X_4 is current maximum wind (knots) in the storm. Results are summarized in top of Table 1. For comparison forecasts were made by 2 persistence techniques which forecasters frequently use, i.e. no change, and persistence of preceding change for forecast period.

Similar data for independent cases taken from the 1973 and 1974 Western Pacific seasons are summarized in lower half of Table 1. The regression forecasts have errors 14 percent smaller than the best of the persistence techniques.

Inspection of the data reveals that small additional corrections to the forecasts can be made using latitude of the storm and season of the year as predictors, but more cases will be needed in the developmental sample before further stratification is justified. Data for other oceans are needed to determine what adjustment should be made in the equations before the technique is applied to storms in those oceans. At least a change in the constants and possibly a change in the coefficients will be required because of difference in mean sea and atmospheric temperatures for different ocean areas.

Table 1

Mean Forecast Errors in Knots

Developmental Cases

Classification	N	Regress.	No Change	Persistence of Change
Max Winds ≤ 65 kt.	24	8.4	12.6	12.3
Max Winds > 65 kt.	37	9.3	16.6	11.9
All Storms	61	8.9	15.0	12.1

Independent Cases

Max Winds ≤ 65 kt.	26	11.1	15.5	13.0
Max Winds > 65 kt.	20	15.8	18.4	18.3
All Storms	46	13.1	16.8	15.3

CONCLUSIONS

Convincing data have been presented indicating that the equivalent black body temperatures of clouds around tropical cyclones have predictive value for forecasting the change of intensity of the storm during the next 24 hours. An objective technique has been developed for making such forecasts. Preliminary tests with independent data indicate the technique is very competitive and probably superior to other techniques.

REFERENCES

1. Dvorak, Vernon F., 1973: A technique for the analysis and forecasting of tropical cyclone intensities from satellite pictures. NOAA Technical Memorandum NESS45, Department of Commerce. 19pp.

2. Dunn, Gordon E. and Banner I. Miller, 1960: Atlantic Hurricanes. Louisiana State University Press. pp 123ff.

3. Howard, Ronald A., James E. Matheson, and D. Warner North, 1972: The decision to seed hurricanes. Science, 176 1191-1201.

4. Rosenthal, Stanley L., 1977: Numerical simulation of tropical cyclone development with latent heat release by the resolvable scales. To be published in Journal of Atmospheric Science.

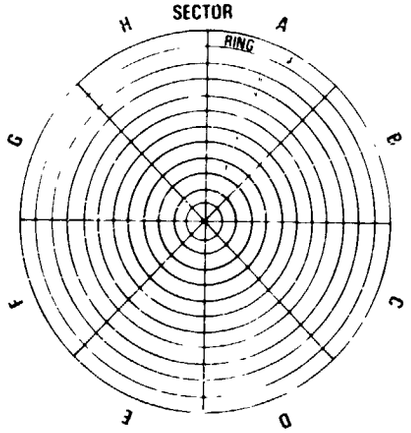

Fig. 1. Grid used in analyzing equivalent black body temperatures (T_{BB}). Spacing between circles is 111 km.

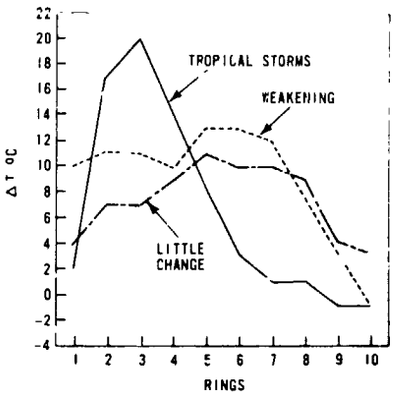

Fig 2. Mean equivalent black body temperatures for the three types of storms indicated are plotted as departures from corresponding means for intensifying storms. (See text).

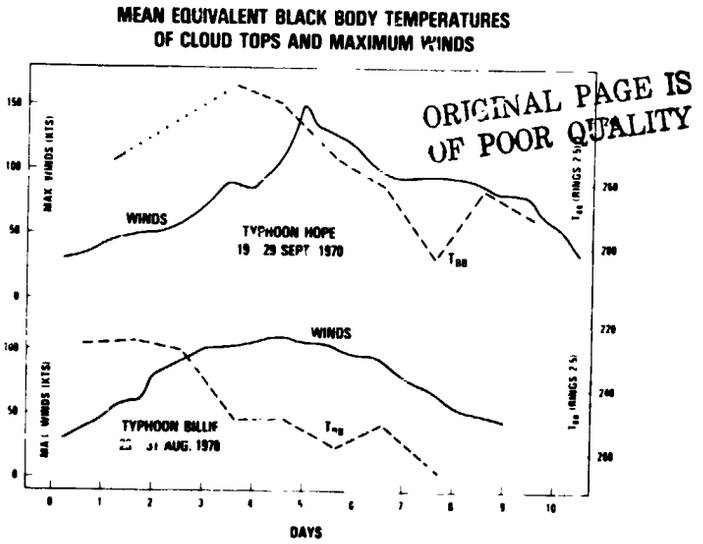

Fig. 3. The mean temperatures are for rings 2-5 of Figure 1. The dotted line indicates missing data. The graphs illustrate lag between maximum winds and mean equivalent black body temperatures ($\overline{T}_{BB}$).

Paper No. 9

N79-20584

OBJECTIVE TROPICAL CYCLONE ANALYSIS AND FORECASTING TECHNIQUE USING CONVENTIONAL AND NIMBUS-5 ELECTRICALLY SCANNING MICROWAVE RADIOMETER MEASUREMENTS

H. E. Hunter, *ADAPT Service Corporation, Reading, Mass.*
E. B Rodgers & W. E. Shenk, *Goddard Space Flight Center, Greenbelt, Maryland*

ABSTRACT

The ADAPT empirical analysis programs, based on finding an optimal representation of the data in the Karhunen-Loeve sense, have been applied to 120 observations of twenty-nine 1973 and 1974 Pacific tropical cyclones. Each observation consists of NIMBUS-5 Electrically Scanning Microwave Radiometer (ESMR) radiation measurements at 267 grid points covering and surrounding the tropical cyclone plus nine other non-satellite derived descriptors. Analysis and forecast algorithms to estimate storm motion and intensity have been developed for times ranging from the observation time up to 72 hours later. The 24 hr wind speed forecasts with an accuracy of 11.7 knots and position forecasts with accuracies 15% better than persistence have been demonstrated using independent tests.

INTRODUCTION

The release of latent heat through condensation and precipitation processes is essential to the development and maintenance of tropical cyclones. With the advent of the NIMBUS-5 Electrically Scanning Microwave Radiometer (ESMR), it has been possible to remotely measure the distribution of rainfall rates (latent heat release) within tropical cyclones over oceans and to relate this rainfall rate distribution to storm intensity (Adler and Rodgers, 1977). To more thoroughly examine this relationship, an empirical analysis developed by the ADAPT corporation was made to relate the ESMR derived tropical cyclone rainfall rate distribution to not only storm intensity but also to storm movement. In this paper the results from the empirical study will be presented.

ADAPT APPROACH

The general concept of the ADAPT approach is to take the data from the original high dimensional data space and transform it to a lower dimensional optimal analysis space. The unique approach allows the vast amount of data obtained from satellite from satellite derived radiation maps to be compacted into a more economical and mathematically convenient format. This is accomplished by applying a conventional transformation which goes under the names of: Karhunen-Loeve, Eigen vector, or Principal Component to data and vectors constructed from the pictures (Andrews, 1972 and Watanabe, 1965). The unique capability of the ADAPT programs is the capability to derive this transformation for large numbers of large data vectors. The grid used to transform the picture to a vector extends 5 degrees north of the center of the storm, 6.5 degrees south of the center of the

storm and 5 degrees east and west of the center of the storm. These 267 radiation points are supplemented by nine conventional measurements. All of the empirical data analysis is then performed in the lower dimensional analysis space. All linear analysis including regression and linear classification algorithm development result in defining lines in the analysis space. The transpose of the Eigen vector matrix is used to transform the answer or result of the empirical analysis back to the original data space.

FORECAST ALGORITHMS

Linear data histories were constructed from the nine non-satellite derived descriptors and 267 satellite derived ESMR radiation measurements for each observation. The resulting histories were transformed to the ADAPT optimal analysis space and in this space more than 20 analysis and forecast algorithms were developed. These algorithms included classification algorithms such as algorithms to separate intensifying versus weakening storms and regression algorithms to forecast properties of the storm such as future wind speed and position. In this paper, we shall only discuss those for which the most significant results were obtained, which were the algorithms for forecasting future wind speed and position.

Tables 1 and 2 summarize the performance for these algorithms, respectively. These tables list this performance for the 12, 24, 48 and 72 hour estimates. The second column in these tables present the performance obtained using persistence calculations based on best track information. The third and fourth columns of these tables present the performance achieved using only the non-satellite derived descriptors. The performance is defined by both the actual value and the percent improvement relative to persistence. The fifth and sixth columns give the actual value and percent improvement relative to persistence using only the satellite derived data. The seventh column was derived using the ADAPT performance map, see Hunter, et al. (1977) and gives the expected performance using both conventional and satellite data in terms of percent improvement over persistence. These results are possible when an adequate number (200-1000) of training cases is available to derive the algorithm. The performance of each algorithm is listed both in terms of the average error using the algorithm and the standard deviation of the estimate about the actual. The standard deviation of the estimated value about the actual value is the parameter which is optimized by a regression analysis and is therefore a better measure of the success of the regression technique then the average error.

ANALYSIS OF ALGORITHMS

One of the most significant results apparent from an examination of Tables 1 and 2 are that as far as the independent test performance demonstrated one has achieved as good a performance using only the conventional data as one was able to obtain using the conventional plus satellite derived information. This result is misleading because it is based on limitations of the data set. Analysis of the algorithms showed: 1) that if one had more (300-1000) training cases the satellite derived measurements should significantly (as shown in Column 7) improve the results presented in Tables 1 and 2 for the longer term forecasts and 2) that even without additional training data the use of satellite data allows one to remove the restriction of using best track data to achieve the results presented in these tables. The removal of the best track data restriction is significant since it allows one to make the fore-

cast prior to obtaining the best track information.

An important ADAPT output for understanding the physics behind an algorithm is the relative importance map obtained by transforming the algorithm through the reverse of the sampling procedure and plotting its absolute values. Figure 1 is such a plot. On this figure, those regions having values of 3 are most important to estimating the 12 hour max wind speed, regions having no numeral present are least important and the regions having the values of 1 and 2 lie in between. Thus, storm intensity is related more to the configuration of the rain bands south of the eye than to any other area.

SUMMARY

The application of the ADAPT and empirical analysis programs to observations of tropical storms has resulted in the development of algorithms which can significantly improve the accuracy of wind speed and long term position forecasts relative to persistence. The limited number of cases available for study, although sufficient to allow full use of the information in the conventional data, severely restricted the use of the information in the satellite pictures.

REFERENCES

Adler, R.F., and E.B. Rodgers, 1977: Satellite-Observed Latent Heat Release in a Tropical Cyclone, Mon. Wea. Rev., 105, 956-963.

Andrews, Harry C., "Introduction to Mathematical Techniques in Pattern Recognition," John Wiley & Sons, Inc. 1972.

Hunter, Rodgers, & Shenk, "Objective Parameter Estimation and Forecasting Using ESMR Measurements," to be presented at the Eleventh Technical Conference on Hurricanes and Tropical Meteorology of the A.M.S., Dec. 1977.

Watanabe, S., "Karhunen-Loeve Expansion and Factor Analysis Theoretical Remarks and Predictions", Transaction of the 4th Prague Conference, 1965, Pages 635 thru 660.

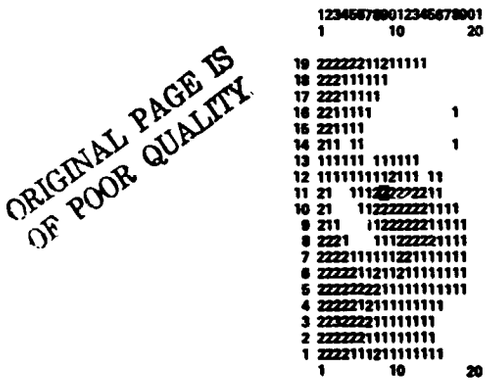

Fig. 1—Importance of ESMR radiation to estimate the 12 hr max. wind.

TABLE 1 – PERFORMANCE OF WIND SPEED FORECAST ALGORITHMS

ALGORITHMS	PERSISTANCE ESTIMATES	PERFORMANCE				
		CONVENTIONAL		SATELLITE DEMONSTRATED		PROJECTED
	KTS	KTS	% IMPROVE	KTS	% IMPROVE	% IMPROVE
12-HR FORECAST						
AVG ERROR	6.8	6.2	7	6.4	6	
STD DEV	9.0	7.9	12	7.9	12	14
24-HR FORECAST						
AVG ERROR	20.0	11.7	41	11.7	41	
STD DEV	23.0	15.5	33	15.4	33	38
48-HR FORECAST						
AVG ERROR	39.0	14.8	62	15	62	
STD DEV	53.0	18.8	65	19.2	64	35
72-HR FORECAST						
AVG ERROR	55.0	20	64	20	64	
STD DEV	76.0	24	68	25	67	31

TABLE 2 – PERFORMANCE OF POSITION FORECAST ALGORITHMS

ALGORITHM	PERSISTANCE ESTIMATES	PERFORMANCE				
		CONVENTIONAL		SATELLITE DEMONSTRATED		PROJECTED
	N.Mi.	N.Mi.	% IMPROVE	N.Mi.	% IMPROVE	% IMPROVE
12-HR LAT FORECAST						
AVG ERROR	25	25	NONE	25	NONE	
STD DEV	40	36	10	35	23	15
12-HR LONG FORECAST						
AVG ERROR	26	26	NONE	26	NONE	
STD DEV	36	36	NONE	36	NONE	5
24-HR LAT FORECAST						
AVG ERROR	57	54	6	54	3	
STD DEV	83	71	14	71	14	25
24-HR LONG FORECAST						
AVG ERROR	63	58	8	61	3	
STD DEV	93	77	17	80	14	30
48-HR LAT FORECAST						
AVG ERROR	132	118	11	121	8	
STD DEV	184	157	15	156	15	25
48-HR LONG FORECAST						
AVG ERROR	157	147	6	148	6	
STD DEV	219	194	11	192	12	30
72-HR LAT FORECAST						
AVG ERROR	220	174	21	185	16	
STD DEV	290	228	22	233	20	15
72-HR LONG FORECAST						
AVG ERROR	275	245	11	265	4	
STD DEV	365	330	10	330	10	25

Paper No. 10

N79-20585

REMOTE SENSING OF HURRICANE WAVES

David B. King and Omar H. Shemdin, *Jet Propulsion Laboratory, Pasadena, California*

ABSTRACT

A program has been undertaken to obtain data on wind generated ocean waves in hurricanes by remote sensing techniques. The sensor, a Synthetic Aperture Radar, has collected the first data ever on the directional wave climate throughout a hurricane. This information has been found to have inconsistencies with present hurricane wave generation models.

INTRODUCTION

During the summer of 1976, we began a program to collect ocean wave data in hurricanes. Our approach was one of remote sensing with the use of a Synthetic Aperture Radar (SAR). This new technique allowed us to collect types of hurricane wave data that had never been done before.

Although active research to understand and model wind generated ocean waves has been carried out for the past twenty years, the problem is not yet fully solved. One reason has been a lack of sufficient high quality data. This is particularly true for the important case of hurricane generated waves. This lack of data is traced to two causes. One is the infrequency with which hurricanes pass over wave recording stations, and the second is the fact that even when hurricanes do, the extreme environment frequently completely destroys the sensors. However, recently the picture has improved somewhat. Good surface data has become available from two programs. One was a consortium of oil companies who instrumented a number of offshore oil platforms in the Gulf of Mexico. The other is an ongoing program by the NOAA Data Buoy Office that has deployed buoys at permanent stations around the U.S. coast.

However, even these two programs have a number of problems. One is that, since the platform is fixed, the data that is recorded represent a single transect of the storm wherever it passed over the sensor. A second problem is that, while these sensors are designed to measure wave height, they cannot measure wave direction.

Our program was designed to remedy these problems. The SAR was placed on board a NASA CV-990 research aircraft that was flown to the storm. Since it remotely sensed the sea surface, it was protected from the extreme environment. Since the aircraft traveled much faster than the storms, it could collect data from all parts of the storm. Finally, the output product was an image of the sea surface which would supply complete information on the directional properties of the waves.

Data Collection

In 1976, Phase I of the hurricane mission was conducted. There were five flights into hurricanes to collect wave data. These were Hurricane Emmy on August 24 and 25, Hurricane Frances on August 31 and Hurricane Gloria on September 28 and 30. All of these storms were in the western Atlantic.

Phase II of the hurricane mission was conducted during 1977. However, this year we had the opportunity to collect data in only one hurricane. This was Hurricane Heather, an eastern Pacific typhoon off the coast of Baja California on October 5.

The primary output product of the SAR after correlation is a photograph-like image strip of the sea surface. The strip represents an area beneath and to the right of the aircraft that is approximately 10 km wide and is as long as the distance the aircraft flew in a given direction.

Data Analysis

Most of the analysis that has been done so far has been done for Hurricane Gloria on September 30. The imagery was plotted with correct reference to the center of the storm. This gave us the first picture ever of the directional wave field throughout a hurricane. A number of points became obvious. The wave pattern was radially asymmetric. The waves in the front half of the storm were better organized, had longer wavelengths and appeared to be traveling outward from the storm in something of an arc. The waves in the rear, particularly the right rear quadrant, appeared to be very disorganized.

The asymmetries can be explained intuitively. The winds are stronger on the right hand side of a moving hurricane. This is due to the added speed caused by the storm's motion. (The winds blow counterclockwise.) Furthermore, the waves generated under this stronger wind travel in the same direction as the storm does and therefore tend to stay in the generating area much longer. Therefore, asymmetries in the wave field should be expected and they should increase with storm speed.

The dominant waves in many parts of the storm were not traveling in the same direction as the local wind. In parts of the left front quadrant, they were traveling at right angles to the local wind. This is not in agreement with the few present hurricane wave generation models available. This is understandable in light of the fact that these models are partly empirical and have been calibrated using available non-directional wave data. However, it does point up the need for better models.

The directionality of the waves was checked and quantified using directional spectral analysis. Selected portions of the imagery were digitized and then corrected for certain geometric distortions. These were then transformed into two dimensional spectra. This gave a plot of wave intensity versus wave length and direction.

Conclusions

Work on this project is continuing. At present we are reprocessing portions of the data so that a detailed comparison of the wave patterns in the different hurricanes can be made. We have also seen the need for a better hurricane wave generation model using this new data and have begun to develop one. Finally, it is expected that the data collection portion of this project will continue next summer, in coordination with the Seasat A satellite.

References

Elachi, C., T. Thompson and D. King, "Observation of the Ocean Wave Pattern under Hurricane Gloria with an Airborne Synthetic Aperture Radar." Science. Accepted for publication.

Shemdin, Omar H. and David B. King, "Hurricane Waves, Currents, and Storm Surge: An Assessment of the State of the Art." Proceedings of the U.S.-Southeast Asia Symposium on "Engineering for Natural Hazards Protection," Manila, Philippines, 1977.

Thompson, Thomas W., Elmer S. McMillan and David B. King, Jr., "JPL Radar Operations, Summer '76 Hurricane Expedition, 17 August 1976 - 3 October 1976." JPL Document 622-18. 10 December 1976.

Paper No. 11

N79-20586

ADVANCES IN LOCAL AREA, MESOSCALE MODELING

Paul R. Swan and In Young Lee+, *Ames Research Center, Moffett Field, CA 94035*

ABSTRACT

A two-layer, mesoscale boundary layer model is being developed and validated against San Francisco Bay Area observational data.

INTRODUCTION

Although many research efforts are being directed to the numerical simulation and study of mesoscale weather phenomena, most of these have been devoted to high priority problems associated with very energetic destructive events such as tornadoes or thunderstorms. There are also, however, socially important consequences to non-violent meteorological phenomena which are mesoscale in extent, and which are confined essentially to the planetary boundary layer (PBL). Among these we might list complex urban heat island effects on local climate, detailed variations of diurnal winds due to terrain features and coastlines, occurrence and dissipation of fog, ventilation of urban areas affected by pollution, and the selection of sites for wind power generators. In addition, the PBL needs to be more adequately simulated for use in global circulation models, possibly also for advanced stratospheric models, and certainly in future attempts to couple atmosphere and ocean circulation models.

The computer model described in this paper is one of two being developed at ARC to fill this gap in meteorological modeling. A wide spectrum of numerical techniques is available for approaching such a task. The present model is of intermediate complexity, and has been configured to provide results economically in terms of computational cost, while retaining representations of all of the physical interactions of interest.

+NRC Resident Research Associate

COMPUTATIONAL APPROACH

On the time scale of a few tens of hours, the PBL may be considered to be the result of the free air mass of the troposphere interacting with the complex surface of the Earth. We, therefore, structure the simulation as an initial-boundary value fluid dynamics problem in which equations are solved for the PBL wind, temperature and moisture fields given initial conditions, the synoptic meteorology aloft, and the physical characteristics of the underlying surface. Driving this set of equations is the diurnally varying solar radiation which heats the surface to an extent depending on its non-uniform thermal characteristics.

In order to reduce the computational problem to modest dimensions, the three-dimensional equations describing such a PBL are first integrated analytically from the surface to the interface with the free atmosphere. The resulting equations then describe the time and space variations of the vertical averages of the PBL horizontal winds, potential temperature, water vapor, and clouds or fog. In addition, equations describing the time and space variations of the depth of the PBL are obtained. The resulting set of equations then constitutes a two-layer model composed of the PBL and the (specified) free atmosphere above. This set of equations is solved numerically on a horizontal grid using finite difference techniques. The initial computer runs described in the next sections used a 20 km grid spacing; the validation runs will eventually use a grid dimension of 2 km or less.

INITIAL SIMULATIONS

The initial test runs of the program were carried out for an area 300 km by 300 km generally east and south of San Francisco. The initial values were taken from an Oakland rawinsonde sounding, and the free atmosphere values were then held fixed throughout the simulation. While observations are not available to verify the results of these runs, the overall behavior of the PBL is clearly interpretable in terms of generally understood phenomena. The PBL winds, not illustrated here, could be seen to be blocked by the coastal mountains and the Mt. Diablo Range, and were channelled through the Santa Clara, Salinas and Central Valleys. There was a northeasterly mountain wind in the Sierra Nevada induced by the lateral temperature differential produced by radiative cooling in this area.

The mixed layer depth, shown in Fig. 1, generally did not change over the ocean, but became shallower over the Sierra Nevada, south of the Central Valley, and south of the Diablo Range, where the wind was relatively strong at all times. Deviations of the potential temperature of the mixed layer from the ocean temperature are shown in Fig. 2. In general, the temperature of the marine layer stays constant and warm air persists over the Livermore, Santa Clara, Salinas and Central Valleys, while cool air exists over the Sierra Nevada region at all times.

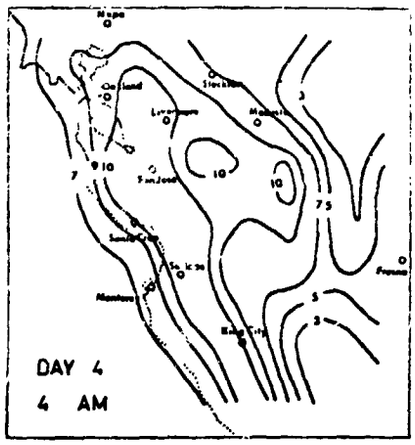

Figure 1

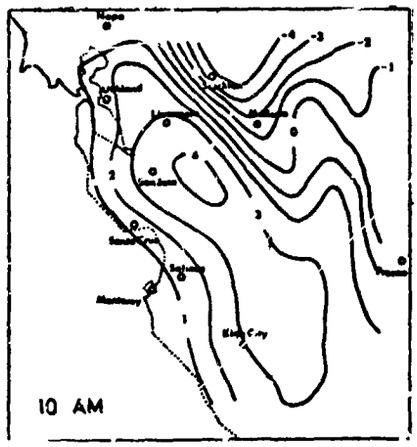

Figure 2

The clouds shown in Fig. 3 are formed when the potential temperature of the mixed layer is cooler than that of the marine layer, and the moist air brought in from the ocean becomes supersaturated. The excess water vapor due to supersaturation then condenses and forms clouds. We expect rain from a cloud whose water content is greater than 1.0 gm/kg, but precipitation had not been included in the model when these initial runs were made.

PRELIMINARY VALIDATIONS

Extensive field observations of the PBL were made by Stanford Research Institute in the S.F. Bay Area for the California Air Resources Board in 1976. We selected for validation purposes two days when the elevated subsidence inversion was particularly strong and persistent. There are, of course, limitations in using observations for model validation. One is that the observations represent point measurements in time and space, while the model predicts averages over large

intervals. A second is that the LIDAR and SODAR soundings measure physical characteristics of the atmosphere which are not the quantities predicted by the model. The interpretations of the echoes from these sounders in terms of PBL depth is somewhat ambiguous, and may require revision as we learn more about the PBL physics. Nevertheless, with all of these reservations, we show in Fig. 4 a comparison at one location in the model. Here the crosses represent the point soundings interpreted as PBL depth, and the continuous line shows the model results as a function of time for one day.

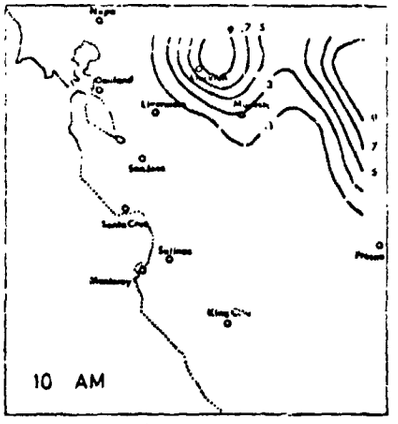

Figure 3

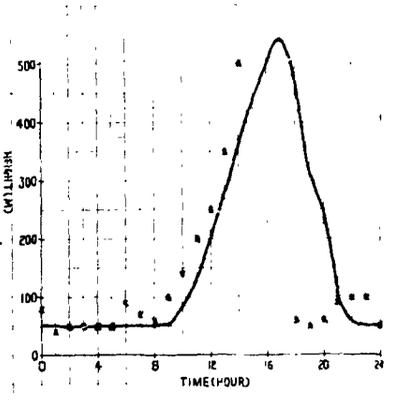

Figure 4

The comparison of these PBL depths at night, and during midday hours, is excellent. However, the observed PBL disappears at least three hours before that of the model in the late afternoon. Most other northern locations in the model show a similar discrepancy. At a location in the southern half of the model, the daytime observed PBL depth is only half that predicted by the model, but the phase of the growth and destruction of the daytime mixed layer is excellent.

The wind direction at the northern location is shown in Fig. 5. Here the circles are model values, with subjectively drawn solid lines; the crosses represent the point observations. The magnitudes of these wind values are in excellent agreement, the computed values being at worst about 60% too large in the early morning hours, but thereafter tracking the observed values to within experimental error. The direction of the wind, however, does not correspond quite as well. The observed nighttime southeast wind changes much

more rapidly to the northwest than does the computed wind. These discrepancies may well be due to the large grid used in these first runs, since the area of these observations included complex terrain effects which are very poorly resolved on the 20 km grid.

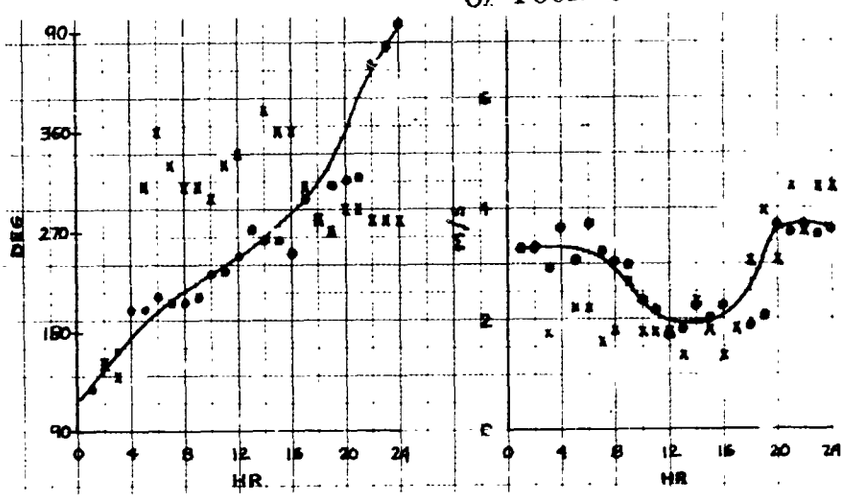

Figure 5

We intend next to adopt a nested grid approach using the 20 km solutions as transverse boundary conditions for a 2 km grid of limited extent. This will enable us to use the large scale (100 km) terrain and shoreline structure to configure the large scale fields properly, and then to use fine scale surface conditions to obtain fields more nearly approximating the point observations.

When these validation studies have been completed, and while research continues on internal parameterizations of the model, we will be using the program winds to advect pollutants in a photochemical dispersion model. This will be the first step in a study of the environmental impact on urban air quality of the use of short-take-off-and-landing jet aircraft as commercial transports, and will use a very detailed airport source inventory which has recently been developed at ARC.

Paper No. 12

N79-20587

OBSERVATIONS OF THE MICROCLIMATE OF A LAKE UNDER COLD AIR ADVECTIVE CONDITIONS

R. G. Bill, Jr., R. A. Sutherland, and J. F. Bartholic, *Institute of Food and Agricultural Sciences, University of Florida, Gainesville, Florida*

ABSTRACT

The moderating effects of Lake Apopka, Florida, on downwind surface temperatures were evaluated under cold air advective conditions. Point temperature measurements north and south of the lake and data obtained from the NOAA satellite and a thermal scanner flown at 1.6 km, indicate that, under conditions of moderate winds (>4m/sec), surface temperatures directly downwind may be higher than surrounding surface temperatures by as much as 5°C. With surface wind speed less than 1m/sec, no substantial temperature effects were observed. Results of this study are being used in land use planning, lake level control and in agriculture for selecting planting sites.

Introduction

The moderating effects of large bodies of water on the surface temperatures of coastal regions have been noted qualitatively by climatologists for many years. On a much smaller scale, agriculturalists have been aware of similar thermal effects produced by the plumes of lakes and have used this information as an aid in the selection of growing sites for crop varieties which are subject to cold damage. For example, in Florida, citrus growers have found through experience that by planting on the southern shores of lakes, they can obtain some moderating effects on minimum temperatures that occur at night during freeze conditions when winds are predominately from the north [Lawrence (1963), Bartholic and Sutherland (1975)]. While these practical effects are well known, surface temperature data is quite sparse [see eg. Geiger (1965)] and no detailed quantitative data is available concerning energy transport, and flow conditions associated with such convective plumes.

The transport mechanisms include both turbulent

and radiative transfer. Under typical nocturnal cold front conditions, lakes, being warmer than the air and surrounding land, release sensible and latent heat. As the moist buoyant plume is advected beyond the lake by the moving air mass, sensible and/or latent heat (depending upon the downwind dewpoint temperature) is transferred by turbulent diffusion to the ground. The radiation energy balance of the surface downwind of the lake may also be affected by advection of water vapor from the evaporating lake surface. That is, local changes in the vertical profiles of absolute humidity may change the net radiation loss from the ground.

In this investigation, aircraft and satellite thermal scanner data was used to access the lake effect. Ground measurements included hourly values of wind speed and direction, and soil, plant, air and dewpoint temperatures.

Description of the Site

Lake Apopka is located in the central portion of the Florida peninsula (see Figure 1). The lake is approximately 13 km across and has a mean depth of 1.65 m. Large areas of citrus exist both south and east of the lake. These are low flat areas with sandy soils not normally well adapted for citrus due to the freeze susceptibility resulting from cold air drainage. There is also a considerable area of citrus growth west of the lake, on land with a relatively high elevation. The area north of the lake is characterized by organic soils and is used for vegetable farming.

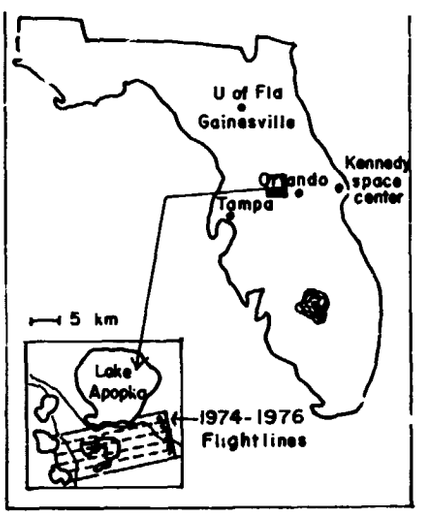

Fig.1 Map showing position in Fla.

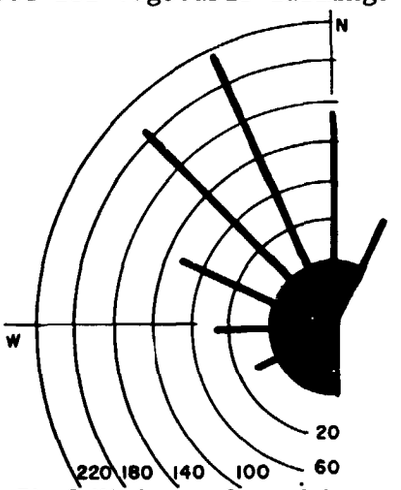

Fig.2 Windrose of total hours from designated directions at Orlando (72 freeze events, '34-'77)

Wind direction during serious freezes is predominately from the N.W. quadrant. A more precise description of wind direction during freeze episodes is shown in Figure 2.

Small Scale Analysis of Temperature Regimes

Because of the NOAA satellite's high resolution, detailed analysis of temperature patterns on a small scale should be possible. It would be particularly helpful if this data could be used to zero in on specific warm areas where plantings could be made and to evaluate the area of temperature modified by Lake Apopka.

Our analysis showed that detailed temperature patterns could be observed. The lakes had the warmest temperatures and the land immediately around the lakes, particularly on the southern side were shown to be warm. Large temperature differences were detectable even with this resolution. Figure 3 shows general temperature patterns for warm, intermediate and cool areas. These general areas have been known from historic records, however, the delineation of the areas has never before been clearly shown. For example, the muck land north of Lake Apopka generally has cooler temperatures than the land south of the lake. This muck and associated low land is clearly delineated as cold and intermediate around the edges of the muck area. It was possible with the Image 100 to overlay the thermal imagery with the general native vegetation map for that area. This overlay analysis showed first that the lakes clearly showed up on the thermal imagery and overlayed nearly perfectly. Second, the low-lying muck land north of the lake and flat wood areas (most of the area in the left half of the scene) which are normally low were in the cold or intermediate temperature categories. Third, the well-drained upland areas now used largely for citrus were almost exclusively in the warmer temperature regimes.

From analysis of the satellite data, the cold muck land and moderated warm area south of Lake Apopka were clearly shown. Detailed changes in temperature downwind and the plume effect, however were not discernible. Thus, aircraft thermal scanner data was obtained south of the lake.

Lake Effect as Detected with an Aircraft-Mounted Thermal Scanner

General features of the lake effect as shown in thermal imagery appear in Figure 4. The figure was produced by first constructing a mosaic from the four

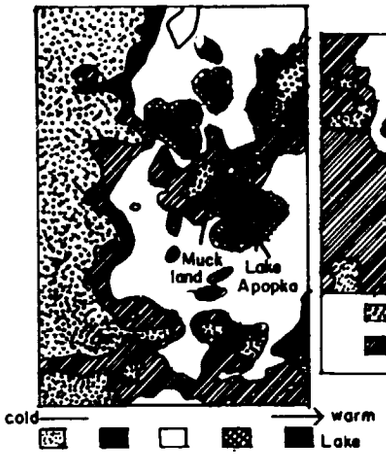

Fig.3 Analysis of NOAA-3 satellite thermal data showing cold temp. patterns in the vacinity of Lake Apopka for 2200, March 4, 1975.

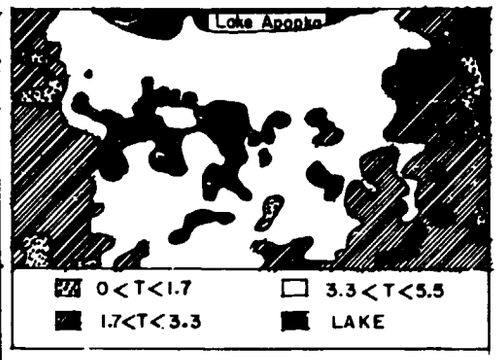

Fig.4. Temperature regimes drawn from a mosaic of aircraft thermal data south of Lake Apopka at 0500 on 10 Jan. 1976.

flightlines, digitizing the data and outlining the regions of various temperature regimes. This particular set of data was obtained from a mission flown at 0500 on 10 Jan. 1976 and shows the same general trends which were found on the 1974 missions which we will discuss in detail. In order to gain a quantative evaluation of the lake effect the 1974 data were digitized on a grid with rows (west-east) spaced 0.3 km apart and columns (north-south) spaced 1.2 km apart. Average elevations were also digitized on the same grid. Some caution must be used at this point since the data has not been corrected for emissivity, however, results from a model which accounts for scattering in the cavity formed by tree rows show that the error variation from grove to grove is less than about $1^{0}C$ except for extremely bare fields [Sutherland and Bartholic (1977)]. Also errors caused by variation in emissivity are diminished by the grid reduction method since the area, when viewed on a large scale, is essentially homogenous.

Since the leeward effect of the lake was to be studied, those columns not immediately south of the lake were eliminated from this particular analysis. Also data points falling on or near smaller lakes were eliminated from the analysis. From examination of the raw data it was apparent that there was little, if any, effect due to elevation on this night. This was corroborated in the analysis which showed elevation to be statistically insignificant. This is to be expected

since wind speeds were high on this night (3-7 m/sec). Figure 5 shows the smoothed curves for the three missions of 2200, 0100 and 0400 on the night of 14-15 February 1974. The 0100 and 0400 data look very similar except that the 0100 temperatures are slightly higher with both showing a steady decline.

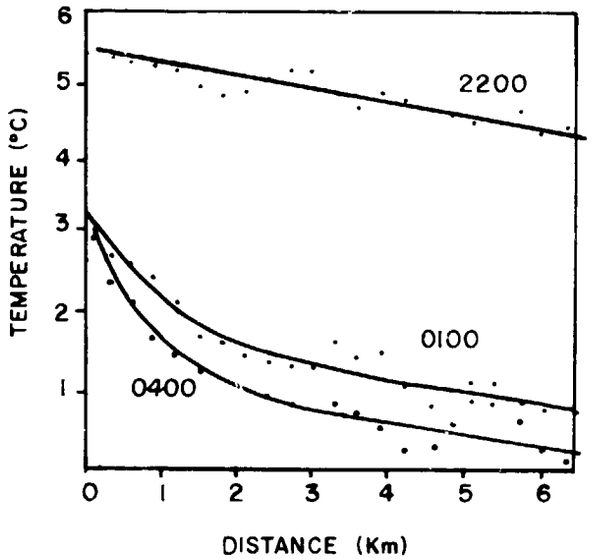

Fig.5. Plot of temperature vs distance from lake for 1974 missions.

References

Bartholic, J.F. and R.A. Sutherland: 1975, "Modification of Nocturnal Crop Temperatures by a Lake," Twelfth Agriculture and Forest Meteorology Conference. April 14-16, 7-9.

Geiger, R.: 1965, The Climate Near the Ground Translated by Scripta Technica Inc. from the 4th German ed., Harvard University Press, Cambridge, Mass. 611 pp.

Lawrence, F.P.: 1963, "Selecting a Grove Site,"Agricultural Extension Service Gainesville Florida, Circular 185A.

Sutherland, R.A., and J.F. Bartholic: 1974, "Aircraft-Mounted Thermal Scanner to Determine Grove Temperatures During Freeze Conditions," Proceeding Fla. State Hort. Soc., 87, 66-69.

Paper No. 13

WIND SPEED AND AEROSOL OPTICAL THICKNESS ESTIMATES FROM AIRCRAFT OBSERVATIONS OF SEA GLITTER

R. S. Fraser, *Goddard Space Flight Center, Greenbelt, Maryland*
Ziauddin Ahmad, *Systems and Applied Sciences Corp., Riverdale, MD*

INTRODUCTION

The surface wind velocity, tropospheric aerosol optical thickness, and trace amounts of tropospheric gases are important parameters for meteorolc ~ and air pollution control. Except for the amount of water vapor, no operational system for measuring these parameters from satellites has been developed. The optical characteristics of the bright glitter pattern of the sunlight reflected from water can, in principle, be used for this purpose. To investigate the validity of this concept, radiances observed from aircraft are used to measure the surface wind speed and aerosol optical thickness.

An elementary explanation of the physics involved begins with consideration of a smooth water surface associated with a calm wind. Then the sea would reflect light like a plane mirror. The brilliant image of the sun would be a few percent of the radiance of the direct sunlight, and the angular extent of the image would be one-half degree, the same as that of the sun itself. As the wind speed increases, the water becomes rougher, and the sun's image broadens out into a glitter pattern. We know, of course, the glitter radiance is strong in the nadir direction, when the sun is at the zenith, but even when the sun is only 25° above the horizon, the glitter has been observed from aircraft in the nadir direction (Hovis, 1977). The wind velocity determines the shape of the glitter pattern, and its brightness can be utilized for measuring optical thickness.

Levanon (1971) has used the observations from the ATS-1 synchronous satellite for determining the surface wind speed with an accuracy of ± 1 m/s. His method involved recording the radiance of an arbitrary point as the glitter pattern crosses it from east to west. The main restriction is that the spot remains free of clouds and that the wind velocity is constant during the two hours required to measure the width of the

glitter pattern.

OBSERVATIONS

Dr. Curran made the aircraft radiance observations used in this study. His purpose was to measure cloud parameters. A scanning radiometer measured the radiance in several spectral channels within 45° of the nadir and in a plane transverse to the aircraft motion. The observations presented here were taken under nearly cloudless skies over the Pacific Ocean. The CV990 aircraft flew at a height of 150 m and with a heading of 292°. The solar zenith angle was 20°, and its azimuth from the scan plane was 41°. Hence, the scan passed along the fringe of the glitter pattern. The λ765 nm channel is chosen, since the atmospheric gaseous absorption is negligible, while aerosol attenuation is dominant. The observed radiances are plotted as points in the accompanying figure. Each point represents an average of 380 instantaneous readings. The error bars of ±10% indicate an uncertainty of ±5% in the solar constant and ±5% in the laboratory calibration.

METHOD

The method of obtaining the wind speed and the aerosol optical thickness is to develop a radiative transfer model of the ocean-atmosphere system that can account for the measured radiances. Reflection from the rough sea surface is computed by the method of Cox and Munk (1955). The sea slopes are assumed to be distributed isotropically, independent of the wind direction. The wind speed (V) in m/s at a height of 14 m is related to the slope variance (s^2) by $V = 0.6 + 195\ s^2$.

The aerosol model consists of a distribution of sizes described by Deirmendjian's (1968) haze L. The particles are assumed to be moderately absorbing spheres with an index of refraction $m = 1.5 - 0.03i$. The vertical distribution of the particles is similar to the profile used by McClatchey et al. (1971). The total aerosol optical thickness of the model is derived from the measured radiances. The other atmospheric constituents are a scattering gas with an optical thickness of 0.037 and ozone with an absorption optical thickness of 0.008.

RESULTS

The surface wind speed depends strongly on the width of the glitter pattern. Accordingly, the value derived with this emphasis is 9.3 m/s, which compares favorably with a measured value of 8.9 m/s, extrapolated to the surface from the aircraft height of 150 m. The expected error in both values is ±1 m/s. After the shape of the glitter pattern has been accounted for, the aerosol optical thickness is derived from the absolute values of the radiance and is 0.43. Its accuracy in this

periment approximately equals the relative radiance error. The error depends on the measurement accuracy (±10%) and on the wind speed estimate (±1 m/s). The radiance of the bright part of the glitter pattern is inversely proportional to the wind speed. The corresponding relative radiance error equals the negative of the relative wind speed error. In this experiment, this relative radiance error is $1/9.3 = \pm 0.11$. The total radiance error, and also the optical thickness error, equals the root mean sum of measurement and wind speed errors, which is ±0.15. No other estimate of the aerosol optical thickness, not even a climatological value for the region, is available for comparison.

Using an aerosol optical thickness of 0.43 and a wind speed of 9.3 m/s in our model, we have computed the radiances for three heights. The radiances just above sea level agree well with measured values on the anti-solar side of the glitter, or on the north-northeastern side. The agreement is not as good on the solar side, perhaps because the sea slope distribution function is skewed, and not symmetrical as assumed.

The width of the computed radiance pattern at the aircraft height (150 m) diverges from the measured value, indicating that we have overestimated the wind speed by not accounting for the scattered light between the sea surface and the aircraft. The radiances at 50 km, or higher, are much reduced in contrast from the sea level values. The path radiance contributes at least one-half of the total radiance and has to be accounted for in estimating both the optical thickness and wind speed. We will investigate the characteristics of the high-level radiances by studying observations of the glitter pattern at a height of 11 km.

The region of the sea covered by the glitter pattern observable from a satellite can be specified by the angle between the half-power points of the high-altitude radiance curve. This angle is 40° and implies that surface facets reflecting light in the direction of the half-power points are inclined $\pm 10^\circ$ from the horizontal. This in turn indicates that the glitter would extend $\pm 10^\circ$ in latitude and longitude from the subsatellite point of a geostationary satellite, when the sun is favorably located at the zenith.

REFERENCES

Cox, C. and Munk, W. (1955), Some Problems in Optical Oceanography, J. Marine Res. 14, 63-78.

Deirmendjian, D. (1969), Electromagnetic Scattering on Spherical Polydispersions (American Elsevier Publishing Co., Inc., New York), 290 p.

Hovis, W. A. (1977), Private communication.

Levanon, N. (1971), Determination of the Sea Surface Slope Distribution and Wind Velocity using Sun Glitter Viewed from a Synchronous Satellite, J. Phys. Ocean. 1, 214-220.

McClatchey, R. A., Fenn. R. W., Selby, J. E. A., Volz, F. E., Garing, J. S. (1971), Optical Properties of the Atmosphere (Air Force Cambridge Research Laboratories, No. AFCRL-71-0279), 85 p.

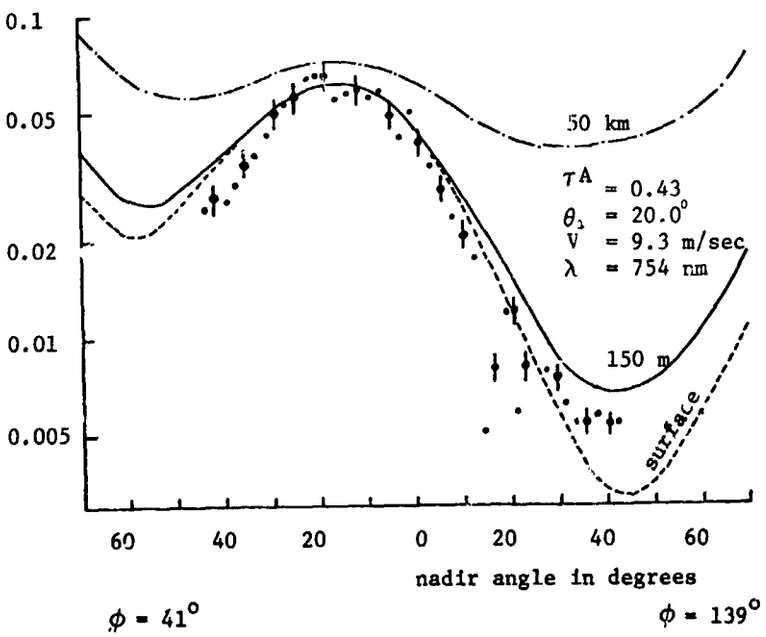

Radiances measured at a height of 150 m (dots) and computed for 3 heights.

Paper No. 14

THE EVALUATION BY NUMERICAL SIMULATION OF THE DESIGN FOR A MICROWAVE PRESSURE SOUNDER (MPS)

Dennis, A. Flower, *Jet Propulsion Laboratory, Pasadena, California*
Gordon E. Peckham *Heriot-Watt University, Edinburgh, Scotland*

ABSTRACT

The potential accuracy of an active multifrequency millimeter-wave technique for the remote measurement of atmospheric pressure at the Earth's surface has been investigated by numerical simulation.

Introduction

Surface pressure is perhaps the single most significant physical parameter for meteorological purposes as it is the driving force for atmospheric circulation. The development of a sufficiently accurate (i.e. better than 3 mb r.m.s. error) remote pressure sensor would be an extremely important breakthrough for operational meteorology and atmospheric dynamics research. The most promising method for making such a measurement was identified by Smith et al (1972), and reported in detail at the NASA Active Microwave Workshop (1975). This paper presents some results of a numerical simulation experiment carried out to support the viability of the technique.

Operating Frequencies of a Microwave Pressure Sounder

Surface pressure can be deduced from measurements of atmospheric transmissivity in the wings of the 60 GHz oxygen absorption band. Since experimentally it is easier to make accurate measurements of a power ratio rather than absolute power, the intensities of echo signals reflected from the ocean surface at pairs of frequencies are compared to obtain the transmissivity. To account for variation in the atmospheric temperature profile, water vapor content, cloud and rain content and sea-surface reflectivity, measurements must be made at several pairs of carefully chosen frequencies. The procedure used to select these frequencies is outlined in this section.

The composite model of sea surface reflectivity (Chan and Fung, 1973) and electromagnetic scattering by cloud and rain droplets (Crane, 1971) can be used to show that the combined frequency dependence in the strength of the nadir echo signal due to these effects may be expressed as $\exp - (a + b\nu + c\nu^2)$ where ν is frequency and the coefficients a, b, and c are dependent on the sea state and atmospheric liquid water content. An index of

pressure, S, which is independent of the sea state and cloud or rain content, can be obtained by combining the return echoes, $P_R(\nu_1)$, at several frequencies where

$$S = \left[\frac{P_R(\nu_2)}{P_R(\nu_1)} \cdot \left(\frac{P_R(\nu_4)}{P_R(\nu_3)}\right)^{\alpha} \cdot \left(\frac{P_R(\nu_6)}{P_R(\nu_5)}\right)^{\beta} \right] - 1$$

and the frequencies ν_1 thru ν_6 and the indices α and β are related mathematically to eliminate the coefficients a, b, and c from S. It is apparent then that three ratios must be measured.

Rosenkranz's (1975) spectroscopic model of oxygen absorption and Waters' (1976) spectroscopic model of water vapor absorption are used to compute zenith attenuation of a U.S. Standard Atmosphere with added water vapor as a function of frequency. To obtain the derivatives of the integrated absorption coefficient with respect to pressure, temperature and water vapor the zenith attenuation is again computed for small changes in the pressure profile, temperature profile and water vapor profile. This derivative data is used to choose sets of frequencies such that the sum of the temperature derivatives and the sum of the water vapor derivatives are simultaneously zero. This makes the index S insensitive to temperature and water vapor changes.

A further constraint is imposed on the choice of frequencies to optimize the sensitivity of S to pressure. The increase in pressure sensitivity which is indicated by the sum of the pressure derivatives and which is obtained by using some frequencies well into the oxygen band is balanced against the reduced signal-to-noise which accompanies this through greater atmospheric absorption.

The application of these constraints has shown that optimum instrument performance is obtained by using a pair of frequencies on each side of the oxygen band with the third pair in the upper wing of the 22 GHz water vapor line. An example of this selection procedure has operating frequencies 27.94, 35.30, 44.76, 52.76, 67.44 and 73.28 GHz and indices $\alpha = -1.65$ and $\beta = 1$. In this case a 3 mb change in surface pressure produces a 2.3% change in the index S while the insensitivity to temperature and water vapor is calculated to be such that a $20^{\circ}C$ change in troposphere temperature or a 1 gm cm^{-2} change in total water vapor content will produce a change in the index equivalent to a surface pressure change of only 0.12 mb.

Numerical Simulation Experiment

The simple form of the U.S. Standard Atmosphere with a smooth water vapor profile added and the simplest of profile variations were used as the basis of the frequency selection procedure. In practice the atmosphere varies greatly from this stylized profile, particularly so for the water vapor content. It is necessary therefore, to demonstrate the validity of the

procedure by examining whether the designed insensitivities are achieved with a wide range of real profiles. Radiosonde measurements provide a data set ideally suited to this purpose. The relevant radiosonde observations made and recorded on punch cards are: pressure, temperature and relative humidity for the surface and height, temperature and relative humidity at 35 standard pressure levels from 1000 to 2 mb.

Numerical simulation consisted of calculating atmospheric transmissivity at each of the frequencies for a vertical path through the atmosphere defined by a radiosonde observation set. Oxygen and water vapor absorption for each layer between the standard pressure levels was computed from the spectroscopic models. The layer thicknesses were obtained directly from the height data and corresponding average values of temperature, pressure and water vapor mass mixing ratio were derived from the recorded observations. An estimate was also included of the absorption by the atmosphere remaining above the highest level for which data was recorded. The integrated transmissivities were combined using equation 1 to give a simulated pressure index. Computations were made for a large number of radiosonde observations and Figure 1 shows the resulting scatter diagram of measured surface pressures against simulated indices. The radiosonde data used were from Cold Bay, Alaska where the surface temperature varied from 4°C to 18°C and the total water vapor content varied between 0.89 and 4.02 gm cm^{-2} and Balboa, Panama with corresponding variations of 23°C to 31°C and 4.13 to 5.61 gm cm^{-2}.

The scatter diagram shows that the relationship between simulated index and surface pressure is satisfactorily represented by a straight line over the range of pressure from 995 to 1020 mb. All of the points lie within a band ±1.5 mb about this straight line so that the pressures as deduced from the simulated indices are within ±1 mb of the actual surface pressures. In Figure 2 the error in pressure (deduced minus actual to the nearest mb) is plotted as a function of both surface temperature and total water vapor content. It can be seen that no correlation exists and that the designed insensitivity of the measurement to temperature and water vapor changes has been achieved.

The scatter of points arises from variability in the atmospheric structure which cannot be modeled and will contribute to the error in the surface pressure which is measured by the microwave sounder. From the Gaussian distribution curve fitted to the histogram of errors inset in Figure 1 the standard deviation of the deduced pressure can be estimated to be about 0.65 mb.

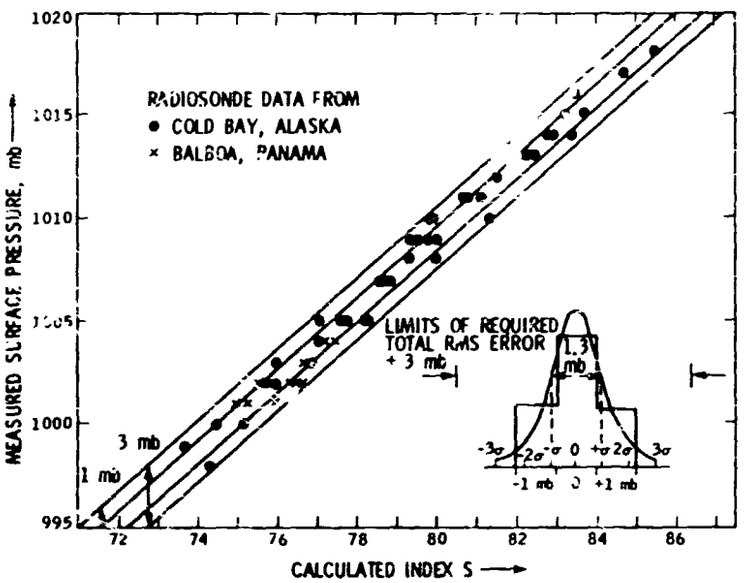

Fig. 1 Scatter Diagram. Numerical Simulation of the Index from a 6-Frequency, 3 Ratio Pressure Sounder.

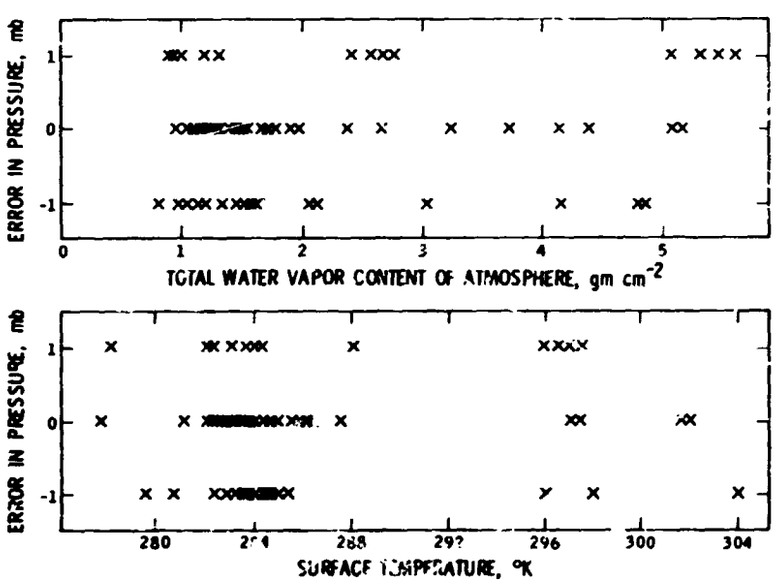

Fig. 2 Error in Pressure vs. Atmospheric Water Vapor and Surface Temperature

Concluding Remarks

A full system analysis has been carried out for the Microwave Pressure Sounder and while this will be reported in detail elsewhere, the main results of this work are summarized here.

The other major error sources are the statistical variation in the signal reflected from the ocean surface and the signal-to-noise error. The characteristics of an MPS system have been defined which will enable surface pressure on the subsatellite path to be deduced with a total r.m.s. error of 1.8 mb in cloud free and light cloud conditions and an r.m.s. error of 2.5 mb when the clouds are moderately heavy. Under more restricted cloud cover conditions measurements can also be made away from nadir so that the pressure gradient can be determined.

An assessment of the microwave system and component performances has indicated that the required instrumental capabilities and accuracies are achievable while solid state microwave sources with sufficient power (~2W) are currently being developed. It is anticipated that an early Shuttle/Spacelab flight will be used to prove the MPS as a technique for providing accurate global surface pressure fields.

Acknowledgments

The authors wish to express their appreciation for the support provided by NASA through Task 175-30-50-04 for the work at JPL and by the UK Science Research Council through Grant SGD 314 for the work in Scotland. Thanks are also due to Heriot-Watt University for granting leave of absence to Dennis A. Flower and to Drs. J.W. Waters and H.W. Lightfoot for their assistance.

References

Chan, H.L. and Fung, A.K.	1973	NASA CR-2327
Crane, R.K.	1971	Proc IEEE 59 173-188
NASA Active Microwave Workshop	1975	Report SP 376 337-345
Rosenkranz, P.W.	1975	IEEE Trans AP23 498-506
Smith, S.D., Colles, M.J. and Peckham, G.E.	1972	Quart J. Roy Met Soc. 98 431-433
Waters, J.W.	1976	In 'Methods of Experimental Physics' Vol. 12B, Chap. 2-3 142-176

Paper No. 15

N79-20590

REMOTE SENSING OF THE BOUNDARY LAYER

C. Prabhakara, *Goddard Space Flight Center, Greenbelt, Maryland*

ABSTRACT

Limited information about the boundary layer stratification can be obtained from remote infrared spectral measurements in the water vapor window region. A global map of the average strength of the water vapor spectral lines in the 9 μm window region derived from Nimbus 4 IRIS data is presented to indicate this boundary layer information. Presence of deep convective layer in the intertropical convergence zone and trade wind inversion over the subtropical oceanic high pressure systems are appropriately revealed in this map.

The planetary boundary layer is formed as a consequence of the dynamics of the large scale circulation and the thermodynamic energy balance that results at the surface.

During day time the solar energy heats the surface and thereby increases the lapse rate of the temperature in the lowest layers near the surface. A part of the absorbed solar energy at the surface goes into the subsurface by conduction, a part is used in evaporation, a part goes into reradiation from the surface and the remaining energy is transported into the atmosphere as sensible heat. In the night time when the solar heating is absent the lapse rate of temperature decreases and the various physical processes mentioned above adjust themselves progressively to a night time state. The temperature and water vapor profile near the surface thus undergo a significant change in response to the solar heating. Transfer of heat and water vapor into the atmosphere closely follow these changes near the surface.

On land surfaces, in particular dry lands, large diurnal changes in the boundary layer stratification are induced by the solar heating. The boundary layer on the water bodies on the other hand undergoes a much smaller diurnal variation as the heat capacity and conductivity of the water bodies is large.

Dynamics of the large scale circulation affect the boundary layer primarily by the vertical motions associated with them. The dynamical influence on the water bodies is not masked by the diurnal cyclical changes produced by the solar heating.

In view of the importance of the boundary layer in the weather and climate problems in this study an attempt is made to get the configuration of this layer on a global basis from satellite infrared measurements.

The information about the boundary layer structure can be obtained from passive infrared remote measurements only in a crude fashion. The main reason for this crudeness is the poor vertical resolution of the retrieved information. The 15 μm temperature retrieval has a vertical resolution of about 5 km near the surface. However water vapor which has a considerably smaller scale height, about 2 km, can help us get a finer vertical resolution. But the water vapor is highly variable both in time and space. This complicates the remote sensing techniques which depend on water vapor as an optically active gas. But over water bodies, the vertical distribution of

water vapor in the first few kilometers depends essentially on the surface temperature and temperature structure in the layers near the surface. For instance in the intertropical convergence zone, water vapor freely convects upward from the surface and the associated temperature profile shows a marked lapse rate. On the other hand in the oceanic regions where subtropical anticyclonic subsidence is present, the subsidence inversion prevents the free convection of water vapor to higher elevations. In this manner a strong correlation is developed between the thermal and water vapor stratifications. This intimate correlation simplifies the physics and allows the remote sensing of the character of the temperature and water vapor profiles in the boundary layer over water bodies.

Infrared spectral measurements made by the Nimbus 4 Infrared Interferometer Spectrometer (IRIS) in the 7-25 μm region of the earth's spectrum reveal crude structure of the water vapor lines with a resolution of about 2.8 cm^{-1}. Two brightness temperature spectra obtained by IRIS are shown in Figure 1 to illustrate this crude water vapor line structure. The water vapor absorption is changing significantly within about 2.8 cm^{-1} to produce these lines. A detailed theoretical study of the manner in which these apparent water vapor lines in the spectrum grow as a function of the optical depth, associated with water vapor in the atmosphere, reveals an interesting property. Namely, the strength, that is the difference between the top and the bottom, of a given line is dependent strongly on the vertical scale height of the water vapor.

In particular the lines in the water vapor window region around 9 μm are sensitive indicators of the vertical scale height of the water vapor in the first few kilometers near the surface. The relatively strong lines in this window region together with the weak continuum absorption produce this result. On oceanic regions these water vapor lines can delineate significant differences in the boundary layer structure of the atmosphere.

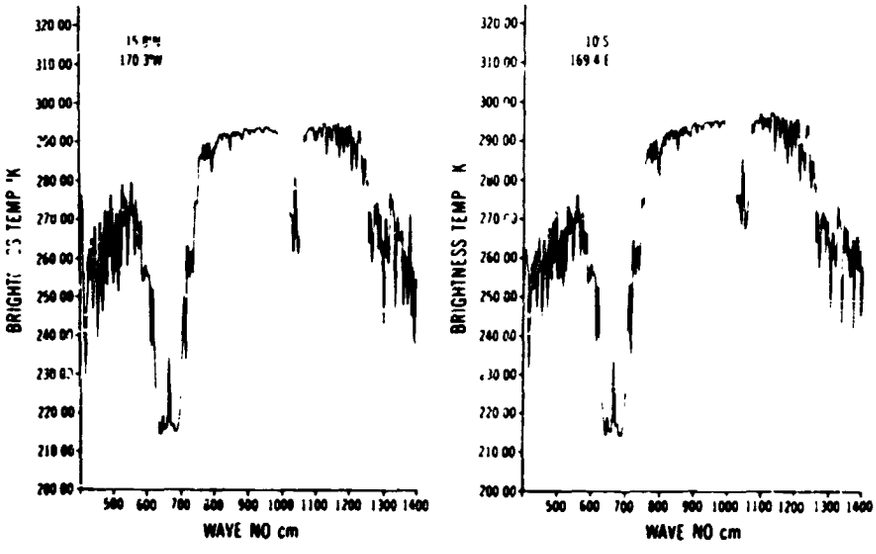

Fig. 1—Brightness temperature spectra, over tropical oceans, measured by the Nimbus 4 IRIS. Notice the water vapor lines in the 9 μm window region (1100 to 1200 cm^{-1}) are stronger in the spectrum on the right by about 30%.

In Figure 2 a global map of the mean line strength in the 9 μm window region derived from the Nimbus 4 IRIS is shown. This map is obtained by compositing cloud free IRIS data for a period of about 70 days (April to June) in 1970. The strength of the 9 μm lines is expressed in terms of the brightness temperature difference from the top to the bottom of the lines. This global map reveals strong water vapor lines in the equatorial regions over the oceans where intertropical convergence takes place. Away from the equator the line strength decreases. However, in the subtropical oceanic region where a subsidence inversion is produced, the 9 μm lines show a minimum. Such minima may be noticed in the subtropical eastern portions of the Atlantic and Pacific oceans both north and south of the equator. Also a region of minimum is seen over the Arabian sea where trade wind inversion exists during the period April May and June.

The information about the boundary layer structure over the land areas is not as readily interpretable as it is on the oceans. The 9 μm line information on the land, shown in Figure 2, is obtained from local noon data of IRIS.

The intertropical convergence zone over North Africa around 12°N is revealed by the 9 μm line strength. The extremely large value of the 9 μm lines, ~20°C, in this region suggest the presence of a deep, moist and probably a convectively unstable layer near the surface. Similar convectively unstable layer is also indicated over India.

This study shows that the remote measurements in the infrared are useful to get a crude structure of the atmospheric boundary layer over the oceanic regions on a seasonal basis. Such an information can be useful in seasonal climate modelling and prediction schemes.

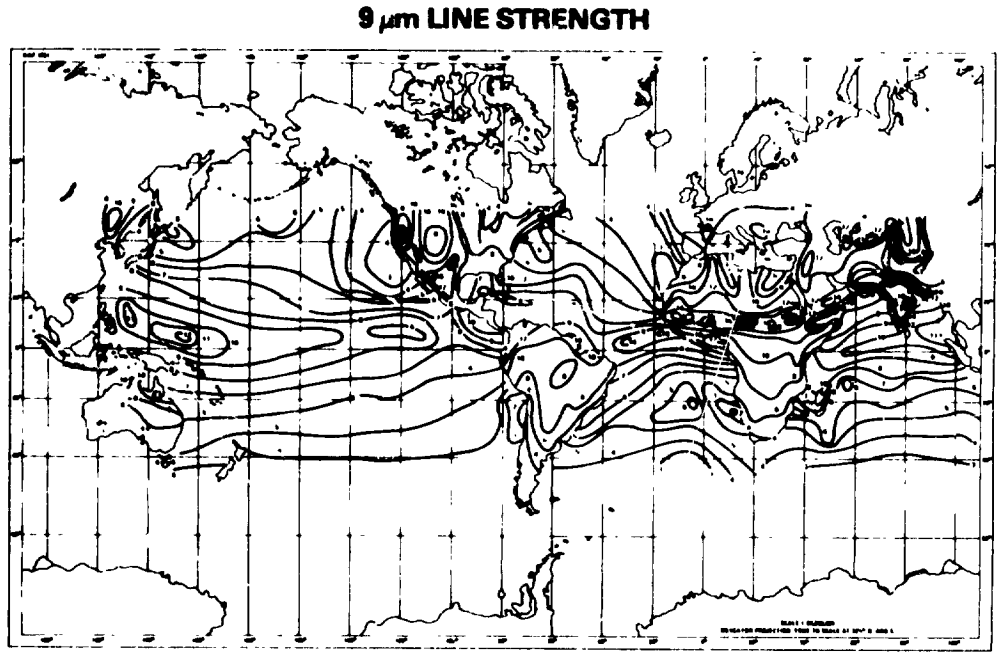

Fig. 2 –Strength of the water vapor lines in the 9 μm window (°C) derived from Nimbus 4 IRIS for the period April, May and June, 1970. The data on the lands is derived from local noon measurements.

Paper No. 16

N79-20591

D16

PROFILING OF ATMOSPHERIC WATER VAPOR WITH MICROWAVE RADIOMETRY

T. T. Wilheit and G. H. Schaerer (NAS/NRC Associate)
NASA Goddard Space Flight Center

ABSTRACT

Weighting functions were developed which express the water vapor information content of microwave radiometric measurements. Retrievals of water vapor profiles are performed using these weighting functions.

There is considerable interest in remote measurements of the vertical distribution of water vapor, particularly under cloudy conditions. The net integrated amount of water vapor has been measured using the 22.235GHz water vapor line (Staelin, et al. 1975) with instruments on the Nimbus-5 and 6 satellites and this technique will be continued on the Nimbus-G and Seasat-A satellites to be launched in 1978. Attempts to use this line for obtaining vertical distribution information have not been fruitful because of the weakness of absorption even at line center. The 183.310GHz line is much stronger and thus provides an intriguing possibility of profiling water vapor. A preliminary analysis of this possibility is the subject of this paper.

If we view the Earth and its atmosphere from space with a microwave radiometer directly at the nadir, assume a specular surface and make the Rayleigh Jeans approximation the upwelling brightness at a given frequency ν can be expressed:

$$T_{B\uparrow} = \int_0^\infty e^{-\int_h^\infty \gamma(\nu,x)dx} \gamma(\nu,h)T(h)dh + e^{-\tau}\left[(1-R)T_{SURF} + R\int_0^\infty e^{-\int_0^h \gamma(\nu,x)dx}\gamma(\nu,h)T(h)dh\right] + e^{-2\tau}T_{CB}$$

where: $\tau = \int_0^\infty \gamma(\nu,x)dx$, R is the reflectivity of the surface, $\gamma(\nu,h)$ is the absorption coefficient of the atmosphere at a height h for a frequency ν and T(h) is the temperature profile of the atmosphere.

This equation may be expressed in the form:

$$T_{B\uparrow} = \int_0^\infty K(\nu,h)T(h)dh$$

where $K(\nu,h)$, the temperature weighting function, is only weakly dependent on the temperature profile. These weighting functions form the basis of all schemes

of retrieving temperature profiles from radiometer measurements, if not explicitly in the retrieval formalism, by guiding the intelligent choice of measurement channels.

Constituent retrievals, however, are inherently more difficult because they enter into the brightness temperature equation through their contributions to γ which appears both in the attenuation factor $e^{-\int \gamma dx}$ and through the radiation factor $\gamma(h)T(h)$ so that the effect of a γ at one location is dependent on γ at all other locations so that one cannot, in general express $T_{B\uparrow}$ in the form:

$$T_{B\uparrow} = \int_0^\infty C(h)\gamma(h)dh$$

We can nevertheless linearize the problem by dealing in small pertubations to the absorption. That is, we can express a small change in the brightness temperature $\delta T_{B\uparrow}$ as a function of a small change in the absorption as a function of height, $\delta\gamma(h)$.

$$\delta T_{B\uparrow} = \int_0^\infty G[h,\rho(h),T(h)]\ \delta\gamma(h)dh$$

and it can be shown that:

$$G[h,\rho(h),T(h)] = \tau(\infty,h)[T(h) - T_{B\uparrow}(h)] + R\tau(0,h)\tau(\infty,0)[T(h), - T_{B\downarrow}(h)]$$

where $\tau(X,Y)$ is the atmospheric transmissivity between points X and Y and $T_{B\uparrow}(h)$ and $T_{B\downarrow}(h)$ represent the up and downwelling brightness temperatures at height h respectively. $G[h,T(h),\gamma(h)]$ will be written henceforth only as $G(h)$ with the understanding that it is implicitly a function of the temperature and absorption coefficient profile as well. The weighting function with respect to absolute water vapor, $\rho(h)$, can then be expressed as

$$G\rho = G(h)\frac{\partial\gamma(h)}{\partial\rho(h)} \leftarrow \text{Partial derivitive}$$

or more conveniently with respect to relative humidity, R(h),

$$G_R(h) = G(h)\frac{\partial\gamma(h)}{\partial\rho(h)}\frac{\partial\rho(h)}{\partial R(h)} = G(h)\frac{\partial\gamma(h)}{\partial\rho(h)}\rho_{SAT}(h)$$

where $\rho_{SAT}(h)$ is the saturation vapor pressure of water at a height h. The weighting functions dealt with hereafter will be these relative humidity weighting functions; they are related to a change in brightness temperature by:

$$\delta T_{B\uparrow} = \int_0^\infty G_R(h)\,\delta R(h)dh$$

Given a set of absorption coefficients for atmospheric constituents (Waters 1976) and reasonable values for surface reflectivities we are in a position to calculate these weighting functions and to examine their properties. We will use a value of 0.3 for the reflectivity of the ocean between 140 and 200GHz based on the dielectric measurements of Ray (1972) and use 0.1 as a typical value for land surfaces keeping in mind that actual land reflectivities can easily range from ca 0.2 down to essentially zero. We will always assume the temperature of the surface to be the same as the lowest level of the atmosphere used. Results will be given here for the 1962 U.S. Standard and Tropical Atmospheres (AFCRL 1965).

In Figure 1, we show weighting functions calculated for 2, 4, 6, 10 and 18GHz below the 183GHz water vapor line for a typical atmosphere over ocean. Note that as one would expect the peak of the weighting function moves to lower altitude as one gets farther from line center and, more, suprisingly, that the weighting functions which probe deeply into the atmosphere actually change sign at low altitudes. That is, an addition of water vapor at high altitudes will decrease the brightness temperature but an increase at low altitude will increase the brightness temperature. This crossover is not found in temperature weighting functions. Figure 2 repeats the same calculations for an assumed reflectivity of 0.1 which would be typical of land surfaces. The only obvious change is that the crossover moves to lower altitude; at zero reflectivity the crossover disappears entirely. The behavior of the peak height and the crossover height as a function of frequency have been examined and the results are summarized in Figure 3. Here we show these heights for both the U.S. Standard and Tropical Atmospheres. Note that for frequencies more than about 7GHz removed from line center the peak height actually goes back up. This is of little practical consequence, however, over oceans since the bulk of the weighting function shifts to below the crossover and reaches another maximum at the surface. Over land, this property suggests difficulty in obtaining water vapor information much below about 4km altitude. One can also note substantial similiarity in the behavior of the weighting functions for the U.S. Standard and Tropical Atmospheres. This should not lead one to believe that the behavior of the weighting can be considered independent of the details of the atmosphere. In Figures 4 and 5 we show weighting functions for 182 and 140GHz respectively for atmospheres with a Tropical Atmosphere temperature profile but various constant relative humidities imposed on them. The number by each curve specifies the relative humidity, in percent, for each. Near the line (182GHz) the effect of varying the humidity is to move the weighting functions up and down while at 140GHz the changing humidity grossly alters the character of the weighting functions.

As a test of the usefulness of these weighting functions, a retrieval scheme using 5 channels was examined. First the expected brightness temperatures over ocean at the five frequencies (183.30, 182.0, 180.0, 174.0, and 140.1GHz) are calculated; these become then the synthetic data set. We then try to retrieve the known profile by taking an initial guess profile and calculating brightness temperatures and weighting functions for each of the five frequencies. The differences between the newly calculated brightness temperatures and the synthetic data set are calculated, then the weighting functions are used to translate these into corrections to the relative humidity profile which is assumed to be piecewise linear with anchor points at the surface and at the peak heights of the 4 highest frequency weighting functions. The adjusted profile is then used to calculate new weighting functions and brightness temperatures and the process is iterated until the calculated brightness temperatures agree with the synthetic data set within 1°K; four iterations are sufficient. In Figures 6 and 7 we show the results of this

process for U.S. Standard and Tropical Atmospheres. The retrieval works well for the smoothly varying U.S. Standard atmosphere but certainly does not resolve the abrupt decrease in the humidity associated with the trade inversion in the tropical atmosphere.

These results certainly suggest that microwave radiometry near the 183GHz water vapor line could yield interesting water vapor profiles, at least over oceans. More channels and more sophisticated retrieval techniques should yield improvements. The effect of clouds should also be quantitatively investigated.

REFERENCES

Air Force Cambridge Research Laboratory (AFCRL), "Handbook of Geophysics and Space Environments," McGraw Hill, New York (1965).

Ray, P. S., "Broadband Complex Refractive Indices of Ice and Water," Applied Optics, 11, 1836–1844, (1972).

Staelin, D. H., A. L. Cassel, K. F. Kunzi, R. L. Pettyjohn, R. K. L. Poon, P. W. Rosenkranz, and J. W. Waters, "Microwave Atmospheric Temperature Sounding: Effects of Clouds on the Nimbus-5 Data," J. Atm. Sci., 32, 1970–1976, (1975).

Waters, J. W., "Absorption and Emission by Atmospheric Gasses," in "Methods of Experimental Physics," Volume 12, Part B, 142–176, Academic Press, New York (1975).

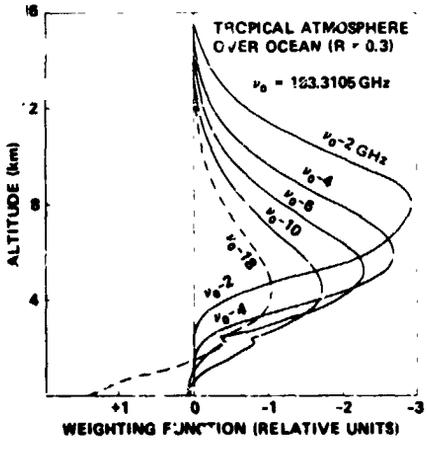

Fig. 1–Relative humidity weighting functions for a Tropical Atmosphere over ocean (R = 0.3)

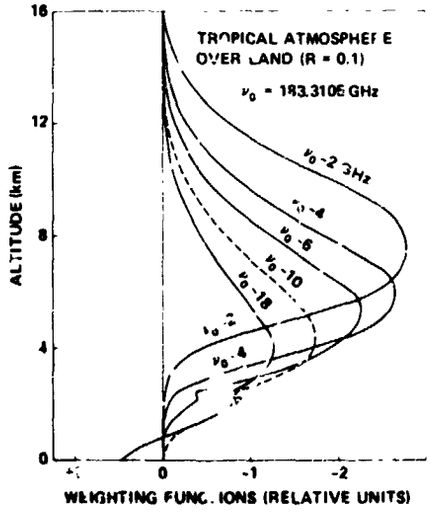

Fig. 2–Relative humidity weighting functions for a Tropical Atmosphere over land (R = 0.1).

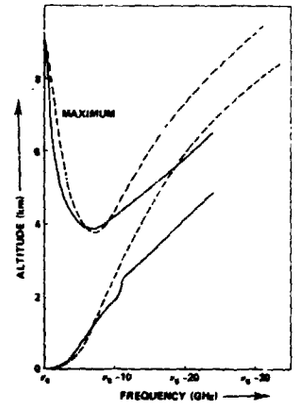

Fig. 3–Relative humidity peak height and crossover height as a function of frequency below line center

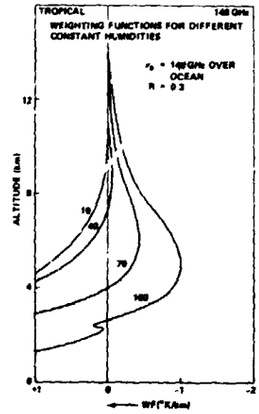

Fig. 4–Weighting functions for tropical temperature profile with several constant relative humidities

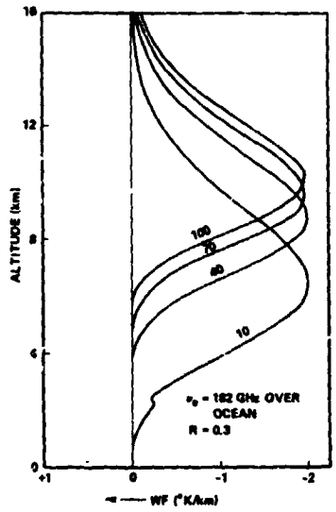

Fig. 5–Weighting functions for tropical temperature profile with several constant relative humidities

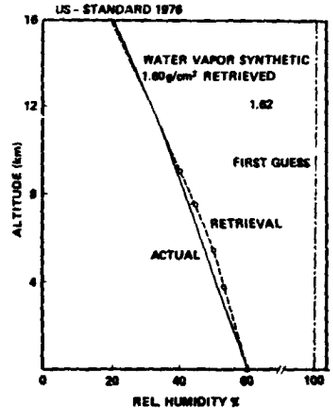

Fig. 6–Relative humidity retrieval for U.S. Standard Atmosphere

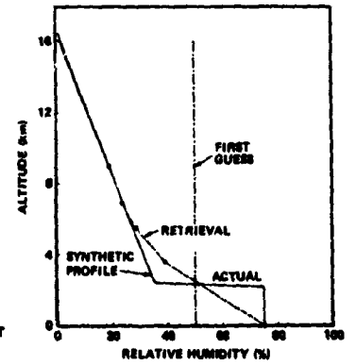

Fig. 7–Relative humidity retrieval for Tropical Atmosphere

Paper No. 17

N79-20592 D17

ADVANCES IN THE REMOTE SENSING OF ATMOSPHERIC TEMPERATURE PROFILES

M. T. Chahine, *Jet Propulsion Laboratory, Pasadena, California*

ABSTRACT

Clear-column temperature profiles with a vertical resolution of 2 km in the troposphere and an accuracy of 1.5 K can be obtained in the presence of multiple layers of broken clouds using narrow band-pass measurements carefully selected in the 4.18 and 15 μm regions of the CO_2 bands.

Introduction

Numerical weather prediction models have already evolved to point where the number of tropospheric layers is greater by more than a factor of two over the number of sounding levels of current sounders. For example, the GSFC/GISS numerical circulation model has eight layers below 100 mb while the VTPR, HIRS and SCAMS Sounders are capable of sounding the troposphere at a maximum of 3 or 4 levels only.

The main reason for this poor vertical resolution is due to the broadness of the weighting functions of the corresponding tropospheric channels. The weighting functions, $\partial\tau(\nu_i,p)/\partial \ln p$, are the kernel of the radiative transfer equation when written in the form

$$I(\nu_i) = B(\nu_i,T_s)\ \tau(\nu_i,p_s) + \int_{\ln p_s}^{o} B[\nu_i,T(p)]\ \frac{\partial\tau(\nu_i,p)}{\partial \ln p}\ d \ln p \qquad (1)$$

where $I(\nu_i)$ is the channel-averaged upwelling radiance at frequency ν_i, B is the Planck blackbody function and τ is the transmittance of an atmospheric column between the satellite and pressure level p. From Eq. (1) it is clear that when the weighting functions are broad the emitted energy reaching the satellite will have components originating from a wide range of atmospheric layers, thereby making the reconstruction of fine-scale vertical details practically impossible.

As a consequence of the broadness of the weighting functions of current sounders and also because of cloud contamination and surface emissivity effects, the rms errors in the retrieved temperature profiles have remained high, above 2 K. Improvements in the accuracy and vertical resolution of satellite temperature profiles, however, can be achieved provided that:

1. An objective cloud-filtering method is developed to obtain global clear-column profiles even in the presence of multiple layers of broken clouds.
2. A set of atmospheric sounding channels with very narrow weighting functions is selected to resolve the details of the vertical thermal structure.
3. A set of surface sounding channels is selected to solve the surface emissivity effects.

An investigation of the above three problems was carried out jointly with L. D. Kaplan (U. of Chicago) and J. Susskind (NASA-GSFC). A set of tropospheric sounding frequencies with substantially narrower weighting functions was carefully chosen from the region of high J-lines of the R branch of the 4.3 μm CO_2 band, and a compatible set of 15 μm channels was selected to sound the stratosphere and to filter out the effects of up to three cloud layers. In addition, three channels were selected from the 3.7 μm atmospheric window to account for the effects of surface emissivity. A feasibility study for implementation of the set of sounding frequencies has been carried out and a design study for the development of such a sounder is currently under way at JPL. From such a sounder system we will be able to:

1. Retrieve clear-column temperature profiles in the presence of up to three cloud layers with an average rms accuracy of 1.5 K at 8 distinct levels below 100 mb.
2. Simultaneously obtain humidity profiles.
3. Determine the location of the tropopause to within 10-20 mb.
4. Map the amount and height of clouds globally.
5. Recover day and night surface temperature of oceans and solid earth.

Cloud-Filtering Method

An analytical method was derived in Refs. 1 and 2 to eliminate the effects of clouds on infrared radiances. The method requires measurements in adjacent fields of view and in two properly selected spectral bands. According to this method it is possible to express the (unknown) clear-column radiance $I(\nu_i)$ as

$$I(\nu_i) = \tilde{I}_1(\nu_i) + \sum_{j=1}^{3} \eta_j \left[\tilde{I}_1(\nu_i) - \tilde{I}_{j+1}(\nu_j)\right] \qquad (2)$$

where $\tilde{I}_1$, $\tilde{I}_2$, $\tilde{I}_3$ and $\tilde{I}_4$ are radiances measured in four adjacent fields of view and η_1, η_2 and η_3 are unknown coefficients independent of frequency. The determination of $I(\nu_i)$ and η_j is carried out simultaneously by iterations. The solution converges uniformly if the high frequency channels from the 4.3 μm band are used to determine $I(\nu)$ and the lower frequency channels from the 15 μm band are used to solve for the coefficients η_j.

Experimental verifications of this method were carried out at JPL using a multidetector spectrometer mounted on the NASA P3A aircraft and the results are described in Ref. 3.

Recently Susskind successfully applied this cloud-filtering

method to analyze the August 18 - 25, 1976 HIRS data. Here, since the sounding frequencies available on HIRS can be used to filter out the effects of only a single cloud layer, Eq. (2) was reduced to just one term as

$$I(\nu_i) = \tilde{I}_1(\nu_i) + \eta[\tilde{I}_1(\nu_i) - \tilde{I}_2(\nu_i)] \qquad (3)$$

The results illustrated in Fig. 1 were derived according to Eq. (3) using 15 μm and 4.3 μm radiance data only, without any a priori information about the height, type or amount of clouds in the fields of view. It is very important to note that the results shown in Fig. 1 are independent of the initial guess, with the average rms errors being 2.5 K for a climatology initial guess and 2.4 K for a forecast initial guess.

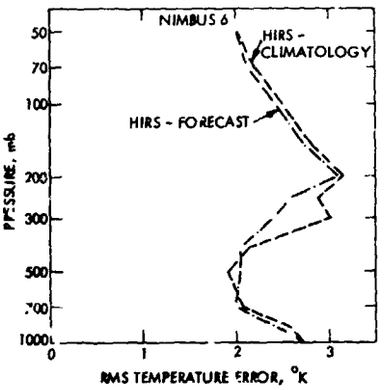

Fig. 1

Narrowing of the Weighting Functions

The main reason for the large errors above 300 mb shown in Fig. 1 is due to the broadness of the HIRS 15 μm weighting functions. Fig. 2a shows the distribution for the HIRS sounding channels of the origins of the emitted energy, defined by $B\,\partial\tau/\partial \ln p$. By comparison the sounding frequencies in Fig. 2b selected for an Advanced Meteorological Temperature Sounder (AMTS) have narrower energy distributions. The reasons for this narrowing have been discussed in detail in Refs. 4 and 5 and are due to:

1. The fact that dependence of the Planck function in the 4.3 μm region on temperature is very strong.
2. The dependence of τ on temperature and pressure in the high J-lines of the 4.3 μm CO_2 band greatly increases the narrowness of $\partial\tau/\partial \ln p$ in the troposphere.

Further narrowing of $\partial\tau/\partial \ln p$ beyond what is shown in Fig. 2b can be obtained by making measurements in wings of the high J-lines, but this step requires a further reduction in the instrument bandpass to $\Delta\nu = 0.2\ cm^{-1}$.

A comparison, based on Refs. 6 and 7 for the U.S. standard atmospheric temperature profile, of the narrowness of the energy distributions, $B\,\partial\tau/\partial \ln p$, for different types of sounding channels is presented in Table 1 using the half-width as a measure for narrowness. The half-width is defined as the distance, in scale heights, between two pressure levels at which the energy distributions have half of their maximum values. From this table it is seen that the narrowness of the AMTS channels in Fig. 2b is within

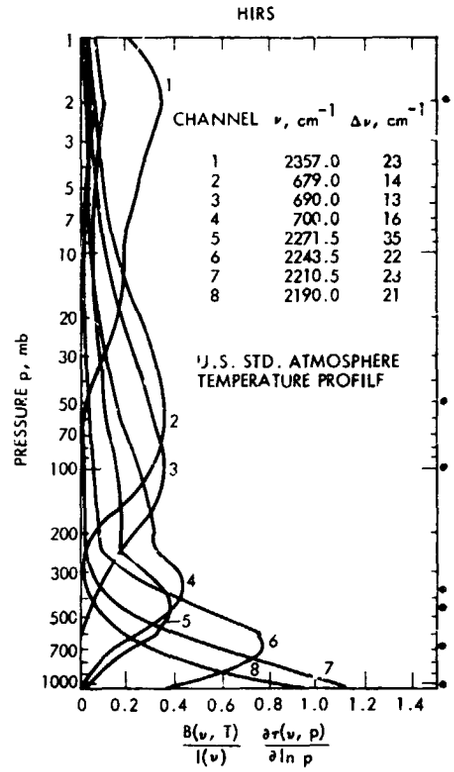

Fig. 2a

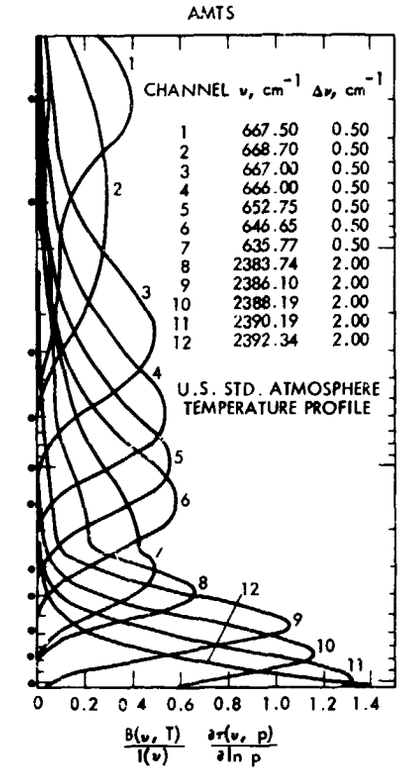

Fig. 2b

	BAND	Δν/ν	HALF-WIDTH IN SCALE HEIGHTS	REMARKS
TROPOSPHERE	15μm	10^{-2}	1.6	VTPR
	60GHz	10^{-3}	1.5	SCAMS
	4.46μm	10^{-2}	1.3	HIRS
	4.18μm	10^{-3}	0.69 *	AMTS
	4.18μm	10^{-4}	0.60	wings of lines
STRATOSPHERE	14.5μm	10^{-2}	2.4	VTPR
	15μm	10^{-3}	1.6 *	AMTS
	15μm	10^{-4}	1.4	
	118GHz	10^{-3}	1.4	

Table 1

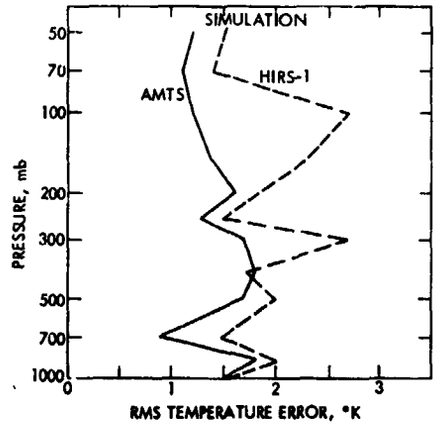

Fig. 3

15% from the highest limit for passive sounders.

Numerical Simulation

The two sets of sounding frequencies shown in Fig. 3 were used in a numerical experiment to investigate improvements in the accuracy of the retrieved profiles as a result of narrowing of the energy distribution. Only one cloud layer was assumed in this experiment for the purpose of comparison with the HIRS data, although the AMTS is capable of eliminating the effects of multiple cloud layers. The amounts of clouds in the fields of view were randomly generated and their height distribution was assumed to vary linearly from 200 mb at the equator to 800 mb at the poles. The initial guess for the HIRS retrieval was taken from climatology. No initial guess is needed (or used) for retrievals with the AMTS channels. The average rms errors in the resulting retrievals were 2 K for the HIRS and 1.5 K for the AMTS. The accuracy of the results derived from such a sounder would have a significant impact on numerical weather prediction.

References

1. Chahine, M. T., 1974: Remote Sounding of Cloudy Atmospheres. Part I. The Single Cloud Layer. J. Atmos. Sci , vol 31, 233-243.
2. Chahine, M. T., 1977: Remote Sounding of Cloudy Atmospheres. Part II. Multiple Cloud Formations. J. Atmos. Sci., vol 34, 744-757.
3. Chahine, M. T., 1977: Remote Sounding of Cloudy Atmospheres. Part III. Experimental Verifications. J. Atmos. Sci., vol 34, 758-765.
4. Kaplan, L. D., 1969: The Use of High-Frequency Infrared Radiometry for Remote Atmospheric Probing with High Vertical Resolution. In Atmospheric Exploration by Remote Probes, Committee on Atmospheric Science (U.S. National Academy of Sciences, Washington, D. C., vol 2, 435-442.
5. Kaplan, L. D., Chahine, M. T., Susskind, J., and Searl, J. E., 1977: Spectral Band Passes for a High Precision Satellite Sounder. Applied Optics, vol 16, 322-325.
6. Susskind, J., and Searl, J. E., Synthetic Atmospheric Spectra Near 15 and 4.3 μm, accepted in J. Quant. Spectrosc. Radiat. Transfer (1977).
7. Susskind, J. and Searl, J. E., Atmospheric Absorption Near 2400 cm^{-1}, accepted in J. Quant. Spectrosc. Radiat. Transfer (1977).

2,7

Paper No. 18

N79-20593

A STATISTICAL METHOD FOR TIME-CONTINUOUS ASSIMILATION OF REMOTE SOUNDING TEMPERATURES

Michael Ghil, *Courant Institute of Mathematical Sciences, New York University, New York, NY 10012*

ABSTRACT

We present a time-continuous statistical method for the four-dimensional assimilation of remote sounding temperatures based on radiometric measurements from polar-orbiting satellites. This method is applied to DST-6 data from the NOAA-4 and Nimbus-6 satellites.

We report on experiments in which the state of the atmosphere throughout the test period was determined using a varying amount of satellite data and in which different methods were used for their assimilation. Data from the NOAA-4 satellite only, from Nimbus-6 only, and from both satellites together were used; the methods tested include different variations of our statistical method, as well as more traditional methods. Using some of the atmospheric states thus determined as initial states, a number of eleven 72-hour forecasts was carried out for each experiment.

The improvement in forecasts at 48 hours and 72 hours for the best assimilation method tested and for the full amount of data available was about 5% in S_1 skill score and 12% in RMS errors. These correspond to the possibility of an extension of about 8-12 hours in the useful length of numerical weather forecasts.

Our conclusions from the study are that: (1) satellite-derived temperature data can have a modest, but statistically significant positive impact on numerical weather prediction in the two-to-three day range; (2) this impact is highly sensitive to the quantity of data available; and (3) the assimilation method plays a major role in the magnitude of the impact for the same data.

1. INTRODUCTION

A major effort is currently under way at a number of research centers in numerical weather prediction to apply statismethods to the four-dimensional (4-D) assimilation of temperature data obtained from radiometric satellite observations. The use of statistical methods is strongly suggested by the large quantity and poor quality of the data.

At the Goddard Institute for Space Studies (GISS) we have

developed a statistical assimilation method (SAM) which operates in a time-continuous manner, along a sub-satellite track. This time-continuous, fully four-dimensional approach is the main feature which distinguishes our method from other attempts, which group all satellite data in 6 to 12 h "windows", and then apply the statistical techniques to the satellite data, as well as to conventional data, in synoptic fashion.

The idea of using cumulative statistical information on observational errors in order to compensate for the deficiencies in the amount and accuracy of the observations has led to the application of statistical methods in the objective analysis of conventional synoptic data (Eliassen, 1954; Gandin, 1963). This application became known in the meteorological literature as "optimal interpolation". The inclusion of forecast information into the specification of an initial state by statistical methods lead to "optimal interpolation" of the differences between observations and forecast values, rather than of the synoptic observations themselves. This approach has been advocated and implemented by Rutherford (1972, 1973).

The application of statistical methods not only to the objective analysis of conventional synoptic observations, but also to the time-continuous assimilation of asynoptic satellite-derived data, has been carried out for a non-divergent barotropic model by Bengtsson and Gustavsson (1971, 1972). The combination of all the ideas above led us to study the blending of satellite data in a time-continuous manner into assimilation runs of the GISS General Circulation Model (Somerville et al. (1974), by the procedure of local "optimal interpolation" of observed-minus-forecast values; the statistically determined corrections are then added at each model time step of the assimilation cycle to the forecast values.

This statistical method was compared in some of our experiments with other methods, of a more traditional nature, to wit: direct insertion (Bengtsson, 1975, p. 24), and successive correction (Cressman, 1959). The detailed asynoptic implementation of these two methods in our experiments is described in Ghil and Dilling (1977).

2. THE METHOD

The vertical temperature profiles obtained from satellite-based radiance measurements are grouped by 10-minute time intervals. A plot of a typical group of temperature data obtained in a 10-minute interval is shown in Figure 1. In the sequel we shall refer for the sake of brevity to satellite-derived temperatures as observed temperatures. In the present implementation of the method, only information at the same mandatory pressure level is used, i.e., the "optimal interpolation" is two-dimensional.

To simplify notation, we shall use a single subscript to indicate location, thus: $k = (i,j)$, where i stands for discretized longitude and j for discretized latitude. Let $\underset{\sim}{k}$ be an

observation point (on a fixed mandatory pressure level), T^0_k the observed temperature, and T^f_k the (interpolated) model temperature at the observation point k. Let γ_k be the difference between the observed and the forecast temperatures at k, $\gamma_k = T^0_k - T^f_k$. We wish to compute corrections δ_ℓ to forecast values at grid points $\ell = (m,n)$ near the observation points k, where k ranges over a group, or "patch", of observations such as the one shown in Figure 1. In the figure, observation points k are marked by T's; grid points ℓ which are affected by the observations after corrections are marked as +'s. More precisely, after applying the corrections provided by our method, the temperature at '+'-points, as well as at 'T'-points, will be different from the forecast value.

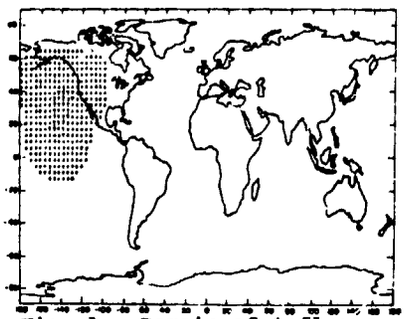

Fig. 1. Domain of influence of satellite temperature retrievals in 10 min. time intervals.

The corrections δ_ℓ are computed by a linear formula,

$$\delta_\ell = \Sigma_k \alpha^k_\ell \gamma_k \; ; \tag{1}$$

here and in the sequel we drop the vector notation for k and ℓ, the multi-index character of k and ℓ being tacitly understood. The coefficients α^k_ℓ in the Equation (1) are defined as the solution of the system of linear equations

$$\underset{\approx}{A}_\ell \underset{\sim}{\alpha}_\ell = \underset{\sim}{\beta}_\ell, \tag{2}$$

where $\underset{\sim}{\alpha}_\ell = (\alpha^1_\ell, \ldots, \alpha^N_\ell)$, and N is the number of observations points in the patch. System (2) is the familiar normal system which arises in all statistical applications based on a least-squares approach.

The statistical information accumulated on observations and forecasts is incorporated into the entries $a^\ell_{kk'}$ of the matrix $\underset{\approx}{A}$ and into the components β^k_ℓ of the right-hand side vector $\underset{\sim}{\beta}_\ell$. These are given by

$$a^\ell_{kk'} = \phi(s_{kk'}), \quad \beta^k_\ell = \phi(s_{k\ell}); \tag{3}$$

here $s_{kk'}$ is the (spherical) distance between the two observation points k and k', and $s_{k\ell}$ is the distance between the observation point k and the grid point ℓ, at which we wish to make the correction. Notice that $\underset{\approx}{A}$ depends on observation points only, and

we can drop the subscript ℓ, while β_ℓ depends on both observation points and the correction point we consider.

The function $\phi(s)$ is a correlation function. The fact that it depends only on the distance s reflects the assumptions of homogeneity and of isotropy we made at the outset concerning the error structure. The function $\phi(s)$ was computed for discrete values of s, s_1 = 100km, s_2 = 300km,..., s_p = (2p-1)x100km. The continuous function $\phi(s)$ used in (3) was obtained by fitting an analytic function $\phi = \phi(s;s_0,c)$, depending on the parameters s_0,c, by a least-squares fit. In other words, we obtained the values of s_0 and of c for which $\phi(s;s_0,c)$ satisfied

$$\Sigma_p \quad [\phi(s_p;s_0,c) - \phi_p]^2 = \text{minimum} \qquad (4)$$

The actual form of ϕ used in the experiments we report on here was exponential,

$$\phi(s;s_0,c) = (1-c)e^{-s/s_0} + c \ . \qquad (5)$$

The method has already been presented in Ghil et al. (1977b). For a more detailed description we have to refer to Ghil and Dilling (1977).

3. DESCRIPTION OF THE EXPERIMENTS

The purpose of our experiments was to study the effect of satellite data on the quality of initial states obtained with the aid of such data, and on the accuracy of forecasts starting from such initial states. Specifically we studied the effect of the quantity and accuracy of the satellite data themselves on the one hand, and of the assimilation methods used to extract the information from the data, on the other.

All the experiments consisted basically of a continuous assimilation run, extending over the entire period for which data were available, and of forecasts started from selected initial states produced by the assimilation run. The experiments differed from each other by the sounding data which were assimilated, and by the method which was used to carry out the assimilation. The assimilation methods used for the satellite data were direct insertion (DIM), asynoptic successive correction (SCM), and time-continuous local statistical assimilation (SAM).

The methods were applied to temperature sounding data from the NOAA-4 and Nimbus-6 satellites during the DST-6 (January-March, 1976) period. A complete assimilation cycle was carried out from 00Z Jan. 29 to 03Z Feb. 21, 1976. The temperature data were supplied by the National Environmental Satellite Service (NESS). Eleven forecasts were carried out, starting at 03Z on Feb. 1, 3, 5, ..., 21. The reason to start the forecasts at 03Z and not 00Z was to achieve as close a parallel as possible with operational practice at the National Meteorological Center (NMC), because NMC uses intermittent assimilation with a ±3h "window" for satellite data.

Thus, an operational NMC forecast started at 00Z uses all asynoptic information up to 03Z; so do our experimental runs started at 03Z, as we rely on time-continuous assimilation. Starting 3h after the insertion of synoptic data also has the effect of letting the model smooth out the initialization shock occurring at synoptic time (see Ghil, 1975, and Ghil et al. (1977a).

Table I. Summary description of impact experiments. The use of data from the VTPR instrument on board the NOAA-4 satellite is denoted by VTPR, the use of the data from the HIRS and SCAMS instruments on board the Nimbus-6 satellite by NIMB. The method by which the data have been assimilated is indicated by the acronyms DIM, SCM or SAM. The experiment in which only conventional synoptic data, and no satellite data at all were used appears as NOSAT. The first digit of the code number refers to the method: DIM = 1, SCM = 2, and SAM = 3; the second digit refers to data source: VTPR = 1, NIMB = 2 and VTPR + NIMB = 3. Additional remarks concerning the method are explained in the text and in Ghil and Dilling (1977).

Experiment No.	Code	Assimilation Method	Data VTPR	Data NIMB	Correlation parameters ρ_0 (km)	c
7578	00	NOSAT	0	0		
8240	12	DIM		X		
8405	22C	SCM*		X		
8352	22	SCM		X		
8310	23	SCM	X	X		
8447	22N	SCM**	X	X		
8574	31	SAM	X		2293	-.124
8472	32	SAM[a]		X	1831	.018
8545	33	SAM	X	X	1842	.015
8566	33a	SAM[a]	X	X	1842	.015
8593	33b	SAM[b]	X	X	1842	.015

* Control experiment with simulated Nimbus-6 data, based on NOSAT 12h forecast

** No insertion of satellite data over data-dense land areas

a Bias removed at observation point

b Bias removed at grid point

A summary description of the experiments is given in Table I. A latitude-scaled correlation function (cf. Ghil and Dilling, 1977), the averaging of NESS data to GISS grid points (id.), and geostrophic wind corrections (ibid.) were used in all SAM experiments. Geostrophic wind correction was used in the DIM and SCM experiments (8240 through 8447) as well.

Experiment 8405 was set up as a control experiment to check the information content of satellite data, and to study the possible smoothing effect of SCM or SAM on the field values produced by assimilation runs. In it the temperature data used as "observations; were model values produced from a NOSAT (see Table I) 12h-forecast, to which simulated observed-minum-forecast differences were added; these differences were computed at the true

Nimbus-6 observation locations, by using a random-number generator function with statistical properties determined from actual data.

Our timing estimates for the different assimilation methods show that the computational cost of implementing more sophisticated assimilation methods is not exaggerated. For example, a 24h forecast takes 40 minutes of CPU time; a 24h NOSAT assimilation runs in 48 minutes; a 24h SCM assimilation runs in 59 minutes; and a 24h SAM run in 96 minutes (cf. Ghil and Dilling, 1977, where details are provided). These estimates all refer to the present version of the GISS GCM running on an Amdahl 470/V6 computer with a core memory of 2 megabytes. In fact, the computational cost of SAM can be considerably reduced by using more efficient numerical methods and programming techniques.

4. DISCUSSION OF RESULTS

We shall only discuss here numerical measures of satellite-data impact on forecast accuracy. A detailed synoptic study of the differences in initial states produced by the assimilation of satellite-derived temperature data appears in Atlas and Sakal (1977) and in Halem et al. (1978). A study of the effect of differences in the model-predicted large-scale fields on local weather forecasts also appears there.

The numerical measures of impact we used were S_1 skill scores and root-mean-square (RMS) differences. The meteorological fields we studied in particular were the sea-level pressure p_s and the height ϕ of the 500-mb geopotential surface. First the difference between values of the field produced by a model forecast and the field values of the NMC objective analysis at the same synoptic time were computed. These differences were computed for the synoptic time 48h and 72h after initial time.

The next step was to compute the RMS value of the difference. The actual impact measure consisted in subtracting the RMS difference for the experiment forecast from the RMS difference for the NOSAT forecast. A positive value of this difference then means positive impact of, or improvement due to satellite data for the given experiment and quantity, while a negative value means negative impact. The computations for skill score impacts were done in analogous fashion. The verification regions over which the impact was measured were North America and Europe.

Because of the random influences on the detailed results we discuss, these results had to be summarized in a way which would allow definite conclusions to be drawn. Such a summary is presented in Table II. For details we have again to refer to Ghil and Dilling (1977).

The mean percentual impacts for each experiment will be denoted in the following discussion by x_j; the subscript j refers to the code number of the experiment. We shall denote the measure of statistical significance for the results by ζ_j. This measure is so defined (Ghil and Dilling, 1977) that we consid

Table II. Summary of results for the numerical measures of impact.

Experiment No.	Code	Impact, %		Statistical Significance (average/standard error)	
		Sl	RMS	Sl	RMS
7578	00	0	0	-	-
8240	12	0.21	2.13	0.13	0.94
8405	22C	0.97	1.51	1.07	1.23
8352	22	1.83	6.31†	1.01	1.82†
8310	23	2.75	5.13	0.94	1.11
8447	22N	2.98	7.36	1.36	1.24
8574	31	1.20	3.66†	0.66	1.19†
8472	32	3.11	5.97	1.39	1.37
8545	33	4.74	9.57	1.94	2.26
8566	33a	4.46	12.41	1.85	2.77
8593	33b	4.79	10.02	2.05	2.49

† incomplete

an experiment j to have yielded significant results, roughly speaking, if $\zeta_j \geq 1$; we have no confidence at all in the results if $\zeta_j \leq 0.5$, and high confidence if $\zeta_j \geq 2$.

Before discussing the results, it is important to remember that Experiment 8405 (code 22C) is a control experiment, as described in Section 3, and that all the results have to be gauged against those of Experiment 8405. We discuss the results for skill scores first. In Table II we start by noticing that the measure of statistical significance for Experiment 8405, is $\zeta_{22C} = 1.07$. Hence the results of the DIM experiment 8240, with $\zeta_{12} = 0.13$, have no confidence whatever attached to them (also $\zeta_{12} < 0.5$), while those of the SCM experiments 8352, 8310, and 8447, with $\zeta_{22} = 1.01$, $\zeta_{23} = 0.94$, and $\zeta_{22N} = 1.36$ respectively, can be considered as marginally significant. The corresponding mean percentual impacts from Table II are $x_{22C} = 0.97$ for the control experiment 8405, and $x_{12} = 0.21$ for the DIM experiment 8240, which is practically negligible; they are $x_{22} = 1.83$, $x_{23} = 2.75$, and $x_{22N} = 2.98$ for the SCM experiments 8352, 8310, and 8447 respectively, with $x_{22N} \tilde{=} x_{23} \tilde{=} 1.5x_{22} \tilde{=} 2x_{22C}$. We already notice a strong correlation between measure of impact and measure of confidence. Moreover, the control experiment 8405 shows that the DIM experiment totally failed to produce favorable impacts, while the SCM experiments produced results considerably better than the performance level set by the control experiment, in fact twice as good, at least. Also Experiment 8310, which used a large amount of data, obtained from two satellites, produced

results which were 50 percent better in mean percentual impact than those of Experiment 8352, utilizing the same assimilation method (SCM) but data from Nimbus-6 only. Furthermore, Experiment 8447, in which no satellite data were inserted over land, reflecting higher reliance on conventional data, produced results comparable to and even better than those of Experiment 8310, while using only data from one satellite (Nimbus-6).

We proceed now to discuss the SAM experiments, 8574 through 8593. The comparison of skill score results, in both impact and significance, of Experiment 8574, which used only NOAA-4 data, Experiment 8472, which used the more abundant Nimbus-6 data, and the remaining SAM experiments, 8545, 8566, 8593, which used data from both satellites, immediately shows the importance of data quantity, independently of the assimilation method. We have in fact $\zeta_{31} = 0.66 < \zeta_{32} = 1.39 < \zeta_j$, $j = 33, 33a, 33b$, with $\zeta_j \tilde{>} 2$; similarly $x_{31} = 1.20 < x_{32} = 3.11 < x_j \tilde{=} 4.65$. Thus Experiment 8472 is comparable to the best SCM experiments 8310 and 8447, while Experiment 8574 produces somewhat poorer results.

The results of three SAM experiments which utilized fully the available data, 8545, 8566, and 8593, are remarkably similar. We have $\zeta_{33} = 1.94$, $\zeta_{33a} = 1.85$, and $\zeta_{33b} = 2.05$; these give us all high statistical confidence in the mean impacts, being very close to and even larger than 2. The mean impacts are $x_{33} = 4.74$, $x_{33a} = 4.46$, and $x_{33b} = 4.79$, that is close to 5 percent. This is certainly not a very large impact, but is quite comparable to improvements in numerical weather prediction which have been considered as important over the last decade; it corresponds approximately to the ability of making a 60h forecast of accuracy which equals that of today's operational 48h forecast.

We remark in passing that the attempts at removing the bias, (cf. Ghil and Dilling, 1977) of satellite-derived temperatures, either at observation points (8566), or at the correction point (8593), did not make much difference in the results. The use of SAM itself, however, certainly did make a difference. It is very interesting to consider the SCM experiment which is similar in other respects to the three SAM experiments we are in the process of discussing, namely Experiment 8310; we immediately notice that the two quantities measuring result, ζ_{23} and x_{23}, have a value which is almost exactly half the corresponding representative value for SAM, $\zeta_{23} = 0.94$, versus 2, and $x_{23} = 2.75$, versus 5.

The values of ζ_{12} and x_{12} for DIM experiment 8240 can be considered zero for all practical intents and purposes of this discussion. We observe at this point that, in a certain sense, SCM is a low-order approximation to SAM, in which the matrix $\underset{\approx}{A}$ of Section 2 is approximated by a diagonal matrix (compare Rutherford, 1972).

The results for RMS errors strongly support those presented here for skill scores; they are given in the fourth and sixth column of Table II. The statistical significance of the RMS results is influenced by data quantity and assimilation method in the same way as the S_1 results, and so are the mean impacts; the values of RMS mean impacts are of the order of 10 to 12 percent for the best SAM experiments, and 5 to 7 percent for the SCM experiments.

It appears in general that differences in initial states correlate reasonably well with impact on forecasts from those initial state (Halem et al. 1978). Our numerical measurements of impact also seem to correlate postively with improvements in the capability of predicting local weather when using the large-scale numerically predicted fields for guidance (loc. cit.).

5. CONCLUDING REMARKS

We have presented a statistical method for the time-continuous, four-dimensional assimilation of temperature data derived from satellite based radiometric measurements (SAM). This method was applied to DST-6 data. It was compared to a direct-insertion method (DIM) and to an asynoptic successive-correction method (SCM). Further experiments considered the influence of data quantity on improvements in initial states and on forecasts from those initial states.

The results of our experiments allow us to draw a number of conclusions: (i) satellite-derived temperature data can have a modest, but statistically significant positive impact on numerical weather forecasts, as verified over the continents of the Northern Hemisphere; (ii) this impact is highly sensitive to the quantity of the data -- the impact of a two-satellite system is larger than that of one satellite by an amount roughly proportional to the quantity of data provided; (iii) the assimilation method plays a major role in the magnitude of the impact for the same data -- direct insertion had a practically null impact, while SCM provided about half the impact obtained with SAM.

The impact for the best method tested and for the full amount of data available was about 5 percent in S_1 skill score and 12 percent in RMS errors; these correspond to the possibility of an extension of about 8-12h in the usefulness of numerical weather prediction (NWP) in the range between 48h and 72h. There are indications that local weather forecasts using large-scale NWP results as guidance can be similarly improved.

We are in the process of further refining our statistical assimilation method of the sounding data and of applying it to data from the entire DST-6 period. We intend also to adapt SAM to the assimilation of cloud-track wind data from geostationary satellites, and we expect eventually to apply it to FGGE (First Global GARP Experiment) data.

Our results suggest that larger impacts of satellite-borne sounding systems on weather forecasting could be brought about by

improvements in two major areas: (a) improved accuracy and vertical resolution of sounder temperature profiles, and (b) improved numerical models for assimilation and forecasting.

Acknowledgements. It is a pleasure to acknowledge the enthusiastic encouragement of Dr. Milton Halem for the development of the method and his invaluable support and collaboration in carrying out the experiments. Interaction with Drs. R. Atlas, M. Cane, R. Dilling, and J. Susskind is also acknowledged with gratitude.

6. REFERENCES

Atlas, R., and D. Sakal (1977). Evaluation and verification tests. Chapter 5 of Halem et al. (1977), pp. 5.1-5.81.

Bengtsson, L. (1975). Four-Dimensional Data Assimilation of Meteorological Observations. GARP Publ. Ser., No. 15, WMO/ICSU Geneva, Switzerland, 76 pp.

_____, and N. Gustavsson (1971). An experiment in the assimilation of data in dynamical analysis. Tellus, 23, 328-336.

_____ (1972). Assimilation of non-synoptic observations. Tellus, 24, 383-399.

Cressman, G. P. (1959). An operational objective analysis system. Mon. Wea. Rev., 85, 367-374

Eliassen, A. (1954). Provisional report on calculation of spatial covariance and autocorrelation of the pressure field. Report No. 5, Inst. Weather and Climate Res., Acad. Sci., Oslo, 11 pp.

Gandin, L. S. (1963). Objective Analysis of Meteorological Fields. Gidrometeorologicheskoe Izdatel'stvo (GIMIZ), Leningrad. English translation by Israel Program for Scientific Translations Jerusalem, 1965 (available from NTIS), 242 pp.

Ghil, M. (1975). Initialization by compatible balancing. Report 75-16, Inst. Comp. Appl. Sci. Eng., NASA Langley Research Center, Hampton, VA 23775, 38 pp.

_____ _____, and R. Dilling (1977). Analysis and assimilation. Chapter 3 of Halem et al. (1977), pp. 3.1-3.150.

_____, B. Shkoller and V. Yangarber (1977a). A balanced diagnostic system compatible with a barotropic prognostic model, Mon. Wea. Rev., in press.

_____, R. Dilling and H. Carus (1977b). A statistical method for the time-continuous assimilation of satellite-derived temperatures, Proc. 5th Conf. Probability and Statistics in Atmos. Sci., Amer. Meteor. Soc., Boston, 320-324.

Halem, M., M. Ghil, R. Atlas, J. Susskind and W. J. Quirk, eds., (1977). The GISS Sounding Temperature Impact Test. NASA Institute for Space Studies, Goddard Space Flight Center, New York, N. Y. 10025 328+xiv pp.

_____ _____, M. Ghil, and R. Atlas (1978). Some experiments

on the effect of remote sounding temperatures upon weather forecasting. Remote Sensing of the Atmosphere: Inversion Methods and Applications, A. L. Fymat and V. E. Zuev (eds.), Elsevier, Amsterdam, submitted for inclusion.

Rutherford, I. D. (1972). Data assimilation by statistical interpolation of forecast error fields, J. Atmos. Sci., __, 809-815.

_____, (1973). Experiments in the updating of P. E. forecasts with real wind geopotential data. Proc. 3rd Conf. Probability and Statistics in Atmos. Sci., Amer. Meteor. Soc., Boston, 198-201.

Somerville, R. C. J., P. H. Stone, M. Halem, J. E. Hansen, J. S. Hogan, L. M. Druyan, G. Russell, A. S. Lacis, W. J. Quirk and J. Tenenbaum (1974). The GISS Model of the Global Atmosphere. J. Atmos. Sci., 31, 84-117.

Paper No. 19

THE EFFECT OF SEA ICE EXTENT ON THE CLIMATOLOGY OF THE GISS GENERAL CIRCULATION MODEL

G. F. Herman, *University of Wisconsin Meteorology Department, Madison*
W. T. Johnson, *Goddard Space Flight Center, Greenbelt, Maryland*

ABSTRACT

Two model simulations were calculated with the GISS general circulation model corresponding to hypothetical maximum and minimum January sea ice conditions in the north and south polar regions.

Results indicated that there were large differences in the Northern Hemisphere circulation between maximum and minimum ice conditions in zonally averaged temperature, vertically averaged eddy sensible heat flux, and mean 500 mb geopotential height. The calculated differences are found to be greater than the inherent variability of the model.

1. INTRODUCTION

At high latitudes the heating of the atmosphere by radiation and convection depends on the distribution of sea ice because of its high reflectivity and low conductivity as compared with the ocean. In order to test the response of a general circulation model to the extreme variations of sea ice margin, we have conducted a sensitivity study with the GISS GCM. Two model calculations were performed with hypothetical maximum and minimum ice conditions, and statistical significance was estimated from a predictability experiment that was carried out for the same period.

2. DESCRIPTION OF EXPERIMENT

a. The GISS General Circulation Model

The model that we employed is a version of the GISS GCM that has been described by Somerville et al. (1974) and Stone et al. (1977). A modification of the grid resolution at high latitudes as described by Halem and Russell (1973) was used to eliminate computational instability associated with the convergence of the meridians at the poles. Solar and thermal radiation and ground temperature (including the ground temperature of continental and sea ice) are computed interactively and depend on changing water vapor and cloud conditions. Simple approximations are used for surface moisture conditions. Tropical convection is treated with a modified form of the Arakawa et al. (1969) parameterization. Sea ice is not an interactive component of the GISS model

because its accretion or ablation is not calculated explicitly. Model pack ice consists of a three meter layer with fixed optical and conductive properties overlying an ocean surface of constant temperature.

b. Boundary and Initial Conditions

The model initial conditions were taken from the 00Z global National Meteorological Center (NMC) analysis for 1 January 1975. The control for the experiment consisted of "minimum" ice conditions which corresponded to the realization of climatologically minimal ice margins occurring *simultaneously* in the Baffin-Davis Straits, Greenland-Norwegian-Barents Seas, and Sea of Okhotsk. These minima were suggested by ice maps prepared by the British Meteorological Office, and the Danish and German hydrographic offices.

The perturbation experiment, referred to as the "maximum" ice case, was carried out with northern hemisphere ice extent that was somewhat greater than would be realized if the ice cover in these seas were simultaneously at their actual climatological maxima, especially in the North Pacific and in the vicinity of Iceland. The regions of ice margin variation for these two experiments are shown in Fig. 1. The model integration was carried out from 1 January 1975 to 14 February 1975.

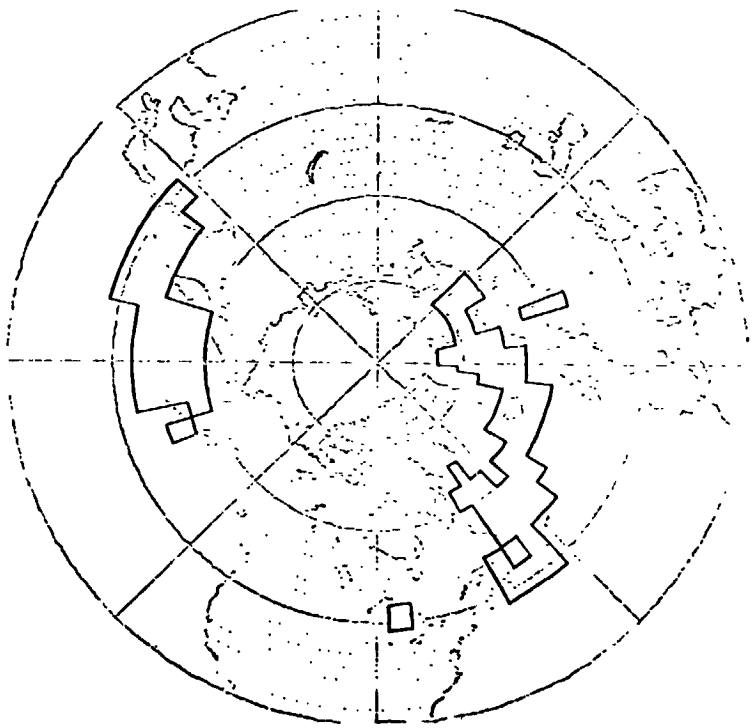

Fig. 1 Regions of ice margin variation

3. RESULTS AND DISCUSSION

a. Zonally Averaged Quantities

Maximum temperature differences of -5 deg. are found in the lowest model layer between 50° and 60°N, and decrease to -1 deg. at 400 mb. Cooler tropospheric temperatures are associated with maximum ice because more ice diminishes the sensible and latent heating of the atmosphere by effectively insulating the atmosphere from the ocean in the regions of strong air mass modification of the North Atlantic and North Pacific.

The zonally averaged wind increased at upper levels of the high-latitudes with increased ice, due to decreased poleward temperatures gradient between 70° and 90°N. Smaller changes in the zonal wind at 400 mb occur at 55°N and 35°N.

There is very little difference between the zonally averaged geopotential heights at 835 and 505 mb equatorward of 55°N, but differences increase poleward. Geopotential height decreases with maximum ice by 90 m at 505 mb and 30 m at 835 mb.

Figure 2 illustrates the latitudinal values of the poleward transport of sensible heat by the mean meridional circulation (MMC), and the net transport by the standing and transient eddies. Larger average eddy heat transports in mid-latitudes are obtained with maximum ice, and differences as large as 21 percent are found at 53°N. The larger poleward heat transport of the maximum ice case results from an enhancement of the lower tropospheric temperature gradient in mid-latitudes. The equatorward sensible heat transport by the model's Hadley cell is also influenced by high latitude ice conditions. Equatorward transport is diminished by 15 percent with maximum ice conditions.

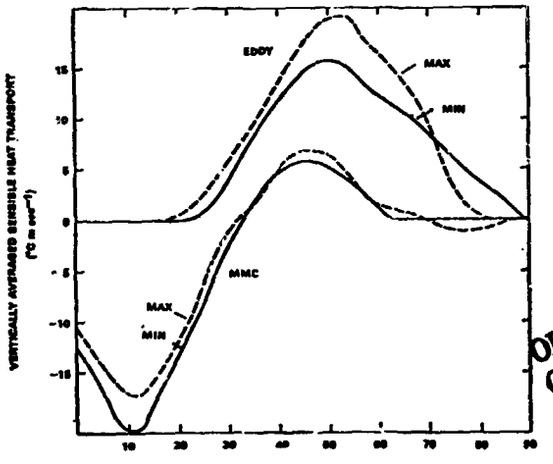

Fig. 2 Heat Transport

b. Hemispheric Fields

The 850 mb temperature differences show that there are warmer temperatures with minimum ice conditions in the Icelandic

regions of the North Atlantic (6-7 degrees), Baffin-Davis (4-6 degrees), and the North Pacific (6-8 degrees). A broad region of large positive temperature differences is found over the northwest United States and British Columbia and is presumably associated with the margin variations in the North Pacific. Temperatures in the central polar region range 2-4 degrees warmer with minimum ice condition.

The pattern of temperature differences is considerably different at 500 mb where a discernable wave pattern has developed. Temperatures are warmer with minimum ice in the Alaska and East Siberian Arctic, but the differences in the Icelandic region are of the opposite sign (i.e., colder) than at 850 mb. An extensive region of colder temperature also has developed from the variation in the Sea of Okhotsk and has spread over the eastern North Pacific and western United States. Smaller regions of colder temperature developed over continental North America and Asia with minimum ice.

The differences of geopotential (Fig. 3) closely follow those of temperature at 500 mb: With minimum ice the Aleutian low is deeper by 120 meters. The Icelandic low also deepens (50 m), and the highs of Asia and Arctic Canada are more intense by 50-60 m.

Fig. 3 500 mb geopotential

c. Significance of Results

Is the calculated change of an atmospheric parameter a true function of changing ice extent, or simply a random state that could be obtained equally well from small errors in the initial temperature or wind field? According to the results of Prof. J. Spar the standard deviation of the 500 mb geopotential height in the GISS model is 45 m in high latitudes of the Northern Hemisphere. For comparison the mean model level 5 height differences between maximum and minimum ice conditions is greater than or equal to 45 m poleward of 70°N, and ranges from 0 to 45 m between 50° and 70°N. The standard deviation of the 850 mb temperature was generally less than 2°C in the Northern Hemisphere with regional maxima of up to 3° over northern North America. The zonal mean temperature deviations we find here are at or above these levels at all latitudes north of about 45°N, but are at or below Spar's levels in the tropics and sub-tropics. It therefore appears that we are observing a true response to the change in the thermal forcing associated with the different ice margins.

4. REMARKS AND CONCLUSIONS

The results indicate that maximum ice extent is associated with colder temperatures at high mid-latitudes, larger poleward temperature gradients, larger eddy sensible heat transports, and in general a slightly more energetic circulation. A negative feedback between ice extent and poleward heat transport is suggested. The important question that remains is whether changes in the atmospheric eddy heat transport caused by maximum ice could ever become large enough to inhibit the growth of the pack ice, or cause it to recede. Unfortunately our model does not simulate the important coupling between the ocean surface temperature and the variable pack ice margin.

We conclude from our model results that ice margin is capable of influencing the mean climatology of the high mid-latitude and polar regions of the Northern Hemisphere through its influence of the sensible and latent heating of the atmosphere in regions of maximum margin variation. The most significant changes occur locally in the vicinity of the changing ice margin, but global changes larger than the inherent variability of the model are observed.

REFERENCES

Arakawa, A., et al., 1969, Proc WMO/IUGG Symp. Weather Pred., Tokyo, Jap. Met. Soc., Vol. IV, p. 8-17.

Halem, M. and G. Russell, 1973, NASA GISS Research review, pp. 144-200.

Somerville, R. C., et al., 1974, J.A.S., 31, 84-117.

Stone, P. H., et al., 1977, M.W.R., 105, 170-194.

Paper No. 20

N79-20595 D20

NUMERICAL SIMULATION OF FLOW NEAR STEEP MOUNTAINS WITH A POTENTIAL ENSTROPHY CONSERVING SCHEME FOR THE SHALLOW WATER EQUATIONS

Akio Arakawa, *Dept. Atmospheric Sciences, UCLA*

ABSTRACT

Numerical experiments show that use of a potential enstrophy conserving scheme drastically improves numerical simulation of flow near steep mountains.

Medium-range numerical prediction experiments showed that a decrease in horizontal grid size improved the predictability, even of large, and presumably already well resolved, planetary waves. This fact suggests that, although the planetary waves should be relatively free from truncation errors in a linearized system, the mechanisms for their generation and subsequent time change are nonlinear and do involve smaller scales which are subject to serious truncation errors.

One of the major sources of such truncation errors which must seriously affect the dynamics of planetary waves is the presence of steep mountains. In nature steep mountains can affect the dynamics of planetary waves (even if they are longitudinally very narrow), provided that they are sufficiently high and have a large enough meridional extent. When the conventional grid sizes are used, even the Rocky mountains, for example, extend at most only a few grid intervals in longitude and, therefore, the dynamical response of the model atmosphere to them can be subject to a serious truncation error.

It is commonly assumed that decrease of errors in finite differencing could be achieved through use of a smaller grid size. But the question of whether the solution with a given grid size is in an approximately convergent range or not is highly scheme-dependent in nonlinear systems. It has been known that some space finite difference schemes for two-dimensional incompressible flow produce spurious energy cascade, while the total energy is conserved. After sufficiently long time integrations with such schemes, significant amount of energy exists in the smallest resolvable scales, where truncation error is large, regardless of the grid size. This means that a decrease in the grid size always affects the solution with such schemes.

It is thus important to seek a scheme which prevents a false energy cascade. Solutions with such a scheme should be relatively smooth and, therefore, relatively little "improvement" is expected when the grid size is decreased. This means that the original solution is already a good approximation.

For a homogeneous incompressible atmosphere, flow over and near mountains is governed by the conservation of (absolute) potential vorticity η/h during advective processes, where η is the (absolute) vorticity and h

is the depth of the fluid. Consequently, the (absolute) potential enstrophy $\frac{1}{2}\overline{\eta^2/h}$ is conserved, where the overbar means the horizontal average. Since $\overline{\eta^2} < \overline{(\eta^2 h_{max}/h)} = \overline{(\eta^2/h)} h_{max}$ = const., there is an upper bound for the (absolute) enstrophy $\frac{1}{2}\overline{\eta^2}$. Therefore, as in a purely two-dimensional flow, a systematic energy cascade is prohibited also for a variable h.

We have found that conventional space finite difference schemes for the momentum equation, when they are applied to the shallow water equations, correspond to very bad advection schemes for the potential vorticity in the presence of steep mountains. In particular, conservation of the potential enstrophy is not guaranteed, even when the scheme guarantees conservation of the enstrophy for a purely two-dimensional flow. Fig. 1 shows examples of potential enstrophy increase in time with such a scheme. The scheme used here is that of the current UCLA general circulation model applied to the shallow water equations. The domain is bounded by two rigid walls at y = 0 and y = 2,000 km and by x = 0 and x = 6,000 km, where cyclic boundary conditions are applied. The mean height of the free surface, Ho, is 5 km; the acceleration of gravity, g, is 9.8 m sec^{-2}; and the coriolis parameter, f, is 10^{-4} sec^{-1}. The bottom topography is a narrow ridge which extends throughout the channel in y and has a triangular shape in x, and centered at x = 3,000 km. Its maximum height is 2 km and its bottom width 1,000 km. The initial conditions are a uniform zonal current of 20 m sec^{-1} and a horizontal free surface. Experiments were performed with three different grid sizes: d = 500 km, 250 km and 125 km. Fig. 2 shows the topography recognized by each of these three grids. We can see in Fig. 1 that there is no improvement in conservation of potential enstrophy by decreasing the grid size from 500 km to 250 km. Even with d = 125 km, there is a considerable increase of potential enstrophy in time.

To overcome this deficiency we redesigned the space finite difference scheme for the momentum equation so that it conserves potential enstrophy as well as total energy.

To compare solutions of the two schemes in simulation of a statistically steady state, we performed a series of experiments in which a surface stress linearly proportional to the wind with coefficient k = 0.25 x 10^{-5} sec^{-1} and a uniform westerly momentum generation of 2.5 x 10^{-5}m sec^{-2} per unit mass is added to the momentum equation. In addition, the maximum height of the mountain is now 4 km and g is reduced to 0.98 m sec^{-2} to partially include the effect of stratification. All other parameters and the topography are the same as the previous experiments. The initial condition has no motion and horizontal free surface H = Ho. Figs. 3 through 5 show the time averages for the period from day 20 to 30.

Fig. 3a: the old scheme with d = 500 km;
Fig. 3b: the new scheme with d = 500 km;
Fig. 4a: The old scheme with d = 250 km;
Fig. 4b: the new scheme with d = 250 km;
Fig. 5a: the old scheme with d = 125 km;
Fig. 5b: the new scheme with d = 125 km.

Figs. 3a and 3b show that with the coarse grid, d = 500 km, the old scheme produces a weak, relatively disorganized flow, while the new scheme produces an organized, dominantly westerly flow with a continuous

meandering jet stream. The old scheme produces a weak ridge at the west side of the mountain, while the new scheme produces a stronger ridge almost right over the mountain. Figs. 4a and 4b show that even with the medium grid, d = 250 km, these situations do not change significantly. Figs. 5a and 5b show, on the other hand, that with the fine grid, d = 125 km, the two schemes produce an almost identical field. By comparing Figs. 3a and 4a with 5a and Figs. 3b and 4b with 5b, we see that, as the grid size is reduced, the characteristics of the produced field changes less with the new scheme than with the old scheme. This indicates that the solution with the new scheme is in an approximately convergent range even with the coarse grid, while those with the old scheme are not.

We have incorporated a horizontal finite difference scheme, designed similarly to the "new" scheme above but for a stratified baroclinic atmosphere on the spherical earth, in the general circulation model.

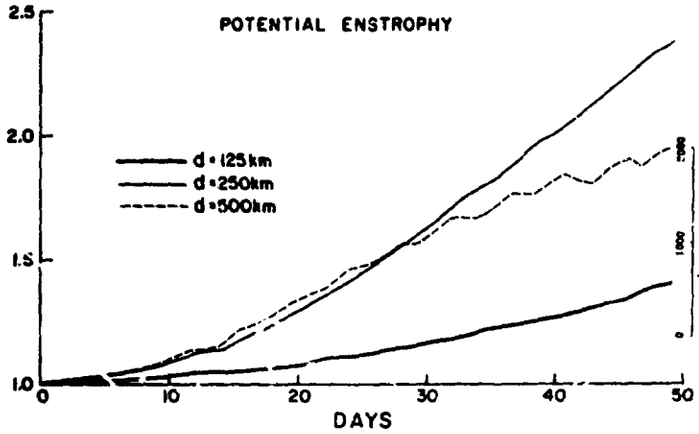

Fig. 1

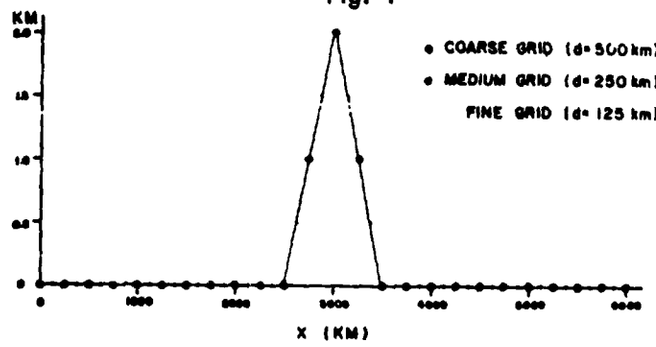

Fig. 2

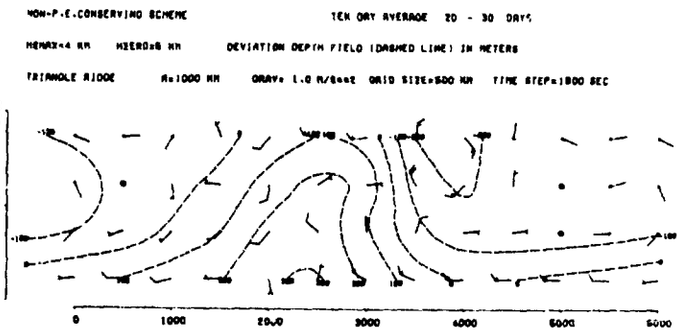

Fig. 3a

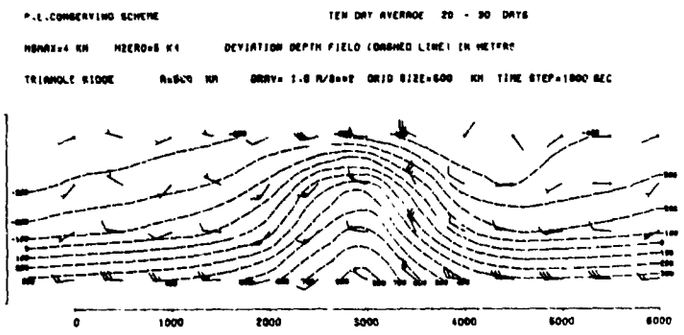

Fig. 3b

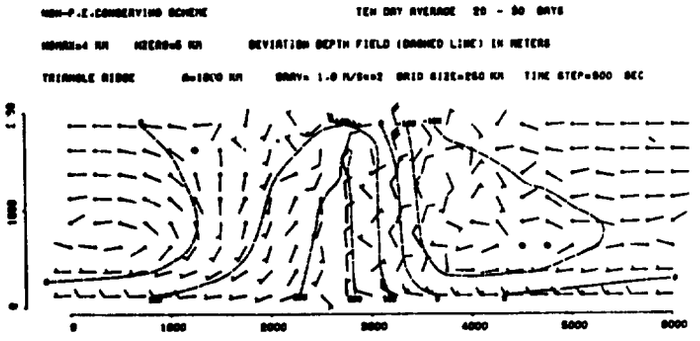

Fig. 4a

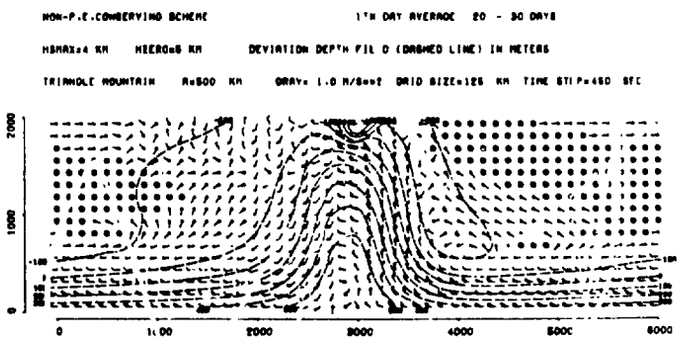

Fig. 5a

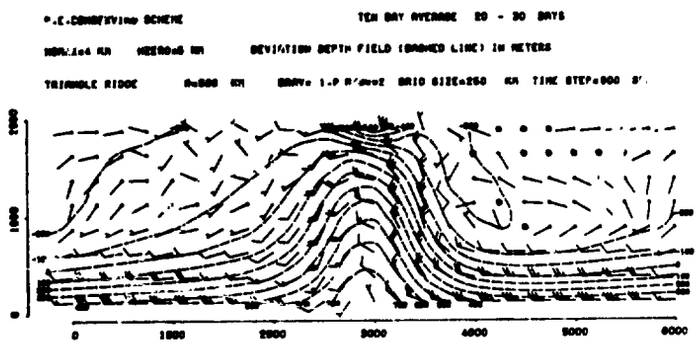

Fig. 4b

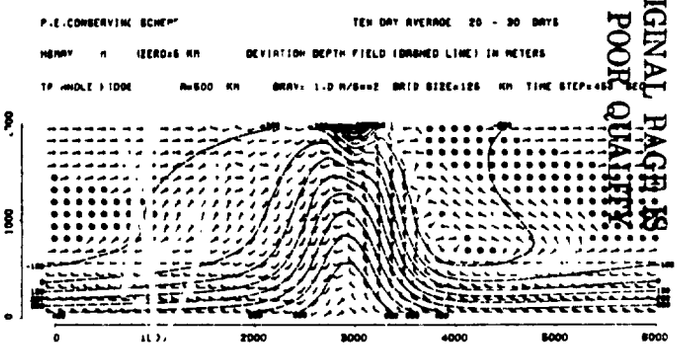

Fig. 5b

D21

N79-20596

Paper No. 21

DESIGN AND TESTING OF A NEW PLANETARY BOUNDARY LAYER PARAMETERIZATION

David A. Randall, *Dept. of Meteorology, M.I.T, Cambridge, MA 02139*

ABSTRACT

A new planetary boundary layer parameterization has been developed. Tests have included forecasting experiments.

INTRODUCTION

Under the direction of Prof. Akio Arakawa, Randall (1976) developed a new parameterization of the planetary boundary layer (PBL) for use in the UCLA General Circulation Model (GCM). Although the final version of the model is still being tested, preliminary versions have been in experimental use for several years. The first applications have included climate simulations for January (Mintz and Schlessinger, 1975; Schlessinger, 1976) and July. More recently, a series of forecasting experiments have been performed for the purpose of evaluating the desirability of incorporating various aspects of the model, including the PBL parameterization, into the Goddard GCM.

The purposes of this brief note are to describe the PBL parameterization, and to discuss the forecasting experiments.

The Purposes of the PBL Parameterization

The PBL plays two critically important roles in the evolution of weather and climate. First, it determines the rates at which sensible heat, moisture, and momentum are exchanged between the atmosphere and the underlying surface, and redistributed by turbulence in the lower troposphere. In fact, we define the PBL to be the layer within which these fluxes are significantly large. But, as emphasized by Arakawa (1974), the PBL also strongly influences the global distributions of both cumuliform and stratiform clouds. Predictions of cloudiness and precipitation are among the most important weather forecasting products, and the central role of clouds and cloud feedback in the evolution of climate is widely recognized. We have therefore made a particular effort to model the interaction of the PBL with clouds, as well as to parameterize the turbulent exchange processes.

The Basic Design of the PBL Parameterization

The surface values of the turbulent fluxes are parameterized according to a slightly revised version of the method of Deardorff (1972). The variation of the surface transfer coefficients with stability and surface roughness are taken into account.

We have adopted a new vertical coordinate in which the PBL top and the earth's surface are both coordinate surfaces (Fig. 1). The PBL then consists identically of a fixed number of model layers. The upper layers of the model feel the effects of the turbulent fluxes only indirectly, as a result of shallowing, in which PBL mass is shed into the free atmosphere, and also through the effects of penetrative cumulus clouds growing up from the PBL.

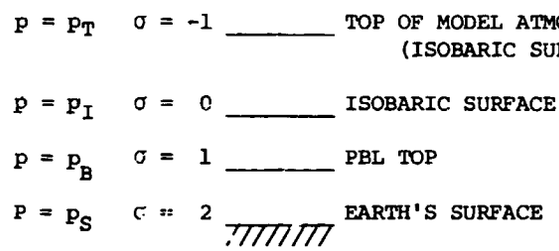

Figure 1. The relation between pressure p and the vertical coordinate σ.

The PBL depth is a prognostic variable which varies continuously in time and space as a result of lateral convergence, turbulent entrainment, and the occasional loss of PBL mass into cumulus clouds. The turbulent entrainment process is parameterized according to the theory of Randall (1978), which includes shallowing as a special case. According to this theory, a certain fraction of the gross total rate of turbulence kinetic energy production is available for partitioning between negative production (as in the entrainment of warm air) and storage in the newly-entrained air.

In middle and high latitudes, the time-averaged PBL depth is mainly determined by a balance between lateral divergence and entrainment, while in the tropics it is mainly determined by a balance between entrainment and the loss of PBL material into cumulus clouds.

The Interaction of the PBL With Clouds

The mutual interaction of the PBL with cumulus cloud ensembles occurs because the cumulus convective circulations carry dry air, moisture, sensible heat, momentum, and turbulence kinetic energy up out of the PBL. The loss of mass tends to produce a shallowing of the PBL. We assume that the

air rising into the clouds carries the vertically averaged intensive properties of the PBL air, so that the vertically-averaged intensive properties of the PBL air, i.e. mean potential temperature, water substance mixing ratio, horizontal velocity, and turbulence kinetic energy density, are not influenced by the cumulus convection.

Because the cumulus cloud air originates in the PBL, the PBL exerts a powerful influence on the life cycles of the clouds. This is particularly true of shallow clouds.

In the UCLA GCM, the value of M_B and the other properties of a cumulus cloud ensemble are determined on the basis of the theory of Arakawa and Schubert (1974), which explicitly takes into account the dynamical interaction of the ensemble with the PBL.

We also consider the possible formation of a layer of stratus, stratocumulus, or fog within the PBL (Fig. 3). The presence of such a cloud layer is considered only if the air at the PBL top is found to be supersaturated. The layer clouds are recognized by the radiation parameterization of the model, and also in the calculation of the entrainment rate, in a way to be described in the next section. Precipitation falls from these clouds only if the PBL mean relative humidity exceeds 100%.

Randall (1976) has derived a criterion for the evaporative destruction of layer clouds by dry penetrative downdrafts. When a layer cloud is found to be unstable in this sense, we allow M_B to increase in such a way as to push the PBL top down to the cloud base level after about two simulated hours. The positive values of M_B represent the loss of PBL mass into cloud fragments which persist after the layer cloud has been destroyed.

The Forecasting Experiments

Although a primary purpose of the forecasting experiments is to evaluate the possibility of incorporating the PBL parameterization into the Goddard GCM, it is not possible simply to transplant the PBL parameterization into the Goddard model, because the parameterization is so thoroughly incorporated into all aspects of the model. Therefore, the experiments have been performed with a six-level version of the UCLA model. The horizontal resolution of the model is 4 degrees of latitude by 5 degrees of longitude. Forecasts have been performed for 5 three-day periods in February 1976, and for 5 three-day periods in August 1975. Results are compared with those obtained with both the "standard" Goddard model and a version of the Goddard model containing the Hoffert-Sud PBL. Figures will be shown at the oral presentation.

REFERENCES

Arakawa, A. and W.H. Schubert, 1974: Interaction of a cumulus cloud ensemble with the large-scale environment, Part I. J. Atmos. Sci., 31, 674-701.

_____, 1974: Modeling clouds and cloud processes for use in climate models. Presented at JOC International Study Conference on the Physical Basis of Climate and Climate Modeling. Stockholm, July-August 1974. (Available from the author at the Department of Atmospheric Sciences, University of California, Los Angeles, 90024.)

Deardorff, J.W., 1972: Parameterization of the planetary boundary layer for use in general circulation models. Mon. Wea. Rev., 100, 93-106.

Mintz, Y., and M. Schlessinger, 1975: Ozone production and transport with the UCLA General Circulation Model. Fourth conference on CIAP, U.S. Department of Transportation.

Randall, D.A., 1976: The interaction of the planetary boundary layer with large-scale circulations. Ph.D. Thesis, The University of California, Los Angeles, 247 pp.

_____, 1978: On the entraining moist boundary layer. Part I: The rate of entrainment, In preparation.

Schlessinger, Michael E., 1976: A numerical simulation of the general circulation of atmospheric ozone. Ph.D. dissertation, UCLA, 375 pp.

Paper No. 22

OPERATION AURORÓZONE: AN EXPERIMENT IN SUN/WEATHER

R. A. Goldberg and E. Hilsenrath, *Goddard Space Flight Center, Greenbelt, Maryland*

ABSTRACT

Operation Aurorozone was a highly coordinated sequence of 33 rocket flights launched from Poker Flat, Alaska, in September 1976. The purpose was to study the effects of aurorally produced X-rays on stratospheric neutral and electrical parameters. The sun/weather coupling between upper and lower regions of the atmosphere is thought to be related to these middle atmospheric parameters. The results reviewed show a consistent depletion of ozone above 1 mb during three independent auroral events, with magnitudes in excess of those expected from the measured energy radiation sources. Simultaneously, enhanced conductivity changes were observed to occur in accord with the measured ionizing radiations.

INTRODUCTION

In recent years there has been a gradual accumulation of evidence that high latitude energetics in the upper atmosphere can perturb and modulate the structure of the middle atmosphere, thereby inducing change in stratospheric and tropospheric phenomena. The depletion of stratospheric ozone during a solar proton event (PCA) has now been clearly demonstrated with Nimbus 4 BUV data (Heath, et al. 1977). Furthermore, Thorne (1977) has suggested a cumulative effect of equivalent magnitude induced by relativistic electron precipitation events (REPS) and Herman and Goldberg (1977) have demonstrated the effects of PCA's and cosmic rays on atmospheric electrical parameters, which may, for example, modulate the frequency of non-tropical thunderstorms.

Operation Aurorozone represents the first concerted experimental effort to trace the X-ray radiation emitted from high latitude energetic precipitating electron sources, into the lower mesosphere and stratosphere; to study its direct effect on key parameters such as ozone, conductivity, ionization, mobility, and the meteorological structure. The operation included a series of highly coordinated rocket, balloon, and ground instrument-supported measurements performed at the Poker Flat Rocket Range (Fairbanks, Alaska) between September 20 and October 2, 1976.

A total of 33 successful rocket flights was launched during the two-week period, including two Nike Tomahawks to measure auroral particle and X-ray energetic structure, seven chemiluminescent and optical ozonesondes, seven conductivity and Gerdien probes to measure stratospheric electrical parameters, and 17 datasondes to measure temperatures, densities and winds. These flights were supported by five large balloon (0.25 to 1.0 million cubic foot) payloads to measure X-rays, conductivity, and cosmic rays near 40km. In addition, four

balloon ozonsondes were employed to measure ozone up to 30km. The nearby Chatanika radar backscatter facility was also coordinated to predict, verify, and map electron particle energetics during the Nike Tomahawk flight periods. Fifteen scientists from several universities and government laboratories participated in this cooperative effort.

Figure 1 depicts the chronological logistics for Operation Aurorozone. Two X-ray events of interest occurred on September 21 and 23. Each of these nighttime sequences was launched into moderately intense X-ray auroral event. The results shown here will demonstrate the magnitude of each event, and show the induced change on the selected middle atmospheric parameters. We also note that a third daytime REP event occurred on October 1, permitting comparison of daytime O_3 before and after the event.

AURORAL PROPERTIES AND ENERGY DEPOSITION IN THE MIDDLE ATMOSPHERE

The electron density contour maps for each auroral event were obtained by the Chatanika radar facility (Vondrack and Wickwar, SRI International) during the Nike Tomahawk flights. The intensity of the auroral events is measured by the magnitude of the electron density contours since electron density is enhanced by auroral electrons. From this, we observed that the September 21 event was reasonably intense during the early upleg portion of the flight (which is in the spatial vicinity above where stratospheric soundings were made), but gradually faded to non-auroral conditions down range. The September 23 event was more intense, and extended down range beyond the downleg portion of the rocket flight. This behavior was also observed with riometers and visibly, with all sky cameras, at Poker Flat and Ft. Yukon (200 miles down range).

The integral particle fluxes for electrons >15 and >40keV were measured with Geiger Mueller detectors (Goldberg and Jones, GSFC) on each Nike Tomahawk.

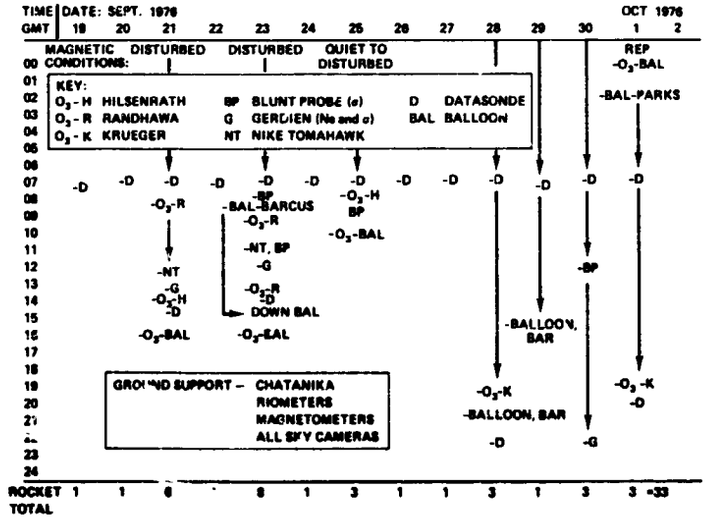

Fig. 1–Aurorozone schedule

This in situ measurement verifies the Chatanika result, and also shows that the more energetic (>40keV) component of the electron flux sustained a greater increase than the low energy component during the second event relative to the first event. Further examination of the auroral ionosphere was obtained from pulsed plasma probes (Szuszczewicz, Naval Research Laboratory), also flown on each Nike Tomahawk.

Each Nike Tomahawk also carried an upward-looking X-ray detector (NaI scintillator) with energy discrimination in four channels between 10 to 40keV and >40keV. Without special precautions such detectors are highly sensitive to contamination from energetic particles, and can be used only at those heights where suitable screening of the particles by the overlying atmosphere occurs. Figure 2 compares, for the two nighttime events, the X-ray energy deposition in the atmosphere by 5–40keV bremsstrahlung X-rays between 80 and 30km (Barcus, Univ. of Denver), with an extrapolation to higher altitudes. In studying these curves, we note the X-ray penetration depth is proportional to X-ray energy. Hence, measurable energy deposition at lower altitudes implies an appreciable high energy component in the bremsstrahlung distribution.

From the figure, we see that the September 21 event provided X-ray radiation which peaked near 60km; the September 23 event was more intense and peaked at a lower altitude. The ratio of the energy depositions as a function of altitude (energy) demonstrates that the second event possessed a stronger component at the high energy end of the distribution. in accord with the measurements of the parent energetic electron distribution discussed earlier. Above 50km, the ratio between the second and first event is about two.

MIDDLE ATMOSPHERE RESULTS

1. Ozone

The ozone results were obtained by both the chemiluminescent (night) and optical (day) sounding techniques. Figure 3 shows the GSFC results for the O_3

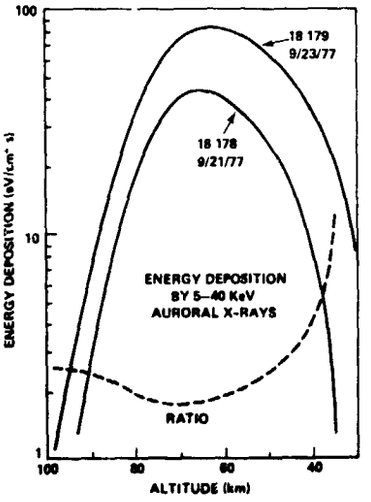

Fig. 2–Energy deposition

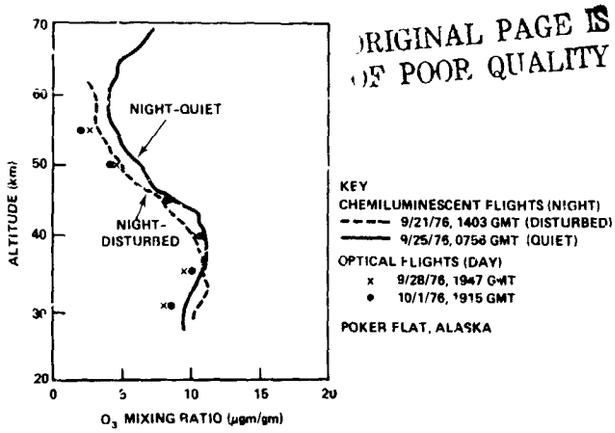

Fig. 3–Ozone profiles

mixing ratio. The two nighttime profiles were obtained on 9/21/77, following the first auroral event, and on 9/25/77, which was used as a control quiet night (Hilsenrath, GSFC). Also shown are profile points for two daytime soundings made one week later (Krueger, GSFC). The results indicate an early nighttime O_3 enhancement (which is expected on the basis of ozone production by atomic oxygen attachment when the sun sets). They then show an O_3 depletion to near daytime values above 50km (1 mb) following the auroral event. Further verification of this effect was found in the two chemiluminescent O_3 soundings (Randhawa, Atmospheric Sciences Laboratory) during the September 23 event. In both cases, a significant depletion (more than 25%) was seen above 50km. The above results are somewhat unexpected, since energy arguments using neutral photo-chemical models cannot account for the observed depletion. Also, a study of the local meteorology provided by the datasonde soundings and satellite synoptic maps does not appear to show any significant circulation or temperature variation which could account for the observed ozone change.

Finally, the daytime soundings before and after the REP have also displayed an equivalent depletion consistent in height and magnitude with the nighttime results. The REP event energetics are not yet available but are required for proper interpretation of this result.

2. Atmospheric Electrical Parameters

An example of the effects of X-ray ionizing radiation is illustrated in Figure 4 (Mitchell, Univ. of Texas at El Paso), which represents the sequence of three conductivity soundings during the second event. The profiles at 2200 (before) and 0137 AST (during) were made with blunt probes. The profile at 0220 AST (following) was made with a Gerdien probe. This latter instrument measures conductivity and ionization simultaneously, permitting an estimate of ion mobility, and hence, ion size.

Below 50km, all three profiles are parallel and nearly equal, reflecting the dominance of cosmic ray ionization in this region. The increased conductivity above 50km is due to ion production by the X-rays and atmospheric chemistry. The lower altitude of the ion ledge found on the second sounding is expected from the X-ray measurement in Figure 2.

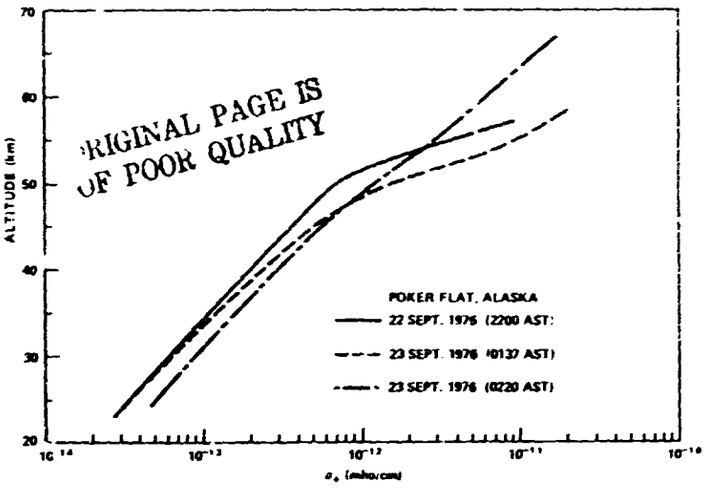

Fig. 4–Conductivity profiles

SUMMARY AND CONCLUSIONS

Two moderate X-ray auroral events and one REP have produced adequate radiation to strongly enhance conductivity and ionization and simultaneously cause an apparent reduction in O_3 above 1.0mb. For the X-ray events, the energetics appear inadequate to explain the magnitude of depletion, although new theoretical work involving ion–neutral chemistry may help explain it. An attempt to repeat this experiment is planned for March 1978.

The importance of such coordinated experiments lies in the ability to simultaneously study cause and effect relationships. These studies are essential for us to grasp the processes responsible for sun/weather correlations. The magnitude of such endeavors, with simultaneous studies in several disciplines, demonstrates the high degree of sophistication and difficulty of performing such experiments. However, without such experiments, it will be extremely difficult to evaluate the role of the middle atmosphere as a buffer region for modulating, transmitting, and reflecting energy inputs from above which are related to solar activity.

REFERENCES

Thorne, R. M., "Energetic Radiation Belt Electron Precipitation: A Natural Depletion Mechanism for Stratospheric Ozone," Science, 195, 287, 1977.

Heath, D. F., A. J. Krueger, and P. J. Crutzen, "Solar Proton Event: Influence on Stratospheric Ozone," Science, 197, 886, 1977.

Herman, J. R. and R. A. Goldberg, "Initiation of Non-Tropical Thunderstorms by Solar Activity," J. Atmospheric and Terrestrial Physics, 1977 (in press)

Paper No. 23

A PRELIMINARY COMPARISON OF THE BUV GLOBAL OZONE BUDGET INFERRED FROM THE BUV ON NIMBUS 4 AND THE DOBSON NETWORK

Donald F. Heath, *Goddard Space Flight Center, Greenbelt, Md.*

(No paper received.)

PAGE 126 INTENTIONALLY BLANK

Paper No. 24

N79-20598

A SIMPLE ALGORITHM FOR INFERRING THE VERTICAL OZONE PROFILE FROM SATELLITE MEASUREMENTS

R. W. L. Thomas, *EG&G/Washington Analytical Services Center, Inc., Wolf Research and Development Group, Riverdale, Maryland*
A. C. Holland, *Wallops Flight Center, Wallops Island, Virginia*

ABSTRACT

A general methodology for establishing and testing remote sensing inversion procedures has yielded a simple procedure for inverting BUV radiances.

INTRODUCTION

Remote sensing inversion strategies have been applied with increasing urgency to the interpretation of satellite data in terms of the properties of both the atmosphere and the surface of the earth. Thus it is becoming increasingly important to provide methods for finding and testing routines which can optimize valid information extraction. One such procedure is to model the satellite measurements through radiative transfer simulation and test inversion strategies by comparing the results generated with those specified as the model inputs.

Algorithm Testing Methodology

During the past few years we have developed, tested and optimized a Monte Carlo model of radiative transfer. The general application of this code has been in the area of evaluating the information content of sky intensity and polarization measurements at various altitudes. The procedure we have established is to plot some function of the predicted measurements against functions of the desired atmospheric or surface parameters. All plots which are single valued when performed for a number of different input models indicate a useful inversion strategy.

A striking example of the success of this philosophy is the study of simulation results for BUV radiances, when we found that the pressures at which the optical depth of the scattering path reached unity were linearly related to the scaled intensities. This immediately indicated a simple mechanism for describing the vertical ozone profile in simple terms, as described below.

Evaluation of the Vertical Ozone Profile

The measurement of the intensity spectrum of solar ultraviolet radiation backscattered by the earth and its atmosphere has been exploited for inferring both the vertical ozone distri-

PAGE 128 INTENTIONALLY BLANK

bution and the total ozone. (1,2)* The fundamental concept of the profile determination is that the ozone layer inhibits penetration of ultraviolet radiation into the atmosphere through absorption. As the wavelength increases from about 2500A° to 3000A° the ozone absorption cross-section falls, allowing the ultraviolet radiation to penetrate deeper into the atmosphere. In this way more scatterers become accessible to the incident radiation, increasing the intensity of radiation reflected back to the top of the atmosphere. Thus, the measurement of returned intensity at various wavelengths provides an indication of the number of scatterers that can be reached by the solar radiation prior to absorption by ozone.

For conditions under which multiple scattering can be neglected, the backscattered radiance I at wavelength λ in a plane parallel atmospheric model is given by:

$$I(\lambda,\theta,\theta_o) = \frac{F_o(\lambda)}{4\pi\cos\theta} S_{11} \beta_\lambda \int_0^1 \exp\{-a(\alpha_\lambda X(n) + \beta_\lambda n\}\, dn, \qquad (1)$$

where $F_o(\lambda)$ is the extraterrestrial solar irradiance

S_{11} is the scattering function (normalized so that its average value over a sphere is unity). For Rayleigh scattering S_{11} may be taken to be $\frac{3}{4}(1+\cos^2\psi)$ where ψ is the scattering angle.

β_λ is the Rayleigh volume atmospheric scattering coefficient (atm.$^{-1}$) for a standard atmosphere model

α_λ is the ozone absorption coefficient (atm.cm)$^{-1}$

X(n) is the amount of ozone in atm. cm, above the point at which the fraction of the standard molecular atmosphere overhead is n

and $\alpha = \sec\theta + \sec\theta_o$

where θ_o is the solar zenith angle and θ is the nadir angle of the receiver.

The parameter n, may be thought of as a scaled value of the pressure, p.

We now define the scaled intensity as

$$Q(k) = \frac{4\pi\cos\theta\, I(k)}{F_o(\lambda) S_{11} \beta_\lambda} \qquad (2)$$

*Numbers in parentheses designate References at end of paper.

(where K = a α_λ in our notation) and assume that the vertical ozone distribution is approximately exponential (3,4) so that we can write

$$X(n) = Cn^{(1/\sigma)} \tag{3}$$

where C and σ are constants that specify the profile. The parameter, σ, is the ratio of the ozone scale height to the atmospheric scale height. Then, neglecting attenuation by scatterers and the penetration of radiation to the ground it can be shown that

$$Q(k) = (k\ C)^{-\sigma}\ \Gamma(1 + \sigma), \tag{4}$$

showing that the gradients of the plot of ℓn Q against ℓn (k) is $-\sigma$. For the BUV system there are six wavelengths below 3000A° providing us with a six point plot per scan. This affords a method of estimating σ either locally (i.e., for each wavelength of interest), or generally by establishing the best linear fit of ℓn Q as a function of ℓn(k).

The key step in our analysis was to relate Q to the point, n(x), in the atmosphere at which the optical depth of the scattering path through the ozone reached a certain value, x. It can be shown (5) that

$$n(x) = \frac{x^{\sigma}\ Q(k)}{\Gamma(1+\sigma)} \tag{5}$$

indicating the pressure reference, n, above which the cumulative ozone is

$$X(n) = x/k. \tag{6}$$

Thus, if we fix the value of x and compute n(x), the result is a linear function of the normalized intensity, Q(k). This explains the linear relationship discovered in our preliminary searches for an inversion strategy.

It is now important to determine an optimal value x_{OPT} for the optical depth, x. The criterion we have established is that the ratio of the computed n(x) to Q(k) should be insensitive to errors in the estimate of the scale height ratio, σ. By (5) we have that

$$\frac{n(k)}{Q(k)} = \frac{x^{\sigma}}{\Gamma(1+\sigma)} \tag{7}$$

and, setting the derivative of the right hand side w.r.t. σ to zero we obtain

$$x_{OPT} = \exp\ \{\psi(1+\sigma)\} \tag{8}$$

where ψ is the digamma function. Now it can be shown by series expansion (6) that $\psi(Z)$ is closely approximated by $\ell n(Z-1/2)$ so that (8) becomes

$$x_{OPT} \simeq \sigma + 1/2 \tag{9}$$

Typically, values of σ between 0.5 and 0.6 seem to apply (4,7) so that x_{OPT} is normally close to unity. It is interesting to note that the maximum of the influence function, representing the impact of various points of the atmosphere on the measurement, occurs where x is equal to σ, so that the optimal penetration depth to be evaluated lies somewhat beneath the influence function peak.

The data reduction procedure indicated by this analysis is as follows. Firstly, an estimate of σ can be made employing relationship (4). If the plot of $\ell n(Q)$ as a function of $\ell n(k)$ is reasonably linear then the mean gradient may be used as an indication of the scale height ratio, σ. Otherwise, a local value of σ may be computed for each wavelength. Equation (9) may then be employed to establish an optimal value for x and for each wavelength a pressure reference. n, may be computed for a specific cumulative ozone amount given by equation (6). The results then appear as computed fractions of the standard atmosphere corresponding to optimized values of cumulative ozone.

For cases in which the scale height ratio is constant the error analysis for the system is trivial since an error in an intensity translates immediately into a corresponding error in n. A certain percentage error in Q(k) would result in the same percentage error in the computed n value.

Results

In order to test the suggested procedure we modelled backscattered intensities for a plane parallel atmosphere and applied the inversion technique to the computed intensities. We employed analytical computations of single scattering and a Monte Carlo simulation system (8) to compute the multiple scattering contributions. Three ozone models were used with total ozone amounts of 0.225, 0.337 and 0.459 atm. cms. The values of σ which were assumed to be independent of altitude were estimated to be 0.83, 0.75 and 0.54 respectively. The receiver was pointing at the nadir and the solar zenith angle was taken to be 60° so that the sum of the secants, a, was 3, and the optical depth, x, was taken to be unity. In Figure 1 we present the computed cumulative molecular atmosphere fraction above the cumulative ozone references, $(a\ \alpha_\lambda)^{-1}$. The actual model atmospheres are represented by the continuous lines and results obtained by the inversion of the single scattering results are shown by the darkened symbols when significantly different from the multiple scattering result. It is clear that the procedure provided results in excellent agreement with the input model for all wavelengths less than 3000A°. For the 3019A° line it seems that a simple empirical correction for multiple scattering may adequately correct the computed distribution when the ozone amount is high.

Figure 2 illustrates the results for a case where the scale height ratio was not constant. Three sets of results are shown. Firstly, we employed σ estimates from the local gradient of the $(\ell n(Q), \ell n(k))$ plot and optimized values of the optical depth, x. Secondly, we employed the same method for evaluating σ but set x to unity, and thirdly, we used the average gradient for σ and

again set x to unity. For the data at 3019A° and 3058A° we assumed a correction could be made for multiple scattering, the results shown being for single scattering only. It is clear that the local gradient method with optimized x provided the most accurate inversion.

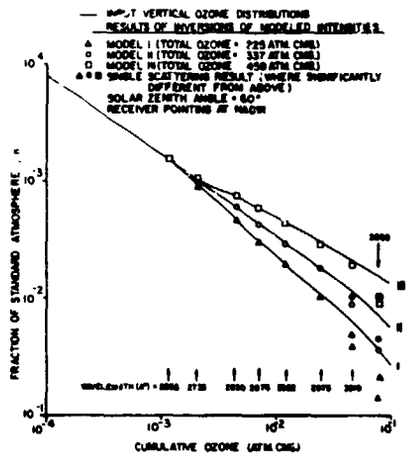

FIGURE 1. COMPARISON OF INPUT VERTICAL OZONE DISTRIBUTIONS WITH THOSE INFERRED BY THE ALGORITHM

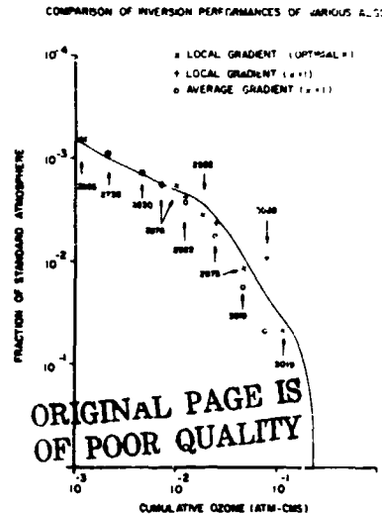

FIGURE 2. COMPARISON OF INVERSION PERFORMANCES OF VARIOUS ALGORITHMS

In conclusion, the proposed procedure represents a robust and stable method of computing the vertical ozone profile. The algorithm possesses the advantage of defining the information available from the measurement set, and, while the local gradient method is heuristic, it appears to work well over the cases we have simulated.

REFERENCES

1. Dave,J.V., and Mateer,C.L.,J.Atm.Sci., 24, 414-27(1967).

2. Mateer,C.L.,Heath,D.F.,and Krueger,A.J.,J.Atm.Sci.,28,1307-11 (1971).

3. Mateer,C.L., NASA Technical Memorandum, X-62,150 (1972).

4. Rawcliffe,R.D., and Elliot, D.C.,J.Geophys.Res.,71,5077-89, (1966).

5. Thomas,R.W.L.,and Holland,A.C.,Appl.Opt.,16,2581 (1977).

6. Handbook of Mathematical Functions, M. Abramowitz and I.A. Stegun, Eds., NBS Applied Mathematics Series (1964).

7. Green,A.E.S., Appl. Opt., 3, 203-8 (1964).

8. Thomas,R.W.L., and Holland,A.C.,Appl.Opt.,16,613-8,(1977).

N79-20599

Paper No. 25

CLIMATOLOGICAL FEATURES REVEALED BY ESMR DERIVED OCEANIC RAINFALL MAPS

M. S. V. Rao, *Systems & Applied Sciences Corporation, Riverdale, Maryland*
J. S. Theon, *Goddard Space Flight Center, Greenbelt, Maryland*

ABSTRACT

Several new climatological patterns become apparent from the analysis of satellite-derived global oceanic rainfall maps. Five interesting features are briefly discussed.

INTRODUCTION

The Electrically Scanning Microwave Radiometer (ESMR) has a selective response to liquid water in the atmosphere. Taking advantage of this characteristic of ESMR, it was possible to derive quantitative rainfall maps over the oceanic areas of the globe from Nimbus 5 satellite microwave data. Weekly, monthly, seasonally and annually averaged maps for the period December 1972 through February 1975 were published in the form of an atlas (Rao et al., 1976). The method adopted to obtain rainfall values from satellite observations and the degree of reliability of the values (in their absolute and relative senses) are discussed fully in that publication.

Analysis of these maps discloses many interesting aspects of global climatology. The objective of the contribution is to describe five major features.

(1) The Characteristics of the ITCZ in the Pacific

Although it has been known for some time that there is a dry zone near the Gilbert Islands in the Pacific (mean position 1°S, 174°E) flanked by wet regions to the north and south (Seelye, 1950) the precise structure of the ITCZ in the Pacific has remained obscure. Extensive observations of tropical cloudiness such as those compiled by the U.S. Department of Commerce and the USAF (1971), and by Sadler, et al. (1976) provide useful information on the subject to the extent to which reliance can be placed on the relationship between cloudiness and rainfall. Rainfall values derived from the ESMR system, not only because of the more complete coverage provided by the satellite but also because of the direct approach in estimation, throw further light on the rain pattern. From the typical ESMR-derived oceanic rainfall map shown in Figure 1, it is seen that as we move eastward along the Equator in the Pacific, the rain belt of the ITCZ bifurcates in the neighborhood of longitude 170°E: the upper branch proceeds eastward, maintaining itself slightly north of the Equator, whereas the lower branch runs east or southeastward and merges with the southern Pacific rain zone (path of storms) in the vicinity of longitude 160°W.

PAGE 134 INTENTIONALLY BLANK

(2) Previously Unrecognized Rain Area in the South Atlantic

In the Atlantic, to the southeast of South America, there is an extensive area of rainfall in the region approximately between latitudes 25°S and 50°S and longitudes 50°W and 25°W (see Fig. 1). This rainy region was not known before; it does not appear on any existing map of global rainfall (e.g. Haurwitz and Austin, 1944), probably because few ships traverse the area. This rain area revealed in ESMR-derived maps is possibly an extension of the southern Pacific rain zone mentioned previously. In other words, rainfall in both the areas could be produced by the same dynamical circulation pattern, the flow being modified and the rain-pattern interrupted at the land protrusion of the South American continent and an area to the immediate west of the land. Furthermore, this rain area is in conformity with the general global pattern of relatively dry regions close to the west coast of continents and wet regions close to the east coast, where greater baroclinity due to increased temperature contrast may be expected.

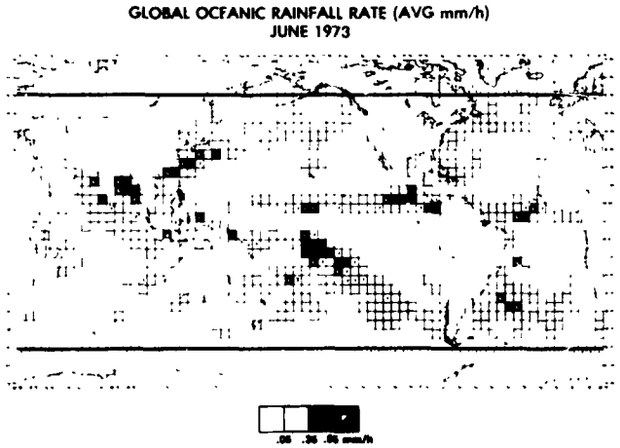

Fig. 1 – ESMR-derived global oceanic rainfall map, illustrating the forking of the ITCZ

(3) The Bimodal Behavior of Rainbelts in the Indian Ocean

Meridional profiles of zonally averaged rainfall rates in the Indian Ocean are displayed in Figure 2. Two distinct rain maxima are evident in the tropics between latitudes 20°N and 20°S (apart from a third extra-tropical maximum obviously related to the polar front, far to the south at about latitude 40°S). The maximum at northern latitudes appears to grow at the expense of the maximum immediately to the south of the Equator as the monsoon advances, and vice versa as it retreats. During June to August, the amplitude of the northern maximum is 3 times that of the other equatorial maximum, whereas during December to February, the southern tropical maximum grows in amplitude to 3 times the northern. This study leads to a modification of the beliefs of two schools of thought in tropical meteorology, one that the atmospheric monsoon current is a progressive advance over the Indian Ocean from the Southern Hemisphere across the Equator to the Southeast Asian land-mass, and the other that monsoon rainfall is due to moisture picked up entirely in the Northern Hemisphere, mainly in the Arabian Sea. It seems necessary to postulate a circulation mechanism involving both the hemispheres, not necessarily de-

manding a regular progression of the entire monsoon airstream from the Southern to the Northern Hemisphere. but affecting both in a coordinated way so as to sustain the bimodal changing wave pattern outlined above. This question is important (considering that the monsoon affects the lives of hundreds of millions of people), and is under further investigation.

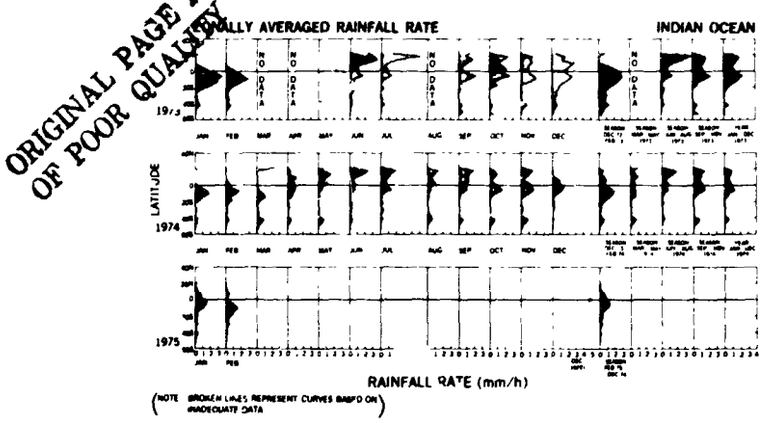

Fig. 2–ESMR-derived zonally averaged rain-rate versus latitude – Indian Ocean

(4) Interannual Variation

The extent of variation of rainfall over the oceans from year to year has been largely a matter of conjecture until the present time. The maps generated from ESMR data provide new insight into this problem. A typical example is the rainfall over the Pacific in the month of January of the years 1973 and 1974 (Fig. 3). In January 1973, intense rainfall occurred over a wide region all along the Equator (between 0° and 8°N) and also to the south of the Equator (between 170°E and 160°W). This was at the time of the El Niño phenomenon (warm ocean current attended with relaxation of upwelling along the coasts of Ecuador and Peru), with its disastrous effect on the plankton and fish in the waters of the Pacific off the west coast of South America. In the corresponding month of 1974 (non-El Niño year) we see that the region was relatively dry. The ratio of rainfall in the Equatorial Pacific in the period December '73–February '74, to the rainfall in the period December '72–February '73 is 1:6. Whether such variation is true for other El Niño and non-El Niño periods can be determined only after satellite rainfall data for many years are processed.

In any event, this is a distinctive example of rainfall anomaly. Investigations of similar anomalies and their correlations are very valuable in weather as well as in climatic studies.

(5) Low Southern Hemispheric Rain Intensity

Conventional meteorological observations over the Southern Hemisphere are sparse. Consequently, although meteorological phenomena occurring over that vast

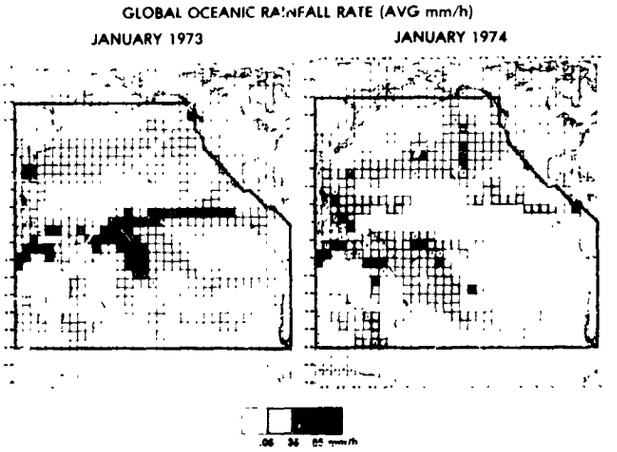

Fig. 3–ESMR-derived Pacific Ocean rainfall maps for January 1973 (El Niño year) and January 1974 (non-El Niño year)

region are of importance to the global general circulation, they are not well understood. ESMR data provides useful information in respect of precipitation in the Southern Hemisphere.

Figure 4 represents the zonal averages of rainfall over the Atlantic Ocean. From a scrutiny of this diagram the following feature is noticed. The polar front in the Southern Hemisphere (around 40°S) is much weaker than its Northern Hemisphere counterpart. The overall rain intensity in the entire Southern Hemisphere is only about 50% of that in the Northern Hemisphere.

The larger land masses in the Northern Hemisphere could certainly lead to higher precipitation, especially over coastal areas. However, the difference in rain rate revealed by ESMR is much too large to be explained by this factor alone.

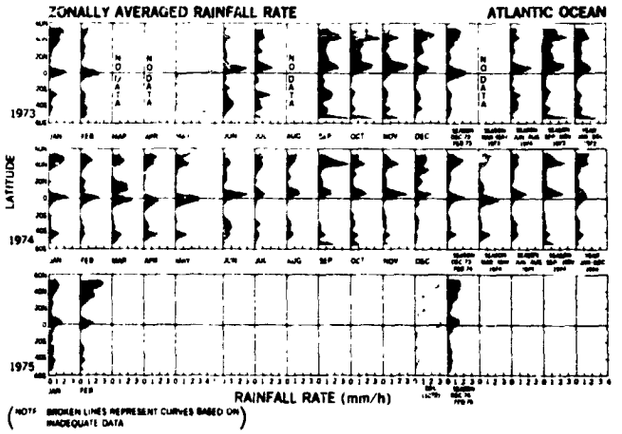

Fig. 4–ESMR-derived zonally averaged rain-rate versus latitude – Atlantic Ocean

REFERENCES

Haurwitz, B. and J. B. Austin, 1944: Climatology, N Y. & London, McGraw-Hill, New York, p. 410.

Rao, M. S V., W. V. Abbott and J S. Theon, 1976: "Satellite-Derived Global Oceanic Rainfall Atlas (1973-1974)," NASA Special Publication 410, Washington, D.C., p. 31.

Sadler, J.C., L. Oda and B. T. Kilonsky, 1976: Pacific Ocean Cloudiness from Satellite Observations, Department of Meteorology, University of Hawaii, Honolulu, p. 137.

Seelye, C. J., 1950: "Rainfall and Its Annual Variability Over the Central and Southwestern Pacific," New Zealand J. Sci. Tech., B 32, pp. 11-24.

U.S. Department of Commerce and USAF, 1971: Global Atlas of Relative Cloud Cover 1967-70, Washington, D.C., p. 231.

Paper No. 26

ON THE INTERANNUAL VARIABILITY OF THE OCEAN ATMOSPHERIC SYSTEM

E. R. Reiter, *Colorado State University, Fort Collins, Colorado*

ABSTRACT

Several feedback mechanisms between ocean and atmosphere are discussed, which seem to have a decisive influence on the interannual variability of the atmosphere and on climatic fluctuations of a time scale of 10 to 50 years. Satellite requirements to monitor these feedback processes are outlined briefly.

The North Pacific Cooling Trend

In a recent study (Reiter, 1977a) it was demonstrated that the North Pacific north of 40°N has been subject to a dramatic cooling trend within the past 15 years. This trend was accompanied by a tightening of the meridional sea surface temperature gradient in the region of the North Pacific Drift and of the Gulf Stream into well-defined oceanic frontal zones (Figs. 1 and 2). The subtropical Pacific has not changed its temperature discernabley during the same time period. The tightening of the meridional gradient of sea surface temperatures (SST) suggests that the Pacific anticyclonic gyre has increased its rotation velocity by a significant degree. From Figs. 1 and 2 it appears that a large amount of cold water appeared south of the Aleutian Islands during recent years. The origin and life history of these water masses is yet unknown. We suspect, however, that they are produced by upwelling.

Using SST records from the North Pacific which go back to 1900, one can identify several periods during which the SST's have undergone significant warming and cooling trends. Comparing these trends to atmospheric temperature trends of the northern hemisphere one finds a remarkable agreement. In Fig. 3 we have outlined schematically possible positive and negative feedback mechanisms that might govern these oceanic and atmosphere temperature trends of severe tens of years of duration. In agreement with these hypothesized feedbacks we have identified a secular increase of the wind stress in the trade-wind region during the last 15 years. At the same time, the curl of the wind stress, which affects the mass transport in the North Equatorial Current, also has increased (Reiter, 1977b).

In order to keep a close watch on the climatic trends which seem to be governed by North Pacific SST trends, satellite surveillance of SST will be essential for many years to come. The accuracy requirements will have to be 0.5°C or better, with

adequate ground-truth calibration against available ship data to safeguard against sensor deterioration. Area resolution at the ocean surface can be of the order of 50 x 50 km for climatic monitoring. Higher resolution would be welcome for studies in "synoptic oceanography" and energy transfer calculations between ocean and atmosphere. One should set a ten-year lifespan for such a monitoring program as a target.

Anticipated economic returns of such an SST monitoring program are manifold. We already know that North Pacific (and also North Atlantic) cooling trends are reflected in the northern hemisphere climate. We suspect that SST trends in the Indian Ocean might affect monsoon precipitation yields over India. Several studies have indicated that hurricane frequencies are tied to low latitude Atlantic SST trends. Monitoring of these SST's therefore, should be considered a priority task. The behavior or trends of southern hemisphere SST's is virtually unknown.

Fisheries around the world most likely would be an appreciative user of such data on a real-time basis.

Feedbacks with Tropical Precipitation

On a shorter time scale (approximately 1 to 4 years in duration) we have demonstrated the existence of surges in the trade-wind systems of both hemispheres, especially of their v-components. Whenever there are anomalously strong winds blowing towards the equator, the intertropical convergence zone (ITCZ) intensifies over the equatorial Pacific, yielding above-normal rainfalls (Fig. 4). Each peak in these equatorward v-component surges is followed by an El Niño episode along the Peruvian coast (Reiter, 1977c). These surges are cut off by upwelling of cool water in the equatorial Pacific, forced by peaks in the curl of the wind stress and resulting "Ekman pumping" (Reiter, 1977b). Fig. 5 sketches possible feedback mechanisms responsible for such surges in the trade-wind v-component. The release of latent heat, which is abnormally high during such surges, appears to be reflected in northern-hemisphere mean temperature fluctuations, as well as in fluctuations of the zonal available potential energy of the atmosphere. The latter parameter constitutes the main energy reservoir on which the general circulation of the atmosphere depends.

We suspect that the correlation between trade-wind behavior and ITCZ intensity extends over larger areas than just the central Pacific. A close monitoring of precipitation amounts in the ITCZ (within 10% accuracy), SST temperatures in the tropical oceans (0.2°C accuracy), low-troposheric winds in the tropics and subtropics (0.5 m/sec speed, 5 degrees direction accuracy) and low-troposhperic moisture content (20% accuracy) become essential requirements. Again, a commitment for several years of such a monitoring program should be asked for. With a better quantitative understanding of the feedback mechanisms shown in Fig. 5 there is the possibility of improved seasonal trend forecasting in the northern hemisphere, perhaps by as much as a year ahead of

time. A more accurate prediction of El Niño episodes might also be expected, with the attendant economic benefits.

Short-Term Feedbacks

McGuirk and Reiter (1976) have discussed a 22- to 26-day vacillation in the atmospheric energy parameters. Seigel (1977) discovered a similar vacillation in the transfer of latent and sensible heat from the oceans to the atmosphere. These transfer vacillations appear to be strongest in regions of strong oceanic frontal zones, as for instance shown in Fig. 2. A significant ocean-atmosphere coupling and feedback has to be suspected, therefore, on a time scale of approximately 3 weeks. Since the atmospheric vacillation discussed by McGuirk and Reiter is mainly evident in the behavior of the amplitudes and phases of planetary long waves, we have hope that a better understanding of sea-air interaction on this time scale might provide us with a tool of extended-range forecasting in the temperate latitudes of the northern hemisphere.

Data requirements in this field of investigation would be SST's in middle latitudes to better than 0.5°C accuracy, measured at least twice a week at any given location, low tropospheric layer-averaged temperatures, measured at least once a day to 0.5°C accuracy, and low tropospheric moisture content. Fall, winter and spring are deemed to be the most interesting seasons for such investigations. A measurement program should cover at least 2 to 3 years of data, with heavy emphasis on several key peri during each year, in which major changes in the energy flux patterns from ocean to atmosphere occur or are anticipated.

REFERENCES

McGuirk, J.P. and E.R. Reiter, 1976: A vacillation in atmospheric energy parameters. J. Atmos. Sci., 33(11), 2079-2093

Reiter, E.R., 1977a: On the recent cooling trend in the North Pacific. (Submitted to Journal of Geophysical Research.)

_____, 1977b: The interannual variability of the ocean - atmosphere system. (Submitted to Journal of the Atmospheric Sciences.)

_____, 1977c: Long-term wind variability in the tropical Pacific, its possible causes and effects. (Submitted to Monthly Weather Review.)

Seigel, A.D., 1977: Oceanic latent and sensible heat flux variability and air-interaction. Environmental Research Papers No. 7, 31 pp., Atmos. Sci. Dept., Colo. State Univ., Ft. Collins, Co. 80523.

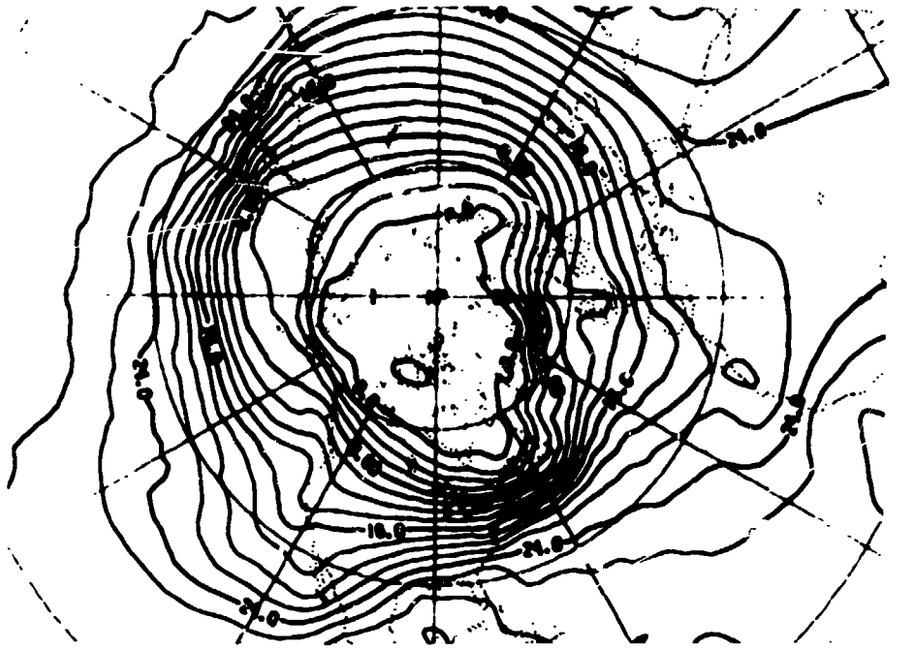

Figure 1. Mean monthly isotherms of surface temperatures, June 1963, analyzed in 2°C intervals.

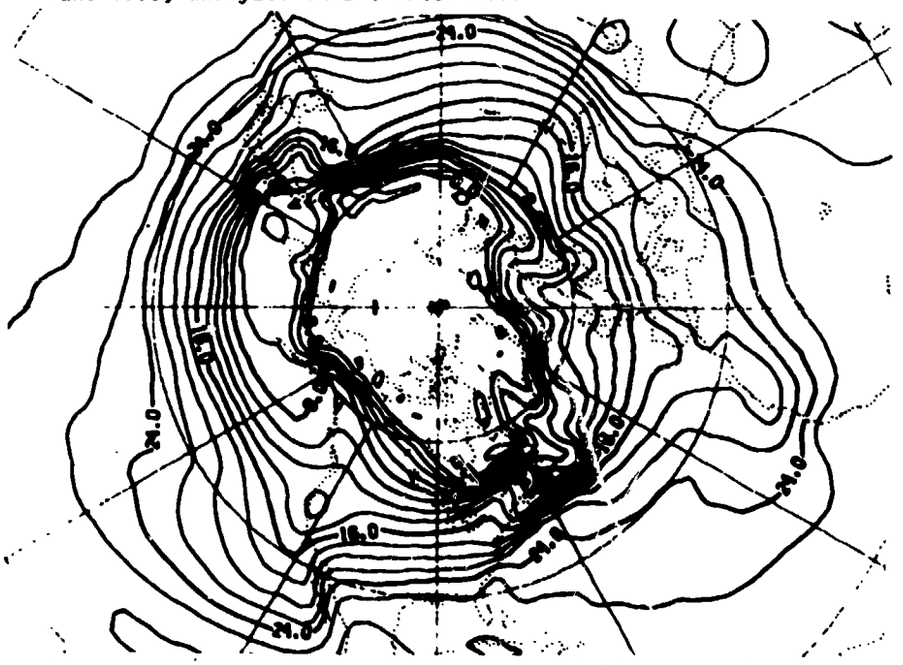

Figure 2. Same as Figure 1, except June 1976. Note the tightening of the meridional SST gradient in the region of the North Pacific Drift and the Gulf Stream between 1963 and 1976.

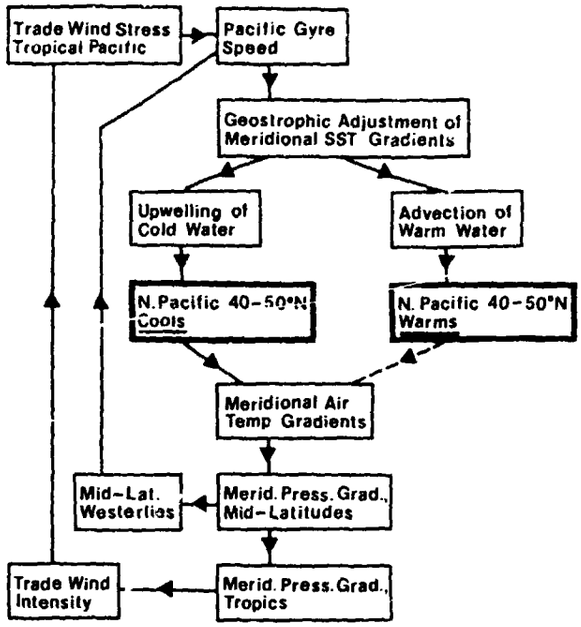

Figure 3. Schematic feedback system between atmospheric and oceanic large-scale circulation.

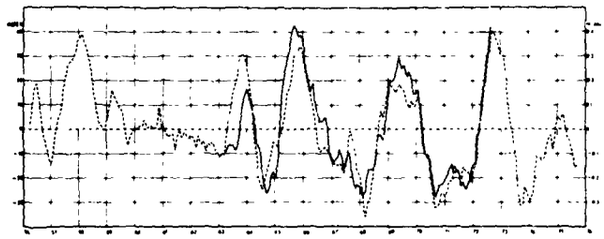

Figure 4. Anomalies from 20-year monthly mean rainfall index for the Line Islands (dashed line, scale on left side of diagram) and average v-component departure (positive) for winds blowing towards the equator) of the trade winds in the North and South Pacific, (solid line, scale in m/sec on right side of diagram). The vertical lines in the coordinate grid pertain to January of each year. Seven-month running averaging has been applied to the monthly departure values.

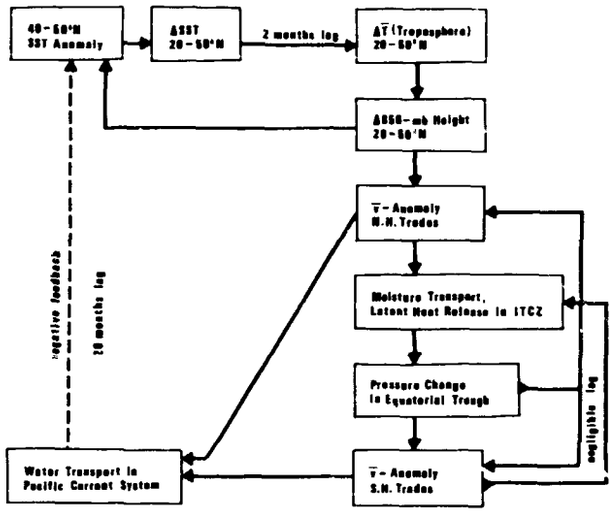

Figure 5. Schematic flow-diagram of feedback mechanisms between mid-latitude sea-surface temperature (SST) anomalies, atmospheric meridional temperature and height gradients, trade-wind circulation and large-scale water transport in the North Pacific. (Solid lines with arrows indicate amplifying [positive] feedback, dashed line symbolizes damping [negative] feedback.)

Paper No. 27

NIMBUS 6 ERB SCANNER STUDIES FOR DEVELOPMENT OF EARTH RADIATION BUDGET SATELLITE SYSTEM (ERBSS)

J. T. Suttles, *Langley Research Center, Hampton, Virginia*
L. M. Avis, *Langley Research Center, Hampton, Virginia*
P. G. Renfroe, *Vought Corporation, Hampton, Virginia*

ABSTRACT

Studies based upon the Nimbus 6 ERB scanner data have been conducted to support the development of the Earth Radiation Budget Satellite System project. The ERB data were processed in terms of Earth targets and angular bins and used to evaluate currently available directional radiation models for the longwave and shortwave spectral ranges. Results indicate that available longwave models are adequate for the most part while available shortwave models are inadequate. An effort has been initiated to develop improved shortwave models for various cloud conditions and various surface types for cloud free conditions.

INTRODUCTION

In order to convert satellite measurements of the Earth radiation budget into useful scientific information, it is necessary to determine the radiation heat flux densities at the top of the atmosphere (30 km) for spatial scales ranging from global to regional [Ref. 1]. Thus, data analysis techniques are required. To obtain the desired accuracies for radiation budget components it is necessary to have accurate directional radiation functions or models for use in the data analysis. In the work described in this paper, the very detailed satellite measurements of the Nimbus 6 Earth Radiation Budget (ERB) scanner instrument [Ref. 2] have been processed and used to evaluate available directional models for Earth emitted longwave radiation and for reflected shortwave radiation

ERB SCANNER DATA PROCESSING

Data from the ERB scanner on the Nimbus 6 spacecraft were processed for the month of August 1975 to determine the viewed point locations and the corresponding viewing zenith and azimuth angles and the solar zenith angle. The ERB scanner measures radiance from the Earth-atmosphere system in both the shortwave reflected (0.2-4.0μm) and longwave, emitted (4.0-50.0μm) spectral range with an effective nadir resolution of about 100 km. To evaluate the radiation characteristics of various surface and atmospheric features the Earth's surface was described by a grid of 2070 target areas, each equivalent to 4.5° × 4.5° at the Equator which corresponds approximately to equal area targets of 500 km by 500 km size. The targets were categorized from atlas

information in terms of various surface types: snow, ice, water, jungle, forest, and desert. The targets were described by the percentage contribution of each of the surface types to the overall target characteristics. In each of these target areas, the ERB scanner data for August 1975 were accumulated and averaged in angular bins. The angular bins were defined by equal increments of the cosine of the zenith angle, for both viewing zenith and solar zenith, and by 45° increments for the azimuth angle. The azimuth angle was defined relative to the Sun-target plane and symmetry about this plane was assumed. This scheme was used for the shortwave analysis but the longwave data were assumed to be independent of the Sun angles and the viewing azimuth so that only viewing zenith bins were considered.

RESULTS

Longwave

Longwave data were processed for all target areas over the globe and results were used to determine target radiance distributions and heat flux densities. To evaluate radiance distribution models, data were used only for targets which consisted of a single surface type. As an example, longwave results for several areas identified as forest regions and normalized by the nadir (zenith = 0°) value are shown in Figure 1. These data along with similarly processed results for the other surface categories were used to generate the results shown in Figure 2. Here data representing the mean limb darkening curves resulting from the ERB data are compared to limb darkening curves derived from analysis of Nimbus 2 data [Ref. 3]. The Nimbus 2 results are shown in the form of a nominal or average curve and upper and lower limit curves which describe variations over a variety of conditions. It is seen from the figure that the ERB derived results fall within the limits of the Nimbus 2 results, with one notable exception, and is in general agreement with those results. The exception is for snow targets in the south polar region where the well-known polar temperature inversion probably accounts for the limb brightening obtained for these cases. This effect will be the subject of continued study. However, it is concluded, in general, that currently available longwave models are adequate for data analysis purposes [Ref. 4] even when no effort is made to screen the data for cloud conditions.

Shortwave

The reflected, shortwave directional radiance distributions present a much more difficult problem since the data must be processed in terms of three angular variables: viewing zenith, viewing azimuth relative to the Sun's azimuth, and Sun zenith. It was necessary, therefore, to accumulate and average these data in bins of all three of these angles and as a result data for only selected, representative targets have been processed and analyzed. As an example, data from a particularly cloudy region

over South America have been plotted in Figure 3 for azimuths near the solar plane and a solar zenith angle near 40°. Here the Stratus and Stratocumulus models derived from airborne measurements [Ref. 5] are compared to the ERB scanner data. An albedo of 0.38 was selected for the models by matching the Stratocumulus model nadir value to the apparent data nadir value. This comparison is typical of the results obtained for a variety of comparisons, i.e., for some surface conditions and angular ranges the models are in good agreement with the ERB data but in other cases significant deviations are found. For example, these results show that the models correlate well with the data in the backscattering (BS) region but deviates at forward scattering (FS) zenith angles above 30°. In addition significant variances, about the mean values plotted, were noted and inspection of histograms revealed that this effect is apparently caused by varying cloud patterns. As a result, an effort was initiated to develop improved reflected shortwave bidirectional radiance models including separation of data into cloudy and clear conditions for various surface types.

Preliminary Improved Shortwave Models

Using water regions as a background surface, locations were identified where conditions were either totally clear or totally cloud covered during the times for which ERB data are available. This identification was made in a subjective process of visual review of the SMS photographic images for the local times of ERB coverage. The accumulation of these results over August 1975 are shown in Figure 4 for the solar plane and for solar zenith angles less than about 26° (i.e., cosine of zenith between 1.0 and 0.9). The Stratus cloud model [Ref. 5] for an albedo of 0.47 is compared with the ERB cloudy scene data. The ERB clear water scene data are shown and compared with a Lambertian model with an albedo of 0.13. It is apparent that improvements in the present models are necessary and that several models will be required to satisfactorily fit the directional radiance characteristics of the various surface and atmospheric features present on Earth.

Initial efforts have been made to develop the required improved shortwave directional models. The cloudy and clear ERB data sets, partially shown in Figure 4, were fit to a spherical harmonic expansion over the zenith-azimuth angular space for the upward facing hemisphere of a target point. A portion of these results for the cloudy data and for solar zenith angles less than 26° in the solar plane are shown in Figure 5. The spherical harmonics fit is shown as the solid line and it is pointed out that this fit is based on a minimization of the difference between the spherical harmonic functions (twelve term expansion) and the data over the entire hemispherical space.

The albedo computed from spherical harmonic fits for various solar angles are plotted in Figure 6 along with calculations of Hunt [Ref. 5]. Hunt's calculations are shown for

moderately thick clouds (optical thickness of 20). The ERB cloudy data are in excellent agreement with Hunt's results. The high data point obtained for the largest solar zenith angle for which results were available resulted from a relatively small number of measurements. As a result the formal standard error, shown by the bar on the figure, is quite high. Error bars for the other points are within the size of the plotting symbols and therefore have not been shown.

CONCLUSIONS

Both longwave and shortwave ERB data have been analyzed. The validity of the Nimbus 2-based limb darkening curves have generally been verified for the longwave data with the exception of the Antarctic snow fields where limb brightening was found in the ERB data. Correlation of the shortwave data with cloud models derived from airborne measurements showed promise yet illustrated the need for improvement. The spherical harmonics technique appears to be a useful method of fitting the ERB data to generate improved models. Further application of the spherical harmonics approach along with development of a cloud screening algorithm are being pursued in continuing studies with the ERB data set.

REFERENCES

1. Woerner, C. V.; and Cooper, J. E.: Earth Radiation Budget Satellite System Studies. NASA TM X-72776, May 1977.

2. Smith, W. L.; Hickey, J.; Howell, H. B., Jacobowitz, H.; Hilleary, D. T.; and Drummond, A. J.: Nimbus 6 Earth Radiation Budget Experiment, Appl. Opt. 16: 306-318, 1977.

3. Raschke, E.; Vonder Haar, T. H.; Pasternak, M.; and Bandeen, W. R.: The Radiation Balance of the Earth-Atmosphere System from Nimbus 3 Radiation Measurements, NASA TN D-7249, 1973.

4. Green, R. N.: Simulation Studies of Wide Field of View Earth Radiation Data Analysis. Proposed NASA TP, November 1977.

5. Avis, L. M.; and Renfroe, P. G.: ERBSS Scanner Performance in the Presence of Radiation Directional Model Errors. NASA Weather and Climate Science Review, November 29-30, 1977.

6. Hunt, G. E.: The Effect of Coarse Angular Discretization on Calculations of the Radiation Emerging From a Model Cloudy Atmosphere, J.Q.S.R.T., 11:309-321, 1971.

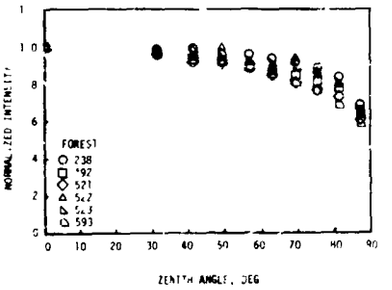

FIGURE 1 Longwave limb darkening for selected forest targets

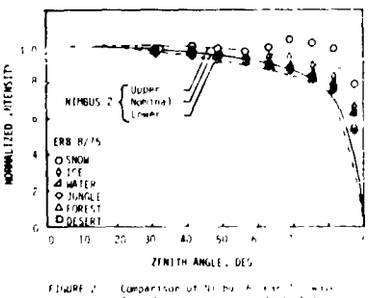

FIGURE 2 Comparison of [illegible] limb darkening [illegible] derived [illegible]

ORIGINAL PAGE IS
OF POOR QUALITY

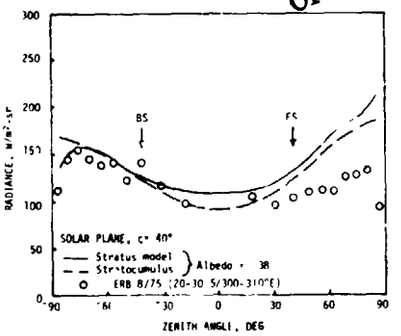

FIGURE 3 Shortwave radiance variation in the solar plane for a target over South America

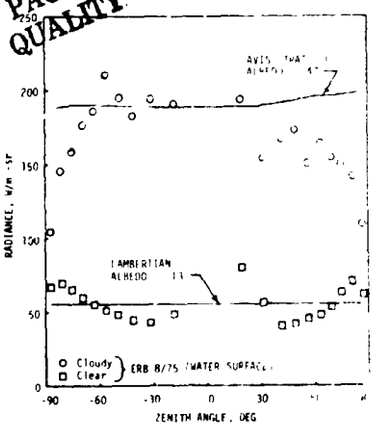

FIGURE 4 Shortwave radiance [illegible] the solar plane for cloudy and [illegible]

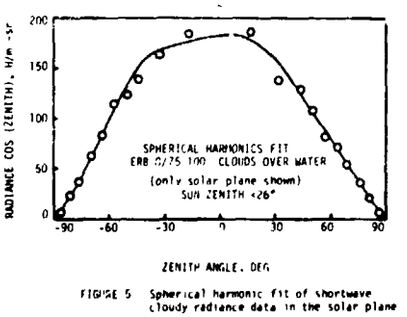

FIGURE 5 Spherical harmonic fit of shortwave cloudy radiance data in the solar plane

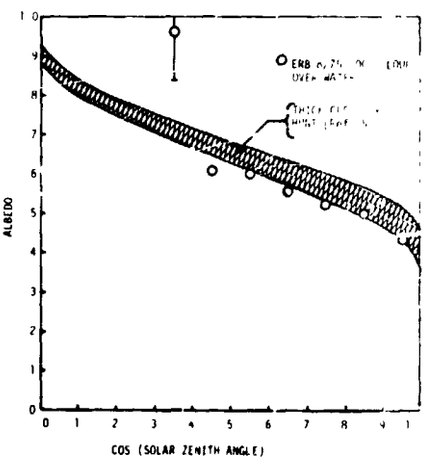

FIGURE 6. Cloud albedos computed from a spherical harmonic fit to Nimbus-6 ERB scanner data

Paper No. 28

SAMPLING ANALYSIS FOR THE EARTH RADIATION BUDGET SATELLITE SYSTEM MISSION

E. F. Harrison, *Langley Research Center, Hampton, Virginia*
G. G. Gibson, *Vought Corporation, Hampton, Virginia*

ABSTRACT

A study has been conducted to identify problems related to sampling the Earth's radiant energy budget and to define a satellite system with sufficient sampling to satisfy science requirements on global, zonal, and regional scales.

INTRODUCTION

Values of Earth albedo and longwave emitted radiation vary significantly with local time, geographical location, and season. Over the globe, albedo changes as much as 300 percent and longwave radiation varies as much as 100 percent (Vonder Haar, 1968). The season of the year also has an important effect on the radiation at a particular latitude. All of these variations demonstrate the importance of making radiation measurements at all latitudes and times of the year. Furthermore, the diurnal variation of radiation is relatively unknown.

ANALYSIS AND DISCUSSION

Various numbers of satellites and orbit inclinations have been analyzed to define the satellite combination that provides sufficient coverage of the Earth for spatial and temporal radiation sampling. Illustrations of latitude coverage or sampling as a function of local time are presented in figures 1 and 2. These results are for a typical 30-day period, which is consistent with the science requirements.

A nominal altitude of 600 km was selected for the 50° inclination orbit because it provides a 2- to 3-year lifetime and a revisit cycle over Earth of 3 days so as to observe each area from several angles. Sampling coverage for the 98.7° inclination orbits was based on the nominal TIROS-N orbit of 833 km altitude. The satellite sensor complement includes a scanner, a medium and a wide field of view radiometer. Although the wide field of view sensor covers from horizon to horizon, only a 10° great circle of arc on Earth (e.g., 10° latitude and 10° longitude at the equator) was used in defining its coverage and sampling capability. The reason for using the 10° angle is twofold: (1) It is commonly employed to provide reasonable approximation for

deconvolution of radiation data from satellite altitudes to the top of the atmosphere (about 30 km); (2) It is approximately the size of the geographical grid proposed for the resolution of the radiation data on a regional scale using the medium field of view sensors.

Figure 1 shows hourly latitude coverage provided by two Sun-synchronous ($i = 98.7^{o}$) orbits with equatorial crossings at 0800 and 1500 hours. The variation in density on this figure indicates the number of times a particular latitude band is covered at a given local time (the greater the density, the more times of coverage). Near-polar latitudes are covered during nearly all times of day. However, low and middle latitudes are only covered during the equatorial crossing hours. Thus, there are large gaps in hourly latitude coverage for Sun-synchronous orbits. More complete coverage can be achieved by covering nearly all the low and middle latitudes at each local hour by adding a single satellite at mid-inclined orbit of about 50° with a faster orbital precessing rate (see figure 2). Thus, an optimum satellite mix for sampling is a combination of high and middle inclinations.

To evaluate this thesis, a figure-of-merit parameter which is based on a product of geographical area (not just latitude) and local time coverage was used to compare the various satellite orbit capabilities. Included in this comparison was the effect on coverage of natural orbit variations. The results are shown in figure 3. As can be seen, two Sun-synchronous satellites together provide an area-local time coverage of less than 30 percent. By combining them with one 80° inclined orbit, the area local time coverage would be increased to only 60-68 percent. Unfortunately, 3 months are required for the 80° inclined orbit to precess through all local times. Meanwhile the Sun's declination will have changed appreciably thus making separation of diurnal effects from seasonal effects difficult, and will also result in biases in the monthly averages. Two Sun-synchronous satellites and a 30° inclined orbit have an area-local time coverage of 71-73 percent; however, the midlatitude coverage is poor. The most effective coverage can be obtained by combining the two Sun-synchronous satellites with one 50° inclined satellite. The area-local time coverage for this combination is 85-87 percent and the low and mid-latitudes are well covered.

An evaluation of scanner coverage was also conducted. Off-track scan modes provide better space-time coverage than the along track scan. Figure 4 compares cross track scanner coverage for several satellite combinations in terms of the capability of covering viewing zenith, θ, viewing azimuth, ψ, and solar zenith, ζ, angles. Again, the two Sun-synchronous satellites with one 50° inclined satellite orbit provide good overall coverage.

In order to further evaluate the capability of the recommended satellite combination ($i = 98^{o}, 98^{o}, 50^{o}$), a simulation model of the Earth's radiation field developed by Campbell and Vonder Haar (1973), was used to calculate the satellite radiation results shown in figures 5 and 6. Monthly average

zonal emitted energy (figure 5) and reflected energy (figure 6) as a function of latitude for the three-satellite, medium field of view system are shown to compare well with the reference values, which were established by assuming essentially unlimited (i.e., 21) satellites.

The model radiation field was further used to calculate the accuracy of results on a regional scale. Figure 7 presents the results of these analyses for regions at the equator for 1 month (May). Accuracies in reflected energy values from 6 to 20 percent and emitted energy accuracies of about 3 percent were estimated for the 50° inclined orbit satellite. Only a slight improvement is achieved with the addition of the two Sun-synchronous satellites. Of course, these two satellites do provide the only coverage of the higher latitudes. Correlations of the radiation field between adjacent regions or with time have not yet been considered.

Recent sampling studies are refining the expected accuracy of the three satellite system for regional resolution by studying the variability of the scene using cloud-cover statistics. The magnitude of measurements of reflected solar radiation exiting the Earth-atmosphere system is strongly dependent on the amount of cloud cover in the radiometer field of view. Reflected shortwave radiation is directly related to cloud cover since the albedo and angular reflectance characteristics of clouds are usually quite different from that of the underlying surface. Figure 8 presents a summary of the results showing the minimum and maximum accuracy limits (standard deviation of the mean) in equatorial regions for each month. It is apparent from the figure that the regional radiation budget measurements at low latitudes is being performed almost solely by the 50° inclined satellite; however, the two Sun-synchronous satellites complement the system by providing the measurements at mid and high latitudes. The results of figure 8 are worse-case analyses assuming no priori knowledge. Persistence of cloud cover, correlation between regions, and refined knowledge of the diurnal cycle which will be established by this mission should allow a determination of regional radiation budget of better than 5 percent, or a reduction of the maximum errors shown in figure 8 by a large factor.

CONCLUSIONS

Based on the results of the sampling studies, two 98° inclined orbits coupled with the 50° inclination orbit appear to satisfy the science requirements for regional resolutions, zonal resolutions, equator-to-pole gradient, and global resolutions. The NOAA Sun-synchronous satellites in the TIROS-N series could adequately cover the high latitudes and an ERBS/AEM satellite having an inclination of 50° could provide sampling in the mid and low latitude areas where variations in radiation energetics are most dynamic.

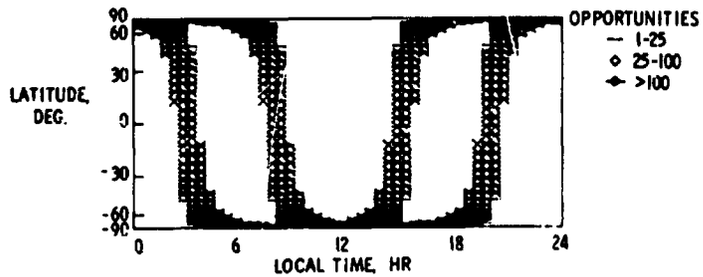

Fig. 1 - Temporal-latitude zonal coverage for two satellites. TIROS (0800) and TIROS (1500), t = 30 days, ECA = 10°.

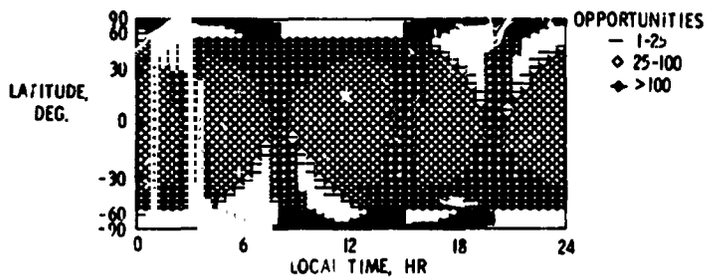

Fig. 2 - Temporal-latitude zonal coverage for three satellites. TIROS (0800), TIROS (1500) and AEM (i = 50°); t = 30 days; ECA = 10°.

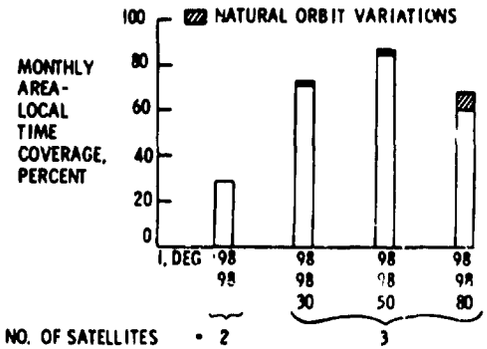

Fig. 3 - Comparison of sampling capability of various satellite combinations.

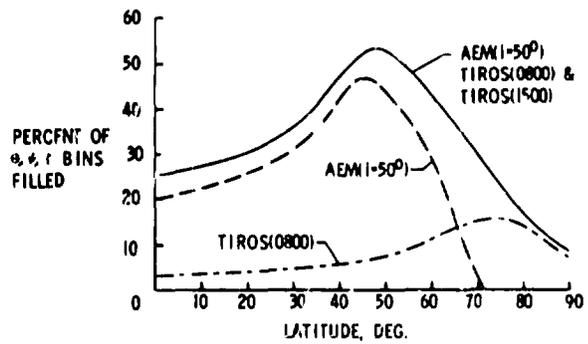

Fig. 4 - Cross-track scanner regional coverage capability. 250 x 250 km regions.

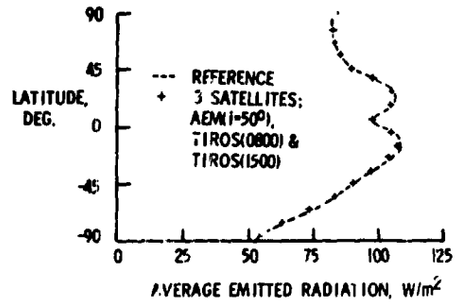

Fig. 5 - Simulated emitted monthly zonal radiation measurements.

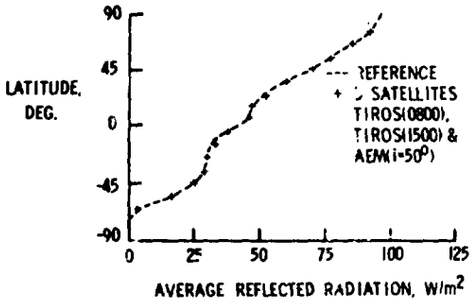

Fig. 6 - Simulated reflected monthly zonal radiation measurements.

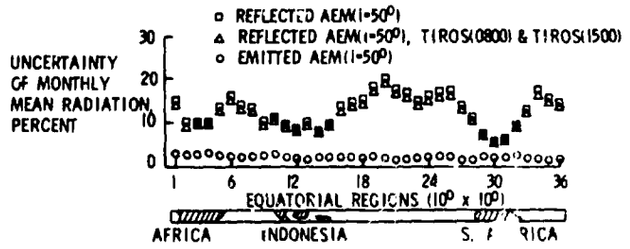

Fig. 7 - Regional radiation accuracy based on sampling of modified Nimbus-3 data. t = 30 days, May.

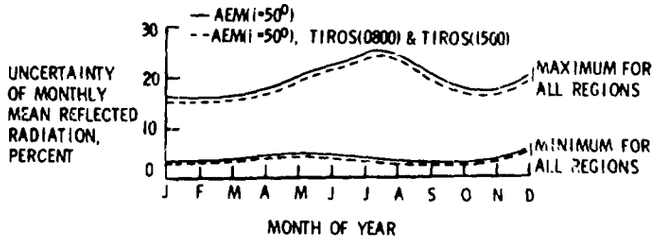

Fig. 8 - Reflected equatorial regional radiation accuracy based on sampling of cloud statistics. t = 30 days.

Paper No. 29

STRATOSPHERIC AEROSOLS AND CLIMATIC CHANGE

James B. Pollack and Owen B. Toon, *Mail Stop 245-3, NASA-Ames Research Center, Moffett Field, CA 94035*

ABSTRACT

The effect of stratospheric aerosols on climate is considered using an aerosol model and a radiative convective 1-D climate model.

Stratospheric sulfuric acid aerosols form a 20 km thick layer centered near 20 km altitude composed of particles about 0.1 μm in radius. The layer has an unperturbed optical depth at 0.55 μm of about 5×10^{-3} (1). Due to the small optical depth, the ambient aerosols are not a significant component of the Earth's climate system. However, large volcanic explosions increase the number and size of the stratospheric particles so that their optical depth becomes large enough to create both obvious optical effects such as brilliant sunsets and diffraction coronas and significant changes in weather and climate. Volcanoes may have been responsible for severe weather during a number of individual years (i.e. 1816) as well as for long periods of cooler weather (i.e. the little ice age 1500--1900) (2,3,4). Volcanoes represent the only known natural particle production source to the layer. However, human activities also might alter the layer. Since the ambient layer is believed to be created from SO_2, OCS, and small nuclei, which the sulfuric acid particles require for their initial formation, any source of these materials must be evaluated for its impact on the aerosol layer. High flying aircraft supply both SO_2 and soot particles, while space shuttle engines supply Al_2O_3 particles directly to the stratosphere. There are also tropospheric sources of OCS and SO_2, although the strength of these sources is poorly known.

Our initial work (2,3,4) showed that direct volcanic injection of particles and SO_2 was undoubtedly of climatic significance. Figure 1 shows calculations of the change in surface temperature for H_2SO_4

particles of a single size, typical of unperturbed conditions, but variable optical depth, and for basaltic glass particles of a constant optical depth, but variable size. The calculations were performed by first calculating the solar energy deposited in the Earth's unperturbed atmosphere using a doubling routine including both aerosol and gaseous absorption and scattering (2.3,4). Then an elaborate infrared routine including aerosol and gaseous absorption and emission was used to find the infrared energy emitted to space for various temperature profiles of fixed shape but variable surface temperature. By equating the total solar energy absorbed to the infrared energy radiated to space, a surface temperature was fixed. The calculations were then repeated under perturbed conditions. The difference between perturbed and unperturbed surface temperatures is an indication of the temperature change that might actually occur after an eruption. Of course, the climate system is too complex for a 1-D model, neglecting feedbacks and time constants, to accurately predict the real temperature changes. However, we did find that, with a crude consideration of relaxation times, our calculations were in good agreement with observations after single eruptions (2). In comparing our calculations to observations we assumed that the H_2SO_4 curve of Figure 1 was relevant. Observations suggest that large ash particles are only important during the first few months after an eruption. Figure 2 shows that, with these assumptions and using observed volcanic activity, volcanic particles have been the dominant factor controlling hemispheric mean temperature during the last century. Prior to 1915 a large number of eruptions occurred and depressed the temperatures. After 1915 eruptions ceased and the Earth warmed up. The CO_2 greenhouse effect was less important than volcanic dust during this period.

Due to the considerable importance of these findings we have tried to improve the weak points of our earlier work. First our early work assumed a fixed temperature profile. We now use a full radiative-convective calculation of the temperature profile. Second, we had assumed that the size of the acid aerosol was fixed, but now we use an aerosol model to predict the acid particle size. There are no observations of acid aerosol size distributions after a large eruption, but, as shown in Figure 1, the sign of the temperature change can depend upon the particle size. Hence calculating the size distribution is an important improvement. Finally, we had not been able to consider the interaction of acid and non-acid

particles, but now we can use the aerosol model to include both particles. For many problems (e.g. space shuttle exhaust, ref. 4), the direct injection of non-acid particles, assumed not to interact with the stratospheric aerosol particles, is not significant because of the small optical depth of the injected particles. However, if large numbers of small particles are injected, sulfuric acid can be nucleated by the small particles and grow to create numerous large particles which can have large optical depth.

There are several techniques for performing radiative convective calculations. Most of these use a time marching calculation which requires hundreds of iterations to converge. Such techniques are very costly so we have devised a matrix inversion technique that converges in only 3-4 iterations. The other major advance in our work is the aerosol model (5,6). This model is a coupled 1-D chemistry-aerosol physics model extending from the ground to 60 km. In the model SO_2 and OCS diffuse upwards from the troposphere as do small particles. The sulfur bearing gases undergo photochemical reactions leading to H_2SO_4 which nucleates the small particles. The particles then grow by adding H_2SO_4 and H_2O, coagulate, sediment, diffuse and, at high altitudes, evaporate. Using observed SO_2, OCS, and tropospheric particle concentrations as boundary conditions the model produces results that are in excellent quantitative agreement with measured size distributions and concentrations in the stratosphere. We are now using the model to investigate various perturbed conditions. Fig. 3 presents size distributions calculated after a simulated eruption whose magnitude was comparable to that of Agung in 1963. We assumed the volcano injected SO_2 but no ash particles. In Fig. 4 we present the large particle mixing ratio for a calculation in which we simulated 50 and 500 space shuttle flights per year. The space shuttle calculation involved the addition of many small non-acid particles to the stratosphere.

Figure 5 shows the calculated temperature changes following the volcanic eruption using the size distributions and number densities calculated in Fig. 3. The magnitude of the calculated temperature decrease at the ground is in good agreement with our earlier studies in which we fixed the temperature profile and assumed a small particle size. In addition, the new calculations show that the stratosphere warms after the eruption as predicted earlier and as observed (3). Also shown in Figure 5 is a calculated temperature change in which the aerosols are omitted in the

infrared calculation. The results show that the stratosphere is warmed by aerosol absorption of upwelling infrared energy, not by absorption of solar energy; and, that the infrared effect is to warm the ground and must be included to obtain a good estimate of the net surface temperature change.

The space shuttle calculations of Figure 4 show only a slight modification of the layer. The change is due to the addition of Al_2O_3 particles which serve as nuclei for H_2SO_4 particles. The H_2SO_4 particle size distribution changes very little due to the added particles so Figure 1 may be used to estimate the temperature change. The nominal 50 shuttle flights per year increase the number of large particles in the stratosphere by about 10% so the perturbation optical depth is about 5×10^{-4} which produces a temperature change of less than $0.01^{\circ}C$. Even if 500 shuttles per year are flown the $\Delta\tau$ will only be about 5×10^{-3} yielding a ΔT of about $0.04^{\circ}C$. More sophisticated calculations of the climatic effect of space shuttles as well as SST's using our new radiative transfer scheme and the aerosol model results are in progress.

References

1. O.B. Toon and J.B. Pollack, "A Global Average Model of Atmospheric Aerosols for Radiative Transfer Calculations," J. Appl. Meteor., 15, 225 (1976).
2. J.B. Pollack, O.B. Toon, A. Summers, B. Baldwin, C. Sagan, and W. Van Camp, "Stratospheric Aerosols and Climatic Change," Nature, 263, 551 (1976).
3. J.B. Pollack, O.B. Toon, C. Sagan, A Summers, B. Baldwin, and W. Van Camp, "Volcanic Explosions and Climatic Change: A Theoretical Assessment," J. Geophys. Res., 81, 1071 (1976).
4. J.B. Pollack, O.B. Toon, A. Summers, W. Van Camp, and B. Baldwin, "Estimates of the Climatic Impact of Aerosols Produced by Space Shuttle, SST's, and Other High Flying Aircraft," J. Appl. Meteor., 15, 247, (1976).
5. R.P. Turco, P. Hamill, O.B. Toon, R.C. Whitten, C.S. Kiang, "A One-Dimensional Model Describing Aerosol Formation and Evolution in the Stratosphere I. Physical Processes and Numerical Analogs, to be submitted to J. Atmos. Sci..
6. O.B. Toon, R.P. Turco, P. Hamill, C.S. Kiang, R.C. Whitten, "A One-Dimensional Model Describing Aerosol Formation and Evolution in the Stratosphere II Sensitivity Studies and Comparison with

Observations," to be submitted to J. Atmos. Sci..

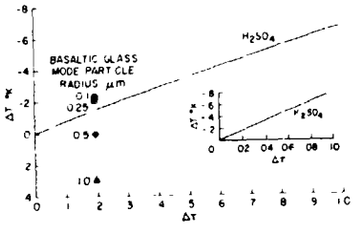

Fig. 1-Surface temperature change for given optical depth perturbations.

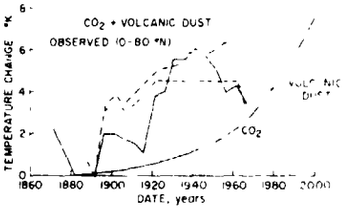

Fig. 2-Calculated and observed temperature changes since 1880.

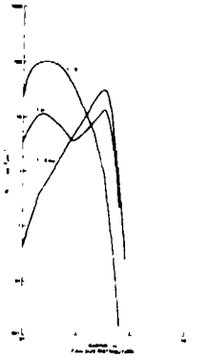

Fig. 3-Calculated size distributions before and after a volcanic eruption.

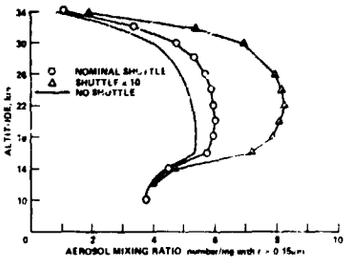

Fig. 4-Large particle mixing ratio for 0, 50 and 500 shuttle flights per year.

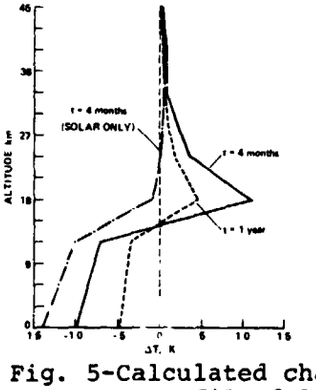

Fig. 5-Calculated changes in temperature profile following a volcanic eruption.

Paper No. 30

N79-20604

MT. AGUNG ERUPTION PROVIDES TEST OF A GLOBAL CLIMATE PERTURBATION

J. E. Hansen, W. C. Wang and A. A. Lacis

ABSTRACT

The Mt. Agung volcanic eruption in 1963 is used as a test case to examine the climatic response to a global-scale radiative perturbation of the earth's atmosphere.

INTRODUCTION

Radiative perturbations of global climate represent a very broad class of mechanisms for natural and man-made climate change. Examples are changes in atmospheric gaseous composition, such as CO_2, water vapor, ozone, freons, and other trace constituents, changes in the atmospheric aerosol content, such as by volcanic emissions or man-made pollution, changes in the surface albedo of the earth and changes in the flux of incoming solar radiation.

A large volcanic eruption provides an excellent opportunity for a case study of the response of the climate system to a global radiative perturbation, including a chance to test our ability to model and understand the nature of the climatic response. Volcanic aerosols, spread globally by stratospheric winds, provide a perturbation for which the forcing function is reasonably well known and for which the climatic response should be rapid enough and strong enough to be measurable, at least in the cases of the largest eruptions.

AGUNG ERUPTION

The eruption of Mt. Agung on the island of Bali (8°S, 115°E) in 1963 was one of the most spectacular volcanic eruptions in recent history. The eruption column extended into the stratosphere, where it deposited aerosols and gases, including sulfur-bearing compounds. The latter are believed to lead to the formation of sulfate aerosols, a major component of the stratospheric aerosols, through gas-to-particle chemical reactions.

Although there have been larger volcanic eruptions than Agung during the last few centuries, for example, Tambora in 1815 and Krakatoa in 1883, Agung occurred at a time when tropospheric temperature measurements were obtained, accurate measurements of the aerosols optical depth were made at several observatories in both hemispheres, and there was direct sampling of the composition of the stratospheric aerosols.

The global spread of the aerosols due to Agung could be tracked by means of their optical effects. As a result of the prevailing stratospheric winds the aerosols girdled the globe east-west within a few weeks, and within several months they had spread to all latitudes. The most reliable estimate of the aerosol optical depth is provided by the increased extinction of starlight measured at astronomical observatories, which indicated that in subtropics and midlatitudes of the Southern Hemisphere the added aerosol optical thickness for wavelengths ~0.5 μm had a peak value of 0.2-0.3 from August to November 1963 and was still substantial (~0.1) by mid-1964.

CLIMATE MODEL

As a first approximation for the expected thermal response of the atmosphere to the increased aerosol amount, we have computed the vertical temperature profile with a one-dimensional radiative-convective model. The basis of the method is to compute the local radiative heating and cooling rates for solar and thermal radiation at each altitude to determine the changing temperature profile with a time marching procedure. At any altitude where the computed temperature lapse rate is steeper than a preassigned maximum value (-6.5°K per kilometer), it is assumed that convection occurs with a vertical energy flux just sufficient to yield that preassigned maximum lapse rate. The relative humidity is kept fixed. Averaging over clear and cloudy regions is performed at each time step before computing the energy balance; climatological percentages of high, medium and low clouds are employed, and it is assumed that the cloud-top altitude remains fixed. A thermal inertia appropriate for the upper ('mixed') layer of the ocean is included at the surface.

This 1-D model was used to compute the expected temperature effect at low latitudes, where the perturbed aerosol amount was the largest. The atmospheric temperature profile was computed for a 'control' case with the normal aerosol model proposed by Toon and Pollack (J. Appl. Meteorol. 15, 1976,) which has sea salt, soil

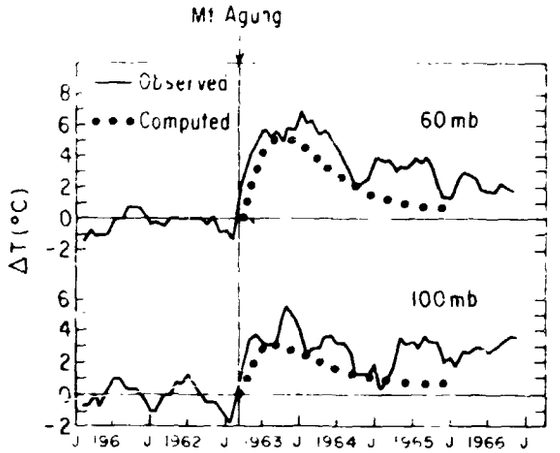

Fig. 1 Observed stratospheric temperatures over Australia, and computed temperatures after Mt. Agung eruption assuming added stratospheric aerosols to be sulfuric acid.

(basalt) and sulfate particles in the troposphere and sulfate (75% H_2SO_4, 25% H_2O in solution) in the stratosphere with the stratospheric aerosol optical depth 0.005. Stratospheric aerosols were then added to this background model, with the vertical distribution of the additional aerosols being 20% in the region from 22-26 km, 60% in 19-22 km, and 20% in 16-19 km, in order to approximate the distribution of the Agung aerosols. The composition of the added aerosols was assumed to be sulfuric acid, except as indicated below. The size distribution of the added aerosols was taken as the same as for the 'normal' stratospheric aerosols, with the effective radius of the distribution 0.2-0.3 μm; initially a substantial amount of larger sized 'dust' particles was present, but in the several weeks required to produce aerosols over a large fraction of the globe the mean size decreased to a few tenths of a micron.

RESULTS

Figure 1 shows the computed and observed temperatures in the stratosphere. The observations (R.E. Newell, J. Atmos. Sci, 27, 977, 1970) were made over Port Hedland, Australia, and are smoothed with a 3 month running mean; at altitudes near 20 km (pressures ~50 mb) the amplitude of the temperature increase was 4-8 degrees throughout the regions from 10°N to 30°S. Part of the observed temperature increase may be due to the quasi-biennial oscillation, but it seems clear that the aerosols did result in stratospheric warming of a few degrees with a time scale for the increase of the order of several weeks.

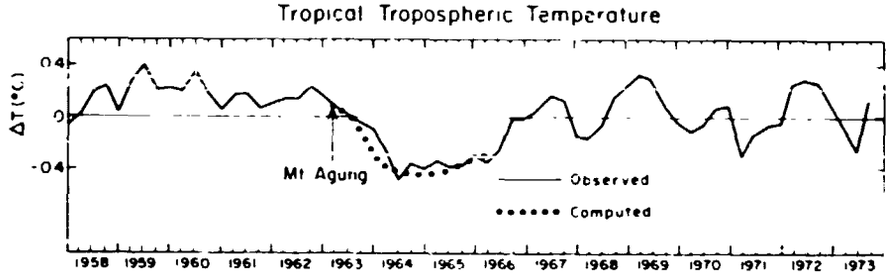

Fig. 2 Observed tropospheric temperatures between 30°N and 30 S, and computed temperatures after Mt. Agung eruption assuming added stratospheric aerosols to be sulfuric acid.

Figure 2 shows the computed and observed (R.E. Newell and B.C. Weare, Science 194, 1413, 1976) temperatures in the troposphere, for the latitude range 30°N - 30°S. More recent analyses of the observations are in substantial agreement with the illustrated observations. It appears that following the Agung eruption the average tropospheric temperatures did indeed decrease by a few tenths of a degree with a time scale of the order of one year, in agreement with the theoretical result.

The physical explanation for the computed effects is straightforward. The overall effect of the added aerosols on the bulk of the atmosphere and the surface is cooling, because sulfuric acid is highly reflective to solar radiation, thus tending to decrease the amount of solar radiation absorbed by the earth/atmosphere system. The aerosols also interact with the thermal radiation, and in fact warm the earth/atmosphere through a 'greenhouse' blocking of radiation from the surface and troposphere; however, aerosols of the assumed size have too small an optical thickness in the infrared for the greenhouse effect to exceed the albedo effect. The impact of the aerosols on the local (stratospheric) temperature is one of heating, because, (i) they absorb thermal radiation from the warmer atmosphere and surface below more effectively than they cool to space, and (ii) they absorb a small amount of solar radiation due to broad absorption bands in the near-infrared.

DISCUSSION

The magnitude, sign, and time delay of the temperature changes computed with a simple 1-D climate model for both the stratosphere and troposphere are in excellent agreement with the observed temperature changes follow-

ing the injection of stratospheric aerosols by Mt. Agung. Despite the simplicity of the model, uncertainties about the input data, and severe limitations in the observational samplings, the results are encouraging with regard to the question of whether global-scale climate perturbations can be reliably modeled and thus predicted.

Of course it is important to be cautious against overinterpretation of either the observations or model results. The observations of aerosol properties and atmospheric temperatures are not nearly as detailed and accurate as desired, and we can not be absolutely certain that the observed temperature variations are not in large part due to other mechanisms or simply to climatic 'noise'. The model for the climate system is grossly oversimplified and particularly fails to properly account for three-dimensional transports. Nevertheless, we believe that the several aspects involved in the agreement of observations and theory are too extensive to be coincidental, and that they provide strong evidence that radiative perturbations of the magnitude of such volcanic emissions do noticeably impact the climate, contrary to some recent opinions (B.J. Mason, Nature 264, 608, 1976). Since potential man-made radiative perturbations are of a similar magnitude, the results also provide evidence that we should indeed be concerned about possible inadvertent modifications of global climate by man.

Finally, we would like to point out that one very useful strategy for investigation of the global climatic system would be detailed observation and analysis of the the next large volcanic explosion. The observations should include global monitoring of the spread, growth and decay of the aerosols, in situ sampling of the aerosol properties, and accurate global monitoring of the climatic response. These data would permit testing of global climate models and aid in-depth analyses of radiative, chemical and dynamical processes, as is essential for obtaining an improved understanding of the physical mechanisms and interactions involved.

Acknowledgements. This work was performed in FY77 and was supported entirely by NASA. Salary support for the authors was provided by the Office of Space Science. Computer costs and associated institutional expenses were provided by the Office of Applications.

Paper No. 31

N79-20605

AN INVESTIGATION OF SURFACE ALBEDO VARIATIONS DURING THE RECENT SAHEL DROUGHT

F. R. Mosher and C. C. Norton, *SSEC, Univ. of Wisconsin*

ABSTRACT

Applications Technology Satellite III data are used to measure surface albedoes in the African Sahel during the 1967 to 1974 drought.

INTRODUCTION

The expansion of the Sahara southward has been discussed for at least a half century but only recently have investigators attempted to explain the mechanism of desertification. The process has generally been attributed to two causative elements; climate and man. All of the earliest and some of the more recent investigations of desertification pointed to non-meteorological causes. Lowdermilk (1935) and Stebbing (1935) proposed that the southward expansion of the Sahara was due, at least in part, to the practice of shifting agriculture and overgrazing. Bernus (1972) studied population movements in the Sahel and found that from 1940 to 1970 the northern limit of the wanderings of nomadic Peuls drifted from 15°N to 18°N. The agriculturists who followed the migration further increased the grazing pressure by reducing the available rangeland.

The meteorological desertification mechanisms proposed thus far have generally been investigated by empirical techniques. Lamb (1973) observed the equatorward shift of the subtropical high pressure belt and pointed to its influence on the Sahelian rainfall variation. Winstanley (1973) noted an expansion of the circumpolar vortex beginning in the late 1950's, and postulated that this expansion was the causative factor for the shift of the subtropical ridge. According to Bryson (1973) the vortex expansion was caused by an increase in aerosols and CO_2 which resulted in an increase in both the latitudinal and vertical temperature gradients. Similarly, Kraus (1977) relates the Southern hemisphere temperature gradient to the ITCZ oscillations.

The bio-geophysical mechanism proposed by Charney

(1975) incorporates both the agricultural and herding practices of man and meteorological processes to explain the reduction of rainfall in the Sahel. He contends that the destructive agricultural techniques utilized and the browsing of livestock denudes the vegetation causing an increase in the surface albedo. The increased albedo results in a net radiative loss which produces general subsidence and drying over the area, thereby inhibiting or reducing the convection necessary for rain.

The geophysical aspects of this mechanism was examined by Charney, Quirk, Chow, & Kornfield (1977) by numerical modelling. They demonstrated that a significant reduction in precipitation could be achieved by increasing the Sahel albedo from .14 to .35. Similarly, Berkofsky (1976) found sinking motion was associated with high albedoes in the Negev desert. Otterman (1974) studied the effects of the sharp contrast between the bright Sinai and the relatively dark Negev. Measurements showed the bright side to be 5°C cooler during the day in August. He proposed that the "thermal depression" in the Sinai could result in reduced convection.

The purpose of our study was to examine the albedo variations in the Sahel during the period 1967 through 1974. We wished to determine the magnitude of any year to year and seasonal albedo changes as well as the relationship between albedo and precipitation. The only quantitative data available with adequate temporal and spatial coverage to determine albedoes over the area of interest during the drought was the Applications Technology Satellite (ATS III) digital tape archive. We found that apparently cloud free data were available for at least one day of the years 1967, 69, 72, 73, & 74 during the dry season (winter); and for at least one day of 1969, 72, 73, & 74 during the rainy (summer) season.

The data were navigated to insure that the same areas were being compared. Although the data were selected because they were the most cloud free, additional surface was exposed through use of a minimum brightness composite (Mosher, 1977) obtained by superimposing several digital areas from different days at similar solar zenith angles and selecting the minimum brightness value for each pixel. This process effectively removed visible clouds except for locations that were cloud covered on all data sets.

ALBEDO MEASUREMENTS

Once the data were navigated, merged into minimum brightness composites, and displayed on McIDAS;

brightness measurement excluding cloudy areas were made for 2° square areas. It was assumed that the mode of each histogram represented the brightness value of the surface in each 2° square area. All the albedoes were derived assuming isotropic scattering.

We eliminated gain changes, sensor degradation, atmospheric contaminants, etc; but normalizing each data set with respect to the area centered at 19N 05W. Comparisons of this Saharan normalization point with White Sands, New Mex. and Salar de Uyuni in Bolivia show approximately ±12% variation in albedo. Then the cosine of the solar zenith angle was applied to each square to normalize all data to local noon. It was then discovered that a systematic error appeared in the albedoes computed from data with sun angles greater than 45°. This effect was corrected by use of an empirical curve derived by measuring the albedoes of identical areas at different solar zenith angles and computing the percent error as a function of zenith angle.

RESULTS

Surface albedo measurements were made for 19 Nov 1967, 15 Sept 69, 6 Jan 70, 19 July 72, 13 Dec 72, 23 Dec 72, 14 Aug 73, 19 Oct 73, 2 July 74, and 21 Sept 74. The pattern of albedoes over the area shows a band of high albedoes extending from northeast Mali through central Mauritania and a relative albedo minimum located near the northern border of Mauritania and Mali. The lines of constant albedo generally parallel the mean isohyets in the Sahel. Most of the data show an albedo gradient that is primarily latitudinal with the largest gradient occurring between 15°N and 19°N as is shown by figure 1. A comparison of our surface albedo patterns with those derived by Rockwood and Cox (1977) using SMS data for 1974 shows a reasonably good correlation.

In order to examine the overall Sahelian surface albedo changes, the area was subdivided into a Saharan area, 18 to 22°N, and a Sahelian area, 12 to 18°N. The data were subdivided into a wet season set consisting of 15 Sept 69, 19 July 72, 14 Aug 73, and 21 Sept 74; and a dry season set consisting of Nov 67, 06 Jan 70, 13 Dec 72, 19 Oct 73, and 2 July 74. A mean albedo for the Sahara and the Sahel was computed for each data set. We then obtained a normalization factor for each mean Sahelian albedo by dividing the mean Sahara value for each data set by the mean Saharan value of all the data sets. The results (fig. 2) show the albedo increase for both the wet and dry

season data, and also point out the tendency for the wet season albedoes to approach those of the dry season as the drought progressed.

The first seasonal change we looked at was the July to Sept 1974 data. Our calculations averaged latitudinally from 16°W to 0°W show relative albedo increases of 14% along 13°N, 25% along 15°N, 30% along 17°N, 5% along 19°N and 21°N. The seasonal change between Sept 1969 and Jan 1970 revealed a similar (but reversed) pattern of albedo changes. An examination of seasonal changes for 1972 and 1973 did not show patterns similar to the 1969 and 1974 albedo changes or comparable magnitudes of albedo change.

The inter-annual variation of surface albedo was examined for both the wet and dry seasons. For the wet season the percentage albedo change for three time intervals were examined: Sept 1969 to July 72; Sept 69 to Aug 73; and Sept 69 to Sept 74. The maximum albedo increases are similar to the maximum observed for the seasonal variation; approximately 100%. The albedo increases are generally higher for the 1969-1972 and 1969-1973 intervals. The dry season albedo change patterns are not as regular or as large as the wet season. The albedo changes between Nov 1967 and Jan 1970, and between Nov 1967 and July, 1974 are mostly within the noise limits of the measurements. The changes are somewhat larger (60%) for the 1967 to 1973 period than for the 1967 to 1972 period (40%); perhaps reflecting the increased intensity of the drought in 1973.

In order to relate albedo and precipitation, we averaged the precipitation for all stations in the 2° square areas and computed correlation coefficents between the annual precipitation and the albedo during the following dry season. Coefficients for 1967, 70, 72, 73, and 74 were -.57, -.71, -.58, .07, and -.72 resp. Only the 1970 and 1974 correlations were significant.

CONCLUSIONS

The measurements indicate the existence of a surface albedo cycle for both the wet and dry seasons during the 1967 to 1974 Sahel drought (Fig. 2). The largest increases of surface albedo from a normal year to a drought year occurred in the wet season. The maximum observed changed for any 2° square was on the order of 100%. The greatest seasonal changes were found to occur during normal years with maximum changes of approximately 80%. The estimated error in the measurement technique is 11% of the surface albedo value.

Figure 1

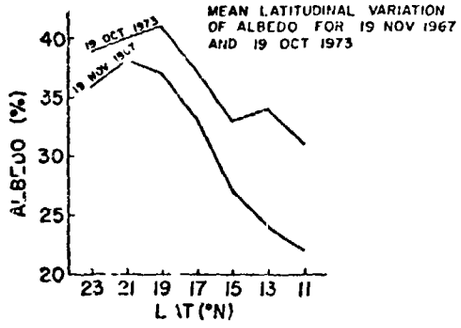

Figure 2

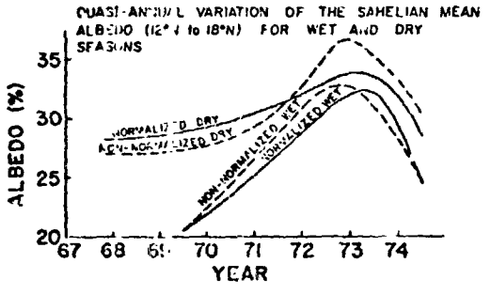

Berkofsky, L., 1976, JAM, 15, pp. 1139-1144.
Bernus, E., 1972, "Drought, Famine, and Population Movements in Africa," James C. Newman, ed.
Bryson, R. A., 1973, Inst. for Env. Studies, Rep. 9, U. of Wisc., Madison.
Charney, J. G., 1975, QJRMS, 101, No. 428, pp. 193-202.
Charney, J. G., Quirk, Chow, and Kornfield, 1977, JAS, 34, pp. 1366-85.
Kraus, E. B., 1977, MWR, pp. 1009-1018.
Lamb, H. H., 1973, "Drought in Africa," Symposium Report, pp. 27-28.
Lowdermilk, W. C., 1935, Pac. Af., 8(4), pp. 409-419.
Mosher, F. R., 1977, Final Rep. NAS5-21798, pp. 111-126.
Otterman, J., 1974, Science, 186, pp. 531-533.
Rockwood, A. A., and S. K. Cox, 1976, Atm. Sci. Paper No. 265, Co. State U., 64pp.
Shenk, W. E., and V. V. Salomonson, 1972, JAM, 11, pp. 214-220.
Stebbing, E. P., 1935, Geogr. J., 85(6), pp. 506-524.
Winstanley, D., 1973, Nature, 243, pp. 464-465.

Paper No. 32

GEOPHYSICAL FLUID FLOW MODEL EXPERIMENTS IN SPHERICAL GEOMETRY

W. W. Fowlis and G. H. Fichtl, *Marshall Space Flight Center, Huntsville, Alabama*

ABSTRACT

An experimental and theoretical program has been undertaken to assist in the design of geophysical fluid flow model experiments for Spacelab. Two new non-intrusive measurement techniques have been developed. A theoretical calculation has been carried out to guide the design of a proposed atmospheric general circulation model experiment.

I. INTRODUCTION

The near zero-gravity environment of Spacelab presents us with the opportunity to perform geophysical fluid model experiments in true spherical geometry. A radial dielectric body force, which is analogous to gravity, can be achieved over a volume of fluid. There is no way such experiments can be carried out in a laboratory on the earth's surface because the dielectric force is weak and its effect is overwhelmed by terrestrial gravity.

Much sophisticated modeling of geophysical fluid flows has previously been carried out and a great deal has been learned about the circulations of, stellar atmospheres, planetary atmospheres and ocean basins. In particular, considerable effort has been expended on atmospheric general circulation models in cylindrical geometries. These models exhibit many large-scale features of the general circulation such as jet-streams and wave-cyclone (baroclinic) instability. These models are found to scale similarly to the real atmosphere giving the same quasi-geostrophic set of equations for both systems (Holton, 1972). A serious limitation of all these models arises, however, when attempts are made to extend their validity to real planetary configurations.

In the spherical model experiments the fluid is contained between two concentric and rotating spheres.

The simulated radial gravity is achieved by applying a voltage across the spheres. Motions are driven by imposing and externally maintaining thermal gradients. The configuration chosen for these gradients depends upon the geophysical fluid flow being modeled.

A model of stellar convection has been accepted for Spacelab I (The Geophysical Fluid Flow Cell/GFFC; Principal Investigator; John Hart, University of Colorado). In this experiment the inner sphere will be maintained at a higher temperature than the outer sphere and the resulting convective flow studied. A model for the general circulation of the earth's atmosphere has been proposed by the author (The Atmospheric General Circulation Experiment (AGCE)). In this experiment the fluid will be subjected to a stable radial temperature gradient and an unstable latitudinal gradient.

The model experiments are valuable for improving our understanding of large scale circulation dynamics. They could be used to check the essential large-scale baroclinic behavior of numerical general circulation models. Further, the models can also provide information for sub-grid scale processes for numerical climate models.

II. THE DIELECTRIC BODY FORCE

The body force per unit volume in an incompressible, charge-free, non-uniform, dielectric fluid in an electric field is given by, $-\frac{1}{2}E^2\nabla\epsilon$, where E is the field and ϵ is the dielectric constant. It has been shown by Hart (1976) that for a liquid the above force can be written as an electrostatic gravity term,

$$g_E = \frac{2\epsilon\gamma}{\alpha\rho}\left(\frac{R_i R_o}{\Delta R}\right)^2 \frac{V^2}{r^5} \qquad (1)$$

where ρ is density, α and γ are thermal coefficients of density and dielectric constant, R_i and R_o are the radii of the inner and outer spheres, $\Delta R = R_o - R_i$, V is the voltage difference and r is radius.

Typical values of the experimental dimensions and properties of the silicone oil to be used in the GFFC are given in table 1. Substitution from table 1 in

TABLE 1

$R_i = 2.00\times10^{-2}$m	$\gamma \simeq \alpha = 1.34\times10^{-3}C^{\circ}$
$R_o = 3.00\times10^{-2}$m	$\epsilon = 2.2\times8.85\times10^{-12}$ mks
$\Delta R = 1.00\times10^{-2}$m	$\rho = 0.82\times10^{3}$kg m^{-3}

equation (1) yields for the mid-gap location, $g_E = 1.8\times10^{-8} V^2$ ms^{-2}. The need to perform these experiments

in space now becomes clear, the ratio g_E/g must be much greater than unity. For a voltage of 10,000 volts, $g_E/g \approx .18$, which is still small.

III. MEASUREMENT TECHNIQUES

During the past year a considerable amount of effort has gone into developing techniques for flow and temperature measurement. Clearly, any probes or wires inserted into the small confined volume of liquid would disturb the flow. Flow measurements will be made using a photochromic dye as a tracer. Photochromic dyes are substances which darken upon exposure to ultraviolet radiation and then clear up again spontaneously. We have succeeded in dissolving a small amount (.02% by weight) of a photochromic dye in the silicone oil and in producing substantial darkening with a mercury discharge lamp. No adverse effects due to the dye in the electric field up to 20,000 volts/cm have been observed.

Temperature measurements will be made using a Moiré fringe technique. In the system chosen a Ronchi ruling is projected through the working fluid and reflected back in such a way that a real image of the original ruling is located in space close to the original ruling. Observation of the two rulings produces a Moiré fringe pattern. If the fluid has no temperature variations and hence no refractive index variations, the fringe pattern is similar to the original ruling, if, however, temperature variations are present, the fringes are distorted to reveal the temperature structure of the fluid. This technique gives only depth integrated information, but these data are satisfactory.

IV. A BAROCLINIC INSTABILITY CALCULATION

We were concerned that if an identical apparatus to the GFFC (see table 1) were used for the AGCE, the effects of viscosity would suppress the instability. So, we have been examining a two-layer, quasi-geostrophic, instability model. Although this model is a simplified model, it has been used extensively by theoretical meteorologists (Holton, 1972), and has proved to be valuable. We included viscosity in the model by allowing for Ekman layers at the boundaries (Greenspan, 1969) and curvature by carrying out the calculation on a β-plane (Holton, 1972). The reader is referred to Fowlis & Hide (1977) for the complete calculation. A summary of the significant results follows.

Figure 1 is a plot of the marginal stability curves for different zonal wave numbers (m); they are plotted as $S (\equiv g\alpha\Delta T_v / f^2 d)$ versus $Ta_m (\equiv \chi^4 / \Gamma_1^4 E^2)$. ($E \equiv \nu / f d^2$, $\chi \equiv \Delta T_H / \Delta T_v$, $\Gamma_1 \equiv h/d$; g is gravity, ΔT_v is the imposed internal vertical temperature difference,

ΔT_H is the imposed horizontal temperature differenc
$\dot{\tau}$ is twice the vertical component of the rotation rat
d is the depth, h is a horizontzal scale and ν is the kinematic viscosity.) Figure 1 is plotted for $\chi = 0.3$, $\nu = 1.0 \times 10^{-2} m^2 s^{-1}$ and the data of table 1 The area inside a given wave-number curve is the region of instability.

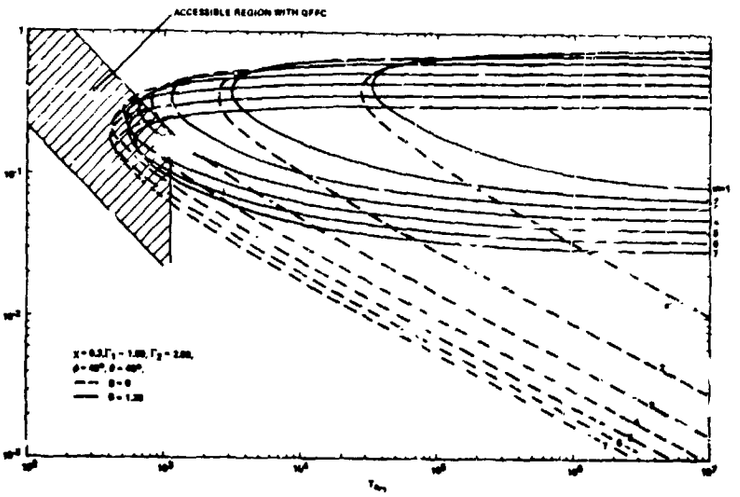

FIGURE 1 PLOTS OF THE MARGINAL STABILITY CURVES FOR DIFFERENT VALUES OF χ AND FOR $\chi = 0.3$. THE DASHED CURVES ARE FOR ... NO CURVATURE ($B = 0$) AND THE CONTINUOUS CURVES ARE FOR $B = 1.33$. OTHER QUANTITIES ARE $\phi = 45°$, $\Gamma_1 = 1.00$ AND $\Gamma_2 = 2.0$. THE SHADED AREA IS THE EXPERIMENTALLY ACCESSIBLE REGION WITH THE GFFC APPARATUS.

S is a measure of vertical stability and Ta_m is an inverse measure of damping effects. Curvature is measured by B . ($B = F\bar{R}/\chi$; $F = \beta d/f$, $\beta = \dot{\tau}/\bar{R}$, $\bar{R}$ is the mean radius.) The dashed curves are for zero curvature ($B = 0$) and the continuous curves for the geometry of the GFFC ($B = 1.33$).

Also in figure 1 the experimentally accessible region with the GFFC is indicated. A major constraint in defining this region is that $\Omega^2 R_c / g_E < 0.1$. (Ω is the rotation rate.) The small overlap of the accessible region and the unstable region means that the GFFC is not suitable for a baroclinic study.

The only practical way to increase the overlap area is to increase g_E and the only practical way to increase g_E is to increase ϵ (see equation (1)). Many dielectric liquids with higher values of ϵ exist and a search is underway to find a suitable one. It is also desirable to increase the diameters of the spheres while keeping the gap constant. Figure 2 shows the stability diagram for spheres of radii 4.5 and 5.5 cm. A value of $\chi = 0.3$ is used and $B = 0.667$, the values of the other

quantities are the same as for figure 1. The experimentally accessible region for a liquid with dielectric

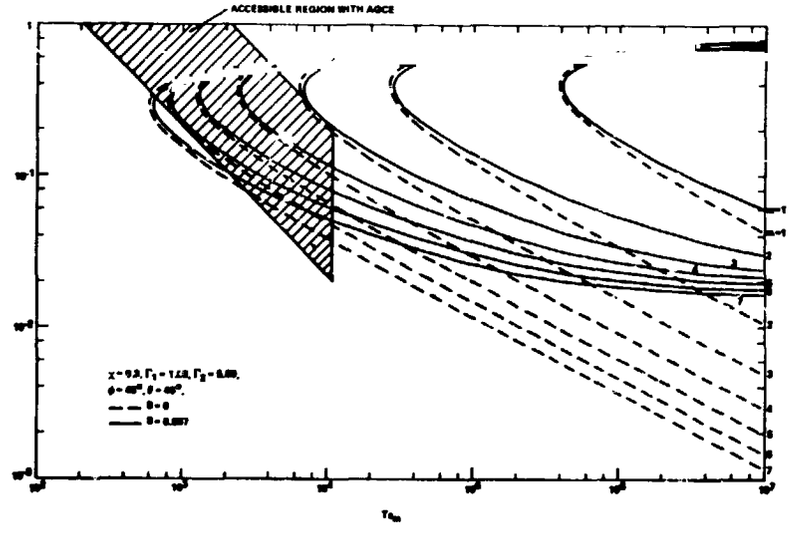

FIGURE 2 PLOTS OF THE MARGINAL STABILITY CURVES FOR DIFFERENT WAVE NUMBERS m AND FOR χ = 0.2. THE DASHED CURVES ARE FOR ZERO CURVATURE (B = 0) AND THE CONTINUOUS CURVES ARE FOR B = 0.007. OTHER QUANTITIES ARE ϕ = 45°, θ = 45°, Γ_1 = 1.00 AND Γ_2 = 0.80. THE SHADED AREA IS THE EXPERIMENTALLY ACCESSIBLE REGION WITH THE PROPOSED AGCE APPARATUS.

constant 20 times the GFFC value is shown. It should be possible to carry out satisfactorily the objectives of the AGCE working in this region.

REFERENCES

Fowlis, W. W. & Arias, S. 1977: The effect of viscosity and curvature on baroclinic instability - a two-layer model. NASA Technical Paper. In preparation.

Greenspan, H. P. 1969: The Theory of Rotating Fluids. Cambridge University Press, Cambridge.

Hart, J. E. 1976: Studies of Earth simulation experiments. NASA Contractor Report NASA CR-2753, NASA, Washington, D. C.

Holton, J. R. 1972: An Introduction to Dynamic Meteorology. International Geophysics Series, Academic Press.

C-3

Paper No. 33

N79-20607

D32

PRELIMINARY TEST OF A COARSE RESOLUTION GCM FOR CLIMATE APPLICATION

J. Hansen, G. Russell, R. Ruedy, K. Kawabata, L. Travis, S. Lebedeff, W. Wang, A. Lacis *(all at GISS)*, P. Stone, *(MIT)*

ABSTRACT

Preliminary steps have been taken to develop a climate model adequate for seasonal and interannual simulations. Tests of the model against the observed seasonal cycle of key climate properties indicate an encouraging capability for climate applications.

INTRODUCTION

The basic equations solved in a general circulation model (GCM) are the conservation equations for mass, energy and momentum, the hydrostatic equation and the ideal gas law. The principal merit in explicit modeling of the atmospheric physics with these fundamental equations is that it allows the possibility of realistically simulating complex interactions and feedbacks among different parts of the climate system. Because of the large computing time required,however,GCM's have not yet been used extensively for seasonal and interannual climate modeling.

Our basic hypothesis is that it should be possible to do realistic climate simulations with a horizontal resolution of the order of 1000 km, because that resolution is adequate to define the main features of the atmospheric flow, such as the meridional circulation and large scale eddies. Although there have been studies which indicate that a considerably finer resolution is required (Wellck, et al., Mon. Wea. Rev. 99, 673, 1971; Manabe, et al., Mon. Wea. Rev. 98, 175, 1970), that conclusion is model-dependent; in particular, the horizontal viscosity in the models used for those studies tends to damp out real atmospheric motions as well as the numerical instabilities it is aimed at.

Our ultimate objective is to obtain a modeling capability which can be used to (1) support the development of observational systems by helping to determine

climate parameters which should be monitored, including definition of accuracy and sampling requirements, and (2) develop techniques for utilization of space-acquired data in climate analysis and prediction, including the ability to help assess and improve climate predictability for time scales ranging from the seasonal 'farmer's forecast' to the 'end-of-century' time frame.

The basic elements in the approach are (1) model development, (2) model verification, with particular emphasis on reproduction of seasonal cycles, (3) climate mechanism experiments, and (4) observing systems simulations. Obviously there must be some simultaneous work on these different elements and a back-and-forth play between them as modeling capabilities are improved. The initial work we report here concerns the first two elements.

MODEL

A prime requirement on a model intended for climate applications is that it not be unduly constrained by climatological specifications, either properties within the atmosphere such as the cloud characteristics or boundary conditions at the upper or lower edges of the model. Thus we are developing the model physics with this requirement in mind, although certain boundary conditions, such as the sea surface temperature, will remain climatologically specified during the early applications. Also attempts to parameterize the horizontal transports by sub-grid-scale motions will be made only after a thorough analysis has been completed of the model capabilities without such parameterizations, including some determination of the extent to which the overall realism of the model's large scale circulation depends upon approximations in the physics and numerics.

Substantial progress has been made in developing the physics of the model. The surface physics is computed with a fractionalized grid, i.e., within a given grid element appropriate proportions of land, ocean, ice and snow are used for computing interactions between the surface and the atmosphere. Moist convection is computed with a cloud model which permits clouds of any depth and mixes horizontal momentum vertically; convection is also allowed to occur in unsaturated air if the temperature lapse rate is unstable, mixing momentum and moisture but not leading to cloud formation. A method for computing atmospheric radiation, which is fully interactive with changes in

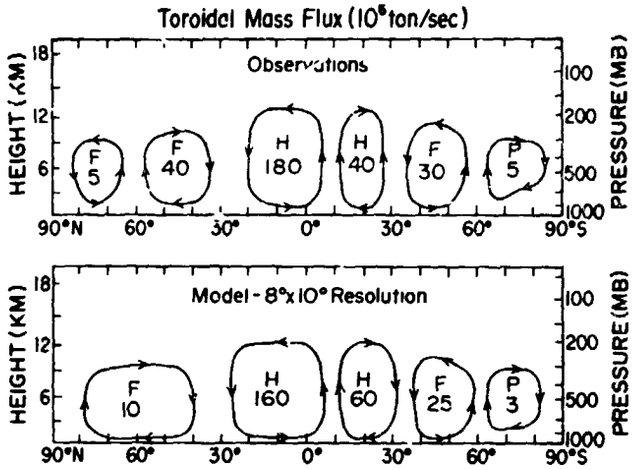

Fig. 1. Observed and computed stream functions for the mean meridional circulation. Observed values are based on Newell et al. (1972).

atmospheric pressure, temperature and composition, has been developed. Ground moisture is computed with a hydrological cycle including evaporation, precipitation and run-off. A parameterization has been developed for computing the snow cover based on the surface air temperature during the preceding few weeks, with the most recent values weighted more heavily.

The finite difference schemes employed are due to Arakawa. Because the computing time varies as approximately the third power of the horizontal resolution, the key problems in the numerics of the model relate to the horizontal differencing scheme. We are currently using Arakawa's Scheme B (Arakawa and Lamb, Methods of Computational Physics 17, 173, 1977), although we are also testing his Scheme C.

SEASONAL CYCLE AS MODEL VERIFICATION

The initial results support the underlying hypothesis about the capability of a coarse-grid model to reproduce the basic nature of the general circulation. Fig. 1, for example, shows the meridional circulation for a model run with 8° by 10° resolution. The 2-3 cell tropospheric flow is as realistic as obtained with fine grid GCM's, and, except for the northern hemisphere Ferrel cell, it is within the observational uncertainty of climatology. Large scale eddy activity in midlatitudes is somewhat too weak, but is also comparable to that for fine-grid GCM's.

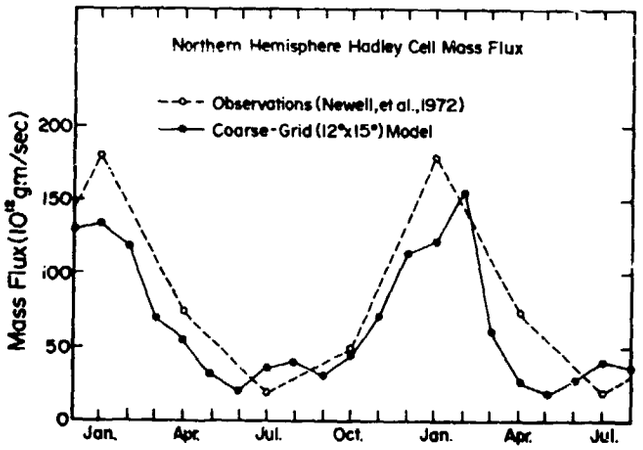

Fig. 2. Observed and computed mass flux in the northern hemisphere Hadley cell as a function of season.

A fundamental test of the model's capability to simulate climate change is provided by the natural seasonal cycle. Fig. 2 shows the strength of the northern hemisphere Hadley cell mass flux as a function of time for a 19-month run of the model at 12° x 15° resolution. The nature of the seasonal variation is realistically reproduced, as it is for the global radiation balance, the global cloud cover and the strength of the zonal winds. The amplitude of the seasonal variations of hemispheric eddy energy is too small, a characteristic which is associated with a generation of excess eddy energy in the tropics during all seasons and a deficiency of eddy activity at mid-latitudes during winter.

Fig. 3 shows the mean land temperature at 30°N latitude as a function of season for the coarse-grid model and for climatology. At this latitude the model is significantly too cold in winter and slightly too warm in summer.

The seasonal behavior of the model provides clues about the source of the primary model deficiencies. By means of appropriate experiments in which different model parameters are varied it is possible to help isolate the aspects of the model physics or numerics which have greatest need for improvement. This procedure has been found to be extremely useful in the initial model development, and it should become even more valuable as the various seasonal cycles in the climate system become

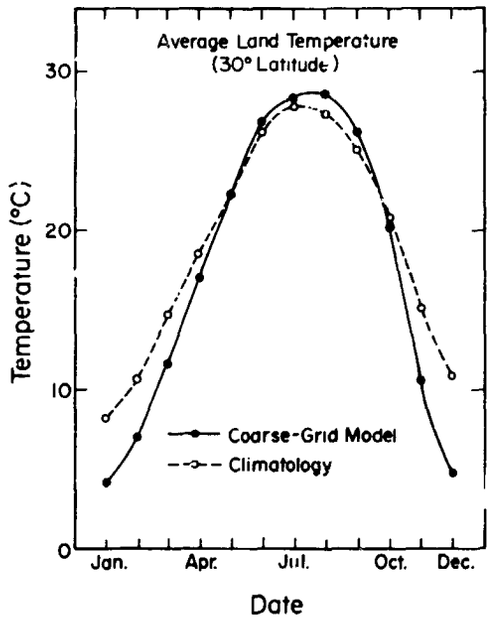

Fig. 3. Observed and computed ground temperatures at 30° N latitude as a function of season. Computations are for the model with 12° by 15° resolution.

more accurately defined by observations.

DISCUSSION

We have found that it is possible to obtain a realistic general circulation of the atmosphere with a coarse resolution model based on the fundamental equations. These results are very encouraging with regard to the prospects for developing a model which permits a realistically complex representation of the physics of the climate system and yet is sufficiently fast that it can be used as a scientific research tool as well as for helping to specify observing systems requirements.

D23

Paper No. 34

N79-20608

INTEGRATION SCHEMES FOR CLIMATE PREDICTION

E. Isaacson,* *Courant Inst. of Math's Sciences, N.Y.U.*

ABSTRACT

To assure the conservation of total mass, momentum, energy, vorticity, etc., a method of modifying any given algorithm is presented. The modified scheme has at least the same order of accuracy as the given scheme.

The long-term solution of differential equations that may arise in climate models, necessitates the use of numerical methods that will maintain the conservation of total: mass, momentum, energy, vorticity, enstrophy, etc. This requirement for preserving the conservative properties of the mathematical models is not of paramount importance, when choosing schemes for short-term numerical solution, as in weather forecasting. That is, by choosing a stable scheme with a sufficiently small, local truncation error, the physical quantities may be adequately conserved for a brief interval of time. But, if one desires to integrate for a period of months to years, then the gradual accumulation of truncation errors will in general destroy the conservation properties that the model has

To overcome this deficiency, many people had developed conserving difference schemes for specific models, e.g. for modern circulation models, such work was pioneered by Arakawa and Mintz, see [1] for references. These developments were not mathematically satisfying, since they did not lead to recipes

*Acknowledgment

Some of this work was done jointly with A. Bayliss and E. Turkel. The ERDA Mathematics and Computing Laboratory, at the Courant Institute of Mathematical Sciences of New York University, generously supported the computing activities under Contract No. EY-76-C-02-3077*000.
The author was supported by the NASA-Goddard Institut for Space Studies grant # NSG-5034.

for constructing conserving schemes for other models. On the other hand, a fruitful way of looking at the problem was discovered independently by Y. K. Sasaki, [5], [6] and by A. Bayliss and E. Isaacson [2]. They found that it was possible to modify any given difference scheme, so as to ensure the total conservation of the appropriate physical quantities. Indeed, Bayliss and Isaacson gave a straightforward recipe for carrying out this procedure for any mathematical system. Subsequently, Isaacson and Turkel [3] explained how this technique might be applied to deal with a model third order equation for the conservation of vorticity. Isaacson [4] is recounted here. With this technique it now becomes feasible to carry out the long-term numerical integration of climate models.

We now give a brief sketch of the conserving modification method. Let the initial-boundary value problem be posed for the partial differential equation for the vector u:

$$u_t = B(u) . \tag{1}$$

Suppose that the solution u satisfies certain functionals

$$g_k[u] = 0 , \quad k = 1,2,\ldots,K . \tag{2}$$

For example, with $B(u) \equiv u_x$ and u a scalar function satisfying periodic boundary conditions $u(0,t) = u(1,t)$, we find that for certain constants depending on the initial data, c_1 and c_2,

$$g_1[u] \equiv \int_0^1 u\,dx - c_1 = 0 ,$$

$$g_2[u] \equiv \int_0^1 (u_x)^2 dx - c_2 = 0 , \tag{3}$$

$$g_3[u] \equiv \int_t^{t+\Delta t}\int_0^1 u_x u_t\,dx\,dt - \int_t^{t+\Delta t}\int_0^1 (u_x)^2\,dx\,dt = 0 .$$

By representing the integrals as sums, we may easily construct approximating functionals

(4) $$G_k[U] = 0 , \quad k = 1,2,3 ,$$

where U is a net function defined at the grid points (x_j,t_n), and $U(x_j,t_n)$ approximates $u(x_j,t_n)$.

Suppose that some algorithm is given for approximating u by a net function W. At time step t_{n+1}, let the given difference operator have the form:

(5) $$W(n+1) = C\{W(n),W(n-1),\ldots,W(n-s)\} \equiv CW(n) .$$

The given difference scheme (5) is modified now to produce a net function U(n+1) which will satisfy (4), the discrete approximation of the functionals (3). That is, a net function V(n+1) is found so that

$$U(n+1) = CU(n) + V(n+1) ,$$

(6) $$G_k[U(n+1)] = 0 , \quad k = 1,2,\ldots,K ,$$

$$\min |V(n+1)| ,$$

(note the norm of the perturbation V(n+1) is as small as possible).

The determination of V(n+1) is a calculus problem for finding a net function that satisfies the K simultaneous non-linear equations (6), and is of minimum norm. The use of Lagrange multipliers is suggested by Sasaki, but we find that it is simpler to solve (6) by linearizing the functionals $G_k[U(n+1)]$ about the "predicted" value CU(n). That is, we set

(7) $$G_k[U(n+1)] \equiv G_k[CU(n) + V(n+1)] \cong G_k[CU(n)] + \text{grad } G_k . V(n+1) \equiv L_k[V(n+1)] = 0 .$$

Here $\text{grad } G_k = \dfrac{\partial G_k}{\partial U(n+1)}$ is evaluated at U(n+1) = CU(n), the scalar product with V(n+1) is taken, and the resulting linear form L_k is set equal to zero. Note that in the example (3), the discrete form of the last functional involves U(n+1) and U(n); nevertheless the gradient is taken only with respect to U(n+1). The solution of the K simultaneous linear equations is given by

(8) $$V(n+1) = \sum_{k=1}^{K} a_k \text{ grad } G_k + P ,$$

where P is an arbitrary vector that is orthogonal to the K gradients. That is

$$P.\text{grad } G_k = 0 , \quad k = 1,2,\ldots,K . \tag{9}$$

Hence if the norm, $|V(n+1)|$, is the Euclidean norm,

$$P = 0$$

provides the solution of minimum norm. The K scalar coefficients a_k are determined by solving the K linear equations in (7) after substituting the expression (8) for V(n+1).

This procedure has been used to

(i) conserve total mass and total energy in a one layer, atmospheric model solved over the sphere by the use of overlapping rectangular stereographic coordinates,

(ii) conserve the three functionals in (3),

(iii) conserve three functionals arising from the equation

$$u_t = u_{xx}+f(x,t) ,$$

with periodic boundary conditions,

(iv) conserve vorticity, enstrophy, and energy for the third order equation $\frac{D}{Dt}\zeta = 0$, with appropriate boundary conditions.

In all cases, the conservative modification method has at least the same order of accuracy as that of the given operator C, provided that the quadrature formula to define G_k is a sufficiently accurate approximation. For a quadrature formula of second order accuracy, we found that the method gave slightly more accurate solutions than did some given second order accurate schemes. In fact, in the example (3), a given first order accurate scheme became almost second order accurate upon being modified. Furthermore, in cases (ii) and (iii) it was found possible to exceed the Courant-Friedrichs-Lewy (CFL) restriction on the size of the time step, without introducing the instability that the given scheme would have acquired. In Sasaki's earlier report he had indicated that this possibility might arise, but this conclusion was influenced by his use of an

additional smoothing operation that in effect was responsible for stabilizing his scheme. In order to ensure stability when the CFL condition is violated, we found it necessary to use constraints $g_k[u]$ that involve spatial derivatives, as in g_2 and g_3 of (3).

Now that such conserving methods have been developed, it remains to experiment with climate models.

[1] Arakawa, A., "Numerical simulation of large-scale atmospheric motions", in Numerical Solution of Field Problems in Continuum Physics, vol. 2, G. Birkhoff and S. Varga, Eds., Am. Math. Soc., Providence, R. I., 1970, pp. 24-40.

[2] Bayliss, A. and E. Isaacson, "How to make your algorithm conservative", Abstract 726-65-6, Notices of the Am. Math. Soc., vol. 22, no. 5, Aug. 1975, pp. A-594,5.

[3] Isaacson, E. and E. Turkel, "Conservation of integral constraints for numerical solutions", Abstract of talk given at SIAM meeting, Oct. 1976, Atlanta, Georgia.

[4] Isaacson, E., "Integration Schemes for Long Term Calculation", ed. R. Vichnevetsky, Publ. IMACS (AICA) 1977.

[5] Sasaki, Y. K., "Variational design of finite difference scheme for initial value problem of conservative system", Univ. of Oklahoma report, Norman, Oklahoma, 1975.

[6] Sasaki, Y. K., "Variational design of finite-difference schemes for initial value problems with an integral invariant", J. Comp. Phy., vol. 21, no. 3, July 1976, pp. 270-8.

Paper No. 35

N79-20609

FAST BUT ACCURATE TECHNIQUES FOR CALCULATING RADIATIVE TERMS IN NUMERICAL ATMOSPHERIC MODELS AND IN REMOTE SENSING APPLICATIONS

Albert Arking, *Goddard Space Flight Center, Greenbelt, Maryland*
Dennis Chesters, *Computer Sciences Corporation, Silver Spring, Maryland*
Ming-Dah Chow, *SAI Comsystems Corporation, McLean, Virginia*

ABSTRACT

New methods have been developed for calculating radiative terms with relatively high accuracy but with sufficient speed so that they can be used in numerical atmospheric models or in high volume processing of satellite measured radiances for remote sensing of atmospheric and surface parameters. Comparison with commonly used methods in both types of applications indicate improvements in calculating transmittances of factors between two and three and in calculating radiances and cooling rates of factors between two and seven.

INTRODUCTION

Absorption and emission of thermal infrared radiation play a very important role in climate processes. Although at any one instant of time advective motion is the principal means of energy transport, radiative transfer tends to dominate when one integrates over periods longer than ten to twenty days and over regions on a planetary scale. Thus, atmospheric models that are to be used for climate studies must incorporate accurate methods for calculating the radiative terms. Another major application of radiative transfer theory is in the retrieval of atmospheric and surface parameters from satellite measured radiances (e.g., remote sounding of the atmosphere). In both applications, it is necessary to make accurate calculations of the infrared radiative terms, repetitively for a wide range of temperature and humidity profiles. At the same time, the computations must be rapid enough so that the models can be run and/or the remote sensing measurements can be processed within reasonable time periods.

The basis for making accurate calculations of the radiative terms are the line parameters of the atmospheric gases, which have been compiled by McClatchey et al. (1973). Using these parameters, and making appropriate assumptions concerning atmospheric composition, shapes of the spectral lines, and the temperature and pressure dependence of the parameters, one can proceed to calculate atmospheric transmittance "line by line" in any portion of the spectrum. Once transmittance is calculated in the appropriate spectral intervals, the radiative terms for any particular application follow easily. Because there may be hundreds of spectral lines that must be taken into account to calculate transmittance at any point in the spectrum and because transmittance is a rapidly varying function of wave number, the line by line method consumes a lot of computer time and is therefore used primarily for computing transmittances for selected standard atmospheric conditions. For high volume computations, the methods employed up to now have been either semi-empirical–e.g., Rodgers and Walshaw (1966) and Sasamori (1968), for atmospheric models–or are statistically derived from line by line computations–e.g., Abel et al. (1976) and Fleming and McMillin (1977).

Two new methods are employed here: one for those portions of the spectrum where the mixing ratios of the absorbing gases do not change and only the temperature variation needs to be

taken into account; the other is used to account for both water vapor and temperature. The formulation of both methods is entirely theoretical and based upon approximations to the exact line by line method.

Temperature Dependence

The temperature dependence of the transmittance is taken into account by expanding the transmittance function into a Taylor-like series about a reference temperature profile $T_0(z)$, taking into account that transmittance is a functional of the temperature profile, and terminating the series after the linear term. Thus, for an arbitrary temperature profile T(z), the transmittance between heights z_1 and z_2 can be written as

$$\tau(z_1, z_2) = \tau_0(z_1, z_2) + \int_{z_1}^{z_2} K_0(z_1, z_2; z')[T(z') - T_0(z')]\, dz' \qquad (1)$$

where $T_0(z_1, z_2)$ is the transmittance for the reference profile. The change in transmittance is thus a linear integral operator, the kernel $K_0(z_1, z_2; z')$ being the functional derivative of transmittance with respect to the temperature function T(z).

In practice, one calculates the transmittance and its functional derivative for only one temperature profile (e.g., the U.S. Standard Atmosphere) for each desired spectral interval, directly from the line parameters. These data are then saved and the transmittance for any arbitrary temperature profile is calculated from Eq. (1); it involves a negligible amount of computer time for most applications.

The accuracy of this method is illustrated in Figure 1. A sample set of 11 widely distributed temperature profiles were arbitrarily chosen for the test; the mean and standard deviation is shown in the graph on the left. The middle graph shows transmittance between the pressure level indicated by the ordinate and zero pressure, calculated for the U.S. Standard Atmosphere for one of the channels (at 717 cm^{-1}) of the Nimbus 6 High resolution Infrared Radiation Sounder (HIRS). The transmittance was then calculated from Eq. (1) for each profile in the sample set and compared with exact line by line calculations; the RMS difference or "error" is illustrated in the graph on the right by the curve labeled "linear expansion." For comparison, the RMS transmission error is shown for the same sample set calculated by the method of Abel et al. (1976)—a regression method which was used for calculating transmittances for processing the Nimbus 6 HIRS data. The table in the lower left shows the mean, RMS, and maximum errors, over the sample set, in the calculated transmittance at the level of maximum error; also shown is the mean, RMS, and maximum errors in the calculated radiance at satellite altitude, expressed as brightness temperature. The comparison between the linear expansion method and the regression method shows an improvement between a factor of two and three in transmittance and a factor of around seven in the calculated radiance.

Water Vapor Dependence

The linear expansion method used to account for the temperature dependence of transmittance works well because the relative variability of temperatures in the atmosphere is small (i.e., $\Delta T/T << 1$) and hence, the higher order terms are negligible. This is not the case for water vapor, since the mixing ratio at any height can change by an order of magnitude. Therefore, a different approach is needed.

First, we note that the underlying parameter in calculating the radiative terms is the absorption coefficient, which is a rapidly varying function of wave number; also, it depends upon the local temperature and pressure and is proportional to the local mixing ratio. If no approximation is made, it would be necessary to compute the absorption coefficient at closely spaced points along the spectrum (e.g., every .01 cm^{-1}) and at the temperature, pressure, and mixing

ratio conditions appropriately spaced along the photon path, and then perform the appropriate integrations. However, by making use of the fact that water vapor is not uniformly mixed in the atmosphere, we can apply approximations that greatly shorten the computing time and still maintain high accuracy in the final results.

Because the water vapor mixing ratio decreases sharply with height, the region of the atmosphere which contributes to the radiative terms involving water vapor is limited to a relatively narrow layer in the troposphere. This makes it possible to choose a reference pressure and temperature (fixed once and for all) at which to compute the absorption coefficient as a function of wave number and to account for variations of temperature and pressure along the atmospheric path by a function independent of wave number. This separation of variables allows us to write the absorption coefficient as

$$k_\nu(p, T) = k_\nu(p_o, T_o)\left[\frac{pq}{p_o q_o} R(T, T_o)\right] \qquad (2)$$

where p, T, and q are the pressure, temperature, and mixing ratio, respectively, with the subscript o denoting reference conditions. The function $R(T, T_o)$ would be a function of wave number and pressure, if no approximations are made. However, if we make the approximation that the pressure and temperature dependence is governed by the wings of the absorption lines, then it follows that the absorption coefficient is simply proportional to pressure, as expressed in Eq. (2). This leaves us with a function which would depend upon wave number and temperature, but we make the additional approximation that one can use the mean value of that function over the spectral interval under consideration. As a result of these two approximations, $R(T, T_o)$ is a function of only a single variable, T; it is readily pre-computed from the line parameters for any spectral region, at appropriately spaced intervals of temperature, and stored for future use.

The calculation of transmittance, which is the underlying function for calculating the radiative terms in any application, is greatly simplified by Eq. (2) but it is still time consuming because of the many wave number points at which $k_\nu(p_o, T_o)$ is computed. We simplify matters further by making use of the k-distribution method (Arking and Grossman, 1972) which makes use of the fact that for homogeneous pressure and temperature conditions, the transmittance depends only upon the distribution of the absorption coefficient k within the spectral interval and not upon its order within the spectral interval. Hence, instead of storing 2000 values of $k_\nu(p_o, T_o)$ for a 20 cm^{-1} wave number interval, we need only store about 20 numbers to represent the distribution function, saving a factor of 100 in storage and related computations.

The accuracy of the method presented here is illustrated in Figure 2, where it is applied to the calculation of the rate of loss of thermal radiation energy in the water vapor spectral bands, for a typical tropical atmosphere. This is the kind of calculation that must be done repetitively in a climate model or a general circulation model. The graph on the left hand side shows the "exact" or line by line calculations of the energy loss (i.e., cooling rate) as a function of pressure; the solid line shows the total cooling rate and the various broken lines show how different layers in the atmosphere radiate in different portions of the water vapor spectrum. The curve labelled "new model" in the graph on the right shows the accuracy of our model, relative to the line by line calculations. For comparison, we show also the accuracy of the Goody model, which was used in the calculations of Rodgers and Walshaw (1966) and is currently used in a number of atmospheric models, including the Goddard general circulation model. Also shown is the error that would be made if one ignored the temperature dependence along the atmospheric path; this is one of the approximations made by Sasamori (1968), the method currently used in the NCAR general circulation model. The maximum error in the new model is about half that of the commonly used models. In addition, the computing time is several times faster than the Goody model.

Conclusions

We have presented two new methods for calculating radiative terms in numerical atmospheric models and in remote sensing applications. In the examples shown here, they are found to be significantly more accurate than the methods in common use. The improvement in the accuracy of calculated transmittance is a factor between two and three, and in calculated radiances and cooling rates a factor between two and seven. The methods are fast enough so that they can be used in general circulation models and in processing remote sounding data without posing an unreasonable burden on computing resources; in fact, for some general circulation models, introduction of the new methods will significantly reduce computer time.

References

Abel, P., W.L. Smith, and A. Arking, 1976: An empirical model for atmospheric transmittance functions and its application to the Nimbus 6 HIRS experiment. Submitted for publication.

Arking, A., and K. Grossman, 1972: The influence of line shape and band structure on temperatures in planetary atmospheres. J. Atmos. Sci. 29, 937-949.

McClatchey, R.A., W.S. Benedict, S A. Clough, D.E. Burch, R.F. Calfee, K. Fox, L.S. Rothman, and J.S. Garing, 1973: AFCRL atmospheric absorption line parameters compilation. AFCRL Environmental Res. Paper No. 434, AFCRL-TR-73-0096.

McMillin, L.M., and H.E. Fleming, 1976: Atmospheric transmittance of an absorbing gas: a computationally fast and accurate transmittance model for absorbing gases with constant mixing ratios in inhomogeneous atmospheres. Appl. Opt. 15, 358-363.

Rodgers, C. D., and C.D. Walshaw, 1966: The computation of infrared cooling rate in planetary atmospheres. Quart. J. Roy. Meteor. Soc. 92, 67-92.

Sasamori, T., 1968: The radiative cooling calculation for application to general circulation experiments. J. Appl. Meteor. 7, 721-729.

Weinreb, M.P., and A.C. Neuendorfer, 1975: Method to apply homogeneous-path transmittance models to inhomogeneous atmospheres. J. Atmos. Sci. 30, 662-666.

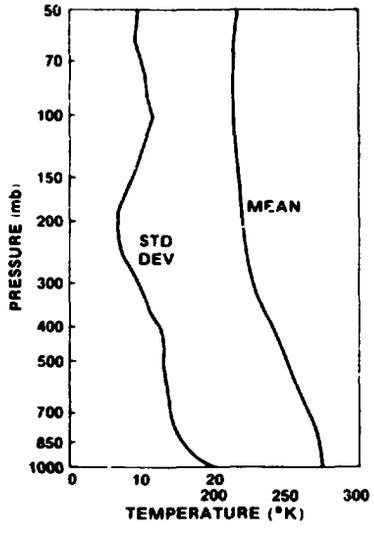

a

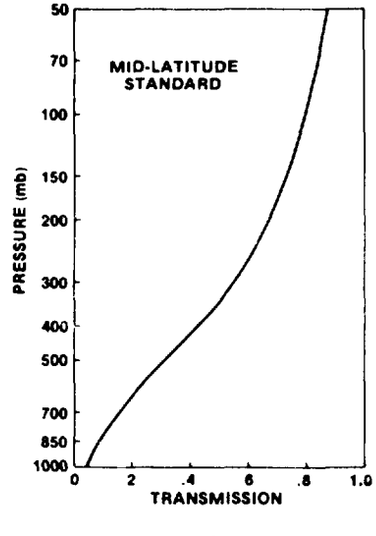

b

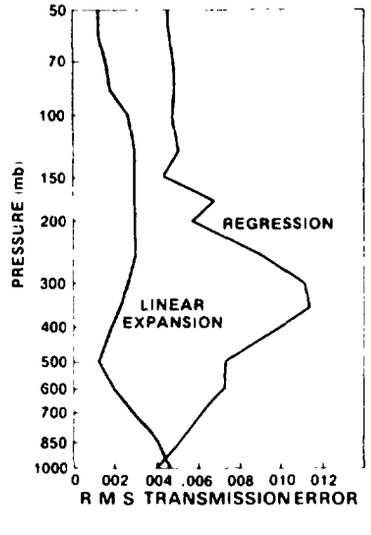

c

	METHOD	ERROR MEAN	RMS	MAX
TRANSMISSION	1	.006	.013	-.030
	2	-.002	.005	-.011
RADIANCE (K)	1	-.14	.39	-.87
	2	.02	.05	-.14

d

Figure 1: (a) The mean and standard deviation of the sample set of 11 temperature profiles selected to test the methods for calculating atmospheric transmittance. (b) Transmittance calculated "exactly" for the U.S. Standard Atmosphere. (c) The RMS "error" or RMS of the difference in calculated transmittance between the exact method and the approximate methods discussed in the text. (d) A table showing the mean, RMS, and the maximum errors, over the sample set, of the calculated transmittance at the level of maximum error and of the calculated radiance at satellite altitude, expressed as brightness temperature.

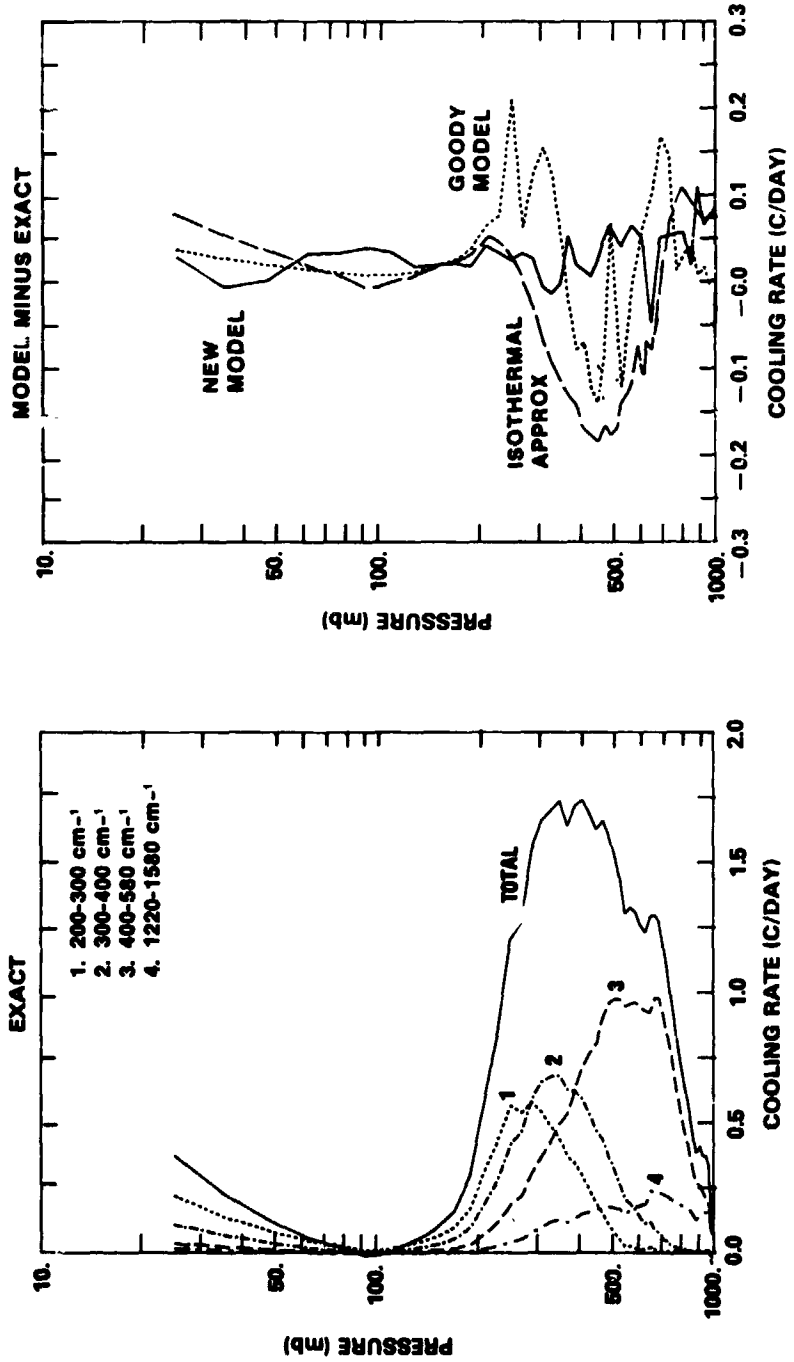

Figure 2: The rate of loss of thermal radiation energy in the water vapor spectral bands, expressed as a cooling rate. The "exact" line by line calculation is shown in (a) and the differences with respect to various approximations is shown in (b).

Paper No. 36

PREDICTABILITY OF CLIMATE WITH SPECIAL REFERENCE TO MONSOON CIRCULATION

J. Shukla and J. Charney, *Massachusetts Institute of Technology, Cambridge, Mass.*

(No paper received.)

Paper No. 37

N79-20610

MOLECULAR MODEL OF ICE NUCLEATION

Dr. P. L. M. Plummer and Dr. B. N. Hale, *Graduate Center for Cloud Physics Research, University of Missouri-Rolla, Rolla, Missouri*

ABSTRACT

Two complementary techniques, semi-empirical quantum mechanical calculations and empirical central field pair potential calculations have been used in developing a model of the interaction of water with simple surfaces.

During the period July 1976, to October 1977, much progress was made toward modeling the interaction of water with simple surfaces. Two complementary techniques were used, semi-empirical quantum mechanical calculations and an empirical central field pair potential calculations. The first has the advantage of being able to give an accurate description of the 'local' level of the interaction of water monomers with surface atoms or molecules. Potential energy curves, electron density plots, vibrational frequencies, binding energies and estimates of static diffusion rates and residence times can be made. However, this approach cannot examine effects on the monomer-surface interaction which are due to the extended nature of the surface since only a small number of molecules can be used to represent the surface because of the complexity of the calculations. On the other hand, the central field pair potential calculations can be used to describe long range effects of the surface on the monomer surface interactions. By calibrating the local properties predicted by the pair potential model with the results of the quantum mechanical calculations, a much more accurate description of the interaction can be obtained than by the use of either technique alone.

A comparison of the preliminary results for water-ice I_h surface obtained by the two methods was given in the publication "Models for Water and Ice Clusters on Simple Surfaces", Colloid and Interface Science, Vol II, 45 (1976). The binding energies obtained for both models were in the range of -6.8 to -9.2 kcal/mole for the basal plane of ice I_h. The techniques differed as to whether the epitaxial or interstitial sites were more stable, but both gave about the same potential barriers between surface sites and similar residence times and diffusion rates.

These preliminary results were expanded and reported in more detail in two publications, "The Water Monomer on the

Basal Plane or Ice I_h An Effective Pair Central Force Potential Model of the Static Interaction" J. Chem. Phys., Oct. 1, 1977 and "Molecular Orbital Calculations of Water-Ice Surface Interactions", J. Glaciology, July, 1978. In the first publication, the results of calculations of water monomer interactions with three different proton configurations of the basal ice surface were reported. Computer generated potential energy surfaces such as the one shown in Fig. 1 were calculated. A fifty molecule aggregate was used to represent the ice surface. The most stable bonding configurations were found to be epitaxial positions for the all 'proton up' surface but interstitial for the all 'proton down' or alternating surfaces. Several possible 'paths' across the surface were investigated and monomer dipole orientation and height above the surface were calculated. The residence time and the mean path length estimated from these calculations were 7×10^{-6} sec and 0.5 microns respectively.

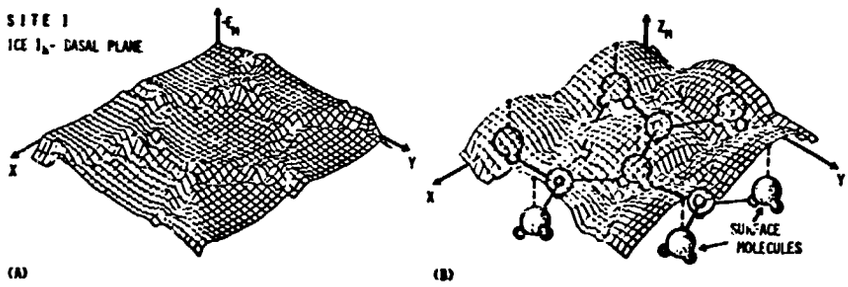

Fig. 1. (a) The minimal potential energy - E_M of the water monomer adsorbed on Site I of the basal plane of ice I_h. E_M is defined to be the optimal binding energy of the adsorbed monomer. The horizontal grid lines are 0.25 Å apart when projected onto the x-y plane. (b) The monomer-ice surface separation Z_M for the optimal monomer binding energy indicated in part (a) above. The x-y scale is the same as in (a). The ice surface molecules are represented schematically beneath the Z_M contour; the small solid circles indicate proton positions. Unshaded molecules are in the second layer.

J. Chem. Phys., Vol. 67, No. 7,1 October 1977

The central force model has also been used to investigate the interaction of water with the basal plane of AgI. Preliminary results of these calculations were reported in "The Water Monomer on the Basal Planes of Ice and AgI: An Effective Pair Potential Study", Proceedings of the IX International Conference on Atmospheric Aerosols, Condensation and Ice Nuclei, Galway, Ireland, Pergamon Press, Oxford (1978). These studies

together with the investigation of the effects of ledges and vacancies in the ice surface are continuing.

In the report of the quantum mechanical studies of the monomer-ice surface interaction, thirteen water molecules were used to represent the surface of ice I_h. These calculations included all valance electrons and were sufficiently extensive to permit 3rd nearest neighbor interactions to be included. Four different possible bonding sites on the basal face and two on the prism face were examined. Binding energies for the 'primary sites' were approximately the same for both faces, $\sim$-8 kcal/mole. These sites were epitaxial and the surface protons alternated in and out of the plane for both faces. It was felt that such an arrangement of protons produced a more "average" environment for an approaching monomer than did a highly polarized site. The interstitial positions had binding energies which ranged from 50 to 85 percent of the primary sites. For this arrangement of protons it appeared that while the stability of the primary sites was approximately the same for the two crystal faces, the interstitial or non-epitaxial sites were much more stable on the basal surface. Electron density maps such as that shown in Fig. 2 were generated for both surfaces. The mean residence time and path length estimated from these calculations were 7×10^{-7} sec and 0.12 microns respectively.

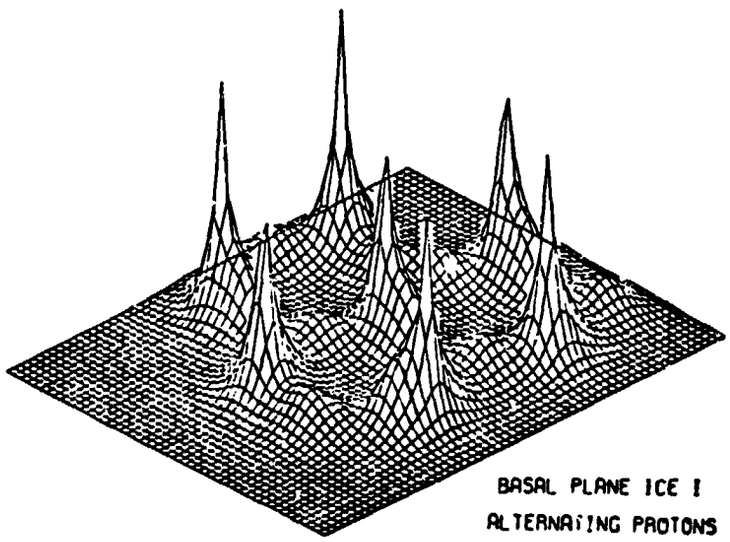

Fig. 2. Electron Density Map

In addition to the neutral ice surfaces, ion-pair defects and isolated ion defects were introduced into the basal ice surface. It was found that for defect pairs in an unrelaxed surface the effect is to increase the monomer surface interaction by about a factor of three, from -8 kcal/mole to -24 kcal/mole. The principal difference between a negatively or positively charged surface site was an increase in the barrier to rotation for the negative site. When the ion defect pair was separated, the monomer surface interaction increased by approximately 50%, to a value greater than the free ion-water interaction. The study of the ion defects is continuing and configurational defects such as L- and D- defects are in progress.

The quantum mechanical approach has also been used to study the water-graphite surface interaction. Preliminary results of these calculations were reported in "Properties of Active Ice Nuclei: Theoretical Studies of Water-Surface Interactions", Proceedings of the Galway Conference, Pergamon Press, Oxford (1978).

In addition to these studies of water-surface interactions, molecular dynamics calculations for small aggregates of water molecules has been underway. Preliminary results for a twenty molecule cluster using the central force potential was reported at the Galway Conference, "Stability and Structure of Pre-nucleation Embryos: A Molecular Dynamics Study of Water Clusters", Pergamon Press, Oxford (1978). The techniques developed in these studies will be used to model the relaxation of the ice surface, both with and without defects and to investigate the kinetics of the monomer surface interaction.

In summary, several of the studies begun under this contract have come to fruition during this past year and will appear in the literature shortly. The experience gained in these studies has enabled the development of new and/or extended techniques and will enhance the continued study of the complex process of ice nucleation and crystal growth.

Paper No. 38

N79-20611

ATMOSPHERIC VARIABILITY EXPERIMENTS (AVE) AND MESOSCALE STRUCTURE

Robert E. Turner and Kelly Hill, *Marshall Space Flight Center, Huntsville, Alabama*

ABSTRACT

Information is presented on accuracy and resolution of AVE data sets.

INTRODUCTION

The NASA Atmospheric Variability Experiment (AVE) was developed to acquire appropriate data with which to conduct research on mesoscale systems. Special emphasis has been placed on studies which involve the processes associated with the onset and development of severe storms systems. Objectives of the AVE research program are: (1) to evaluate the accuracy and representativeness of quantitative satellite data relative to their application to mesoscale interpretations; (2) to investigate the variability of atmospheric parameters and systems of a scale smaller than that normally detected from data available at intervals of 12h; (3) to determine interrelationships of all different scales of motion and the association with the development of severe weather; and (4) to provide necessary inputs to improve the development process for numerical mesoscale prediction models.

Experiments have been conducted during eight individual periods utilizing a network of as many as 54 standard rawinsonde stations which acquire data at intervals of every 3h when meteorological conditions were predicted to contain the particular mesoscale systems of interest. Table 1 presents general information about each experiment. This paper presents information for the user relative to the accuracy and resoltuion of the AVE data sets and aspects pertaining to its use in studies requiring space and time continuity.

Mesoscale Structure Revealed by the AVE Data

Analyses of AVE data often concern the variability of important meteorological parameters plotted and

analyzed at individual stations. Actual vertical profiles of the three hourly values of height and wind speed and direction and temperature with time have been analyzed. Time cross sections of wind speed and direction and temperature for each individual station were plotted. Typical average and standard deviation values of the variability on the three hourly scales are seen generally to increase with height, apparently reflecting the increase in the amplitude of large scale features. The question as to what degree these observed tendencies represent real atmospheric variability on short time scale arises. Some degree of confidence can be placed in their reality only if they exceed the changes expected solely because of errors in individual measurements. Tendency uncertainities will depend on the degree of independence of measurement errors at successive observations, and the most appropriate assumption to be made here is uncertain. A reasonable significance criterion would be to require the three hourly changes to exceed errors in individual measurements. On the basis of this criterion, the temperature and height tendencies appear to be only marginally significant on the average, but the standard deviations indicate that occasionally real variability is reflected.

The meteorologist sometimes requires knowledge of atmospheric variables at times intermediate to the standard observation hours. To obtain them, subjective or objective interpolation of the standard observations is necessary. The simplest procedure is linear interpolation. Comparison of actual observations with linearly interpolated values will illustrate another aspect of atmospheric variability on small time scales. The largest difference between actual and interpolated heights (~40 gpm), wind speed (~15ms^{-1}), wind direction (~20 degree), and temperature (~6^{o}Celsius) are found between the 0000GMT on one day to 0000 GMT the next day of the experiment. Are these differences significant? Noting that the interpolated values will also be in error, a reasonable significance criterion is to require that the differences exceed double the observational uncertainity. On this basis, one would say that, to within limits determined by observational error, linear interpolation satisfactorily explains the variability in the height field, but only to a small degree in the other parameters.

These results, however, cannot be taken as a generality as it is apparent that the degree to which linear, or any, interpolation can explain observed variability is, in part, fortuitous. While the 12

hourly data happen to roughly delineate the large scale height variation, they do not at all describe that in the wind speed. In this latter case, no manner of interpolation would satisfactorily depict the true variation if based only on the standard observations. If the standard hours of observation were three hours earlier, however, a large part of the variability in the wind speed could be represented by linear interpolation. It can also be seen in the graphs that at certain levels and times, when there is little large scale variability, significant fluctuations exist on smaller scales which could frustrate one's best efforts at meaningful interpolation.

Previous analyses have shown that significant variability exists on small time scales. A scan of the data graphs shows that much of the three hourly variability is related to the movement of a large scale trough, but significant oscillations of higher frequency are also evident. The question of whether these reflect the passage of organized systems of small scale arises. Kreitzberg and Brown (1), using 90 minute sounding data from a meso-network of stations, found such oscillations to possess space and time continuity. They associate them with mesoscale features in the 200 to 500 kilometer wavelength range.

To illustrate the relationship of temporal variability and mesoscale systems in the lower troposphere, time cross sections of the thermal and wind field over the experiment area were analyzed in graph form. Observations were available every three hours. The analyses were constructed from the 25 millibar data, the location of which at each observation time is indicated by the vertical profile. The isopleth intervals were 4^{o} Kelvin in the thermal field and 10 meters per second and 10 degrees in the wind speed and direction fields.

Each of the fields display undulations and centers of maxima and minima on scales seldom revealed to the meteorologist. Many of these features have periods of at least three hours and receive independent confirmation from at least two consecutive observations. Much of the detail involved in the analyses on the basis of single observations cannot be discounted entirely as due to observational uncertainity, but indicates the presence of features on scales smaller than those clearly resolved by the data.

In the AVE wind data the short term variability at some levels and times acquires magnitudes similar

to those discussed above. Certainly the most spectacular changes would be observed in the wind direction in the first 1 or 2 kilometers. It appears that 1 kilometer is a characteristic vertical wavelength of the features displayed in the time sections so that one might expect appreciable differences in the variability over such depths.

Wind profiles in the lower stratosphere are found to contain considerable detail most notably of features with vertical wavelengths of ½ to 2 kilometers. Several soundings at single stations have shown these features to maintain their identity for periods ranging from several hours to perhaps as long as a day according to Weinstein, Reiter and Scoggins (2). These same authors feel that the perturbations are best explained as manifestations of passing inertial waves, while Danielsen (3), has found theoretical support for the idea that they are related to waves of the shear gravity or inertial gravity types. The high time resoltuion and spatial extensiveness of the experiment data presents the opportunity to study these wind features to the degree necessary to resolve their origin.

Some spatial aspects of these features have received attention. Examination of the wind data between selected stations, by means of profiles and cross section, revealed that three wind maxima identifiable arrive at one station approximately 12 hours after their appearance at the other one. One might then infer a wavelength of about 600 kilometers (twice the distance between the stations), the term is being used somewhat cautiously since the shape and orientation of the mesojet are unknown. However, Kreitzberg's (1) estimates of the scale of these features parallel to and across the mean flow bracket this value, and also indicate the orientation to be along the flow. The shape and orientation of these features as suggested by Kreitzberg's study together with the observations made seem consistent with the general direction of movement along that of the mean flow from west to east. It does appear that the AVE winds will prove valuable in more extensive studies of these mesoscale wind features.

Conclusions

It is apparent that the investigations of atmospheric variability and structure using the unique data of the AVE experiments are far from exhaustive. They do indicate that much of the value awaits the detailed depiction of atmospheric structure with these data.

The application of dynamic and numeric methods or models should aid in the understanding and description of the physical mechanisms responsible for and associated with the mesoscale features. These in turn will indicate the proper approaches to prognostic techniques for prediction of various atmospheric parameters.

REFERENCES

Kreitzberg, C. W. and H. A. Brown, Mesoscale Weather Systems within an Occlusion, Journal of Applied Meteorology, Vol. 9, pp 417-432, 1970.

Weinstein, A. L., E. R. Reiter, and J. R. Scoggins, Mesoscale Structure of 11-20km Winds, Journal of Applied Meteorology, Vol. 5, pp. 49-57, 1966.

Danielsen, E. F., The Laminar Structure of the Atmosphere and Its Relation to the Concept of a Tropopause, Journal of Meteorology and Geophysics, Vol. 3, pp 292-332, 1959.

TABLE 1. SUMMARY OF NASA'S AVE AND AVSSE* EXPERIMENTS

Experiment	Date	Observation Times, GMT	Experiment Size and Location
AVE 1	19-22 Feb. 1964		31 rawinsonde stations in 18 states
	19	00,03,06,09,12,15,18,21	
	20	00,03,06,09,12,15,18,21	
	21	00,03,06,09,12,15,18,21	
	22	00,03,06,09,12,15,18,21	
	23	00	
AVE 2	11-12 May 1974		54 rawinsonde stations encompassing most of the states east of 105°W.
	11	12,15,18,21	
	12	00,03,06,09,12	
AVE 3	6-7 Feb. 1975		41 rawinsonde stations covering most of the states east of 105°W.
	6	00,06,12,15,18,21	
		00,06,12	
AVE 4	24-25 Apr. 1975		42 rawinsonde stations were used within the same area as AVE 3.
	24	00,06,12,15,18,21	
AVSSE 1	27-28 Apr. 1975		24 rawinsonde stations were used that covered parts of 13 southwestern and southern states.
	27	12,15,18,21	
		00,03,12	
AVSSE 2	6-7 May 1975		23 rawinsonde stations covering almost the same area as AVSSE 1.
	6	12,15,18,21	
	7	00,03,12	
AVE 5	11-12 Jun. 1976		23 rawinsonde stations in 15 of the north-central states.
	11	00,12,15,18,21	
	12	00,03,12	
AVE 6	27-28 May 1977		22 rawinsonde stations in the Great Plains and Mississippi Valley.
	27	00,12,15,18,21	
	28	00,03,12	

*Atmospheric Variability and Severe Storms Experiment (Same as AVE)

Paper No. 39

MECHANISMS OF THUNDERSTORM RELATED TO MOTION AND SEVERITY

J. R. Connell, *University of Tennessee Space Institute, Tullahoma, Tennessee*

ABSTRACT

A research program has been undertaken to better understand the relation of vertical shear of the horizontal wind in the environment and of momentum exchange to thunderstorm motion and intensity.

INTRODUCTION

While positive and negative buoyancy forces due to several causes are very important to thunderstorm dynamics, this study focuses upon the dynamics resulting from the exchange of momentum between the cloud layer environmental air and the updrafts which carry the subcloud inflow-updraft momentum into the cloud layer.

Two phenomena of importance have been observed clearly enough by several means as reported in the literature: (1) vortex pairs (possibly trains) due to interaction like that of a jet in a crossflow and (2) penetrating downdrafts to the ground from middle level intrusion. Figure 1a shows a result from a fluid laboratory and Figure 1b shows a result from dual-doppler radar measurements of a thunderstorm airflow. The force distributions from these effects are such that additional forcing of updraft in specific locations could modify the intensity and motion of a thunderstorm. Also vertical vorticity is generated by these effects such that they can be considered to contribute to tornado dynamics.

The present study is directed at interpreting high-resolution-rawinsonde wind data from AVE IV. It uses a simple model of wind shear effect in each of a set of "critical" sublayers of the cloud layer. The product is a shear index number whose magnitude is modeled to increase if a storm is to be more intense. The velocity of motion of the storm is modeled such that it is objectively selected from a

large number of variations around the cloud layer mean wind velocity as part of the process of selecting the largest shear index, SI, computed for the sounding. It should be pointed out that no solution of equations of motion is involved in the model application.

An "eleven-layer" model has been used as shown in Figure 2. The model is basically a hypothetical one which derives two parts from observations: (1) the choices for size and location of the eleven layers and (2) the choice of the precise analytical form of the index of storm intensity, ESI; comprised of a wind shear index, SI and a total energy difference index, EI.

A severe event is defined here as a wind over 25 m s^{-1}(W), hailstorm over 1 cm in size (H) or a tornado (T). Figure 3 is a map of the detected severe events of AVE IV.

The details of the model application to thunderstorm prediction are given for a 6-layer model in NASA CR-150220. The soundings are considered in three categories using time and space together: (1) proximity, (2) precedence and (3) non-proximity.

CURRENT RESULTS

The original 6-layer ESI model proved better than SPOT index and was as good as SWEAT index except that there was a rather large false alarm area, See Figures 4 and 5 for the 0600 24 March conditions. The 11-layer ESI improved somewhat upon the 6-layer ESI. (See the solid isopleths on Figure 6 . A further criterion was applied to model the cumulus inhibiting influence of a low-level but non-surface dry layer. This resulted in reduction of the false alarm area drastically.

Three difficulties remain. The use of the model for prediction from three hours or greater away from event time has not been successful. A small false alarm area in Texas has not been removed. Finally a check on the cause and effect relation between storms and the water vapor profiles used for reduction of false alarm must be made.

CONTINUING WORK

The 11-layer model is being improved to include a variable pressure height of cloud base and a corresponding adjustment of the height of the eleven layers.

This will better locate the level of wind shear effect on the updraft relative to the cloud base and the inflow layer to the cloud.

A considerable simplification and saving of computer time is being implemented with regard to the prediction of storm velocity. Instead of a scheme of selecting by maximum SI from many model guesses of storm velocity, a correlation between the radar-observed motion of storms and vector wind differences in different layers of the air will be used to develop a three-step one shot prediction.

A mesoscale analysis is being produced so that 3-hour radiosonde data may be advected layer by layer to reconstruct fictitious estimates of vertical soundings in data sparse regions. This is intended to provide a test of improved predictability by the 11-layer model for smaller regions.

FUTURE WORK

A. Without additional measurements in the right places around thunderstorms or suitable 3-dimensional simulations of the significant processes by numerical or fluid laboratory studies, only a small number of reasonably effective efforts can be undertaken for continuation of this present approach. The author is beginning a 3-D numerical simulation program using a tested scheme developed and provided by Los Alamos Scientific Laboratory. A second simulation using a water tunnel has been quite successful for studies of a jet in a uniform crossflow at the U.T. Space Institute. Additional studies are proposed which would focus on the dynamic effects of vertical shear of wind as it relates to thunderstorm-geometry updrafts in wind shears.

B. Another approach to understanding thunderstorm motion and severity is to use satellite imagery. New methods of looking at precursor conditions seem to be needed and to be possible. In brief, one method is to make an analysis of cloud top temperature topography intended to sort out small wave motions having characteristic speeds and directions in relation to thunderstorms. This is somewhat like earlier successful analyses of ocean wave vectors across the Pacific by statistical and Fourier analysis methods.

LIST OF FIGURES

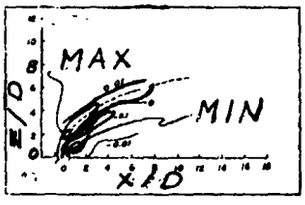

1(a) left.

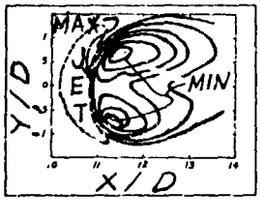

1(a) right.

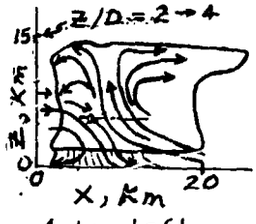

1(b) left.

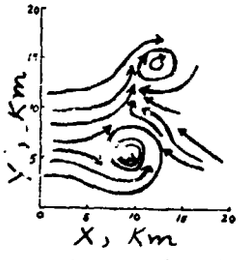

1(b) right.

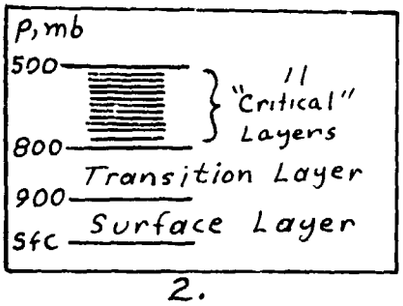

2.

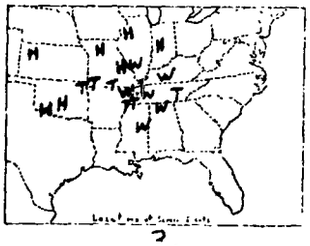

3.

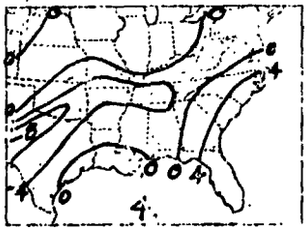

4.

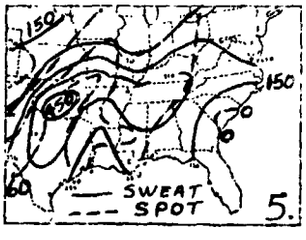

5.

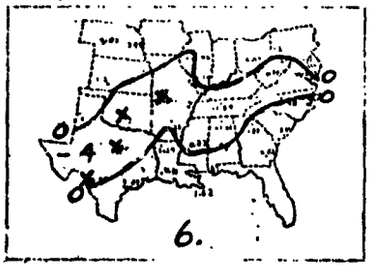

6.

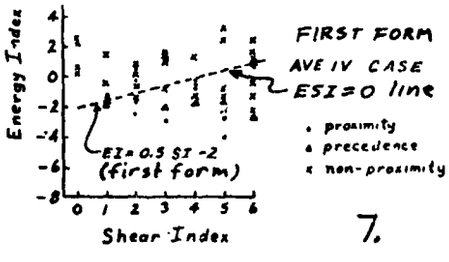

7.

Paper No. 40

GENERAL SOLUTIONS FOR THE MOVEMENT OF STORMS

Robert C. Costen, *Langley Research Center, Hampton, Virginia*

ABSTRACT

Diagnostic solutions are presented for the displacement velocity of a storm vortex and the velocity of the centroid of the storm's convection.

INTRODUCTION

The purpose of this paper is to present general solutions for the movement of hurricanes and severe local storms including effects of propagation. These storms are treated as finite disturbances in the fluid velocity field $\vec{v}(\vec{r},t)$, which satisfies the momentum equation in the general form

$$\frac{\partial \vec{v}}{\partial t} + \vec{f} = 0 \tag{1}$$

where $\vec{f}(\vec{r},t)$ represents the remaining terms, including the pressure, viscous, geopotential, and Coriolis terms. The form of equation (1) emphasizes the generality of this approach. Other equations in physics and mechanics also have the same form and may be treated similarly. The vorticity and divergence equations are given by

$$\frac{\partial \vec{c}}{\partial t} + \text{curl } \vec{f} = 0 \tag{2}$$

and

$$\frac{\partial D}{\partial t} + \text{div}_3 \vec{f} = 0 \tag{3}$$

where $\vec{c} = \text{curl } \vec{v}$ and $D = \text{div}_3 \vec{v}$. The reason for including D is that it has a direct correspondence to convection.

A "disturbance" is defined by $\partial\vec{v}/\partial t \neq 0$; the disturbance may consist of a $\vec{c}$-disturbance ($\partial\vec{c}/\partial t \neq 0$), or a D-disturbance ($\partial D/\partial t \neq 0$), or both. These two disturbances are distinct, although they may intersect in $(\vec{r},t)$. A $\vec{c}$-disturbance is termed a "local" $\vec{c}$-disturbance if it is surrounded by a layer of finite thickness wherein $\partial\vec{c}/\partial t = \text{curl } \vec{f} = 0$; similarly, a D-disturbance is local if it is surrounded by a layer of finite thickness wherein $\partial D/\partial t = \text{div}_3 \vec{f} = 0$.

Hurricanes and severe local storms are good approximations to local disturbances as defined above, for these storms are surrounded by regions of relative quiescence. Our approach to finding solutions for the movement of these disturbances is (a) to derive general equations for the displacement velocity of vortex lines and the velocity of divergence elements, and (b) to integrate these equations over their respective volumes of local disturbance and thus obtain the displacement velocity of the storm vortex and the velocity of the centroid of convection. Although the derivations are omitted, the principal results are presented and discussed in the following sections.

Equation for the Displacement Velocity of Vortex Lines-The displacement velocity of vortex lines is denoted by $\vec{U}(\vec{r},t)$ and satisfies the equation

$$\vec{U} \times \vec{c} + \vec{f} = \text{grad } \phi \tag{4}$$

where $\phi(\vec{r},t)$ is an arbitrary scalar field. Equation (4) implies that the circulation of $\vec{v}$ about arbitrary circuits that move with velocity $\vec{U}$ is conserved; i.e.,

$$\frac{d}{dt} \oint \vec{v} \cdot d\vec{\gamma} = 0 \tag{5}$$

where γ is an arbitrary circuit that is taken to be moving with velocity $\vec{U}_\gamma$ where $\vec{U}_\gamma$ is, in general, distinct from the fluid velocity $\vec{v}$. Since $\oint \vec{v} \cdot d\gamma$ is purely a function of t, it is appropriate to take its total time derivative. The differential form of the equation for conservation of circulation is given by

$$\frac{\partial \vec{c}}{\partial t} - \text{curl}(\vec{U} \times \vec{c}) = 0 \tag{6}$$

which is consistent with equations (2) and (4). Equation (4) was previously derived by the author and solved for the drift of buoyant-core vortices. Equations (5) and (6) are generalizations of equations originally obtained by Helmholtz and Kelvin for idealized fluids and circuits that were restricted to move with the fluid velocity $\vec{v}$.

Equation for the Velocity of Divergence Elements- The velocity of divergence elements is denoted by $\vec{W}(\vec{r},t)$ and satisfies the equation

$$-D\vec{W} + \vec{f} = \text{curl } \vec{A} \tag{7}$$

where $\vec{A}(\vec{r},t)$ is an arbitrary vector field. Equation (7) implies that the efflux of $\vec{v}$ through arbitrary closed surfaces σ that move with velocity $\vec{W}$ is conserved; i.e.,

$$\frac{d}{dt}\oiint \vec{v} \cdot \hat{n} d\sigma = 0 \tag{8}$$

where σ is an arbitrary closed surface (with outward unit normal $\hat{n}$) that is taken to be moving with velocity $\vec{W}$, where $\vec{W}$ is, in general, distinct from the fluid velocity $\vec{v}$ and from $\vec{U}$. The differential form of this equation for the conservation of efflux is given by

$$\frac{\partial D}{\partial t} + \mathrm{div}_3 D\vec{W} = 0 \tag{9}$$

which is also consistent with equations (3) and (7). Equation (9) has the character of Maxwell's equation for the conservation of electric charge with $D\vec{W}$ as the current. This current may be definite at points where D vanishes, thus permitting D to change sign, since the magnitude of $\vec{W}$ is not bounded by physical constraints. Similar comments apply to $\vec{U}$ and $\vec{c}$ in equation (6).

Displacement Velocity of a Storm Vortex- In this section the divergence field may be arbitrarily disturbed; however, disturbances in the vorticity field are assumed to be contained in some volume V of the atmosphere, where S is the closed bounding surface and $\hat{n}$ its outward unit normal. The equations that apply in the exterior region are

$$\left.\begin{aligned} \frac{\partial \vec{c}}{\partial t} = \mathrm{curl}\ \vec{f} = 0 \\ \vec{f} = \mathrm{grad}\ \xi \end{aligned}\right\} \quad \text{(on/outside } S\text{)} \tag{10}$$

The displacement velocity of this local vorticity disturbance (storm vortex) is given by

$$\vec{R}_G = -\frac{\vec{G}}{G^2} \times \iiint (\vec{f} - \vec{g}) dV \tag{11}$$

where $\vec{G}$ is termed the gyration of $\vec{v}$ on S and is defined by

$$\vec{G} = \oiint \hat{n} \times \vec{v} dS = \iiint \vec{c} dV \tag{12}$$

where $\vec{R}_G$ is the moment vector of $\vec{G}$ defined by

$$\vec{G} \times \vec{R}_G = \iint \vec{c} \times \vec{r} dV \tag{13}$$

with $\vec{r}$ denoting the position vector, and where $\vec{g}$ is a vector field in V that must be constructed to insure that contributions from the arbitrary field ϕ in equation (4) vanish upon integration. This constructed field has the form

$$\vec{g} = \text{grad}\ \psi \tag{14}$$

where ψ satisfies Laplace's equation

$$\text{div}_3\text{grad}\ \psi = 0 \quad (\text{in } V) \tag{15}$$

with the Dirichlet boundary condition

$$\psi = \xi + \text{const.} \quad (\text{on } S) \tag{16}$$

Velocity of the Centroid of Convection- In this section the vorticity field may be arbitrarily disturbed; however, disturbances in the divergence field are assumed to be contained in some volume V' of the atmosphere, where S' is the closed bounding surface and $\hat{n}$ its outward unit normal. The equations that apply in the exterior region are

$$\frac{\partial D}{\partial t} = \text{div}_3\vec{f} = 0 \quad (\text{on/outside } S') \tag{17}$$

The velocity of this local D-disturbance (identified with the storm's convection) is given by

$$\dot{\vec{R}}_E = E^{-1}\iiint(\vec{f} - \vec{h})dV' \tag{18}$$

where E is the efflux of $\vec{v}$ through S', defined as

$$E = \oiint \vec{v}\cdot\hat{n}dS' = \iiint D dV' \tag{19}$$

where $\vec{R}_E$ is the centroid of E given by

$$\vec{R}_E = E^{-1}\iiint D\vec{r}dV' \tag{20}$$

and where $\vec{h}$ is a vector field in V' that must be constructed to insure that contributions from the arbitrary field $\vec{A}$ in equation (7) vanish upon integration. This constructed field has the form

$$\vec{h} = \text{grad}\ \chi \tag{21}$$

where χ satisfies Laplace's equation

$$\text{div}_3\text{grad}\ \chi = 0 \quad (\text{in } V') \tag{22}$$

with the Neumann boundary condition

$$\frac{\partial\chi}{\partial n} = \hat{n}\cdot\vec{f} \quad (\text{on } S') \tag{23}$$

Discussion- Solutions (11) and (18) allow us to determine diagnostically, from a knowledge of the field $\vec{f}$, the instantaneous displacement velocity of a storm vortex (provided $\vec{G}$ is definite), and the velocity of the storm's centroid of convection (provided E is definite). Since these two velocities obey different equations, the longevity of combined disturbances (severe storms) should depend upon whether $\dot{\vec{R}}_G$ and $\dot{\vec{R}}_E$ approximately concur or strongly diverge.

Paper No. 41

N79-20614

EQUATIONS FOR THE DYNAMICS OF GUST FRONTS AND SHOCK WAVES

Robert C. Costen, *Langley Research Center, Hampton, Virginia*

ABSTRACT

Equations are presented for the growth or decay rates of moving and deforming vortex sheets (gust fronts) and shock waves. The equations exhibit a cross-coupling between these two types of surface discontinuity.

INTRODUCTION

The purpose of this paper is to present equations for the dynamics of moving and deforming vortex sheets (fronts and gust fronts) and shock waves in the atmosphere. The fluid velocity $\vec{v}(\vec{r},t)$ is taken to satisfy the momentum equation written in the general form

$$\frac{\partial \vec{v}}{\partial t} + \vec{f} = 0 \qquad (1)$$

where $\vec{f}(\vec{r},t)$ represents the remaining terms, including pressure, geopotential, viscous, Coriolis, electrodynamic, and source terms. Equation (1) emphasizes the generality of results to be presented, for, besides velocity, $\vec{v}$ could be taken to represent the product of fluid density and velocity, or other vector combinations. The results are also applicable to other vector equations in physics and mechanics that have the same form as equation (1).

Surface of Discontinuity-Take surface S to be a moving and deforming surface of discontinuity with curvature C, unit normal $\hat{n}$ and speed of displacement N, as shown in figure 1, where N is, in general, distinct from $\vec{v}$. The speed of displacement $N > 0$ for motion in the sense of $\hat{n}$, and $C > 0$ for concavity in the sense of $\hat{n}$.

The field $\vec{v}$ is bounded on S but may be discontinuous across it, where the discontinuity in $\vec{v}$ is denoted by

$$[\vec{v}] = \vec{v}^{+} - \vec{v}^{-} \qquad (2)$$

with $+$ signs relative to $\hat{n}$. The field $\vec{f}$ may be discontinuous and unbounded, but must be integrable across S

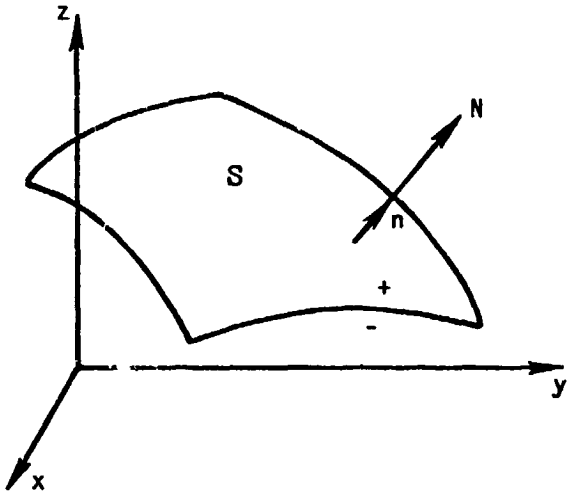

Figure 1.- Moving and deforming surface of discontinuity S with unit normal $\hat{n}$ and speed of displacement N.

$$\vec{F} = \lim_{\varepsilon \to 0} \int_{-\varepsilon}^{\varepsilon} \vec{f} dn \tag{3}$$

where $\vec{F}$ is a surface density in contrast to the volumetric density $\vec{f}$. Equation (1) has the derivative equations

$$\frac{\partial \vec{c}}{\partial t} + \text{curl } \vec{f} = 0 \tag{4}$$

$$\frac{\partial D}{\partial t} + \text{div}_3 \vec{f} = 0 \tag{5}$$

Since $\vec{v}$ is discontinuous and bounded, $\vec{c}$ and D are discontinuous, unbounded, but integrable across S

$$\vec{\zeta} = \hat{n} \times [\vec{v}] = \lim_{\varepsilon \to 0} \int_{-\varepsilon}^{\varepsilon} \vec{c} dn \tag{6}$$

$$\delta = \hat{n} \cdot [\vec{v}] = \lim_{\varepsilon \to 0} \int_{-\varepsilon}^{\varepsilon} D dn \tag{7}$$

where $\vec{\zeta}$ is the discontinuity in tangential velocity across a vortex sheet, and δ is the discontinuity in normal velocity across a shock wave.

Dynamic Equations-In order to obtain dynamic equations for $\vec{\zeta}$ and δ, equations (1), (4), and (5) are integrated over a volume

that moves with the surface S and is bisected by it; the limit is then taken as the normal dimensions of this volume shrink to zero on both sides, and the following equations result:

$$N\,[\vec{v}] = \vec{F} \tag{8}$$

$$\left(\frac{\partial}{\partial t} + N\frac{\partial}{\partial n}\right)\vec{\zeta} = NC\,\vec{\zeta} + N[\vec{c} - \hat{n}c_n] - \hat{n} \times [\vec{f}] + (\vec{\zeta} \cdot \nabla)\,(N\hat{n})$$

$$+ \hat{n} \times \nabla\,(N\delta) \tag{9}$$

$$\left(\frac{\partial}{\partial t} + N\frac{\partial}{\partial n}\right)\delta = NC\,\delta + N[D] - \hat{n} \cdot [\vec{f}] - \hat{n} \cdot \mathrm{curl}(N\vec{\zeta}) \tag{10}$$

where $(\partial/\partial t + N\partial/\partial n)$ is the displacement derivative giving the time rate of change following S, where equation (8) has been applied in equations (9) and (10), and where equation (9) is written for brevity in Cartesian notation. Equation (8), (for $\vec{v}$ taken to represent fluid density times velocity) is one of the Rankine-Hugoniot relations. Equation (10) is similar to a result derived earlier by the author for electric charge and current.

Discussion-Equation (9) enables one to obtain diagnostically the rate of intensification or decay of a gust front from knowledge of its speed of displacement, its curvature, and the conditions ahead of and behind the front. Result (10) similarly applies to shock waves and flame fronts. The last terms of equations (9) and (10) are cross-coupling terms that apply for nonuniform, moving shocks and vortex sheets.

Paper No. 42

STEREOGRAPHIC CLOUD HEIGHTS FROM SMS/GOES IMAGERY

R. A. Minzner, *Goddard Space Flight Center, Greenbelt, Maryland*
W. E. Shenk, *Goddard Space Flight Center, Greenbelt, Maryland*
R. D. Teagle, *Defense Mapping Agency Topographic Center, Wash., DC*
J. Steranka, *General Electric Co., MATSCO, Beltsville, Maryland*

ABSTRACT

Stereographic pairs of SMS/GOES images, generated simultaneously by the spin-scan cameras of each of two geostationary satellites (SMS 1 and SMS 2), separated by 32 dgrees of longitude on February 1, 1975, have been analyzed photogrametrically to yield cloud heights with a two-sigma uncertainty of 500 meters. These cloud heights compare favorably with heights of the same clouds measured by radar and IR methods. The same SMS image pairs were used to measure mountain-top heights with a mean deviation of 0.24 km from cartographic values.

BACKGROUND

The study of tropical cyclones and severe thunderstorms has been greatly enhanced by the availability of imagery of cloud fields observed from geosynchronous satellites such as ATS, SMS, and more recently GOES. The measurements of cloud-motion vectors from successive full-scan images obtained at the normal 30-minute interval by means of the ATS, SMS, and GOES sensors has permitted the inference of general wind fields over extensive portions of the globe, Hubert and Whitney, 1974. Limited-scan images obtained at a repetition rate equal to or less than 7.5 minutes from these satellites has led to more detailed circulation information (Gentry et al., 1976). Accurate cloud-height information applied to the cloud-motion vectors would improve the circulation information and could also benefit the determination of temperature and moisture profiles obtained from radiance sounding measurements. The simultaneous SMS/GOES infrared imagery which yields radiance temperatures of the tops of opaque clouds provides some information regarding the height of these clouds. Because of the limited resolution of the infrared portion of the SMS/GOES imagery and the variable unknown opacity of various clouds, the values of the heights inferred from IR data are subject to large uncertainties. Therefore, some other, more precise methods for cloud-height determination would greatly enhance the utility of SMS/GOES imagery.

METHOD AND RESULTS

The launch of SMS 2 in February, 1976 with an initial subsatellite point of about 107 degrees west longitude, while SMS 1 was located at 75 degrees west, provided an opportunity for generation of pairs of SMS images from which cloud heights might be extracted stereographically. The suggestion of obtaining cloud heights from SMS images was fostered by the success at obtaining cloud heights from photographs obtained during one orbit of the unmanned Apollo-6 satellite (Shenk, 1971; and Shenk et al., 1975.

Stereographic pairs of images were obtained by synchronizing the SMS-2 spin-scan camera with that of SMS 1 so that the northernmost limb of the earth was viewed by both satellites within a few seconds of each other. With this adjustment, both cameras continued to view the same latitude band of the earth within a few seconds of each other over the entire north-to-south stepping of the cameras. Thus, even though it takes 20 minutes for a full-disk image to be generated, the corresponding portions of the images generated by the two cameras represent essentially simultaneous pictures of identical swaths of cloud fields, and thus, these image pairs are suitable for stereographic compilation. The x axis of each image is defined to be parallel to the line between the subsatellite points of the two geostationary satellites.

The 32-degree angle between the image plane of the SMS-1 sensors and that of the SMS-2 sensors, plus the fact that both images represent a transformation of a near hemispherical surface onto a plane surface, caused problems in making the stereographical analysis. A specially designed mechanical-optical instrument provided a solution to these problems. True cloud heights can be deduced by measuring the apparent height of the cloud in the stereo model with the micrometer-controlled reference spot and scaling that model height to true height in accordance with an appropriate algorithm. This algorithm accounts for the curvature of the earth between the sea-level reference point, from which the cloud height is being measured, and the subsatellite point of the more remote satellite. With the aid of these devices, cloud-top heights were measured within a 2-sigma repeatability of about 500 meters (Minzner, et al., 1976; and Teagle, 1976), and cloud fields were contoured over extensive portions of the western hemisphere.

A sample compilation is shown in Figure 1. In this figure, depicting the Gulf of St. Lawrence and surrounding land masses including Nova Scotia, cloud masses are grouped into three height ranges, with the heights of particular features designated in hundreds of meters. The viewpoint of this image is from SMS 2 at 107 degrees west, and the compilation of cloud heights in this image provided the basis for estimating the limits of the region

over which this particular technique of cloud-height stereography is applicable. This limit appears to be about 67 degrees of great-circle arc from the more remote subsatellite point, and permits the definition of the entire region over which the cloud-height stereography is applicable. For the location of the two satellites on February 17, 1975, this region is defined by the gore on the earth's surface depicted in Figure 2.

ACCURACY OF METHOD

The stereographic analysis of an active storm over southeastern United States provided an interesting set of cloud-top heights which in Table 1 are compared with a set of cloud heights obtained by ground-based radar and with a set of cloud heights obtained from satellite-measured infrared radiances. The general agreement and the nature of the mean systematic differences between these sets provides validity to the stereo heights. The radar heights are consistently found to be about one kilometer lower than the stereographic heights, with a mean difference of about -1.16 km and, a standard deviation of 0.83 km. This difference is accountable by the fact that radar echos of clouds represent primarily a reflection from precipitation rather than from the tops of visible clouds, and the upper portion of the cloud usually contains little or no precipitation. The infrared heights also are seen to be consistently lower than the stereographic heights with a mean difference of about -1.455 km and a standard deviation of 0.51 km. Again this difference is explainable by the physics of the infrared emissivity of clouds, whereby the infrared radiance is characteristic of some point within or below the cloud top rather than the top itself.

Further validity was given to these stereographic heights by the comparison of the stereographically measured values of the heights of 16 mountain peaks and one lake surface in the Peruvian Andes, with values published on topographic maps. These results are shown in Table II. These 17 comparisons show the stereo heights to be greater than the map values by a mean value of 0.24 km, with a standard deviation of 0.36 km. These deviations, which suggest a small positive systematic error in the stereo values, represent errors in contour lines on the maps as well as the errors in the stereo measurements. The height of the surface of Lake Titicaca is of special interest since its stereo value was measured relative to a synthetic sea-level plane formed stereographically from two computer-generated grid systems which match the most precisely known shape of the earth.

A few cloud-height measurements made later with an improved version of the special mechanical-optical viewing instrument indicates that the two-sigma repeatability in cloud heights measured with optical-mechanical methods from SMS imagery may be as low as 350 m. A plan for an improved determination of the absolute

accuracy of the stereographic method by comparing stereographic cloud-top heights with cloud-top heights measured by dedicated aircraft has been prepared. This plan is awaiting implementation.

CONCLUSIONS

The work described above demonstrates that stereo imagery from two SMS or GOES satellites may be processed to provide cloud heights with sufficient accuracy for many meteorological purposes. The mechanical optical technique, however, requires the use of hard-copy prints or transparencies, and consequently is not suitable for a real-time or near-real time operation. To circumvent this limitation, a man-interactive computerized method for extracting cloud heights from digital stereo imagery is being investigated.

REFERENCES

Gentry, R. C., E. Rodgers, W. E. Shenk, and V. Oliver, Deriving Winds for Hurricanes Using Short Interval Satellite Imagery, Proceedings of Seventh Conference on Aerospace and Aeronautical Meteorology and Symposium on Remote Sensing from Satellites, Melbourne, Florida, November 16-19, 115-118, 1976.

Hubert, L. F. and L. F. Whitney, Jr., Compatibility of Low-Cloud Vectors and Rawins for Synoptic Scale Analysis NOAA Technical Report, NESS 70, p. 26, 1974. National Oceanographic and Atmospheric Administration, U.S. Department of Commerce, Washington, DC, 1974.

Minzner, R.A., W.E. Shenk, J. Steranka, and R.D. Teagle, Cloud Heights Determined Stereographically from Imagery Recorded Simultaneously by Two Synchronous Meteorological Satellites, SMS 1 and SMS 2, EOS 57, 593, 1976.

Shenk, W. E., Cloud Comparisons between Apollo-6 Photography and ATS-3 and ESSA-3 photography, NASA TN D-6470, p. 47, Goddard Space Flight Center, Greenbelt, Maryland, 1971.

Shenk, W. E., R. J. Holub, and R. A. Neff, Stereographic Cloud Analysis from Apollo-6 Photographs Over a Cold Front, Bull. Amer. Meteor. Soc. 56, 4-16, 1975.

Teagle, R. D., Cloud Heights Determined Stereographically from SMS Imagery, Report of DMATC to Goddard Space Flight Center, p. 29, Greenbelt, Maryland 1976.

TABLE I

COMPARISON OF RADAR- AND IR-DERIVED CLOUD-TOP HEIGHTS WITH STEREOGRAPHICALLY DERIVED VALUES FOR PARTICULAR CLOUDS OVER SOUTHEASTERN U S. AT 1900Z ON FEBRUARY 17, 1975

CLOUD	STEREO H (km)	RADAR h (km)	Δh h-H (km)	IR h (km)	Δh h-H (km)
A	14.0	12.2	-1.8		
B	14.0	12.2	-1.8		
C	14.0	12.2	-1.8		
D	14.7	13.7	-1.0		
E	14.0	13.7	-0.3		
F	15.2	14.0	-1.2	13.0	-2.2
G	14.0	13.1	-0.9	13.0	-1.0
H	14.0	13.7	-0.3	12.25	-1.75
I	14.0	13.7	-0.3	13.0	-1.0
J	14.0	14.0	0.0	13.0	-1.0
K	14.0	13.7	-0.3	13.0	-1.0
L	13.0	----	----	12.2	-0.8
M	12.0	10.1	-1.9	10.1	-1.9
N	13.7	11.3	-2.4	----	----
O	13.0	10.7	-2.3	11.0	-2.0
P	12.0	----	----	10.6	-1.4
Q	12.0	----	----	10.1	-1.9

$\overline{\Delta h}$ = -1.164 km, $\overline{\Delta h}$ = -1.450 km,

σh = 0.853 km, σh = 0.509 km,

Δh = -1.16±0.83 km; Δh = -1.45±0.51 km.

TABLE II

COMPARISON OF STEREOGRAPHICALLY DETERMINED HEIGHTS OF MOUNTAINS AND A LAKE IN THE PERUVIAN ANDES WITH VALUES CITED ON A TOPOGRAPHICAL MAP

POINT	MAP ELEVATION h (km)	SMS STEREO ELEVATION H (km)	Δh H-h (km)
1	6.20	6.35	+ 0.15
2	6.40	6.10	- 0.30
3	6.45	6.35	+ 0.10
4	6.63	6.70	+ 0.07
5	6.10	6.50	+ 0.40
6	5.80	5.95	+ 0.15
7	5.60	6.50	+ 0.90
8	5.90	6.40	+ 0.50
9	6.10	6.25	+ 0.15
10	6.61	6.50	- 0.11
11	6.00	6.30	+ 0.30
12	5.80	5.68	- 0.12
13	5.70	5.60	- 0.11
14	5.90	6.10	+ 0.20
15	5.80	6.80	+ 1.00
16	5.80	6.40	+ 0.60
*	3.81	4.11	+ 0.30

$\overline{\Delta h}$ = 0.236 km

σh = 0.360 km

Δh = 0.24±0.36 km

* Lake Titicaca

FIGURE 1

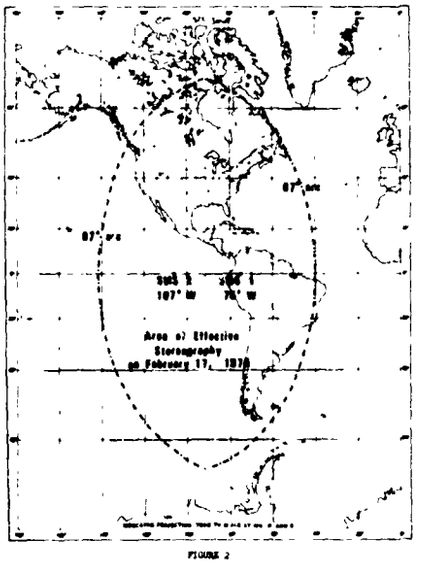

FIGURE 2

Paper No. 43

N79-20616

WIND ESTIMATES FROM CLOUD MOTIONS: RESULTS OF AN IN SITU AIRCRAFT VERIFICATION EXPERIMENT

A. F. Hasler and W. E. Shenk, *NASA/Goddard Space Flight Center*

ABSTRACT

A world wide system of 5 geostationary satellites is being established with a primary objective: the estimation of winds from cloud motions. A series of aircraft experiments has been carried out to perform an in situ verification of the satellite cloud winds, under undisturbed to moderately disturbed oceanic weather regimes. Future experiments will test the cloud motion/wind relationship in severe storm environments and over land. Results to date indicate good agreement ($|\vec{V}_{wind} - \vec{V}_{cloud}| \leq 1.8$ m sec^{-1}) between the cloud motions and the cloud base wind (950 mb) for trade wind cumulus and suppressed cumuli in subtropical high regions. For a small sample of cirrus clouds, the relationship is just as good between the cloud motion and the mean wind in the cloud layer. In high wind frontal regimes the cloud motions compare best to the mean wind in the cloud layer with $|\vec{V}_{wind} - \vec{V}_{cloud}| \leq 2.7$ m sec^{-1}.

INTRODUCTION

An improved method for verification of satellite cloud winds by in situ aircraft wind measurements has been developed. The results using this method are not limited by large differences in time and space between the cloud motions and the wind measurements which limit the validity of other verification techniques used to date (Hasler et al., 1976). Phases I, II, and III of an experiment using this method was performed and described by Hasler et al, (1976, 1977). In Phase I, a small sample of cumulus clouds (6) and one cirrus cloud were tracked by the NCAR Sabreliner in December 1972 in the northwest Caribbean under conditions of moderate winds and moderate vertical wind shear, However, since the sample was too small to have statistical significance, additional phases of the experiment have been conducted to expand the data base. Phase II of the experiment was flown in April 1974 in the southwest Caribbean near Panama. Nineteen low-level clouds were tracked by the NASA C-130 and NCAR Sabreliner under moderate trade wind conditions while four additional cirrus clouds were tracked by the NCAR Sabreliner. Phase III was conducted in July 1974 in the Gulf of Mexico under light wind conditions where 15 low clouds were tracked. Phase IV was accomplished in Jan. - Feb. 1976 in the western Atlantic during high wind baroclinic weather situations near Bermuda which resulted in 25 additional cloud tracking cases. Phase V of the experiment tracked 11 more clouds during February 1977 in the eastern Atlantic under the high wind suppressed convection conditions in the Azores subtropical high. The conditions of the first five phases of the experiment are summerized in Table 1 for the 77 total clouds that have been tracked.

Table 1
Dates, Locations and Conditions for In Situ Verification of Cloud Winds

Phase I	Dec. 1972	Northwest Caribbean (Florida, Puerto Rico)	Moderate Winds ~12 m sec^{-1}
Phase II	April 1974	Southwest Caribbean (Panama)	Moderate Winds ~10 m sec^{-1}
Phase III	July 1974	Gulf of Mexico	Light Winds ~5 m sec^{-1}
Phase IV	Jan. - Feb. 1976	Western Atlantic (Bermuda ~32°N)	High Winds ~17 m sec^{-1}
Phase V	Feb. 1977	Eastern Atlantic (Azores ~38°N)	High Winds ~17 m sec^{-1}

TECHNIQUES

Figure 1 gives an over all view of the experimental procedures used. Hasler et al. (1976, 1977) describe the procedures used to compare aircraft measured cloud motions with winds measured by low level aircraft equipped with inertial navigation systems. The cloud motions have also been measured by tracking clouds on SMS pictures using the Atmospheric and Oceanographic Information Processing System (AOIPS) described by Billingsley (1976) and CSC (1977). Since the clouds were always tracked on a sequence of 1 km resolution SMS pictures of 1 hour or longer, the expected error would be .5 m sec^{-1} according to Hasler and Rodgers (1977). Combining this error with the error in the aircraft wind measurement of 1.4 m sec^{-1} (Kelley and Zruber, 1973) gives a total expected error of 1.5 m sec^{-1} for comparisons of satellite measured cloud motions with aircraft winds.

RESULTS

The aircraft measured cloud motions vs the winds for the 5 phases of the experiment are presented in Table 2. This summary indicates the following: (1) on the average the cloud motions differed from the cloud base (950 mb) winds by less than $|\vec{V}_c - \vec{V}_w| = 1.2 - 1.8$ m sec^{-1} for trade wind cumulus and cumuli in subtropical high weather regimes. (2) The average vector difference between the cloud motion and the mean wind in the cloud layer was 2.7 m sec^{-1} for frontal high-wind high shear (baroclinic) conditions. (3) The average difference between cirrus cloud motions and the mean wind in the cloud layer was 1.6 m sec^{-1}.

Table 3 compares the aircraft cloud tracking results with the same 16 clouds tracked by satellite for Phase IV conducted in the western Atlantic. Although 67% of aircraft tracked cloud motions differ from the satellite cloud motions by 1.8 m sec^{-1} or less, the comparisons between the cloud motions and the winds give substantially the same results by the two methods.

In Table 4 the effects of systematic difference between the satellite measured cloud motions and the winds are presented. The clouds moved systematically only 1.0 m sec^{-1} slower and 1.3° to the left of the mean wind in the cloud layer. These small differences mean that there is little chance of improving the results by subtracting out systematic errors (2.3 m sec^{-1} to 2.2 m sec^{-1}). However, the larger

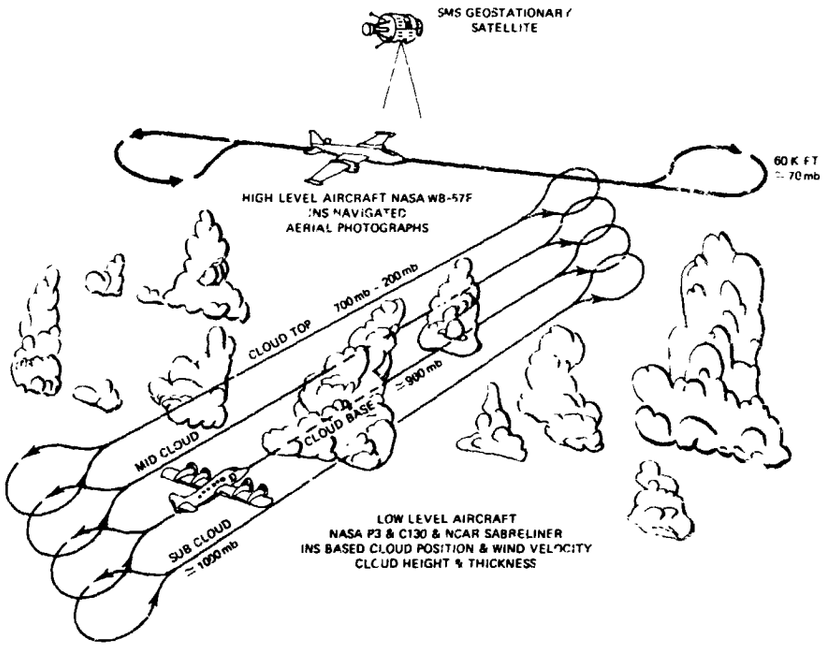

Figure 1. Overall View of Experiment Featuring Aircraft Flight Patterns

Table 2
Wind Estimates from Cloud Motions Phases I-V of an In Situ Aircraft Verification Experiment

	NO. OF CASES	AVE WIND SPEED (m sec⁻¹)	$\vec{V}$ CLOUD − $\vec{V}$ WIND 150m	CLOUD BASE	MID CLOUD	CLOUD TOP	(m sec⁻¹) MEAN IN CLOUD LAYER
1. LOW LEVEL (CUMULUS)							
TROPIC (I, II, & III) G. OF MEXICO & CARRIBEAN 10°-20°N	40	5-12	1 3	1.2	3 1	6 1	
EASTERN ATLANTIC (V) 38°N	7	17	3 6	1 8	5.7	9.4	
WESTERN ATLANTIC (IV) 32 N	25	17	4.3	3.8	2.8	5.5	2 '
TOTAL (CUMULUS)	72						
2. HIGH LEVEL (CIRRUS)	5	11		2.2	2.0	2.8	1.8

systematic differences between the cloud motions and the 150 m wind give some prospect of finding a correction factor, as shown by the improvement of $|\vec{V}_a - \vec{V}_i|$ = 4.1 m sec^{-1} to 2.6 m sec^{-1} when systematic differences are removed.

Table 3
Satellite Cloud Winds vs Aircraft Cloud Winds also Compared with Aircraft INS Winds Western Atlantic (32° N) ; Jan. - Feb. 1976; $\bar{v}$ = 17 m sec^{-1}

$$\left|\vec{V}_{A/C} - \vec{V}_s\right|_{67\%} = 1.8 \text{ m sec}^{-1}$$

	150m	CLOUD BASE	MID CLOUD	CLOUD TOP	MEAN CLOUD
$\left\|\vec{V}_{A/C} - \vec{V}_w\right\|_{67\%}$ (m sec^{-1}) =	3.9	3.8	3.3	6.9	2.9
$\left\|\vec{V}_s - \vec{V}_w\right\|_{67\%}$ (m sec^{-1}) =	4.2	4.1	3.0	4.9	2.5

16 CASES

Table 4
Satellite Cloud Winds vs In Situ Aircraft Winds, Western Atlantic (32°N)
Jan. - Feb. 1976; $\bar{v}$ = 17 m sec^{-1}, Systematic Differences

$\overline{\left\|\vec{V}_s - \vec{V}_I\right\|}$ (m sec^{-1})	150m 4.1	CLOUD BASE 3.6	MID CLOUD 3.0	CLOUD TOP 5.3	MEAN CLOUD 2.3
SYSTEMATIC ΔS SPEED DIFFERENCES (m sec^{-1})	-1.2	.5	.8	2.5	1.0
SYSTEMATIC ΔD DIRECTION DIFFERENCE (DEG)	-8.1	-5.1	3.5	6.5	1.3
SYSTEMATIC DIFFERENCES REMOVED	2.6	2.9	2.9	4.8	2.2

19 CASES

CONCLUSIONS

In trade-wind and subtropical high oceanic weather regimes the 950 mb wind field can be estimated accurately by measuring low level cumulus motions from SMS satellite pictures. Cirrus cloud motions give a good estimate of the mean wind in the cloud layer. In high wind, high shear, baroclinic oceanic frontal regimes low level cumulus cloud motions measured from satellites estimate the mean wind in the cloud layer, but the estimate is not as accurate as for the trade wind and subtropical high regimes.

FUTURE WORK

Although the relationship between cloud motions and the wind has been fairly well established for undisturbed and moderately disturbed conditions, it will require further in situ verification to be able to extrapolate these results to the severe storms environment with confidence. This is especially true for land areas where large vertical shears can exist in a few hundred meters near the top of the boundary layer. In addition more comparisons are needed for cirrus, especially in high wind speed and shear regions like jet streams.

REFERENCES

Billingsley, J. B., 1976: Interactive Image Processing for Meteorological Applications at NASA/Goddard Space Flight Center. In *Preprints of the 7th Conference on Aerospace and Aeronautical Meteorology and Symposium on Remote Sensing from Satellites.* pp. 268-275.

Computer Sciences Corporation, 1977: Atmospheric and Oceanographic Information Processing System Meteorology Package (METPAK) Users Guide, Task Assignment 619, 1-1 to 1-6.

Hasler, A. F., W. Shenk, and W. Skillman, 1976: Wind Estimates from Motions - Phase I of an *In Situ* Aircraft Verification Experiment, *Journal of Applied Meteorology*, V. 15, No. 1, pp. 10-15.

Hasler, A. F., W. E. Shenk, and W. C. Skillman, 1977: Wind Estimates from Cloud Motions: Preliminary Results of Phases I, II, and III of an *In Situ* Aircraft Verification Experiment, *Journal of Applied Meteorology*, V. 16, No. 8, pp. 812-815.

Hasler, A. F., and E. B. Rodgers, 1977: An Error Analysis of Tropical Cyclone Divergence and Vorticity Fields Derived from Satellite Cloud Winds on the Atmospheric and Oceanographic Image Processing Systems (AOIPS) in *Preprint Volume 11th Technical Conference on Hurricanes and Tropical Meteorology*.

Kelley, N. O., and M. N. Zruber, 1973: Instrumentation Aboard the *Electra. Atmos. Tech.*, No. 1, NCAR, 76 pp.

Paper No. 44

AN ERROR ANALYSIS OF TROPICAL CYCLONE DIVERGENCE AND VORTICITY FIELDS DERIVED FROM SATELLITE CLOUD WINDS ON THE ATMOSPHERIC AND OCEANOGRAPHIC INFORMATION PROCESSING SYSTEM (AOIPS)*

A. F. Hasler and E. B. Rodgers, *NASA/Goddard Space Flight Center, Greenbelt, MD.*

ABSTRACT

An advanced Man-Interactive image and data processing system (AOIPS) has been developed at Goddard Space Flight Center to extract basic meteorological parameters from satellite data and to perform further analyses. The errors in the satellite derived cloud wind fields for tropical cyclones are investigated. The propagation of these errors through the AOIPS system and their effects on the analysis of horizontal divergence and relative vorticity are evaluated.

INTRODUCTION

It has been demonstrated by Rodgers et al. (1977) that low level and high level wind fields of tropical cyclones can be estimated with high spatial density from geostationary satellite short interval image sequences. These wind fields were derived from cloud motion measurements made on an advanced interactive image and data processing system (AOIPS) at the Goddard Space Flight Center. The wind fields are objectively analyzed and second order parameters such as horizontal divergence and relative vorticity are computed. The utility of these wind fields and the derived quantities depend on three factors: (1) How accurately the cloud motions are measured, (2) how well the cloud motions represent the wind and (3) the quality of the objective analysis. Suchman and Martin (1976) made an assessment of these factors for GATE data sets, but because of the many variables in measurement and analysis, it is necessary to do an error analysis with respect to each dynamical feature of interest.

Hasler et al. (1976, 1977) have shown that trade wind cumulus cloud motions represent the wind at 950 mb within 1.3 m sec^{-1} with no systematic (only random) differences of significance. Cirrus clouds were shown to differ randomly from the mean wind in the cloud layer by 1.6 m sec^{-1}. While extrapolation of these results to the hurricane environment is somewhat speculative, Rodgers et al. (1977) argue that the small vertical shear observed near the center of hurricanes would allow the low level clouds to move with the wind at cloud base. Comparisons of cloud motions with aircraft penetrations of the hurricane by Rodgers et al. (1977) show an average speed difference of 2.5 m sec^{-1}. However, comparisons of this type have limited validity due to the large time and space differences between the two measurements.

*This paper has been condensed from a paper by the same title and authors which will appear in the preprint volume 11th Technical Conference on Hurricanes and Tropical Meteorology (1977).

In summary, cloud motions may estimate the winds in hurricanes as well as about 1.5 m sec^{-1}, but agreement could be worse especially in regions of high vertical shear.

DESCRIPTION OF THE MEASUREMENT AND ANALYSIS SYSTEM

The Atmospheric and Oceanographic Information Processing System (AOIPS) is an advanced interactive image display, measurement, and data analysis system. The design and configuration of AOIPS is described by Billingsley (1976) and the METPAK software system is documented in a users guide by CSC (1977).

ERROR ANALYSIS PROCEDURE

The error analysis consisted of two parts: (1) The estimation of random errors in the cloud motion measurement and (2) artificially inducing random errors in the raw winds and observing their effects on the various parameters. To estimate the random errors in the cloud motion measurement the analyst remeasured about 25 vectors from each wind field. The remeasurements were made at least several days after the original measurement to make them as independent as possible. For the cases described here, most of the measurements were made by the cursor tracking technique. The magnitude of the vector difference was taken between the original vector set and the remeasured vectors. ($|\vec{V} - \vec{V}_{REMEASURED}| = MVD$) The MVD's were then ranked and the two thirds (67%) largest was determined, which is roughly equivalent to a standard deviation of one sigma. This technique does not estimate the size of systematic errors due to the choice of cloud motions not representative of a particular layer. This possible source of error will have to be investigated at a future time. However, a cloud height algorithm developed by Mosher (Suomi, 1975) was used to avoid the selection of clouds from the wrong layer. Random measurement errors are adequately estimated by the repeatibility tests. Systematic errors due to registration inaccuracy less than the estimated one pixel would give a uniform velocity error of less than 2 m sec^{-1} for the cases to be discussed. Hasler (1972) has shown that systematic errors of this magnitude would cause an error of less than 3×10^{-6} sec^{-1} for divergence and vorticity fields and is independent of scale size. This error would not be significant for the cases discussed here.

Since the major sources of error which can be objectively estimated are random, a technique was devised to measure the effect of random errors on the wind fields and the parameters derived from them. A Monte Carlo error analysis procedure was used which propagates a random error through the entire AOIPS/METPAK measurement and analysis system. A random number generator is used to perturb the x and y coordinates of the start and end points of each wind vector with an error which is normally distributed and has a standard deviation which can be varied. The unperturbed and perturbed vector sets are then subtracted to determine the effect of the error on the wind speed, direction, divergence, vorticity, etc. The effects of measurement time interval, image resolution, measurement technique, number of vectors per unit area and analysis constants such as grid spacing and degree of smoothing can be evaluated.

RESULTS

The error analysis was performed on several wind fields from hurricanes Eloise (Sept. 1975), Caroline (August 1975), and Holly (Oct. 1976). Rodgers et al. (1977) derived wind fields representative of approximately 200 mb and 950 mb wind fields for Hurricane Eloise from 2 km resolution 7.5 min short interval image sequences

with a total measurement interval of 22 minutes. The 200 mb wind vector field is shown in Figure 1 where speed is proportional to the length of the arrows. The error analysis results are presented in Table 1. For 20 remeasured vectors the repeatibility error was $|\vec{V} - \vec{V}_R|_{67\%} = 3.3$ m sec^{-1}. This is about half as good as one would expect to do based on resolution and time interval alone (2 km ÷ 22 min ➡ 1.5 m sec^{-1}). For a perturbation with standard deviation $\sigma = 1.0$ pixels the difference between the original 77 vectors and the 77 perturbed vectors was about the same: two thirds of the differences were equal or less than 3.1 m sec^{-1} ($|\vec{V} - \vec{V}_p|_{67\%}$). The unperturbed and perturbed wind fields were interpolated to uniform grid points using the Cressman objective analysis with the smoothing factors (γ) equalling 1.5 times the grid interval. The grid interval was about .45° latitude and longitude. Subtracting the analyzed unperturbed from the analyzed perturbed wind field at the 625 grid points resulted in $|\vec{V} - \vec{V}_p|_{67\%} = 1.6$ m sec^{-1}. A possible explanation for this factor of two improvement is as follows: since more than one vector contributes to the wind at a grid point the random errors tend to cancel out.

The horizontal divergence of the analyzed unperturbed and perturbed fields were contoured as shown in Figures 2 and 3. In Figure 2 a strongly divergent field is highlighted by a maximum divergence greater than 151 x 10^{-6} sec^{-1}. The perturbed divergence field ($\sigma = 1.0$ pixels) shown in Figure 3 is very similar with a maximum divergence greater than 166 x 10^{-6} sec^{-1}. When the unperturbed divergence field was subtracted from the perturbed at the grid points we obtained $|DIV - DIV_p|_{67\%} =$ 8.4 x 10^{-6} sec^{-1} as shown in Table 1. This is only 5% of the maximum value of the unperturbed field and means that contours greater than 8.4 x 10^{-6} sec^{-1} have significance at the 67% level or better. Table 1 also shows that doubling the perturbation ($\sigma = 2.0$) roughly doubles the effect on the wind and divergence fields. The remainder of the results are reported by Hasler and Rodgers (1977).

SUMMARY AND CONCLUSIONS

A Monte Carlo error analysis procedure has been developed for estimating the random error in wind fields derived from satellite observed cloud motions. The technique has been applied to high density low and high level hurricane wind fields measured by Rodgers et al. (1977) from short interval SMS image sequences on AOIPS.

Table 1
Error Analysis of Hurricane Eloise 200 mb Wind Field 1937 - 1959Z Sept. 22, 1975
Determined from 2 km Resolution 7-1/2 min Rapid Scan SMS Images

ORIGINAL DATA FIELDS VS. FIELDS PERTURBED BY RANDOM ERROR

20 VECTORS REMEASURED	77 RAW VECTORS	ANALYZED FIELDS USING CRESSMAN OBJECTIVE ANALYSIS (γ=1.5) GRID INTERVAL = .45°			PERTURBATION
		WIND	DIVERGENCE		
$\lvert\vec{V} - \vec{V}_R\rvert_{67\%}$ (m sec^{-1})	$\lvert\vec{V} - \vec{V}_p\rvert_{67\%}$ (m sec^{-1})	$\lvert\vec{V} - \vec{V}_p\rvert_{67\%}$ (m sec^{-1})	$\lvert DIV - DIV_p\rvert_{67\%}$ (10^{-6} sec^{-1})	$\frac{\Delta D}{D\ MAX}$	$\sigma_x = \sigma_y$ (PIXELS)
3.3	3.1	1.6	8.4	5%	1
	6.2	3.4	16.6	9%	2

D MAX ≅ 170 x 10^{-6} sec^{-1}

MONTE CARLO ERROR ANALYSIS PROPAGATES RANDOM ERRORS THRUGUH ENTIRE AOIPS DATA ANALYSIS SYSTEM

Figure 1. Hurricane Eloise 200 mb wind field determined from short internal (7.5 min) SMS images 1937 - 1959Z Sept. 22, 1975. Vector length is proportional to speed, with the highest wind speeds equal to 30 m sec^{-1}.

Figure 2. Hurricane Eloise 200 mb divergence field derived from the wind vector field in Figure 1. Cressman objective analysis was used with smoothing factor $\gamma = 1.5$ times the grid interval of about .45° latitude. Units are 10^{-6} sec^{-1}.

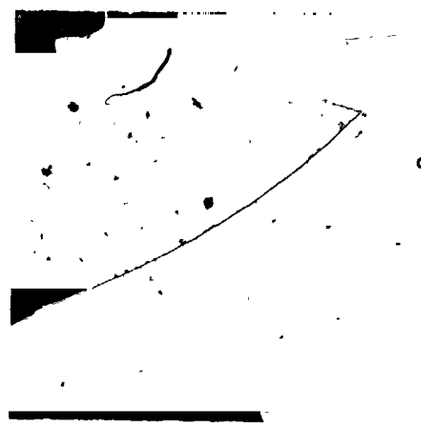

Figure 3. Same as Figure 2 except that the original 77 vectors shown in Figure 1 were perturbed with a random error with standard deviation of $\sigma = 1.0$ pixels (Eloise perturbed divergence).

Random errors of two times the image resolution divided by the total time interval can be expected in the raw vectors for cursor tracking of clouds. For a typical short interval sequence case we get 2 x 1 km ÷ 22 min ⇒ 1.5 m sec^{-1}. Typical objective analysis of wind fields appears to give a factor of 2 improvement in the wind error at grid points. For a number of "short interval" wind fields measured by Rodgers et al. (1977) random errors in the raw vectors ranged from 1.5 - 4.1 m sec^{-1}. Even in the worst case, strong divergence and vorticity features ($\geq 100\ 10^{-6}$ sec^{-1}) were resolved, but the highest resolution, longest total time interval, and most accurate measurement techniques are necessary to resolve weaker features.

REFERENCES

Billingsley, J. B., 1976: Interactive Image Processing for Meteorological Applications at NASA/Goddard Space Flight Center. In *Preprints of 7th Conference on Aerospace and Aeronautical Meteorology and Symposium on Remote Sensing from Satellites.* pp. 268-275.

Computer Sciences Corporation, 1977: Atmospheric and Oceanographic Information Processing System Meteorology Package (METPAK) Users Guide. Task Assignment 619, 1-1 to 1-6.

Hasler, A. F., 1972: Properties of Tropical Cloud Clusters Determined from Geostationary Satellite Pictures. Ph.D. thesis, University of Wisconsin, 317 pp; also Annual Sci. Rept., Contract NAS 5-11542, 1970-71, Space Sci. Eng. Center, University of Wisconsin, pp. 166-270.

Hasler, A. F., W. Shenk, and W. Skillman, 1976: Wind Estimates from Motions - Phase 1 of an *In-Situ* Aircraft Verification Experiment, *Journal of Applied Meteorology*, V. 15, No. 1, pp. 10-15.

Hasler, A. F., W. E. Shenk, and W. C. Skillman, 1977: Wind Estimates from Cloud Motions: Preliminary Results of Phases I, II, and III of an *In-Situ* Aircraft Verification Experiment, *Journal Applied Meteorology*, V. 16, No. 8, pp. 812-815.

Hasler, A. F., and E. B. Rodgers, 1977: An Error Analysis of Tropical Cyclone Divergence and Vorticity Fields Derived from Satellite Cloud Winds on the Atmospheric and Oceanographic Information Processing System. In *Preprint Volume, 11th Technical Conference on Hurricanes and Tropical Meteorology.*

Rodgers, E., R. C. Gentry, W. E. Shenk and V. Oliver, 1977: The Benefits of Using Short Interval Satellite Imagery to Derive Winds for Tropical Cyclones. In *Preprint Volume, 11th Technical Conference on Hurricanes and Tropical Meteorology.*

Suchman, D. and D. Martin, 1976: Wind Sets from SMS Images: An Assessment of Quality for GATE. *Journal Applied Meteorology.* V. 15, No. 12, pp. 1265-1278.

Suomi, V. E., Principal Investigator, 1975: Man computer Interactive Data Access System (McIDAS). Final Report Contract NAS5-23296, University of Wisconsin, Madison.

Paper No. 45

N79-20618

MESOSCALE CONVERGENCE PRECEDING THUNDERSTORM DEVELOPMENT DETERMINED FROM CLOUD MOTIONS

Cynthia A. Peslen, *Goddard Space Flight Center, Greenbelt, Maryland*

ABSTRACT

Convergence has been determined from wind vectors derived from cloudtracking on 5 minute interval SMS-2 data using the AOIPS.

INTRODUCTION

Convergence for a severe local storms area is examined using wind vectors derived from cloudtracking on SMS-2 five minute interval visible digital image data. The cloudtracking area is located in Central Plains, where on May 6, 1975, thunderstorm development occurred ahead of a well-defined dry line.

Cloudtracking is performed on an interactive image processing system designated the Atmospheric and Oceanographic Information Processing System (AOIPS).[1] This system allows the user to interactively modify satellite digital image data and to display the results on television monitors. Low level cumulus clouds are selected with the assistance of a cloud top height algorithm which provides for the variable emissivity properties of clouds.[2] Convergence is derived from the wind vectors using a Software Objective Analysis Package (SOAP).[3]

The objective of this paper is to present a satellite representation of convergence ahead of a dry line in an area of future thunderstorm development. The AOIPS wind vectors and their associated convergence fields were studied for three, 10 minute averaged time periods: 1758-1808 GMT, 1903-1913 GMT, and 2002-2012 GMT. Two 500 × 500 km^2 areas were studied along the north-south extent of the dry line (Fig. 1). The northernmost area (Area 1) included portions of Nebraska, Iowa, Kansas, and Missouri. The second area (Area 2) overlapped the southern boundary of the northernmost area. This area included portions of Kansas, Missouri, Oklahoma, and Arkansas. Severe hail-producing thunderstorms occurred within both areas in the afternoon.

RESULTS

Figures 2a, 2b, and 2c show the convergence fields at 1758-1808 GMT, 1903-1913 GMT, and 2002-2012 GMT for Area 1. Figures 3a, 3b,

PAGE 246 INTENTIONALLY BLANK

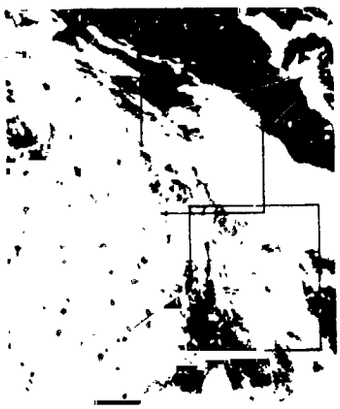

Fig. 1—Cloudtracking areas for 6 May 1975.

and 3c show the convergence fields for Area 2 and for the same time periods. The dotted lines represent contour values of convergence; the smooth lines represent contour values of divergence. The units are in 10^{-6} sec^{-1}. The dry line is located at the cloud, no-cloud boundary at the left edges of the satellite images.

There are a number of interesting meteorological features evident in the sequence of convergence fields. In both areas, a zone of convergence is consistently located ahead of the dry line and in areas of thunderstorm development. The magnitude of the convergence varies between 10^{-5} sec^{-1} to 10^{-4} sec^{-1} with consistently smaller values in Area 2. These are encouraging results since the immediate vicinity of a dry line is a highly preferred zone for thunderstorm development and apparent surface streamline convergence between moist and dry air. This zone of convergence remains spatially consistent with time in areas of adequate wind vector resolution. For example, in Figures 2a, 2b, and 2c, a northwest-southeast oriented zone of convergence is consistently located ahead of the dry line. Weak gradients and smaller values of convergence occur at 1758-1808 GMT and become progressively stronger with time. A hail-producing thunderstorm develops within this zone of convergence shortly after the 2002-2012 GMT period (Fig. 2c). A few remarks need to be made about the density of wind vectors in this sequence of images. The number of acceptable cumulus tracers decreases with time due to vertical motions, entrainment, and the cloud's own growth and dissipation. Mid-level clouds and cirrus clouds obscure the low level cloud field during their development. These effects appear in the sequence of convergence fields as a southward concentration of contours since most of the low level clouds still exist at lower latitudes in the satellite images. As the thunderstorms develop southward, fewer acceptable cumulus

Fig. 2a—Convergence field for 1758-1808 GMT (Area 1)

Fig. 2b—Convergence field for 1903-1913 GMT (Area 1)

Fig. 2c—Convergence field for 2002-2012 GMT (Area 1)

Fig. 3a—Convergence field for 1758-1808 GMT (Area 2)

Fig. 3b—Convergence field for 1903-1913 GMT (Area 2)

Fig. 3c--Convergence field for 2002-2012 GMT (Area 2)

tracers are located at higher latitudes within the dry line area. The large areas of divergence which are located along the image's edges and in areas of obvious convection at higher latitudes are a consequence of low wind vector density. The area of confidence exists immediately ahead of the dry line in areas of low level cumulus development.

Continuity in the convergence fields is also apparent in Figures 3a, 3b, and 3c. A well-defined zone of convergence is consistently located in an area of thunderstorm development along the dry line. At the upper left corner of Figure 3a, a zone of convergence occurs in an area of convection with a maximum value of -5.3×10^{-5} sec^{-1}. This zone reappears in the succeeding images with little change in the magnitude of the convergence. The interpolation involving the convergence fields is most accurate ahead of the dry line. Areas of suspect interpolation occur along the image's edges especially at the bottom edge of Figure 3b. The occurrence of severe weather is also related to this zone of convergence. Hail-producing thunderstorms occur in this area between 1900 GMT and 2200 GMT.

CONCLUSIONS

Preliminary results demonstrate the capability to study selected severe local storm features using satellite-derived wind fields. A significant feature, which is revealed by the satellite-derived winds, is a preferred zone of convergence located ahead of a dry line and in areas of future thunderstorm development. The magnitude of the convergence remains spatially consistent with time until the development of hail-producing thunderstorms.

Additional research is being done on other severe local storm days and for parameters such as deformation, relative vorticity, vorticity production, and vorticity advection. An exhaustive analysis is also planned to determine the accuracy of satellite wind vectors and their dynamic parameters.

REFERENCES

1. Computer Sciences Corporation, 1976: Atmospheric and Oceanographic Information Processing System Meteorology Package (METPAK) Users Guide, Task Assignment 619, 1-1 to 1-6.

2. Smith, Eric A., 1975: The McIDAS System. IEEE Transactions on Geo-Science Electronics, 13: 123-136.

3. Computer Sciences Corporation, 1976: Software Objective Analysis Package Mathematical Algorithms, Task Assignment 666, 2-1 to 2-5.

Paper No. 46

N79-20519

HIGH RESOLUTION TROPICAL CYCLONE WIND FIELDS DETERMINED FROM CLOUD MOTIONS

Edward B. Rodgers, ... Cecil Gentry,* William E. Shenk, and Vincent Oliver,**
NASA/GSFC, Greenbelt, Maryland

ABSTRACT

Full resolution rapid scan infrared and visible images from the VISSR sensor on board SMS-2/GEOS-1 satellite have made it possible to maximize the number of tropical cyclone upper and lower tropospheric wind vectors by a factor of 6(2) over that of the images taken at 30 minute (15 minute) intervals. These full resolution rapid scan visible images have also made it possible to derive low level winds near the center of tropical cyclones.

INTRODUCTION

For the purpose of maintaining and improving the hurricane warning services, numerical-dynamical models that forecast hurricane motion and intensity are needed. The success of these models, of course, is dependent on how well th initial meteorological parameters are known. Of particular need are the initial wind data at several levels above the surface to the lower stratosphere, extending outwards from the center to include the environment surrounding the tropical cyclone. Within the tropical cyclone cloud system, the only real source of wind data is obtained from hurricane reconnaissance aircraft flights. However, the quantity of wind data obtained from these flights are not sufficient to be used i these numerical-dynamical models and, in fact, the tendency in recent years has been to reduce the quantity of wind data by decreasing the number of flights. Therefore, there is a great need to obtain additional wind data from another source.

An excellent source for the upper troposphere has been through the use of cloud tracking techniques. These techniques have been developed for the infrared and visible images that have been obtained operationally from the family of geo-synchronous satellites at approximately 30 minute intervals. However, l success has been found using this technique in obtaining winds at lower levels. One reason for the lack of success, is that many of the clouds of the type and size best suited for tracers near the cloud base level do not persist or maintain their shape for even 30 minutes. Another problem is that the cirrus associated with the storm often obscures the low level clouds during the thirty minute ti period. A solution to this problem, as suggested by Fujita, et al. (1975), is to increase the temporal resolution between satellite derived images.

*General Electric Space Division (MATSCO), Beltsville, Md. 20705
**NOAA/NESS, Camp Springs, Md. 20032

To verify this, a cooperative project between the NASA and NOAA agencies was initiated to examine tropical cyclones during the 1975-1977 hurricane seasons with rapid scan full resolution infrared and visible images. The purpose of this project was to develop better means for obtaining wind data needed by the hurricane forecaster and to determine the optimum space and temporal resolution of the satellite data used to derive such winds. Limited scan visible and infrared images were obtained at 7.5 minute interval from SMS-2 in 1975 for hurricane Eloise (22 September) and tropical cyclone Caroline (28, 29 and 30 August); and at 3 minute intervals from GEOS-1 in 1976 for tropical cyclones Belle (5 August) and Holly (26 October). Through the utilization of a man-interactive system called the Atmospheric and Oceanographic Information Processing System (AOIPS) at NASA/GSFC, winds derived from cloud motion were obtained (CSC, 1976). Only the results from hurricane Eloise and tropical storm Holly will be presented in this paper since similar results were found from cyclones Caroline and Belle.

RESULTS

The results from the wind analysis of hurricane Eloise are presented in Tables 1 and 2. Low level clouds were tracked using at least 3 successive visible images whose spatial resolution were 1, 2 and 4km and whose time interval between images were 7.5, 15 and 30 minutes. No cloud elements were tracked that could not be delineated in all images. The number of low level cloud elements tracked for hurricane Eloise at radii distance from the center of approximate 222, 444, 666km for the given temporal resolution is shown in Table 1.

It can be seen from the table that the improved temporal resolution increased the number of traceable cloud elements. The shorter interval data not only improved the cloud continuity but also eliminated the ambiguity caused by tracking cloud growth rather than displacement. From the center to 666km, the 7.5 minute interval images increased the number of wind vectors by a factor of 6(2) over that of the 30 minute (15 minute) interval images. Within 222km from the center, cloud elements could only be tracked using shorter interval images.

Improved spatial resolution also increased the number of low level cloud elements tracked. It is particularly important to have full resolution images for tracking cloud elements near the eye wall that are difficult to delineate because of the cirrus; and over land, where slower moving clouds moved less than one pixel distance for the 2km and 4km visible resolution images.

Cirrus clouds near the tropopause were examined next for hurricane Eloise using visible and infrared images at 7.5 and 30 minute intervals. The purpose of using the infrared images was to determine if rapid scan images would be of any

Table 1

Hurricane Eloise 22 September 1975 1900 GMT
Number of Low Level Winds

Distance from Center (km)	0-222	0-444	0-666
30 min 1 km Vis	0	1	8
15 min 1 km Vis	0	6	18
7.5 min 1 km Vis	3	20	44

Table 2

Hurricane Eloise 22 September 1975 1900 GMT
Number of High Level Winds

Distance from Center (km)	0–222	0–444	0–666
30 min 8km IR	0	3	6
2km Vis	0	5	9
7.5 min 8km IR	1	13	30
2km Vis	10	44	71

value at night. The spatial resolution used for the visible (infrared) images was at 2km (8km). Table 2 summarizes these results. It can be seen from the table that within 666km from the center, approximately 2 times as many clouds could be tracked using the visible as compared to the infrared images. This is attributed to the fact that the structure of cirrus clouds is best delineated with higher spatial resolution visible images. As found with the low level clouds, the improved temporal resolution again increased the number of clouds that could be tracked by a factor of 6.

One of the problems that was encountered in using larger interval visible and infrared images to track high clouds, was the ambiguities introduced by tracking cloud patterns that were repetitive. Because of the repetitive patterns, the correct displacement of these cloud patterns could only be ascertained using rapid scan data. Therefore, for the Eloise case, it was advantageous to use rapid scan data to track upper level clouds from both visible and infrared images.

It was found from low level cloud motion analysis for both tropical cyclones Eloise and Caroline that cloud elements near the center could be detected and tracked using high resolution rapid scan visible images. It is hypothesized that the cloud derived winds may infer the low level wind flow within a tropical cyclone. Maritime cumulus clouds in a non-hurricane type circulation (whose cloud tops were as high as 200 mb) have been found from aircraft observation to move nearly with the ambient flow at the cloud base level (Hasler, et al. 1976, although there is no aircraft verification that convective clouds move with the wind flow at the cloud base within a hurricane type circulation, the small vertical shear and the large upward flux of angular momentum near the center may suggest that it does (Frank 1977). To examine this hypothesis, winds obtained from NOAA research aircraft at an approximate altitude of 1 km outside and 1/2km inside the cloud structure for hurricane Eloise (22245–0440 GMT, 22 and 23 September 1975) and for hurricane Caroline (1634–2332 GMT, 30 August 1975) were compared to cloud derived winds. Some small bright convective cells that persisted during the time period were used to infer low level winds near the center. However, many of the larger bright convective cells that moved slower were not used to derive these winds. Results for Eloise are seen in Figure 1. It is seen from this figure that the cloud derived winds compare reasonably well with the aircraft derived winds over the same area relative to the storm centers, even though the time of the aircraft measurements was off as much as 6 hours. The average difference in absolute value represented by the two methods is approximately 2.5 m/sec. This difference was also found for hurricane Caroline. Considering the time difference in the two types of measurements, this result is no greater than would have occurred if the winds were obtained by aircraft for each case because of the great natural variability of hurricane winds (Gentry 1964).

Table 3

Tropical Storm Holly 26 October 1976 1300 GMT
Number of Low Level Winds

Distance from Center (km)	0–222	0–444	0–666
30 min 1 km Vis	4	29	48
3 min 1 km Vis	80	225	285

These results differ from the findings of Gentry, et al. (1970) in which they tracked large bright convective cells near the center of hurricane Gladys on 17 October 1968 using the 14 minute interval visible images from MSS camera on ATS-3. It was found that these clouds moved from 1/3 to 1/2 of the speed of the low level winds. The difference may be attributed to the ambiguity caused by cloud growth when tracking large cells using 4km visible resolution images at a 14 minute interval.

The results from tropical cyclone Holly obtained from the GEOS-1 images during the 1976 hurricane season are presented in Table 3. It can be seen from this table that the rapid scan images again maximized the number of wind vectors obtained from cloud motion. In this case, within 666km from the center, the increase was again by a factor of 6 in using rapid scan images compared to 30 minutes interval images. Figure 2 dramatizes the results for tropical storm Holly. The figure shows the distribution and number of low level winds that can be derived from cloud motions using 3 minute interval images. No winds could be obtained north of the center because the images were unavailable due to the starting time of rapid scan. A point of interest, seen in Figure 2, is the maximum wind of 50 kts to the east of the center obtained from the rapid scan images verifies the tropical storm status reported by reconnaissance aircraft.

CONCLUSIONS

From this study, it was found that greater spatial and temporal satellite image resolution has made it possible to maximize the number of upper and lower tropospheric wind vectors by as much as a factor of 6(2) over that of the 30 minute (15 minute) interval images. Rapid scan full resolution infrared and visible images have eliminated the "erroneous winds" caused by cloud growth and cloud repetition. With the full resolution rapid scan images, it was shown that it is possible to derive low level winds near the center of the tropical cyclone.

REFERENCES

Computer Science Corporation, 1975: Atmospheric and Oceanographic Information Processing System Meteorology Package (METPAK) Users Guide, Task Assignment 619, 87 pp.

Frank, W. M., 1977: The structure and energetics of tropical cyclone 1 storm structure, Mon. Wea. Rev., 105: 1119–1185.

Fujita, T. T., E. W. Pearl, and W. E. Shenk, 1975: Satellite-tracked cumulus velocities, J. Appl. Meteor., 14: 407–413.

Gentry, R. C., 1964: A study of rainbands, National Hurricane Research Project Report No. 69, U.S. Dept. of Commerce, 85 pp.

Gentry, R. C., T. T. Fujita, and R. Sheets, 1970: Aircraft, spacecraft, satellite and radar observation of hurricane Gladys 1968, J. Appl. Meteor., 9: 837–850.

Hasler, A. F., W. E. Shenk, and W. Skillman, 1976: Wind estimation from cloud motion: Phase 1 of an in situ aircraft verification experiment, J. Appl. Meteor., 15: 10–15.

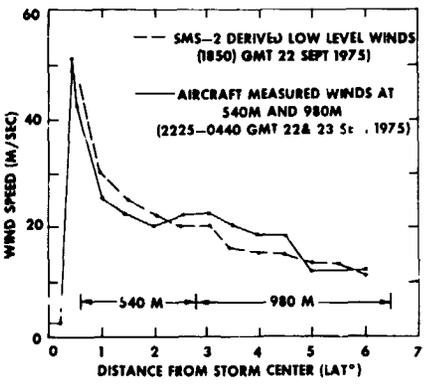

Figure 1. Comparison of wind speeds derived from cloud motions between 3 consecutive SMS-2 satellite visible imagery at 7.5-minute intervals with winds measured 4 to 6 hours later by reconnaissance aircraft flying at 540 and 980 meters in Hurricane Eloise 22 September 1975.

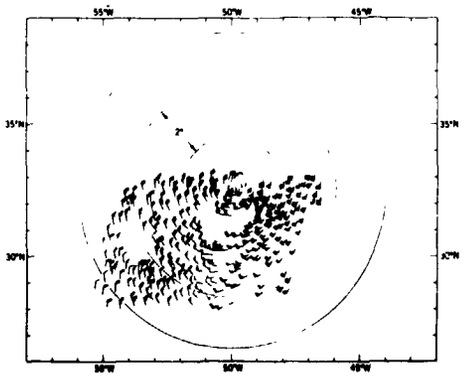

Figure 2. Low level winds derived from cloud movements between 4 successive GOES-1 pictures with 1 km resolution and at 3-minute intervals (1342, 1345, 1348, 1351 GMT) wind speed in kts.

Paper No. 47

THE DATA SYSTEMS TEST – DRESS REHERSAL FOR FGGE

J. R. Greaves, *Goddard Space Flight Center, Greenbelt, Maryland*

ABSTRACT

A series of Data Systems Tests conducted by NASA as a precursor to the First GARP Global Experiment is described. Included is a description of the global data sets acquired and the influence the tests have had on the observing system, the data processing plans and research activities of the Global Experiment itself

INTRODUCTION

The Global Atmospheric Research Program (GARP) is an international cooperative effort whose major objectives are (1) to extend the range, scope, and accuracy of weather forecasts and (2) to understand the physical basis of climate and climatic fluctuations. Early in the development of GARP, the idea of an extensive, global observing experiment was conceived to serve as a focal point in the pursuit of the first GARP objective. An international experiment called the First GARP Global Experiment (FGGE) is now scheduled for implementation in December of 1978. The approach will be to observe the global atmosphere and ocean in detail for a full year by means of a coordinated international effort. Nearly all of the 145 member countries of the World Meteorological Organization will participate.

A unique combination of observing systems will be used for The Global Weather Experiment. The 700 upper air, 3500 surface synoptic, 6000 ships, and several thousand commercial aircraft comprising the bulk of the surface-based World Weather Watch Global Observing System will be combined with the following array of observing systems:

- Four operational polar orbiting meteorological satellites
- Five operational geostationary meteorological satellites
- Two research meteorological satellites
- Up to fifty specially equipped ships for upper air sounding in the tropics
- Approximately 300 constant level balloons for tropical wind measurements
- Approximately 300 drifting buoys, largely in the Southern Hemisphere

- Approximately 20 specially equipped commercial aircraft for measurements of wind and temperature at flight level, and
- Approximately ten dedicated aircraft flying designated tracks over the oceans, dropping sounding instruments to obtain information from flight level to the surface.

FGGE will be the most comprehensive observational program of the Earth's atmosphere yet attempted. Its size and complexity are such that early large-scale systems tests are required in order to assure successful planning and implementation of the full global experiment. The concept of conducting a series of Data Systems Tests (DST) was developed by NASA. These tests were to serve as a precursor for FGGE and provide a broad operational review of many of the observational, data management, and data utilization systems of the Global Experiment itself. The GARP Project Office at NASA's Goddard Space Flight Center was charged with the implementation and operational management of the Data Systems Tests. The basic approach was to use current operational satellites and conventional meteorological data along with the data from research satellites, to approximate the elements of the proposed observation system for FGGE. An extremely valuable by-product of the DST has been the collection of global sets of meteorological data better than any that have been obtained previously.

The DST Experiments

Six Data Systems Tests of varying lengths, purposes, and participation have been conducted. Of these, the first four were more limited tests of individual subsystems. The final two DST periods consisted of comprehensive end-to-end systems tests. A summary of the data sources and schedules of the six DST periods is shown in Figure 1.

The last two tests, DST-5 and 6, were each of 60 days duration and were conducted under summer and winter conditions paralleling the two Special Observing Periods planned for the Global Experiment in 1979. These two tests produced the most comprehensive sets of global meteorological data yet assembled. The data sources included the following:

- Surface-based Conventional Observations
- Operational Satellite Data - Temperature soundings, sea surface temperature and cloud-track winds
- Experimental Satellite Data - Temperature soundings from a combined infrared/microwave retrieval system, weekly mean sea ice coverage and daily rain rate maps from a passive microwave system and earth energy budget products including solar irradiance, and monthly mean longwave flux, net radiation and planetary albedo.

- Experimental Cloud-track Winds - An interactive computer system was developed at the University of Wisconsin to produce high density multi-level wind fields in near real time.
- Constant Level Balloons - Reports from approximately 120 constant level (approximately 15 km) balloon platforms in the tropical latitudes were collected.
- Airline Observations - An agreement was reached with a number of foreign airlines whereby in-flight meteorological data were obtained from specially-equipped commercial aircraft. As part of the Aircraft Integrated Data Systems (AIDS), tape recorders on wide-bodied jets recorded flight-level wind, temperature, altitude, and position.
- Carrier Balloons - During DST-5, a complete systems test was carried out with thirteen constant level (approximately 25 km) carrier balloons being launched near the equator. Each balloon carried 64 dropsondes which transmitted temperature, humidity and wind information back to the carrier balloon as they fell.

NOAA/NMC collected and merged the data from the various sources into internally consistent global data sets. In this regard, their role in the DST paralleled that of the Space-based and Special Observing System Data Center planned for FGGE. NMC also used the merged data sets to produce global grid point analyses of selected meteorological parameters at 6 and 12 hour synoptic time intervals. These data sets have been distributed to the major numerical modelling groups in this country and abroad for research studies on the FGGE-related problems of observational network design, data management and forecast model impacts. An Announcement of Opportunity to work with the DST data sets has recently been issued in order to involve a larger segment of the meteorological community in the application of satellite data to the forecasting problem. A data base management system has been developed within the Computer Systems Branch at Goddard to provide flexible access to the DST data sets.

Preliminary Findings

The important aspect of the Data Systems Tests has been the insight gained into the central problems of conducting the Global Weather Experiment: the adequacy of the observing system, the data processing plans and the utilization of the data in numerical forecasting models. As a result of the DST experience, significant changes have been made in both the planned observational program and the procedures for managing the data flow.

In the Southern Hemisphere, the AIDS concept was proven to be a valuable source of upper air data. The AIDS units recorded wind and temperature data on tape for later collection and analysis. To provide a faster turn-around, the Aircraft to Satellite

Data Relay (ASDAR) system was developed by NASA and is being readied for use during the Global Experiment. ASDAR generates the same data products as AIDS, but the data are transmitted through a geosynchronous satellite to ground monitoring stations in near real time. A prototype system is now flying on a commercial B-747 and some 20 additional units will be installed for use during FGGE.

The problems which occurred in assembling the DST data sets have convinced all participants that new types and sources of data require improved techniques to manage the data flow. Significant errors can be introduced into the data base, and without adequate control these errors might not be found until substantial efforts have been made to actually use the data. The two key implications of the DST's which have influenced the data management plans for FGGE are:

(1) greatly improved monitoring of the observing and telecommunications systems
(2) an operational readiness evaluation of the data flow prior to the start of the FGGE.

In the formative stages of GARP planning there was considerable optimism that we stood at the threshold of significant improvements in our ability to predict weather. This optimism was based upon advances which had been made in three areas: (1) An increased scientific understanding of those atmospheric processes that produce weather, coupled with the development of analytic models of the atmosphere; (2) the development of faster and more sophisticated computers; and (3) the emergence of the meteorological satellite as a powerful data-gathering tool. In initial studies of the utilization of data acquired during the DST periods, it has now become clear that the problem of assimilating the satellite data into the atmospheric models is more complex than had previously been thought. While impact tests have demonstrated modest improvements in the forecasts through the addition of satellite sounding data, significantly improved analysis techniques are required. The problem is to merge the continuous satellite data with the discreet blocks of conventional data in an optimal fashion so as to minimize the resultant analysis and forecast errors. The continued research to be carried out with the DST data sets is aimed at overcoming the known deficiencies of the prediction models and at building a firm foundation for accomplishing the objectives of FGGE.

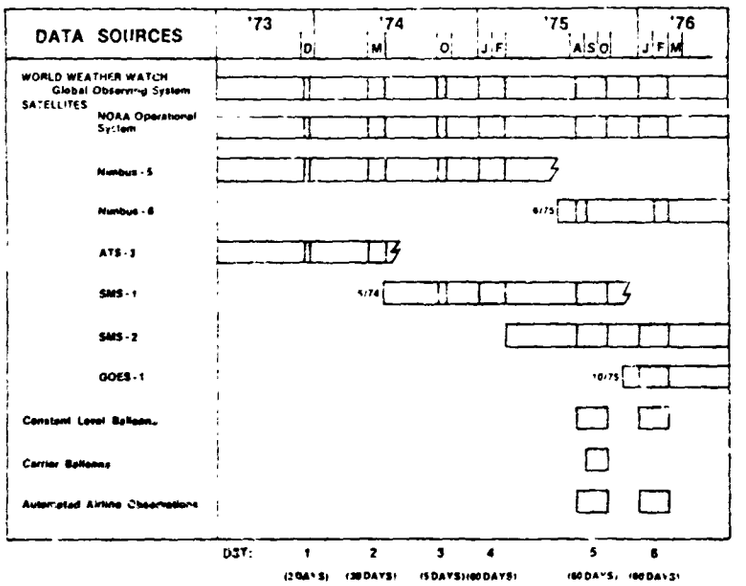

Figure 1. Data sources and schedules for the six DST periods.

Paper No. 48

N79-20621

COMMERCIAL AIRCRAFT DERIVED HIGH RESOLUTION WIND AND TEMPERATURE DATA FROM THE TROPICS FOR FGGE – IMPLICATIONS FOR NASA

R. Steinberg, *NASA Lewis Research Center, Cleveland, Ohio*

ABSTRACT

Two programs involving over 100 commercial aircraft have been initiated to provide global high resolution in-situ windfield and temperature data during the FGGE. The concepts developed for these programs could have important implications for both meteorology and aviation in the near term.

INTRODUCTION

Because of the weak coupling between mass and motion in the tropics, particularly complete observations are required. Except for the FGGE Special Observing Systems (which are temporary), only remote measurements are normally made in large areas of the tropics a the southern hemisphere. Actual windfield and temperature measurements are essential near the equator and a certain minimum number o in-situ observations are needed in other latitudes in order to deduce meteorological data from remote measurements with sufficient accura

It was recognized that this requirement for in-situ data could in part be met by utilizing some of the over 400 inertial navigation syster (INS) equipped commercial aircraft which routinely transit the tropics and the southern hemisphere. These aircraft are in effect fully automated meteorological data collection platforms, capable of providing latitude, longitude, altitude, wind angle, wind velocity, and temperatu at 4 second intervals. In some cases this information is stored on tap along with other aircraft performance data, however in most instance: it is discarded.

Two programs have been developed by Lewis Research Center t explore the potential of this new data source for the FGGE and beyond. The first, called AIDS (Aircraft Integrated Data Systems) makes use c existing, sophisticated, airborne data processing and storage systems currently being flown on a number of commercial aircraft, to provide meteorological information. The second program called ASDAR

(Aircraft to Satellite Data Relay) provides for the acquisition and near real-time relay via satellite of meteorological data from commercial aircraft to meet FGGE requirements and explore the future needs of operational meteorology.

AIDS Program for the FGGE

The concept of using AIDS equipped aircraft to provide high resolution meteorological data (supported by NOAA, NCAR, and NASA) was successfully demonstrated during the GATE (GARP Atlantic Tropical Experiment) in 1974. At the request of the World Meteorological Organization (WMO) a similar but larger program is now being organized for the FGGE. It is expected that over 80 B-747 and DC-10 AIDS equipped aircraft, including 5 concordes will be providing aireps.[1] Figure 1 shows the anticipated data density from these aircraft. The AIDS program will provide over 3000 aireps per day. The data will be sent on tape to the Special Aircraft Data Center (in the Netherlands) for further processing and then forwarded to the level IIB data center in Sweden.

ASDAR Program for the FGGE

It was suggested by the author[2] that while AIDS data base could meet research requirements, the real impact of this concept would only be felt if aireps could be provided in near real-time to meet operational needs. NOAA agreed and asked NASA to develop a low-cost communications system to provide aireps from commercial aircraft, in near real-time on a fully automated basis. The communications system, called ASDAR, shown in figure 2, was the result. It consists of a 401 MHz transmitter, a 468 MHz receiver (now being replaced with a clock), a digital interface unit and power supply. The complete system including the antenna, shown in figure 3, and all associated installation hardware weighs about 34 kg. The first ASDAR system has been installed on a Pan American B-747 and has provided aireps, see figure 4, on a fully

---

[1] Each airep consists of latitude, longitude, altitude, time, temperature, wind angle, and wind velocity.

[2] Julian, P., and R. Steinberg 1975: Commercial Aircraft as a Source of Automated Meteorological Data for GATE and DST. Bulletin American Meteorological Society, 38, 243-251.

automated basis for several months. A few minor technical problems have been experienced, however, in the main, the results shown in figure 5, have been exceptional. To date we have been able to transmit data from the aircraft to the satellite with an elevation angle as small as 0^{o} and a single satellite has provided coverage from 20^{o} to 180^{o} west longitude.

The ASDAR program is now under the auspicies of NOAA in the United States while international direction is being provided by the WMO. It is expected that between 15 and 20 ASDAR equipped aircraft will participate in the FGGE.

Additional Tropics/Southern Hemisphere Data for FGGE

Examination of figure 1 will show that there are still significant data and frequency voids in the tropical oceans. One way of reducing this deficiency for the FGGE (now being actively explored by the WMO) is for key aircraft which always transit the tropics to be provided with a low-cost Weather Data Recorder (WDR). For example the wide-bodied fleets of Australia (Qantas), New Zealand (Air New Zealand), Brazil (Varig) and France (UTA) representing 33 aircraft are always on tropical routes in data sparse areas. A United States air carrier (Pan American) is also switching to an all B-747 fleet in the Pacific. In fact every Pan American flight across the Pacific (see fig. 6) is now a B-747 or B-747SP (cruises at 45 000 ft). The potential for providing a significant improvement in the tropical data base, at several levels, using the WDR on selected routes is impressive.

The WDR is a small cassette data logger weighing just 8.18 kg (18 lb) and requires 25 watts of power. It will interface any INS equipped B-747 or DC-10 aircraft and can store data for a minimum of 30 days. In quantities of 30 units a WDR flight certified system costs 11 900 dollars.

Future Implications

There are at least 200 INS equipped aircraft which transit the tropics each day. Each is in actuality a meteorological data collection platform. These aircraft, if ASDAR equipped, could provide a 1000 percent increase in the number of real-time aireps (200 km resolution) coming from the tropics and the southern hemisphere. Such an improvement in the present data base could be of major importance to

weather forecasting as well as providing a spin-off for airline flight planning. United States air carriers used over 10 billion gallons of fuel last year! If we can translate high resolution wind and temperature temperature information into more accurate airline route forecasting the savings could be significant. Currently fuel accounts for over 40 percent of airline operating costs. A 1-percent savings in minimum time track forecast can save 100 million gallons of fuel a year.

The FGGE may provide NASA with a unique opportunity to evaluate the importance of aircraft to satellite communications in improving the present world-wide meteorological data base as well as assessing the potential spin-off in fuel savings to the airline industry.

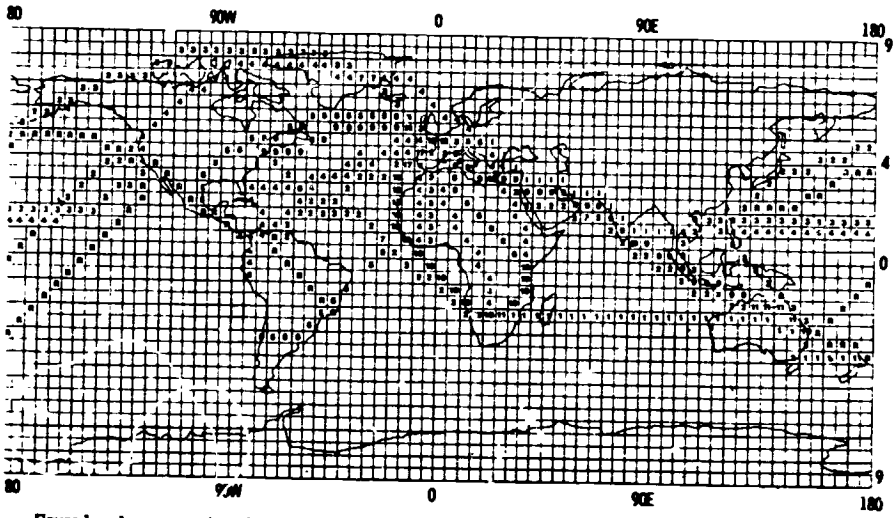

Figure 1. - Average number of met data sets expected per day as a function of location from aids fleet of 80 aircraft.
Note: Data is preliminary
R indicates less than 1 data set/day.

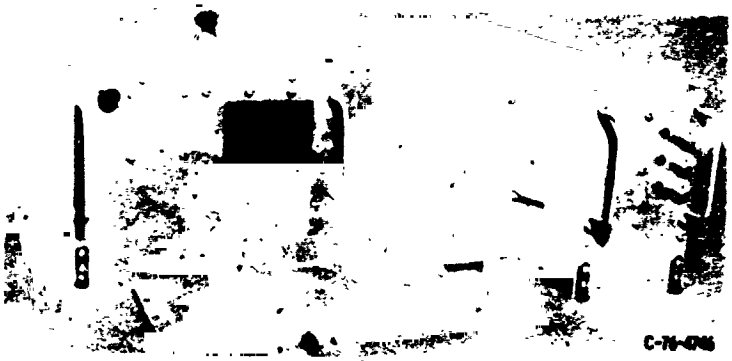

Figure 2. - Complete ASDAR system (except for antenna); transmitter, receiver and digital interface unit in box on left - power supply on right - diplexer in foreground and preamplifier in background.

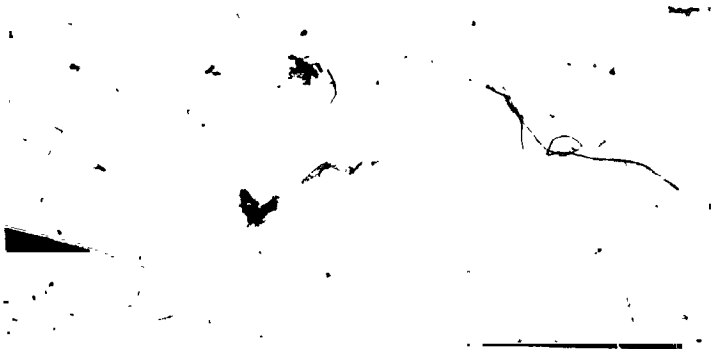

Figure 3. - Prototype ASDAR coplanar Stripline transmit-receive antenna mounted on Pan American B-747 aircraft.

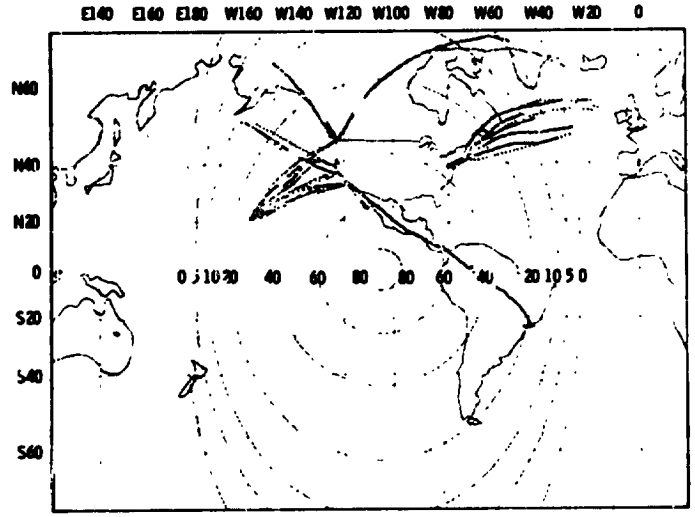

Figure 5. - ASDAR data record points with contours of constant elevation to the receive satellite.

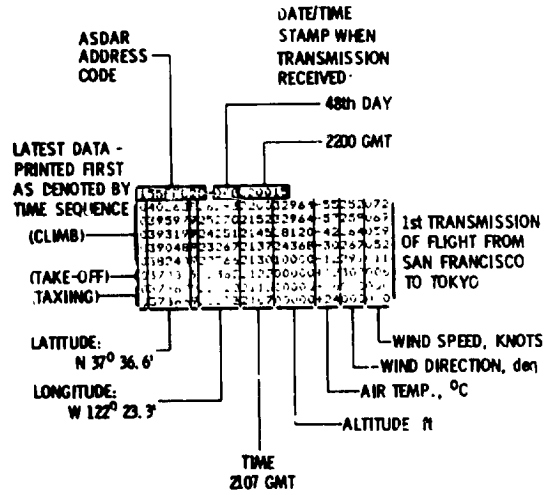

Figure 4. - ASDAR printout obtained, via satellite relay, from National Satellite Service.

Figure 6. - Current Pan American B-747 and B-747 SP routes in the Pacific.

Paper No. 49

N79-20622

A SUMMARY OF NIMBUS-6 TEMPERATURE RETRIEVAL ACCURACY STATISTICS FOR DST-5 AND DST-6

C. M. Hayden, *National Environmental Satellite Service, Madison, Wisconsin*

INTRODUCTION

This summary addresses statistics compiled from Nimbus-6 temperature retrievals processed during the 18 August-4 September 1975 DST-5, and the 1 February-4March 1976 DST-6. No claim is made that such a summary comprises a thorough evaluation. Statistical characteristics are but one of many aspects of a data set. However, statistics have the advantages of generality and familiarity; and most importantly, the statistical properties of any data type are essential to modern objective analysis schemes which properly weight different data relative to their known characteristics. For the last reason it is hoped that this report will serve the users of the DST level 2 data sets in properly interpreting and utilizing the temperature profiles derived from Nimbus-6 measurements.

All statistics included here have been compiled from samples of colocated satellite sounding and radiosonde measurements. The colocation window is 222 km in space and 6 hours in time. The window is undesirably large, but tighter restriction causes the elimination of important areas (e.g., the satellite is over the U.S. almost precisely between radiosonde launch times). To some extent the window problem has been alleviated by making comparisons with values interpolated in space and time from objective analyses (which did not utilize the Nimbus data). The samples do not include the entire DST periods but are large enough to be representative. Four statistical aspects are considered: a) the mean and standard deviation of difference between satellite, radiosonde, and objective analysis values for the total sample; b) the root-mean-square (rms) difference between satellite and analysis values categorized by the activity of the meteorological situation; c) the spatial error correlation of the satellite data as compared to radiosonde and analysis values; and d) the accuracy of temperature gradients implicit in satellite temperature data as compared to radiosonde and analysis values.

Mean and Standard Deviation of Differences

Figure 1 presents mean and standard deviation differences for Nimbus-6 layer temperatures (between mandatory pressure levels) as compared to radiosonde and analysis values. Also shown is the difference between radiosonde and analysis. The most important

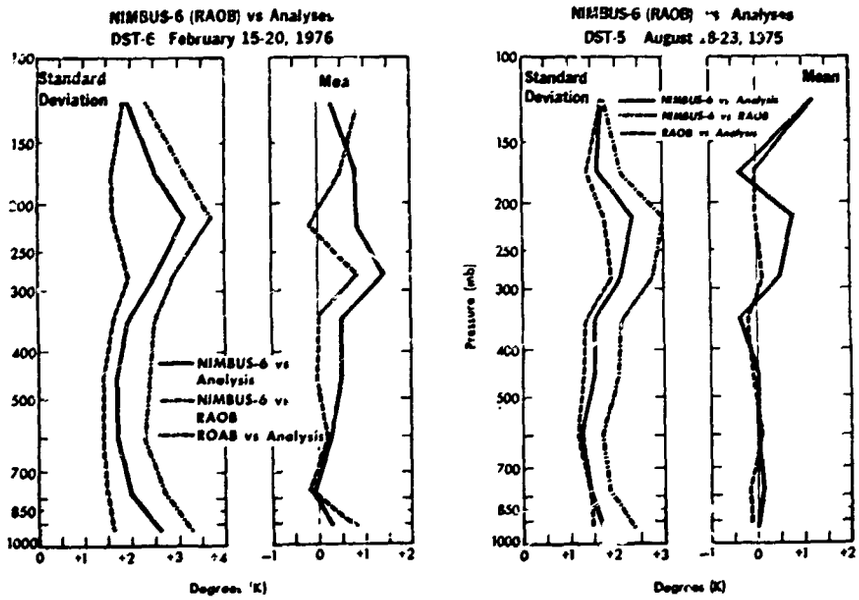

Fig. 1 - Standard deviation and mean deviation of Nimbus-6 temperature profiles as compared to radiosonde and objective analysis.

feature is that for the troposphere (below 300 mb and excluding the surface) the basic accuracy of Nimbus vs. radiosonde is approximately 2.0K for DST-5 and 2.5K for DST-6. These figures are each improved by approximately 0.5K if the satellite data are compared to values from analyses which smooth the high frequency oscillations of radiosonde data. Accuracy deteriorates in the tropopause region by approximately 1.0K due to poor resolution in the radiation measurements. Accuracy above 50 mb (not shown) is poor for DST-5 and very poor for DST-6, and the data should not be used.

A second important feature is that "mean" or bias errors are prevalent in the satellite data. This is obvious at tropopause levels for both DST periods (satellite values too warm) and over virtually the entire atmosphere for DST-6. Even for DST-5, bias errors exist locally within synoptic features. This problem is also believed to be caused fundamentally by resolution deficiencies both in the measurement and the data processing.

RMS Differences vs. Atmospheric Activity

Figure 2 addresses the usefulness of the Nimbus temperature

data. As an average figure, the rms difference between Nimbus-6 and objective analysis values (interpolated in space and time) is approximately as large as the difference between analysis estimates of the "truth" 12 hours apart. This feature is represented by the points on the ordinates of the graphs of figure 2. Given this fact, it is easy to jump to the erroneous conclusion that satellite data are probably useless except in the sparsest data regions. However, the figure illustrates that the satellite error is quite independent of the magnitude of the 12 hour change in the "truth." (The sample is sequentially reduced to the more active cases along the abscissa; the satellite rms stays constant while the "activity" rms rises). Therefore, the data are valuable in the active and interesting meteorological areas. This feature could be incorporated into an objective analysis scheme such that the data get more weight (relative, for example, to the first guess field) as the atmospheric activity increases.

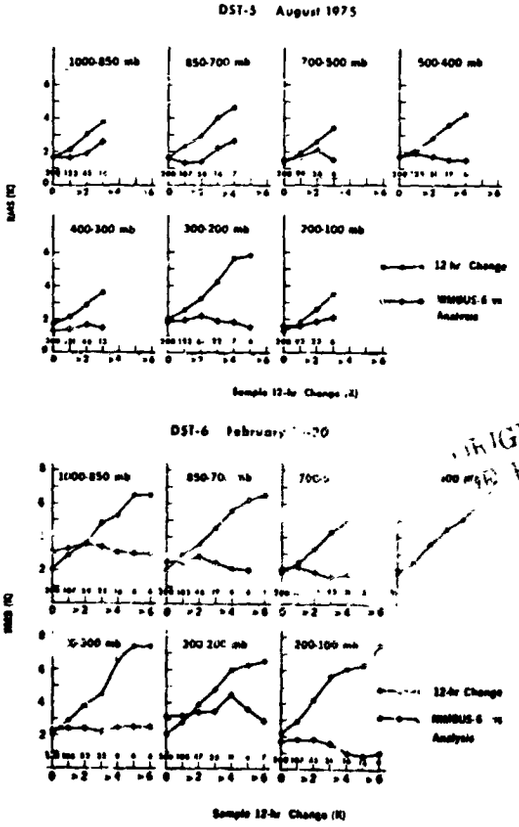

Fig. 2 - RMS discrepancies of Nimbus-6 as compared with objective analysis temperatures categorized by analyzed 12 hour temperature changes.

Spatial Error Correlation

The value of a piece of data depends on its independence from other a priori information. If a data value is perfectly correlated with another data value, the second offers no new information, except in terms of confidence. In general, correlation between data is an undesirable feature unless the data are perfectly accurate.

The previous two sections affirm that satellite temperature data are not perfectly accurate! Figure 3 of this section shows that the errors are spatially correlated (with notable similarity between DST-5 and DST-6). From the meteorological standpoint, if any temperature sounding in a synoptic system is too warm, other soundings in that system will also be too warm. Strong error correlation exists to a distance commensurate with the scale of the major synoptic systems. The figure highlights that the correlation is most evident when comparison is made with objective analysis estimates of the "truth". Thus it is a dominant feature in the eventual application of the data, and it should be considered in any objective analysis scheme. Note that the correlation should not in this case be interpreted to increase confidence in the data.

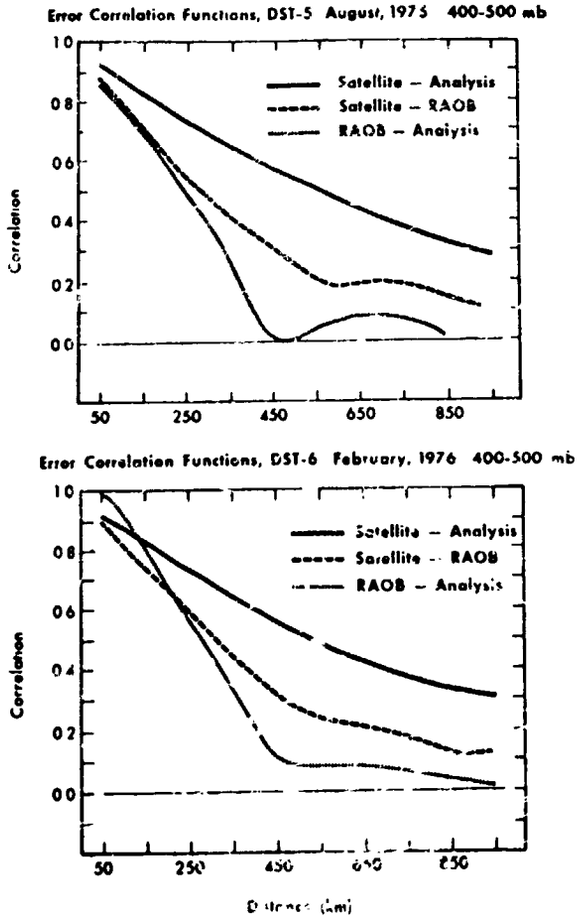

Fig. 3 - Spatial error correlation functions for Nimbus 6 temperature values in mid troposphere.

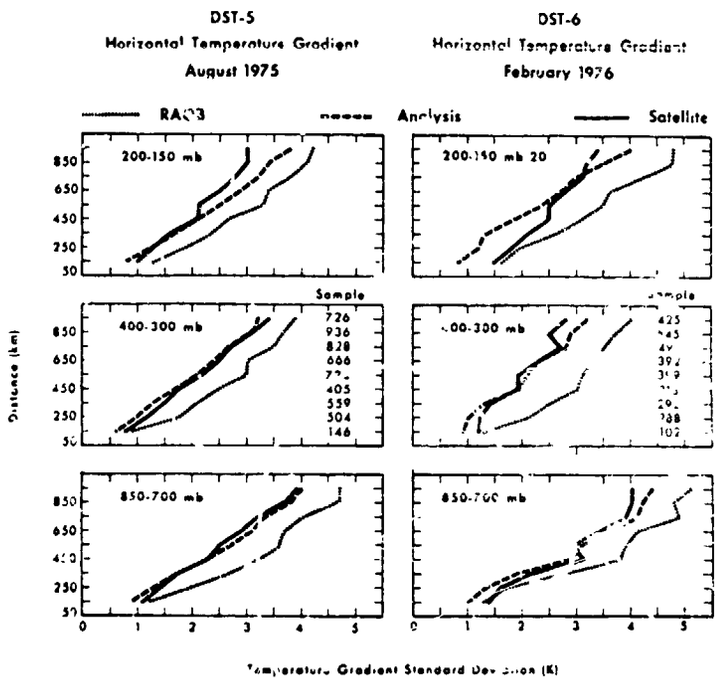

Fig. 4 - Horizontal temperature gradient represented by Nimbus 6 data, radiosonde data, and objective analysis values.

Temperature Gradient Accuracy

To a large extent the error correlation featured above is a manifestation of the bias error mentioned in the section on mean and standard deviation of differences. A way of avoiding this deficiency in the data is to use the values in a relative sense. That is, instead of applying the satellite temperatures as absolute values, they might be used only to indicate temperature gradient, as obtained from adjacent measurements. In this way the bias common to the two values is removed.

Figure 4 examines the accuracy of gradients represented by satellite measurements as compared to those represented by radiosondes and objective analyses. The approximate distance over which the gradients are measured is shown on the ordinate, whereas the standard deviation of the gradient sample is shown on the abscissa. In all cases the gradient represented by satellite temperature observations is substantially smaller than that given by radiosondes, but approximately equivalent to that represented by the smoother objective analyses. In terms of application to objective analysis, the satellite data on temperature gradient appears to be quite adequate.

Conclusion

Some basic conclusions may be drawn from the above discussion. Satellite temperature soundings as represented by the DST data sets continue to show substantial differences when compared to radiosonde data. The discrepancies are mitigated by comparison to the smoother objective analysis values but still appreciable. Nevertheless, the satellite data are valuable in meteorologically active areas and should possibly be given greater weight there. A significant problem exists in terms of spatially correlated bias errors in the observations. However, the satellite data appear to faithfully represent temperature gradient information, at least on the scale incorporated in synoptic objective analysis, and should possibly be processed and utilized in that manner.

C-4

Paper No. 50

MICROWAVE RADIOMETRIC MEASUREMENTS OF SEA-SURFACE PARAMETERS

B. M. Kendall and J. C. Blume, *Langley Research Center, Hampton, Virginia*

ABSTRACT

A technique to remotely measure sea-surface temperature and salinity (for concentrations greater than 5 parts-per-thousand) with accuracies of 1°C and 1 part-per-thousand (°/oo), respectively, was demonstrated with a two-frequency microwave radiometer system.

INTRODUCTION

Because the microwave emission of ocean water is dependent on temperature and salinity, it is possible to utilize microwave radiometers to sense water surface temperature and salinity remotely. The emission is more dependent on salinity at the lower microwave frequencies and more dependent on temperature at the higher microwave frequencies. Thus a system comprising two microwave radiometers, operating at 1.43 and 2.65 GHz can provide a remote measurement of both parameters. The use of a dual-frequency microwave radiometer system has an advantage over other types of remote sensing instruments in that it can both operate at night and probe through clouds. Corrections to the radiometer apparent temperature for various atmospheric and water surface effects are necessary for accurate inversion of the measurements to obtain surface water temperature and salinity. Inversion algorithms developed for this purpose were used to produce contour maps of these quantities.

Radiometer System

The L-band (1.43 GHz) and S-band (2.65 GHz) radiometer system used in this investigation constitute a third generation of advanced switched radiometers. These radiometers are based on the application of two concepts to the switched input type receiver. The first concept is to equalize the temperature of the reference noise source at the circulator switch with

the temperature of the lossy microwave components between the antenna terminal and receiver input and maintain this temperature extremely constant (±0.03 kelvin). The second concept is to use a feed-back loop to inject pulsed portions from a constant noise source (avalanche diode) into the received noise power at the antenna terminals until the noise power of both circulator switch inputs is the same. The pulse frequency, which determines the average value of the injected noise power, is a measure of the noise power (radiation) received by the antenna. As a result of these two design improvements, the radiometers are nearly independent of gain variations and errors that are contributed by front-end losses. The radiometers therefore exhibit the long term stability that is necessary to achieve absolute brightness temperature measurements to within a few tenths kelvin.

A simplified block diagram of the radiometer system is shown in figure 1. The S-band and L-band radiometers have resolutions of ±0.08 kelvin and ±0.09 kelvin respectively, and both have an absolute accuracy, with suitable calibration, of better than ±0.2K.

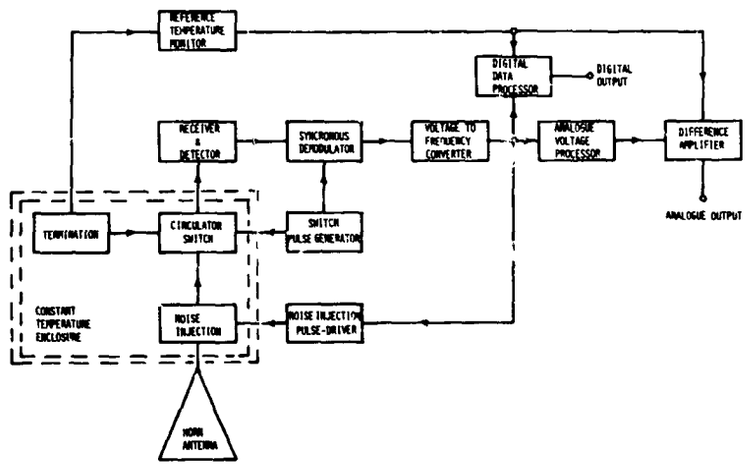

Figure 1.-Simplified block diagram of precision radiometer

Measurement of Radiometric Apparent Temperature

Quantitative measurements of the thermal emissic from the sea surface require corrections for the radiative and transmissive properties of the intervening atmosphere and sky, antenna beam efficiency, and sea surface roughness. At the measurement wavelengths of 11 and 21 cm there are four principal atmospheric and sky effects which must be considered: extra-terrestrial background radiation; radiation frc galatic and discrete celestial radio sources; attenua tion from oxygen and water vapor; and radiation from the sun. Unless the sea surface is perfectly smooth, (no wave) a surface roughness correct is necessary at some microwave frequencies due to the emissivity-roughness dependence. For the exact measurement of the apparent temperature, the antenna should have a "pencil" beam pattern. Since this is impossible to achieve, an antenna pattern correction also must be made.

Determination of Salinity and Temperature

The brightness temperature measured by an ideal radiometer is related to the molecular temperature of a radiating surface via the emissivity of the surface The emissivity of a dielectric surface at a particula wavelength is determined by its complex dielectric constant which for sea water is a function only of temperature and salinity. Plots of brightness temperature versus salinity and surface temperature at 1.43 GHz and 2.65 GHz were derived from experimental measurements of the dielectric constant of sea water at 1.43 GHz and 2.65 GHz.

In order to invert the brightness temperatures t corresponding values of temperature and salinity a regression equation was developed. The regression cc efficients were found from input data consisting of tables of brightness temperatures, one at 2.65 GHz ar one at 1.43 GHz, as a function of salinity and molecu lar surface temperature.

Flight Test

The L and S-band radiometer system was installed on a NASA C-54 aircraft, and a functional check-out flight was conducted from the NASA Wallops Flight Center over the lower part of the Chesapeake Bay and adjacent Atlantic Ocean. A flight over the entrance to the Chesapeake Bay was selected because the mixing of fresh and salt water there should result in high

salinity gradients, and instrument performance could therefore be verified over a wide range of salinity concentrations. Both radiometers were calibrated before the flight by using a specially designed liquid nitrogen cryogenic antenna load placed under and closely coupled to the antenna. The measured radiometric data together with latitude and longitude coordinates from the aircraft's inertial navigation system were recorded on digital magnetic tape and computer-processed. The sea truth data were obtained from several locations in the measurement area. A comparison was made of the radiometrically measured values of surface temperature and salinity with those taken at the sea truth locations. The resulting error mean deviation of -0.52 °/oo and + 0.55°C and error standard deviation of 0.92 °/oo and 0.59°C for salinity and surface temperature respectively seem to indicate that the desired accuracy of 1 °/oo for salinity and 1°C for temperature was achieved. The calculated values of salinity and surface temperature were plotted as a function of geographic position. A contour map of the salinity distribution is shown by isohalines with 2 °/oo increments in figure 2. A contour map of the surface temperature in 2°C steps is shown in figure 3.

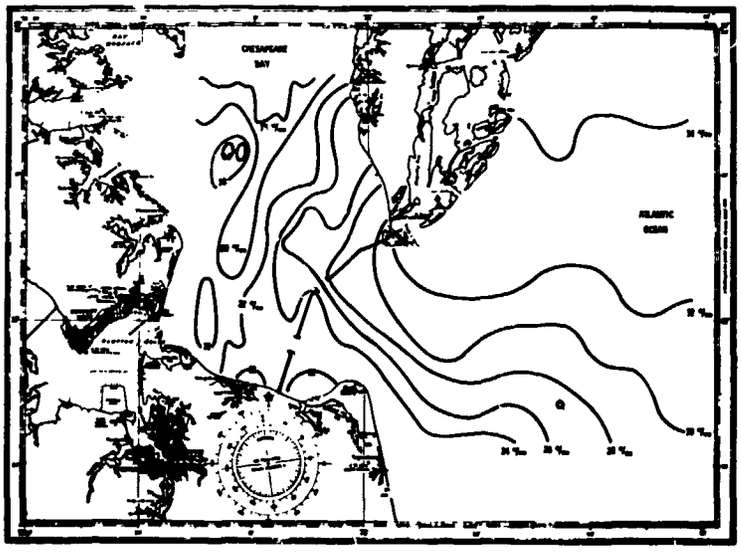

Figure 2.- Isohalines of the lower Chesapeake Bay

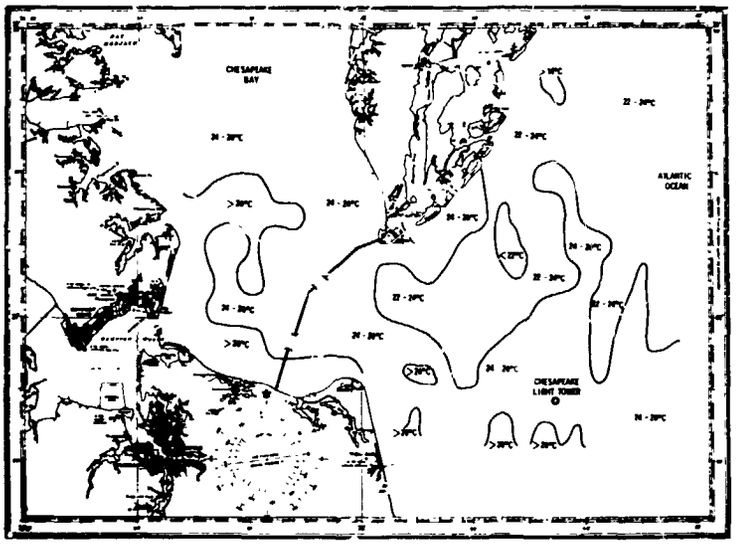

Figure 3.- Temperature contours at the lower Chesapeake Bay

Concluding Remarks

A dual-frequency (1.43 and 2.65 GHz) radiometer system was developed to measure salinity to 1 °/oo (for S > 5 °/oo) and sea-surface temperature to 1°C. This system utilized a null-balancing feedback circuit with noise injection for stabilization. It was operated from an aircraft over the lower Chesapeake Bay and adjacent coastal area of the Atlantic Ocean to map salinity and sea-surface temperature. To obtain the stated accuracies the radiometer data were corrected for cosmic radiation, atmospheric effects, sea surface roughness, and antenna beam efficiency.

D47

N79-20624

Paper No. 51

CLOUD CENSUS AND RAINFALL ESTIMATION FROM SATELLITE IMAGES
NASA CONTRACT NAS5-23462

F. R. Mosher, D. P. Wylie, J. H. Chu

ABSTRACT

A program has been undertaken to develop techniques for measurement of cloud and rainfall parameters from satellite images.

INTRODUCTION

Meteorological satellites produce images of clouds. With the exception of cloud drift winds, very few quantitative products have been derived from cloud images. The purpose of this study is to develop quantitative techniques to measure and use cloud parameters, and to estimate convective rainfall and latent heating using satellite image data. The effort is divided into three phases. The first phase, which was just completed, was a study of the potential users of cloud measurements and rainfall data: their requirements, the availability of existing techniques, and the future developments required to meet the potential user requirements. In the second phase we are currently performing scientific studies and developing the objective cloud parameter and rainfall estimation techniques. The final phase will be to demonstrate and transfer the techniques to appropriate users.

CONCLUSIONS FROM POTENTIAL USER SURVEY

Of all the various user groups, the climate modeling community has the most pressing needs for cloud data for developing radiation and latent heating parameterization schemes. They also have the most stringent accuracy requirements as stated in the GARP requirements. In addition, cloud climatologies are also required to verify the performance of models. Presently available cloud measurement products such as the Air Force 3-D Nephanalysis or sounding retrieval cloud heights are not sufficiently accurate to meet the parameterization needs. The presently available climatologies (Miller and Feddes, 1971) of total cloud cover without height discrimination are not sufficient

to meet the verification requirements of the modeling community.

The needs of the aviation community for cloud information have been recognized. The Air Force produces the 3-Dimensional Nephananlysis (3DNEPH) every three hours to meet their cloud information needs for programming reconnaissance satellites and flight operations. NOAA produces weather depiction fax charts based on surface observations of clouds and has initiated an experimental satellite cloud analysis fax chart for use by flight service forcasters. The initial reaction to the NOAA/NESS satellite cloud analysis has been favorable.

The most pressing forecast needs for cloud information is for short time mesoscale forecasts of fog and convective storms. The analysis techniques of determining cloud heights, thickness, growth rates, etc. are presently at hand. However, a new generation of hardware is necessary to provide the forecast offices with real time access to quantitative satellite data.

The user survey showed the three main users of precipitation data to be general circulation modeling groups, agricultural crop prediction groups, flood forecasters and water management groups. The general circulation modeling groups are concerned mainly with global latent heat release. Their needs are reflected in the GARP data requirements of precipitation. Agricultural crop predictions require high spatial resolution land data. In contrast, the flood forecasters require high time resolution over limited land regions. Systems which can provide precipitation data include raingauge networks, radar, satellite microwave sensors, and satellite visual and infrared images. In general all the systems are only accurate to within a factor of 2. Each of the systems has special strengths, but each also has some weakness. Hence, no one system is ideal for meeting all the user requirements. The ultimate operational system will probably be a composite of several systems. Composite systems of satellite microwave over water and imaging techniques over land are feasible for global precipitation data, as would be a composite of raingauge calibrated digitized radar and geostationary image techniques for hydrological and flash flood forecasts.

TECHNIQUE DEVELOPMENT

The technique development phase has been divided into two stages. The first stage involves collection of data sets for processing and verification, and the

analysis of the physical basis for the subsequent technique development. This is the current stage of progress on this effort.

The techniques which presently exist for the cloud census include a cloud height program (Mosher, 1975) which uses the visible data to compute the optical thickness and emissivity required to correct the infrared temperature. Currently a modified standard atmospheric sounding is used to convert the temperature to a height. However, a height comparison to aircraft cloud reports showed errors of up to 100mb caused by the sounding conversion. The program is presently being modified to allow the use of synoptic radiosonde soundings.

The optical thickness is computed using a plane-parallel homogeneous assumption for visible light scattering. Using an average extinction coefficient, it is possible to convert the optical thickness to physical thickness. However, McKee and Cox (1974) have shown through Monte-Carlo simulation that the effects of the cloud edges can cause significant departures from plane-parallel theory. To investigate the finite cloud, non-homogeneous problem, a geometric cloud scattering model was developed. The model consists of building blocks of cuboidal cells whose transfer function was calculated by a Monte-Carlo simulation (Davis, 1976). The blocks are stacked to construct a cloud, and the interactions between the block faces are computed. Figure 1 shows brightness cross sections across a simulated cloud. The sun is on the left with a 13° zenith angle. The cloud has dimensions of optical thickness of 100 x 400 x 30 (6.3 x 24.5 x 1.8km). Experiments were run varying the cloud thickness, placing liquid water concentrations in the cloud center, putting a tower on the cloud, and putting a hole in the cloud center. The simulations showed the edges of the cuboidal cloud to cause a brightness gradient across the cloud top. Putting a liquid water concentration in the center 3 x 3 pixels of the top half of the cloud resulted in a brightness increase as shown by figure 1. This liquid water concentration placed at the bottom half caused only slight brightness increase however. When a tower was placed on top of the cloud, the net effect was to generate a dark spot as is shown by figure 1 because of light leakage out the sides of the tower. A hole in the cloud also generated a similar appearing dark spot to that of the tower. Further work is required to verify the simulations and then incorporate the results into an improved thickness and cloud property determination. Efforts are also progressing on techniques to determine cloud type and size

distributions. A cloud census of the GATE area for phase III will be produced and related to cloud parameterization schemes using GATE data and radiation measurements. Processing of GATE radiosondes has begun for use in providing the dynamical parameters for comparison to cloudiness.

In the rainfall efforts, arrangements have been made for an exchange of satellite and calibrated radar data with McGill University in Montreal. This data will be used as ground-truth for testing satellite rain estimation techniques in mid-latitudes.

The existing techniques for rainfall estimation have also been examined for possible improvements. The scheme developed by Griffith et.al. (1978) which correlated rain rates with the area of the cloud has been modified. In the old scheme, the rain volumetric rate was weighted to account for varying rainfall observed in the different growth stages of the cloud. The maximum area reached by the anvil was used as a base for separating growth and decay stages. This technique is not conducive to forecast situations since it requires the convection to mature before measurements can be made. For this reason we have changed the rainestimation scheme to include the anvil growth rate.

$$R = K_1 A + K_2 \, dA/dt$$

In this scheme the coefficients K_1 and K_2 are not changed over the clouds life cycle. The weighting for the heavy rainfall is accounted for by the growth term dA/dt. Anvil growth rates by themselves are partially correlated with volumetric rain rates (figure 2). In the GATE data a correlation coefficient of 0.67 was found between the volumetric rain rates and the anvil growth rates over a 1 hour period during the growth phase of the clouds. While anvil growth rate does not fully explain all the variations in rain rates, it does provide rainestimations that are slightly better than the old scheme.

Using the Montreal and GATE data, we will examine the environment of the clouds for factors which can affect the cloud's precipitation efficiency. Profiles of wind, temperature, and humidity will be studied for their effect on the rainfall efficiency. Convection studies will also attempt to relate the intensity of the convection to the depth of the moist inflow layer to the clouds and the temperature stability. These parameters will be studied so that a better understanding of the satellite data can be made.

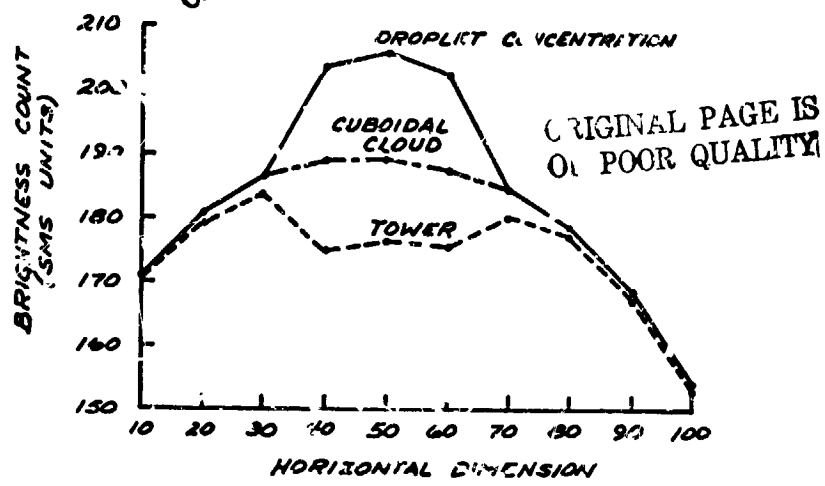

figure 1 Theoretical brightness plot across a finite cuboidal cloud.

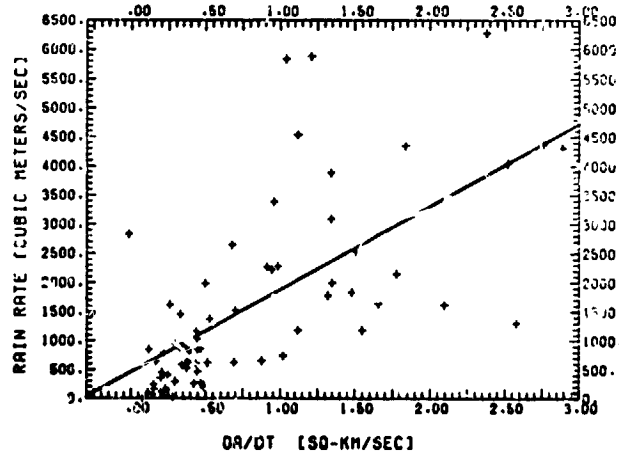

figure 2 Measurements of cloud anvil growth rates vs. volumetric rain rate.

Davis,R. 1976. U. of Wis.Ph.D.thesis, Madison, Wis.
Griffith,C.G.,W.L.Woodley, D.W.Martin, and J.Stout, 1978. To be published Mon. Wea. Rev.
McKee,T.B.and S.K.Cox, 1974. JAS 31, 1885-1892.
Miller,D.B.and R.G. Fedes, 1971.Global Atlas of Relative Cloud Cover, 1967-70.U.S.Dept. of Comm.273pp.
Mosher,F.R.1975. Final Rep. NAS5-23296

Paper No. 52

COMPARISON OF THE LAST TWO WINTER SEASON MONTHLY ZONAL CLOUD FRACTIONS AS DERIVED FROM NIMBUS-6 ERB DATA

Robert J. Curran, *Goddard Space Flight Center, Greenbelt, Maryland*

ABSTRACT

Monthly zonal albedo determinations made by Nimbus-6 ERB have been used to form monthly zonal cloud fractions. The Fall-Winter-Spring seasons of 1975-76 are compared with the same seasons 1976-77.

The radiation exchange between the earth, sun and free space is the ultimate driver of the meteorological and oceanographic processes which form the earth's climate. The major constituent of the earth-atmosphere system which moderates the radiation exchanges is atmospheric clouds. The earth's global albedo, which is the ratio of the solar flux reflected from the earth to that incident, is approximately 0.30. Close to one half of this global albedo is due to clouds, emphasizing their importance to the energetics of the system.

Regions of the earth with minimal cloud cover for extended periods of time absorb most of the sunlight incident on them and thus act as sources of energy to the system. Similarly, relatively cloud free regions tend to loose much energy by emission of longwave radiation to space. Subtle changes in the temporal and spacial distribution of clouds can strongly effect the magnitude and position of the sources and sinks of radiation energy from the sources to the sinks, measurements of the statistical properties of cloud are necessary.

Satellite imagery such as that from the geosynchronous meteorological satellites demonstrate the strong differences in reflectance between clouds and the clear surface/atmosphere. These reflectance differences are greatest for tropical and mid latitudes where most albedos range between 0.15 and 0.25. Cloud albedos, for many of the cloud masses found in these latitudes, are 0.50 or greater. These differences allow large scale measured albedos to be decomposed into cloud obscured and cloud free fractions. The present study uses albedos derived from measurements made by the Earth Radiation Budget (ERB) instrument on the Nimbus-6 meteorological satellite.

The Nimbus-6 satellite is sun-sunchronous and thus observes such latitude at fixed local time. Nimbus-6 was placed in orbit such that all latitudes between 60N and 60S are observed within one hour of local noon. Monthly, zonal determinations of the albedo were gathered from July 1975 to present. The low spectral resolution channels were used to form a data set covering the winter season 75/76 and the winter season 76/77.

To separate cloud contributions from the measured data it is necessary to form a model of the expected cloud free albedo distribution. A model was formed by taking into account the latitude distributions of land and water, the monthly extent of ice and snow cover and the solar zenith angle dependent effects of the cloudfree atmosphere.

The water surface albedo varies with solar zenith angle in accordance with the data of Knodratyev. Ice and snow cover data were gathered from the Nimbus-6 Electronically Scanning Microwave Radiometer (ESMR) and from minimum albedo products from the NOAA Scanning Radiometer.

Calculations of the zonal cloud fractions for the Fall-Winter-Spring seasons of last year are shown graphically in Figure 1. The two major features identifiable in the figure are the southern hemisphere maximum at approximately 65° south latitude and the variable northern hemisphere maximum which is roughly situated in the northern mid to high latitudes. The position and seasonal variation in the southern hemisphere maximum agree with the data of Van Loon.

Figure 2 gives the monthly zonal albedo differences between the winter of 75/76 and that of 76/77. Because the same instrument is being used to collect the data and because the satellite orbit is sunsychronous and thus reproducible from year to year this data set is ideal for differential studies as comparisons evident in January is suspect and thought to be an artifact of the January 1977 data processing. Therefore, for much of the comparisons January is excluded.

The differences in cloud fraction amplify the albedo differences. Large increases in cloud fraction may be noted in the fall and early winter 76/77. These increases are followed by decreases in northern hemisphere low latitude cloud fractions in the late winter and early spring.

The decreases in low latitude cloud fractions are defensible because of the lack of large enough surface albedo changes. However, between 40^{0} and 50^{0} latitude changes in cloud cover may be partially explained in terms of changes in the position of the ice/snow boundary between the two years. Efforts are proceeding to assess the impact of these contributions. The magnitude of the albedo differences at 40^{0} to 50^{0} are greater than that expected from snow cover alone and must be, at least partially the result of changes in cloud cover.

References

Kondrat'ev, K. (editor), "Radiation Characteristics of the Atomsphere and the Earth's Surface, " merind Publishing C. Pvt. LTS., New Delhi (1973)

Van Loon, H., 1972: Cloudiness and precipitation in the southern hemisphere. Meteor Monogr. 13, Chapter 6.

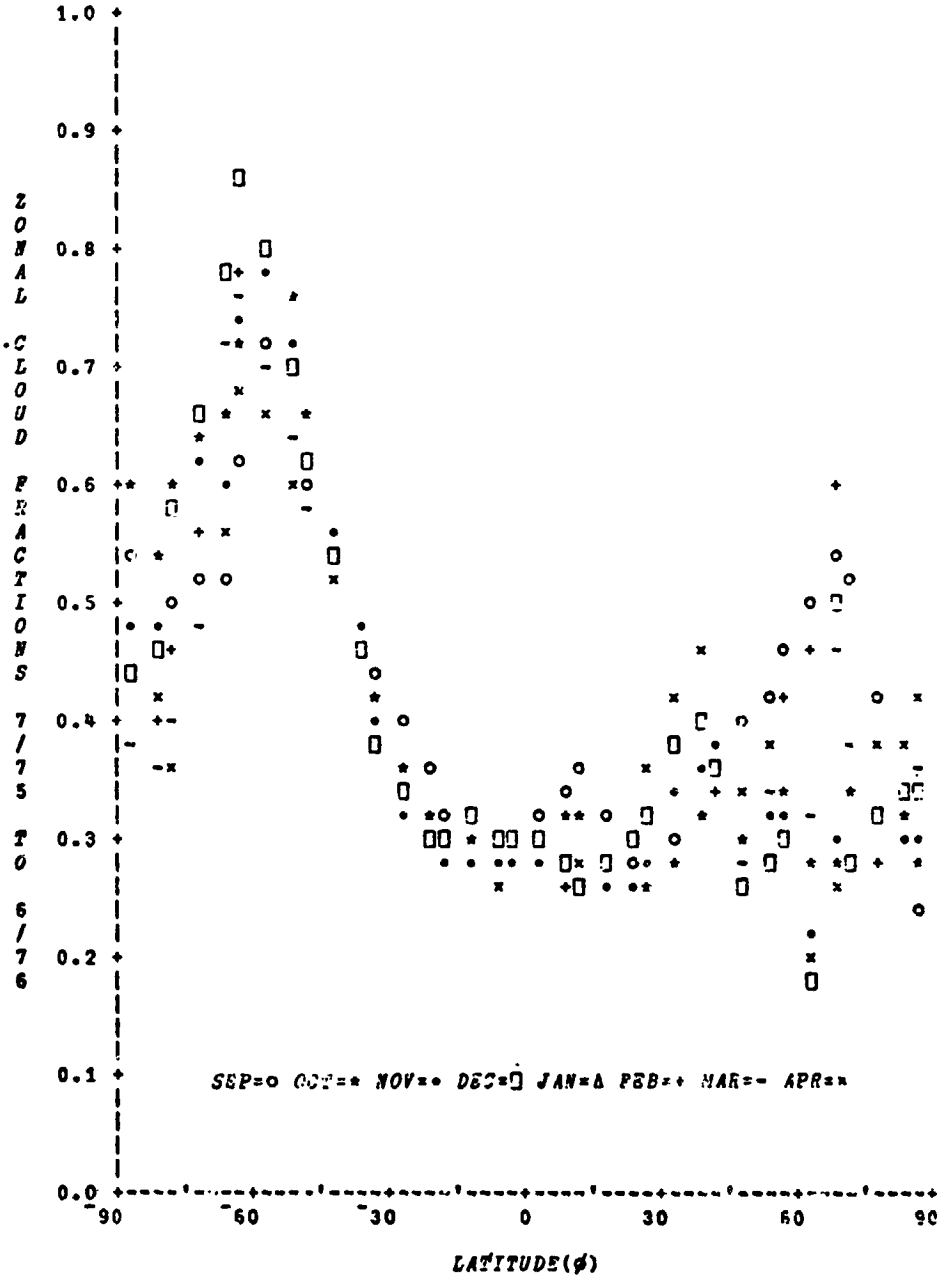

Figure 1. Derived Monthly Zonal Cloud Fractions for the Months September 1975 to April 1976. January 1976 has been excluded from this graph.

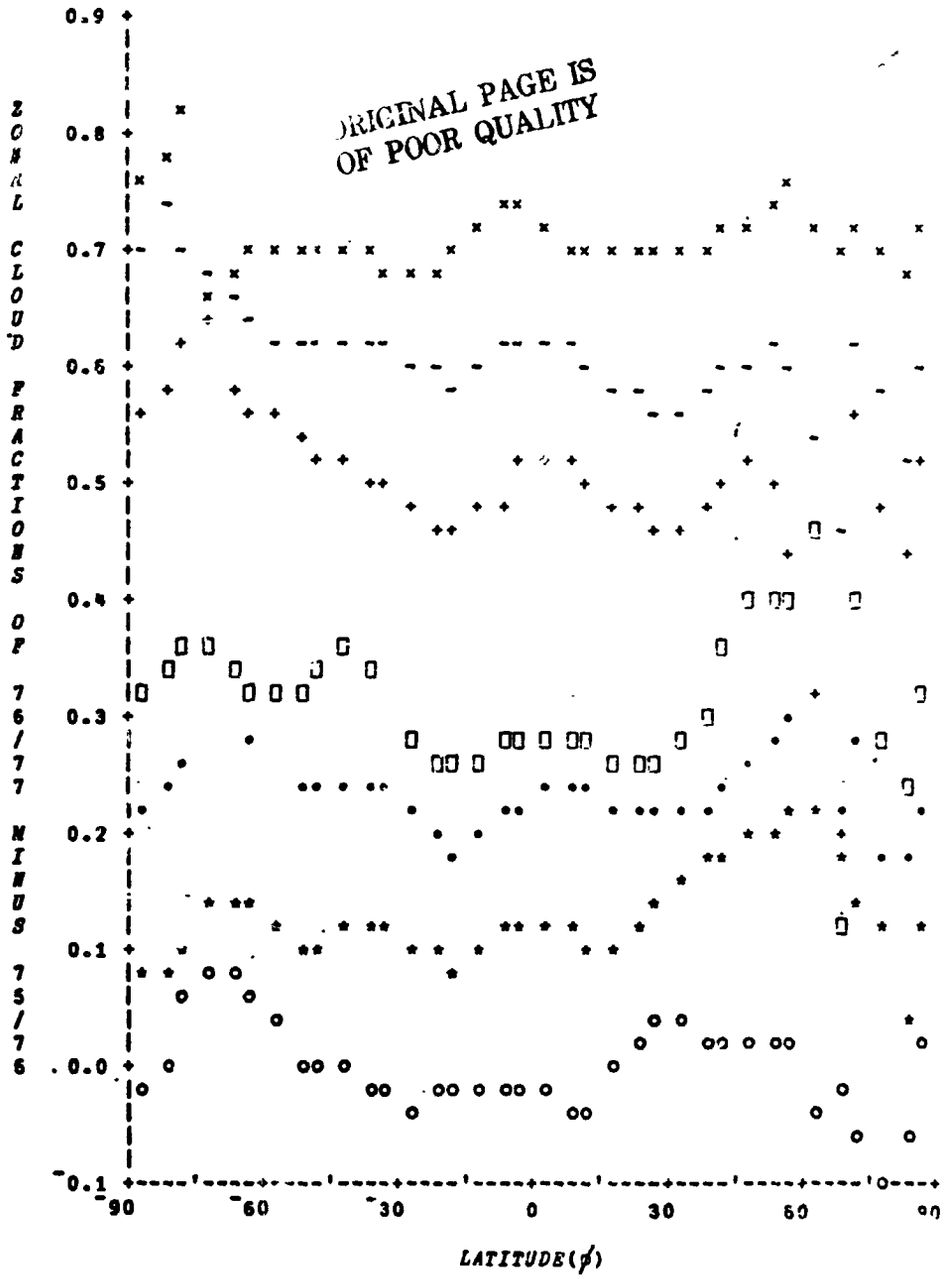

Figure 2. Zonal plots of the differences in monthly cloud fractions. For each succeeding month 0.1 has been added to the differences. Because the January data is questionable and tends to confuse the plot, it has been deleted from this Figure.

Paper No. 53

N79-20626

ELECTROCHEMICAL CONCENTRATION CELL OZONESONDE PERFORMANCE EVALUATION

A. L. Torres and A. R. Bandy, *Drexel University, Philadelphia, Pa.*

ABSTRACT

A large number of electrochemical concentration cell ozonesondes have been calibrated relative to ultraviolet photometric absorption (254 nm) to determine their precision and accuracy. The average agreement with UV photometry was found to be good, but with considerable variation from one ECC ozonesonde to another. Applying individual calibrations to vertical ozone profiles reduced the systematic differences between ECC ozonesonde total ozone values and Dobson spectrophotometric determinations of the same quantity, but did not improve random differences.

INTRODUCTION

Electrochemical concentration cell (ECC) ozonesondes were developed by Komhyr (1, 2) for use in obtaining vertical profiles of ozone up to about 35 km. The sensor is based on the oxidation of iodide ions to iodine by ozone, and the subsequent electrochemical conversion of iodine back to the iodide form.

A program was initiated at Drexel University, in cooperation with NASA's Wallops Flight Center, to evaluate the quality of ozone data obtained by the use of ECC ozonesondes. As a part of this program, a system was set up whereby ozonesondes were calibrated relative to a laboratory-grade ozone monitor prior to their use in atmospheric soundings. Ultraviolet photometric absorption (254 nm) was chosen as the primary calibration standard, while Dasibi Environmental Corporation ozone monitors were used as convenient secondary standards. This report describes some of the results found thus far, especially those relating to the precision and accuracy obtainable with the ECC ozonesonde.

EXPERIMENTAL

The UV photometer was constructed around a 3 m glass absorption cell with quartz windows. A vycor-jacketed mercury penlamp, and bandpass filters were used to produce and isolate 254 nm light. The detector photomultiplier signal was converted to voltage with a parallel RC filter, the output of which was read man-

PAGE 294 INTENTIONALLY BLANK

ually using a 5½-digit digital multimeter. Ozone concentrations were computed from the UV data using the relation

$$[O_3]\,(\text{ppbv}) = \frac{10^9 T}{273 P k L} \log \frac{I_0}{I} \qquad 1)$$

where T = temperature
P = total pressure (atm)
k = absorption coefficient (135 cm^{-1} atm^{-1} [3])
L = pathlength (cm)
I0 = intensity with ozone-free air
I = intensity with ozonated air.

A small ozone generator produced 0 - 200 ppbv ozone at 5 ℓ min^{-1} during the calibrations.

ECC ozonesondes were calibrated relative to a Dasibi ozone monitor by simultaneous sampling of ozonated air (0 - 250 ppbv) from a common manifold. The ozonesonde was electronically coupled to a 1680 MHz meteorological radiosonde for data transmission to a nearby receiver. Step changes in ozone concentrations were used to determine the instrument's response time.

RESULTS AND DISCUSSION

Well over a hundred ECC ozonesondes have now been calibtated relative to UV absorption. When the individual intercepts and slopes are averaged, the result is

$$[O_3]_{ECC} = 0 \pm 5 \text{ nb} + (0.99 \pm 0.06)\ [O_3]_{UV} \qquad 2)$$

where the uncertainties represent one standard deviation about the means. The ECC ozonesonde is seen to agree with UV photometry quite well on the average, but with considerable variation from one ozonesonde to another. The uncertainty in the slope for example, is about 10% at the 90% confidence level. Many of the calibrations were carried out by simultaneously connecting two ozonesondes and the Dasibi to a common manifold. The calibration variations between pair-member ozonesondes indicated the variations to be an ozonesonde problem, and not a result of drifts in the calibration equipment.

The time required for an ECC ozonesonde to complete 85% of its final response to a step-change in ozone concentration averaged 51 seconds. This may result in a slight distortion of vertical ozone profiles because of the climb-rate, but will have relatively little effect on the total ozone obtained by integrating the profile.

The individual calibrations were used to correct the vertical ozone profiles in 30 test flights, 20 in 1976 and 10 in 1977. The total ozone values from the ozonesondes were then compared with Dobson ozone spectrophotometer measurements made at the time of the soundings. Applying the corrections reduced the average percentage difference (systematic error) between the ozonesonde and Dobson measurements from 7.1 to 1.3% for the 1976 data, and

from -5.7 to -1.4% for the 1977 data. The corrections had no significant effect on the random variations, which were of the order of 10%.

REFERENCES

1. W. D. Komhyr, "A Carbon-Iodine Sensor for Atmospheric Soundings," Proc. Ozone Symposium, W.M.O., Albuquerque, N.M. (1964)
2. W. D. Komhyr and T. B. Harris, "Development of and ECC Ozonesonde," NOAA Technical Report ERL-APCL18, Boulder, Colo. Feb. 1971
3. W. B. Demore and M. Patapoff, Environ. Sci. Technol., Vol. 10 No. 9, 897 (1976) and references therein

Paper No. 54

DECONVOLUTION OF EARTH RADIATION BUDGET DATA

R. N. Green and G. L. Smith, *Langley Research Center, Hampton, VA*

ABSTRACT

The theory of deconvolution of wide field of view Earth radiation measurements is applied to Nimbus 6 ERB data and results with a 15° regional resolution are presented

INTRODUCTION

The Earth Radiation Budget (ERB) instrument on the Nimbus 6 spacecraft has two wide-field-of-view detectors for measuring solar (shortwave) radiation reflected from the Earth and Earth emitted (longwave) radiation These measurements have very low spatial resolution. The problem of relating these wide-field-of view measurements at spacecraft altitude to the flux at the top of the atmosphere is one of resolution enhancement and has been treated theoretically. The case of Earth emitted radiation permits considerable simplifications, whereby the solution may be expressed simply in terms of spherical harmonics. Because of the statistical nature of the problem, the spherical harmonic coefficients are evaluated by a least squares method rather than by use of the orthogonality of spherical harmonics. This paper presents results thus far obtained from the application of this theory to Nimbus 6 ERB data. The case of reflected solar radiation has been studied by computer simulations and shown to be feasible.

RESULTS

The ERB instrument has operated since July 1975, shortly after launch of the Nimbus 6 spacecraft, to the present has has provided much Earth radiation budget data with its WFOV channels. We have analyzed the Earth emitted radiation data for the month of August 1975, during which time ERB was operated on a duty cycle 2 days on and 2 days off. During this time, six complete duty cycles of data were collected. Each duty cycle of data has been analyzed separately, resulting in a short time history of the Earth emitted radiation.

Each day, the spacecraft completes 14 orbits, so that requiring 2 1/2 data points per cycle results in a maximum of five cycles resolvable in the longitudinal direction. Accordingly, for each duty cycle spherical harmonic coefficients were computed

through fifth degree and fifth order, for a total of 36 coefficients. These coefficients are computed at satellite altitude from the data and converted to top of the atmosphere values by the factor $1/\lambda_j$, where λ_j was computed using a nominal limb-darkening function. It was found that through the fourth degree, the zonal coefficients predominated, and coefficients corresponding to longitudinal variations were relatively small. For fifth degree, the longitudinal variations were as large as the zonal. The time histories of the zonal coefficients through fourth order are shown in figure 1. It is seen that the time variations are small; because they are so small it is not clear whether they are due to real fluctuations of the atmosphere, sampling variations, or some other effect. In addition, the spherical harmonic coefficients were computed out to twelfth degree and twelfth order for the full month of data. The resulting degree dispersion σ_n for the month is shown in figure 2, as a function of degree. For $n = 3$ through 11, log σ_n appears to vary quite linearly with n, with the exception of $n = 6$, which is low and $n = 7$, which is high by a corresponding amount. The reasons for these results are presently under study.

The zonal distribution of radiation for August 1975 as deconvoluted to the top of the atmosphere is shown in figure 3. For comparison, the zonal distribution as inferred from the data by using a simple inverse square relation is shown as a dotted line. It is seen that the zonal results do not differ markedly between the two methods; this is because there is little effect on the zonal distribution due to high degree terms, which are the terms most attenuated by the WFOV measurement.

The global distribution of Earth emitted radiation for August 1975 as deconvoluted to the top of the atmosphere is shown in figure 4. This map was constructed using terms through twelfth degree, corresponding to 15° resolution on the globe. It is seen that the results are resonable, although definitive statements must await comparison with other measurement techniques, e.g., the scanner results.

CONCLUDING REMARKS

The implications of these results to atmospheric physics are being investigated. This analysis needs to be done for a much longer data period. Finally, parameter estimation should be applied to the problem of deconvolution of reflected shortwave radiation.

ACKNOWLEDGEMENT

The authors are grateful to Dr. Herb Jacobowitz, Ben Howell and other members of the Meteorological Satellite of NOAA for providing us with ERB data and for discussions with respect to the data.

REFERENCES

1. Smith, W. L.; Hickey, J.; Howell, H. B.; Jacobowitz, H.; Hilleary, D. T.; and Drummond, A. J.: Nimbus 6 Earth Radiation Budget Experiment, Applied Optics, Vol. 16, No. 2, Feb. 1977, pp. 306-318.

2. Smith, G. L.; and Green R. N.: "A Technique for Analysis of Low Resolution Measurements of Earth Radiation Budget," Second Conference on Atmospheric Radiation, American Meteorological Society, Washington, D.C., Oct. 29-31, 1975.

3. Smith, G. L.; and Green, R. N.: "Theoretical Analysis of Wide Field of View Radiometer Measurements of Earth Energy Budget," Fifth Annual Remote Sensing of Earth Resources Conference, Tullahoma, Tennessee, March 29-31, 1976.

4. Smith, G. L.; Green, R. N.; and Campbell, G. G.: "A Statistical Interpretation Technique for Wide Angle Radiometer Measurements of Earth Energy," Fourth Conference on Probabil and Statistics in Atmospheric Science, American Meteorologic Society, Tallahassee, Florida, Nov. 1975.

5. Smith, G. L.; and Green, R. N.: "The Analysis of Wide Field of View Radiometer Measurements of Earth Radiation Budget," COSPAR XIX Plenary Meeting, Philadelphia, Pennsylvania, June 1976.

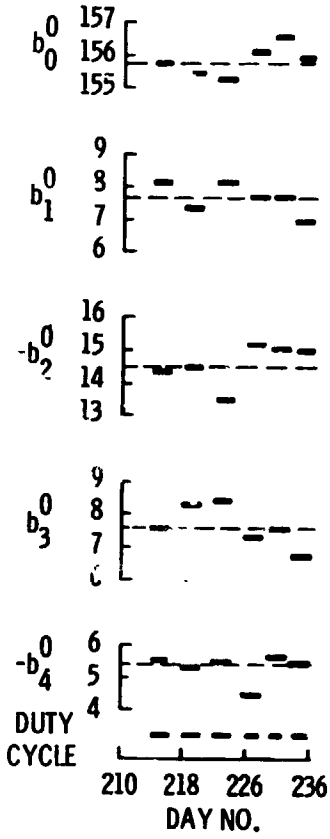

Fig. 1-Time variation of lowest degree zonal terms for Earth emitted radiation, August 1975

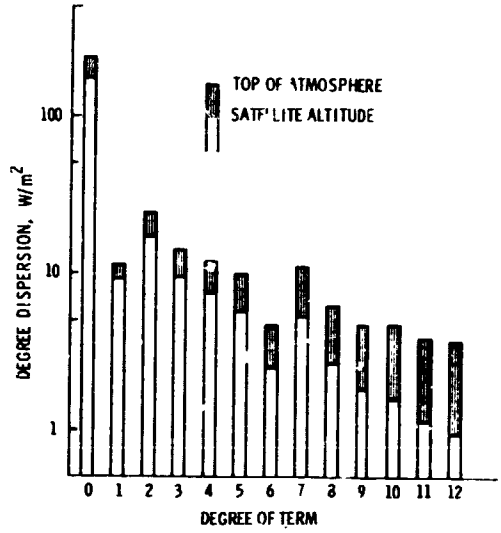

Fig. 2-Degree dispersion of Earth emitted radiation, August 1975.

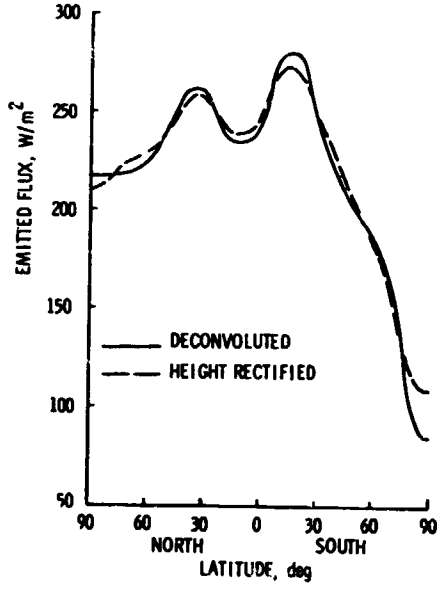

Fig. 3-Zonal distribution of Earth emitted radiation

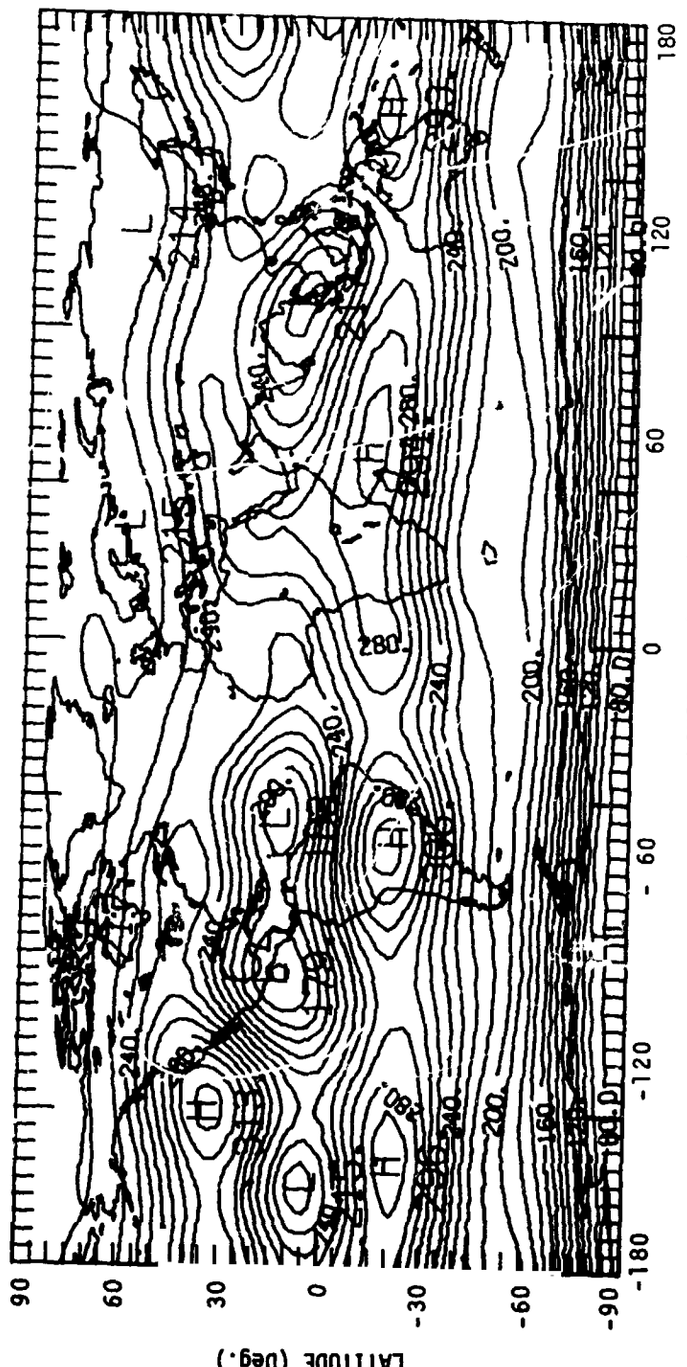

Fig. 4-Map of Earth emitted radiation at top of atmosphere for August 1975

N79-20628 D53

Paper No. 55

SIMULATION STUDY OF A METHOD FOR ANALYZING WIDE FIELD OF VIEW RADIOMETER MEASUREMENTS FROM SATELLITES AND SOME ANALYSIS OF ESSA 7 DATA

W. L. Weaver, *Langley Research Center, Hampton, Virginia*

ABSTRACT

A method of relating wide field of view radiometer measurements from satellites to the Earth longwave flux field is simulated and is used to obtain zonal and global averages of longwave (LW) flux for ESSA 7.

INTRODUCTION

A study was performed in which irradiance measurements calculated over a simulated model of the Earth's longwave radiation field were reduced to longwave Earth fluxes using shape factors. This method has been used extensively to analyze data from wide field of view (WFOV) radiometers on satellites. Results from the method are relatively simple to interpret, and successful results do not depend on uniform sampling. Sets of irradiance measurements were generated, and average fluxes were estimated on zonal and global scales.

Measurements from the low resolution infrared radiometer (LRIR) on the ESSA 7 satellite were reduced to Earth fluxes using a shape factor, and some zonal and global averages of the longwave flux are presented.

SIMULATION STUDY

Program Description and Scope of Study - The longwave Earth flux model was based on data obtained from the Nimbus 3 satellite. It was comprised of 1654 flux regions, each with an area approximately equal to a $5^\circ \times 5^\circ$ region at the equator. A discrete irradiance, I_i, from a region of flux, W_i, is illustrated in figure 1 and is given by:

$$I_i = W_i \, M(\tau_i) \, R(\theta_i) \cos \tau_i A_i / \pi \ell_i^2$$

where R is geometric response of radiometer
M is directional model of radiation field

A total measurement is the summation of I_i for all regions whose centers are in the radiometer field of view (FOV). Unrestricted and restricted FOV flat plate and spherical sensors were considered. Unrestricted FOV (UFOV) sensors have a horizon to

PAGE 304 INTENTIONALLY BLANK

horizon view and the restricted FOV (RFOV) sensors view a region with an Earth central angle (ECA) of 20 degrees. Two radiation directional models were used: Lambertian (diffuse) and a limb darkening function based on Nimbus 3 data. Sets of measurements were generated by specifying M, R, orbit characteristics, number of orbits, and data points per orbit. An estimated value of flux is related to a measurement of irradiance through a shape factor, F, by W = I/F. Shape factors used in the study account for the radiometer geometric response, but to simplify computations of the shape factors, the Earth radiation field was assumed to be Lambertian. An estimate of average flux in a 10 degree latitude zone for a set of measurements was obtained by averaging all values of flux derived from measurements whose centers were in the given zone. Estimates of average zonal flux were compared to average fluxes (actual) obtained from the simulated flux model. The figure of merit used to evaluate the method is the area-weighted average of the absolute errors in the zonal estimates (AZE). A shape factor was calculated for each data set which minimized the AZE. This optimum shape factor was then compared to the input shape factor. The error in the estimate of the global average of flux was the area-weighted average of the errors (non-absolute) in the zonal estimates.

Results - Minimum errors in the AZE were generally achieved within 15 orbits and 40 points per orbit. Figure 2 demonstrates this point for flat plate radiometers at an altitude of 600 km over a Lambertian directional model. The minimum errors are seen to be about the same for the UFOV and the RFOV measurements with magnitudes of errors less than 1.5 percent. The calculated values of the optimum shape factors for the minimum-error cases were always very nearly the same as the input values. That is, the shape factor calculated from geometric considerations appears to be a good estimator of average zonal flux. Errors in global estimates were less than 0.2 percent. Figure 3 shows how the AZE is affected by satellite altitude. The errors are seen to be about minimum at 600 km and increase to 2 percent at 1000 km for the UFOV sensor, but remain about the same for the RFOV sensor. The trend of results was similar for measurements with a spherical sensor, but the magnitude of the errors was slightly higher for the spherical sensor.

Figure 4 compares estimated values of average zonal flux with actual average values for several minimum-error cases. Figure 4a shows very good agreement between estimated and actual zonal averages for both Lambertian and non-Lambertian directional models. The average absolute zonal errors and global errors are nearly identical for the two cases. Figure 4b also indicates good agreement for the RFOV data and a Lambertian directional model. The errors almost double, however, for the non-Lambertian case. When the optimum shape factor was used to estimate the zonal averages for the non-Lambertian data set of figure 4b, the errors were reduced to about the same as those for the Lambertian case. Thus, if the directional characteristics of the radiation

field are known, a geometric shape factor may be found to compensate.

ANALYSIS OF ESSA 7 DATA

The ESSA 7 data (Sept. 1968 thru May 1969) are an important part of radiation measurements of the late 1960's. ESSA 7 had flat plate radiometers opposite each other on the outer circumference of a spinning satellite. The plates were wired electrically in series, and the composite signal was an average measurement over a spin period of 6.5 seconds. Sets of these plates with different surface coatings allowed separation of short and long wave radiation. This type of coating was known to degrade, and Dr. Fred House of Drexel University developed a scheme for their calibration using solar input measurements at Sun ingression and egression.

The ESSA 7 orbit was nearly circular with an average altitude of about 1450 km and was Sun-synchronous with a northward nodal crossing of 3 p.m. local time. The irradiances were reduced to fluxes at 30 km altitude using a shape factor developed by Dr. House and which approximated that of a cylinder. Figure 5 shows estimated zonal averages of LW flux for the first 3 months of the data period. Global averages are also shown. These estimates are lower than those derived from Nimbus 3 and 6 data. For example, using August, 1975 data from the WFOV sensors on Nimbus 6, I estimated a global average LW flux of 240.7 W/m^2. Differences in fluxes may be attributed to the different nodal crossing times. The Nimbus satellites were in Sun-synchronous orbits with 12 noon nodal crossing, and 12 noon orbits generally result in higher LW flux than afternoon orbits.

CONCLUSIONS

A simulation study showed that minimum errors in estimates of zonal and global averages of LW flux are achieved with a relatively small satellite data sample. Errors are about minimum at 600 km altitude and then increase with altitude for UFOV sensors. Errors remain about constant to 1000 km for RFOV sensors. No significant differences in flux estimates are seen between UFOV measurements for a Lambertian and non-Lambertian radiation model. Increased errors in RFOV measurements for a non-Lambertian radiation model may be reduced if the model is known. Zonal and global averages of LW flux derived from ESSA 7 data are lower than those from Nimbus 3 and 6. Differences in flux may result from differences in the orbits.

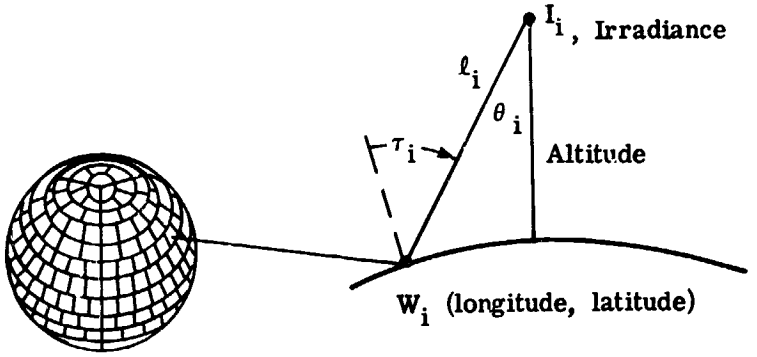

Fig. 1 - Irradiance calculated at satellite from region of simulated flux model

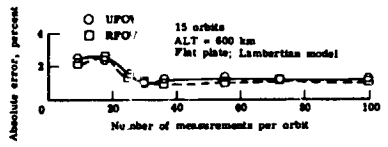

Fig. 2 - Effect of number of measurements per orbit on zonal errors

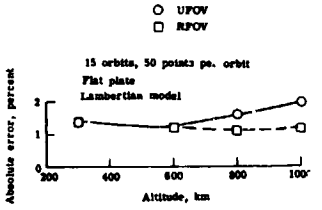

Fig. 3 - Effect of altitude on zonal error

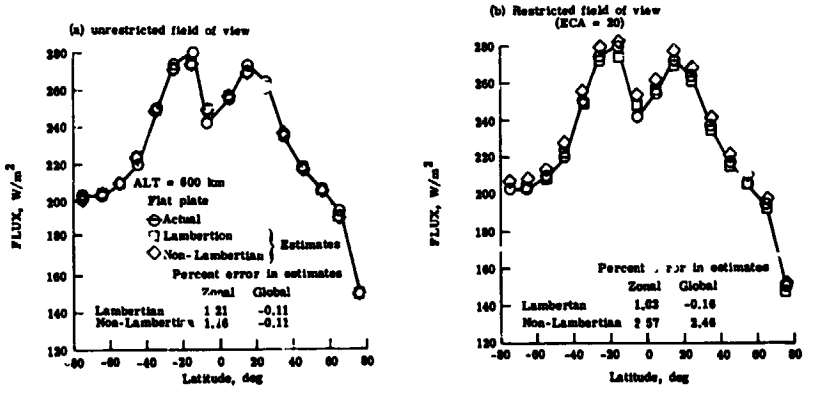

Fig. 4 - Comparisons of estimated with actual average zonal fluxes

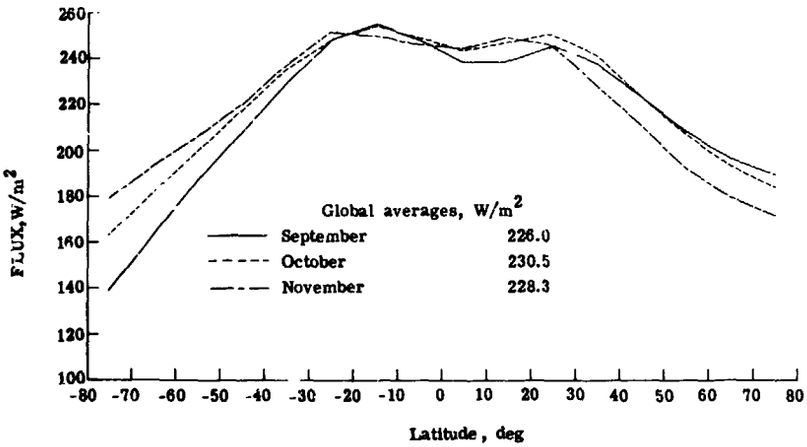

Fig. 5 - Average zonal LW fluxes inferred from ESSA 7 measurements

Paper No. 56

ERBSS SCANNER PERFORMANCE IN THE PRESENCE OF RADIATION DIRECTIONAL MODEL ERRORS

L. M. Avis, *Langley Research Center, Hampton, Virginia*
P. G. Renfroe, *Vought Corporation, Hampton, Virginia*

ABSTRACT

Simulation studies of the ERBSS scanner have been performed to determine the sensitivity of the inferred flux at the top of the atmosphere to radiation directional model errors for candidate scan plane orientations.

INTRODUCTION

The data reduction algorithms for Earth energy budget contain assumed directional characteristics of radiation emitted and scattered from the Earth-atmosphere system. The sensitivity of inferred flux to errors in the assumed radiation directional characteristics for the wide-and medium field-of-view sensors and for the scanner have been studied by mission simulations.

The radiation directional characteristics are defined by models which express, for a given surface element at the top of the atmosphere, the exitting flux per unit solid angle for each direction out to space as a fraction of the total hemispherical flux exitting the surface element. Then, in principle, a single scanner flux measurement can be converted into an inferred hemispherical flux from the FOV footprint. The variance in the inferred flux is generally reduced by multiple flux samples to a degree dependent upon the sampling distribution in space and time, the spatial and temporal variability of the flux, and the directional model errors.

SHORTWAVE DIRECTIONAL MODELS

Figure 1 shows the geometry of the solar radiation scattering process. All directional models are functions of the solar zenith angle ζ, the exit ray zenith angle θ and the exit ray azimuth angle ψ relative to the principle plane (the Sunline-zenith plane). Symmetry about the principle plane is presently assumed.

The directional models described in this paper are derived from airborne radiometer measurements reported in the literature (refs. 1-4). Progress toward directional models based on Nimbus-6 ERB data is discussed in the paper "Nimbus 6 ERB Scanner Studies for Development of Earth Radiation Budget Satellite System (ERBSS)."

Three shortwave (0.2-5μm) directional models have been employed in ERBSS mission simulations:

(1) a composite of the Lambertian model and a highly anisotropic model exhibiting strong forward scattering and moderate backscattering at large solar zenith angles, the "composite model;"

(2) the "stratocumulus cloud model;"

(3) the "stratus cloud model."

The relative contributions of the Lambertian and the anisotropic to the composite model are variable from 100 percent Lambertian to 100 percent anisotropic. The composite model, illustrated in figure 2, is representative of clouds, snow, ocean, and land surfaces according to airborne radiometer measurements reported in the literature.

The stratocumulus cloud model, illustrated in figure 3, is an empirical fit to measurements of flux from clouds of irregular density ranging from non-uniform stratus to discrete cumulus clouds.

The stratus cloud model, illustrated in figure 4, applies to more or less uniform stratus clouds.

ERROR ANALYSIS

An analysis of the potential errors in the inferred flux as a function of the scanner orientation was performed for simulated ERBSS missions over a 1-month period. Two TIROS missions considered included 3 p.m. and 8 p.m. equatorial crossings on the ascending node and are detailed in Table I. Here also are described two AEM missions, a 607 km altitude orbit for the off-track scan angle and a 635 km altitude orbit for the along track scan case. The 607 km AEM at 56° inclination was chosen to provide scanner coverage of each 250 X 250 km region for each local hour as the orbit precesses with respect to the Earth-Sun line. It was necessary, however, to select a different orbit altitude for the along-track scanner to insure good regional coverage in the tropic zones although this does not allow complete coverage of all local hours.

The scanner characteristics were selected to simulate the current single axis philosophy and to satisfy the data rates compatible with TIROS. A 3° FOV was chosen with a 6.4 sec. sweep interval and .05333 sec. sampling rate scanner with additional details listed in Table I. These simulated scanner footprints on the 30 km top-of-atmosphere sphere are shown in figure 5. Only a half scan sweep is illustrated since they are symmetric about the nadir track. The FOV's at nadir are contiguous for the TIROS; however, successive AEM sweeps produce coverage gaps. Four scan sweep angles were considered for this study: 0° (along track), 45° and 135° (off-track), and 90° (cross-track).

In order to assess the error potential of these scan sweep angles associated with the proposed satellite missions, an analysis technique suggested by R. Green was employed. In this analysis, the stratus cloud model was used to simulate a realistic Earth

radiance field. The simulated data were analyzed using a composite model in which the Lambertian model was weighed equally with the stratus model. In this way, analyzed fluxes could be compared to simulated, actual fluxes to define flux errors. These calculations were taken over a 30 day period for the Sun near an equinox. Although these results do not yield complete, or absolute error determinations, they do provide a basis for comparing scanner performance for various orbits and scan modes. Both 5° latitude zones and a series of 250 X 250 km regions were included in this study with one region at each latitude from the equator to the pole.

Every combination of the three satellites and four scan sweep angles was solved for both zonal and regional errors. It was observed from all these results that the general mass of data points represents errors less than 10 percent, except near the poles, where the solar zenith angle approaches its maximum. The sample results plotted in figure 6 indicate that the cross-track scan sweep angle produces significantly lower errors over most of the globe than the other angles. While providing more complete coverage at the higher latitudes, the cross-track scanner errors there are much greater than at the mid and lower latitudes. This is due to greater model differences at the high solar zenith angles.

REFERENCES

1. Brennan, B.; and Bandeen, W. R.: Anisotropic Reflectance Characteristics of Natural Earth Surfaces, Appl. Opt. 9: 405-412, 1970.

2. Cherrix, G. T.; and Sparkman, B. A.: A Preliminary Report on Bidirectional Reflectances of Stratocumulus Clouds Measured With an Airborne Medium Resolution Radiometer. NASA TM X-55659, Feb. 1967.

3. Raschke, E.; Vonder Harr, T. H.; Pasternak, M.; and Bandeen, W. R.: The Radiation Balance of the Earth-Atmosphere System from Nimbus 3 Radiation Measurements, NASA TN D-7249, April 1973.

4. Salomonson, V. V.: Anisotropy in Reflected Solar Radiation, Atmos. Sci. Pap. No. 128 (Contract NAS-147) Colorado State University, 1968.

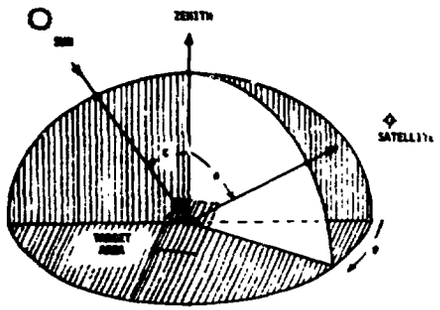

FIGURE 1. SATELLITE-SUN-TARGET GEOMETRY

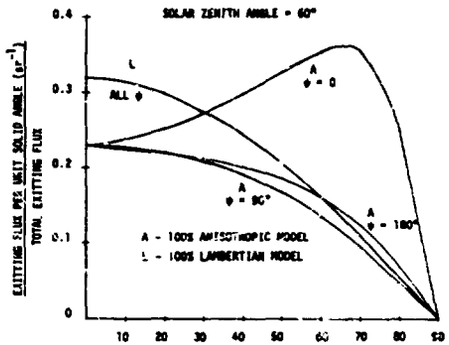

FIG. 2.- COMPOSITE SHORTWAVE DIRECTIONAL MODEL

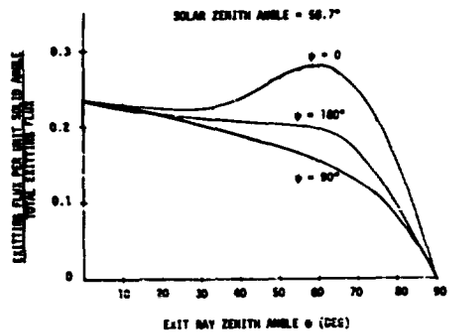

FIG. 3.- STRATOCUMULUS CLOUD SHORTWAVE DIRECTIONAL MODEL

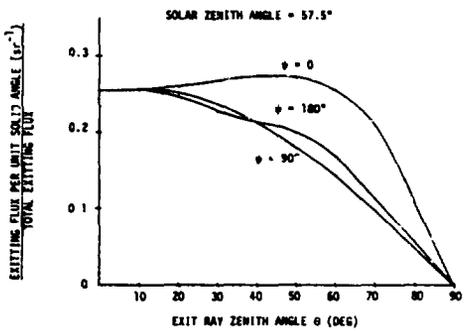

FIG. 4- STRATUS CLOUD SHORTWAVE DIRECTIONAL MODEL

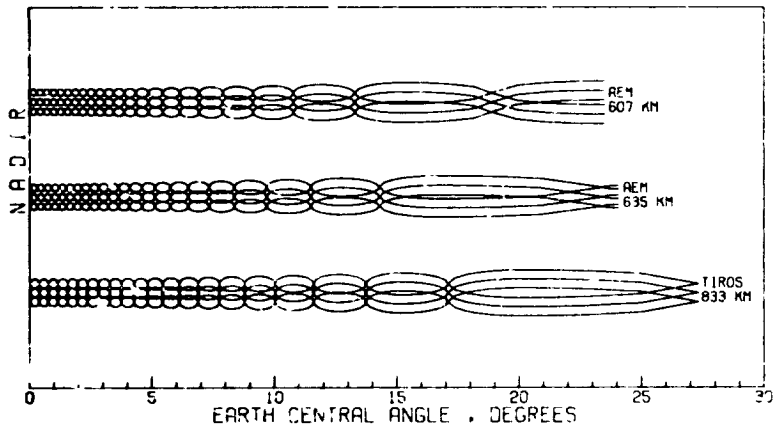

FIGURE 5. ERBSS Simulated Scanner Footprints (3° FOV , 39km FOA)

	T..S	AEM	AEK
ALTITUDE	83.. km	607.	635
INCLINATION	Sun Sync. 98.7°	56.	56.
GROUND TRACK REPEAT CYCLE	7 days	3	12
ORBIT PERIOD	6095 396 sec	5810.211	5845 179
LONG. BETWEEN SUCCESSIVE ORBITS	-24.41°	-24.55	-24.69
TRUE ANOMOLY	37799°	.39654	39417
FOV (ECA degrees)	.3766°	.27064	.28378
FOV	3.°	3.	3.
S... ANGLE/SAMPLE	3.°	3.	3
SCANNER ROTATION RATE	6.4 sec/rev.	6.4	6.4
SAMPLE RATE	.05333 sec.	.05333	.05333
LIMB (scan angle)	62.663°	66.530	.008
LIMB (ECA degrees)	27.317°	23.470	.992
LIMIT (scan angle)	61.5°	64.5	5
LIMIT (ECA degrees)	25.04°	15.23	6 59
LIMIT (viewing zenith)	81.54°	79.73	81.09
SAMPLES/SCAN SWEEP	42	44	44

TABLE I. ERBSS SIMULATED SCANNER CHARACTERISTICS

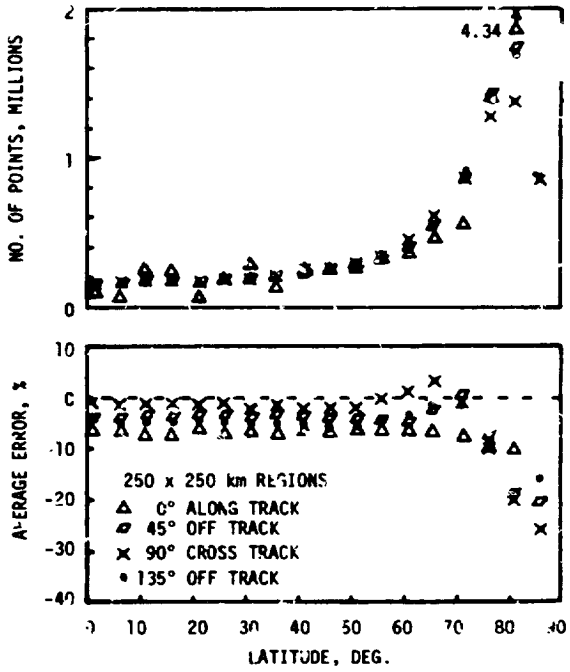

FIGURE 6. ERBSS shortwave regional error estimates for a simulated scanner.

Paper No. 57

CLOUD COVER MODELING

O. E. Smith, *Marshall Space Flight Center, Alabama*

ABSTRACT

Results from two investigations in modeling cloud cover are presented. These being a univariate model and a multivariate model for cloud cover.

INTRODUCTION

The Worldwide Cloud Cover model (Ref. 1,2, 3) was developed for the purpose of simulating the consequences of cloud cover on earth-viewing space missions (Ref. 4.). This cloud model was successfully used in the time-line planning for the Skylab Earth resources mission. This cloud model used standard ground based cloud observations, satellite cloud data available in the 1967-1971 time period, and cloud summaries to establish 29 homogeneous cloud regions.

To model cloud cover for the purpose of studying the relationships between cloudiness, precipitation, and Earth radiation budget requires a more detailed approach than was used in the early worldwide cloud cover model. An objective procedure to classify homogeneous cloud regions is desired. A means to do this is to use the parameters of an appropriate probability distribution function as a model for cloud cover.

Cloud Cover Modeling Univariate Distribution

If an adequate underlying multivariate theoretical statistical distribution can be found to represent cloud cover, then the properties of that distribution function can be used to model temporal and spatial distribution of cloudiness and to classify regions that have similar cloudiness characteristics.

Using the empirical frequency summaries generated for the worldwide cloud model, Falls (Ref. 5) concluded that the univariate Beta distribution adequately describes the variation in the amounts of cloud cover. The Beta probability density function used for cloud cover is

$$f(x) = \frac{\Gamma(\gamma + \eta)}{\Gamma(\gamma)\Gamma(\eta)} x^{\gamma-1}(1-x)^{\eta-1}$$

The range of the variable, x, is bounded at 0 and 1; zero corresponding to no clouds and unity corresponds to 10 tenths or over cast and fractions in between denote tenths of cloud cover. The parameters η and γ are greater than zero. Estimates from the sample are obtained by $\eta^* = \frac{(1-\bar{x})}{s^2}[\bar{x}(1-\bar{x}) - s^2]$

$$\gamma^* = \frac{\bar{x}\eta^*}{1-\bar{x}}$$

where $\bar{x}$ and s^2 are sample mean and sample variance. This density function can take on many shapes exhibited by cloud cover. The characteristics of the shapes and parameters are shown in Fig. 1.

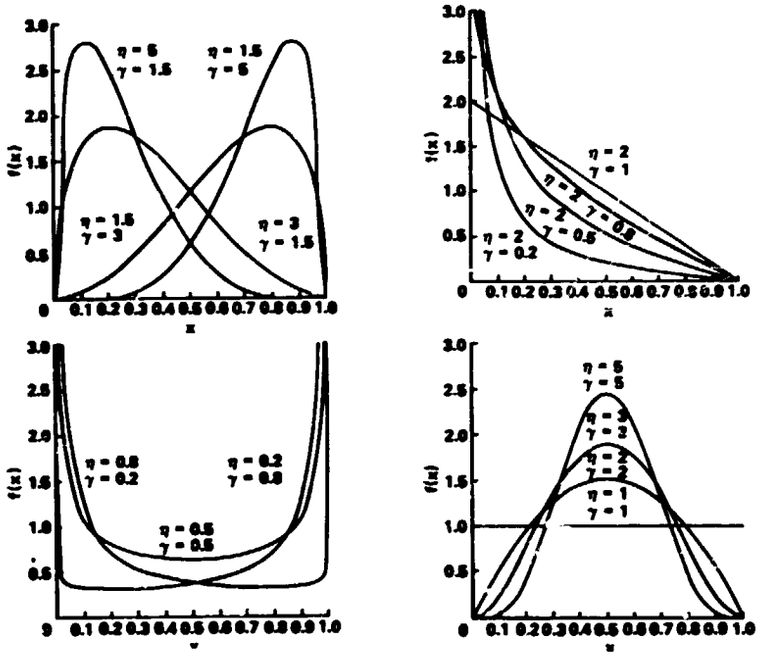

Fig. 1 Beta distributions with different parameter values.

Intuitively, the probability density function for cloudiness observed in a small viewing area should be U-shaped and grow bell shape as the viewing area increases. Regions with high insidence of few clouds should be skewed to the left and regions with a high frequency of cloudiness should be skewed to the right. The effects of viewing areas on the attending distribution can best be determined from satellite cloud data. The ground based observer sees a sky dome of approximately 55.6 km (30 n. mi). Once this effect is determined the classification of similar

cloud regions can be objectively derived.

Incidentally this Beta distribution was investigated as a possible model for solar radiation (total and normal insidence) for a data sample for Albuquerque, N. M. The radiation data was transformed to have the limits of zero and unity on the assumption that the lower limits is zero and the upper limit is 2 Langleys. The resulting "fits" were very poor. This preliminary investigation indicates mixed distributions of solar radiation even after making stratified samples based on cloudiness and cloud type.

A Multivariate Model

To extend our investigations of cloud distribution to space and time and conditional probability analysis a multivariate probability distribution function is required. Thus, we may expect that the multivariate Beta distribution, sometimes called the Dirchlet distribution would be a natural extension for describing the bivariate case. However, a theoretical requirement of the Dirchlet distribution is that the variables be negatively correlated and this constraint is contrary with actual situations. Consequently, a different approach was required--one allowing for both positive and negative correlations.

Peizer and Pratt (Ref. 6) provide a possible approach, that of using the normal distribution for approximating tail probabilities in the Beta distribution. Thus, if one assumes that the correlation between two sites or different in time is structurally related to the correlation present in the bivariate normal distribution, one may be able to extend work of Peizer and Pratt to the multivariate setting, that of approximating joint probabilities using the bivariate normal distribution (BVN). This approximation would appear to work adequately for those cases where the univariate normal approximation gives satisfactory approximations to the Beta distribution

An example result using this technique to give joint probability of cloudiness by categories follows.

The sites selected for this analysis were Fort Worth and Houston, Texas. Daily records (Jan. 1971 to Dec. 1975) on cloud cover, measured in tenths were recorded every third hour by standard ground base observing practices.

The data was grouped into the categories as shown in Tabl 1.

Table I

Category/Tenths
1/0; 2/1, 2, 3; 3/4, 5; 4/6, 7, 8, 9; 5/10

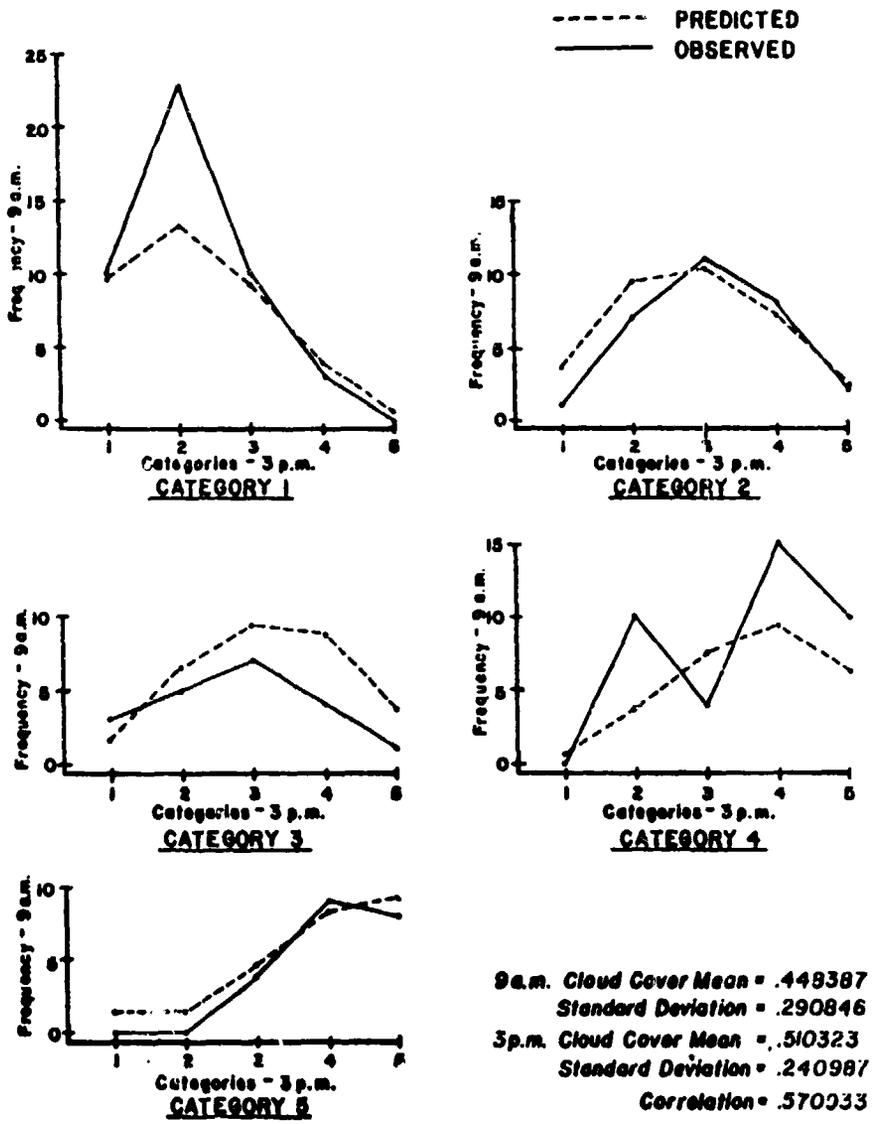

Fig. 2
OBSERVED AND PREDICTED FREQUENCIES FOR FORT WORTH AT 9 A.M. AND FORT WORTH AT 3 P.M. BASED ON JULY DATA FOR 1971-75.

Since Falls Ref. 5 demonstrated that the Beta distribution adequately describes variation in categorical data, this investigation was restricted to categorical data. However, the approximation program is not restricted to categorical data.

A complete set of probabilities (25 values) have been calculated for the Fort Worth 9 a.m. and Fort Worth 3 p.m. combination. These values are presented in Fig. 2. Each of the five portions of figure represents a category level for 9 a.m. and the abseissas represent the categories for 3 p.m.

Figure 2 values were determined based on observed and expected frequencies for 5 years (155 values). The agreement is quite satisfactory with a couple of exceptions. Values for Category 1 for 9 a.m. and Category for 3 p.m. shows a wide divergence. Also the five values predicted for 3 p.m. and Category 4 for 9 a.m. show substantial disagreement.

These discrepancies between observed and predicted values can be explained by analyzing how well the Beta model describes univariate cloud cover in the various data sets. Another consideration is that better agreement may be obtained by using more class interval e.g., one-tenth. This would give greater flexibility in selecting the required integration limits for these joint frequencies.

Conclusions:

Although only two statistical methods have been reported in this paper, there are other techniques and statistical concepts in cloud modeling that should be investigated.

References:

1. Sherr, P.E. et al, Worldwide cloud cover distribution for use in computer simulations; NASA CR-161226, June, 1968
2. Greaves, J.R. et al, Development of a global cloud cover model for simulating Earth-viewing space missions, NASA CR-61345, April 1971.
3. Chang, P.T., and J.H. Willand, Further development in cloud statistics, (or computer simulations) NASA CR 61389 July 1972.
4. Brown, S.C., Simulating the consequence of cloud cover on Earth viewing space missions, Bull. Amer. Meterol. Soc., 51, 126-131, 1970.
5. Falls, L.W., The Beta Distribution: A statistical model for World cloud cover, JGR, Vol 79, No. 9, 1261-1264, 1974
6. Peizer, P.B. & J.W. Pratt, A normal approximation for binomial, F, Beta..., J. Amer. Stat. Ass. V. 63, 1968.

D56

N79-20631

Paper No. 58

A SUMMARY OF MONTHLY MEAN SIMULATION EXPERIMENTS WITH THE GISS MODEL

Jerome Spar, *The City College, New York, N. Y. 10031*

Abstract

The statistical results of 8 monthly mean simulation experiments with the GISS general circulation model are summarized for the Northern Hemisphere in terms of the fields of sea-level pressure, 500-mb. height, and 850-mb. temperature.

Introduction

While general circulation models are capable of simulating certain properties of the global climate, it has not yet been demonstrated that they can reproduce climatic anomalies, such as the deviation of an individual monthly mean atmospheric state from the climatological average. This paper presents a summary of results from a series of monthly mean simulation experiments with the GISS model (Somerville et al., 1974), in which global forecasts were marched out from initial conditions on the first day of the month and averaged over the month.

The experiments to date have included four "forecasts" for January 1973, 1974, and 1975 (Spar et al., 1976; Spar, 1977) and February 1976, one initial state random perturbation" experiment for January 1975 (Spar, et al., 1978), two "sea-surface temperature (SST) anomaly" experiments for January 1974 (Spar et al., 1976) and February 1976, and one "replication" experiment for February 1976.

All computations were initialized with 00 GMT global data on the first day of the month, provided by the National Meteorological Center (NMC). NMC data were also used to verify the simulations of the monthly mean states. Climatological fields used in the verification program were obtained from NCAR.

Experiments

In the perturbation experiment, random "errors" were distributed over the initial state three times to obtain a total set of four simulations for the same month. The dispersion of the simulations was analyzed to evaluate the effect of initial state uncertainty on the simulation of the monthly mean state.

The first SST anomaly experiment, for January 1974, was carried out with the sea temperatures updated daily to match the observed values. In the second SST anomaly experiment, for February 1976, the daily SST values were averaged over the month, and the fixed field of observed monthly mean SST values was used in place of the climatological SST field for the month.

In the replication experiment, two presumably identical simulation runs were performed with the same initial and boundary conditions, but with different schedules of interruptions and restarts on the computer, to provide information on the inherent computational "noise level" of the monthly mean simulations.

For the purpose of this presentation, all the experimental results are summarized in two tables of statistical data for the Northern Hemisphere only. The three variables analyzed are sea-level pressure (SLP), 500 mb. height (Z-5), and 850-mb temperature (T-8) on the GISS model grid (4° of latitude by 5° of longitude). Table 1 shows the root-mean-square (rms) errors for the three fields, while Table 2 gives the S-1 (gradient) skill scores for SLP and Z-5 only. Also shown in the tables are rms differences and S-1 comparison scores between certain simulation fields.

The columns in the tables labelled F denote "forecasts" computed with climatological SSTs as boundary conditions. Those labelled CL represent "forecasts" of climatology, in which the climatological monthly mean state was verified against the observed monthly mean state. Columns labelled A indicate simulations computed with observed (anomalous) SSTs as boundary conditions. The F and A computations were done with the same model, while F* and A* were computed with an earlier and slightly different version. P denotes a simulation computed from one of the three random perturbations of the initial state (P_1, P_2, P_3). The columns labelled F_2

represent the second forecast in the February 1976 replication experiment.

Results

(At the time this was written, the "climatology forecast", CL, for February 1976 was not yet available. The following discussion is therefore incomplete, but it will be supplemented if the CL computations are completed in time for the oral presentation.)

The January data indicate that the model simulations are consistently superior to climatology at 500-mb. and 850-mb., but not at sea level.

The SST daily update experiment of January 1974 shows no beneficial impact on the simulations of the use of observed surface boundary conditions. However, the observed monthly mean SST data for February 1976 did have a beneficial effect. The difference may be due to "noise" in the daily SST data.

The perturbation experiment indicates only a relatively minor influence of random initial state errors on the monthly mean simulations, espcially at 500-mb.

The replication experiment suggests that there may be a limit to the accuracy of any monthly mean simulation, due purely to computational problems.

References

Somerville, R.C.J., P.H. Stone, M. Halem, J.E. Hansen J. S. Hogan, L. M. Druyan, G. Russell, A. A. Lacis, W. J. Quirk, and J. Tenenbaum, 1974: The GISS model of the global atmosphere. J.Atmos, Sci, 31,84-117

Spar, J., R. Atlas, and E. Kuo, 1976: Monthly mean forecast experiments with the GISS model. Mon.Wea. Rev., 104, 1215-1241.

Spar, J., 1977: Monthly mean forecast experiments with the GISS model. Mon.Wea. Rev., 105, 535-539.

Spar, J., J.J. Notario, and W. J. Quirk, 1978: An initial state perturbation experiment with the GISS model. (To be published in Mon. Wea. Rev., January 1978.)

Table 1. Summary of root-mean-square (rms) errors and differences over the Northern Hemisphere of GISS model monthly mean simulations of sea-level pressure, SLP (mb), 500-mb height, Z-5 (m), and 850-mb temperature, T-8(^{o}K). CL denotes climatology. F and A represent simulations computed with climatological and observed SSTs, respectively. F* and A* were computed with a slightly differentearlier version of the model. P indicates simulations computed from perturbed initial conditions.

			rms errors												
Month	January 1973		January 1974				January 1975					February 1976			
Simulation / variable	CL	F	CL	F	F*	A*	CL	F	P_1	P_2	P_3	CL	F	F_2	A
SLP (mb)	8.7	10.0	9.2	8.6	7.3	7.4	6.6	5.3	5.2	5.5	5.4		8.8	8.8	7.2
Z-5 (m)	94	72	108	80	76	83	82	64	60	57	61		80	82	66
T-8 (^{o}K)	4.3	4.1	5.1	4.7	4.6	4.7	4.5	4.1	4.0	3.9	4.1		4.4	4.4	4.3

	rms differences				
		P_1-P_2	P_1-P_3	$F-F_2$	$A-F_2$
SLP (mb)		2.3	2.5	1.8	3.8
Z-5 (m)		31	28	19	39
T-8 (^{o}K)		1.7	1.8	1.2	1.6

Table 2. Summary of S-1 skill scores and comparison scores over the Northern Hemisphere of GISS model monthly mean simulations. (See Table 1 for explanation of symbols.)

S-1 skill scores

Month	January 1973		January 1974				January 1975					February 1976			
Simulation / variable	CL	F	CL	F	F*	A*	CL	F	P_1	P_2	P_3	CL	F	F_2	A
SLP	81	81	89	79	67	70	73	64	62	63	64		74	76	72
Z-5	55	45	60	53	45	49	52	42	39	40	41		42	44	41

S-1 comparison scores

			P_1-P_2	P_1-P_3	$F-F_2$	$A-F_2$
SLP			53	54	43	49
Z-5			28	27	23	27

Paper No. 59

N79-20632

SPECTRAL ENERGETICS AND PREDICTABILITY STUDIES

J. Tenenbaum, *State University of New York, Purchase, New York*

ABSTRACT

One and two-dimensional spectral analyses have been performed on the GISS general circulation model. The one-dimensional results imply that low eddy kinetic energy is caused by low conversions from the zonal mean kinetic energy. The two-dimensional results confirm that low wave number spectral coefficients approach the predictability limit slower than high wave number coefficients and suggest ways of estimating the rate of approach to the predictability limit.

INTRODUCTION

Numerous studies have been made of the limits of atmospheric predictability and the implications for forecasts in the range of several days to several weeks The conclusions are that energy in the high wave number portion of the spectrum propagates to all wavelengths in a period of 1 to 2 weeks. This spreading of energy in wave-number space prevents forecasts of a specific variable at a specific space-time point after the predictability limit. The diagnostic value of the details of this spreading are substantial.

Most general circulation models possess unrealistically low eddy kinetic energies, K_E. While some increase occurs as resolution increases, the additional energy seems to appear at the larger scales (Manabe et al., 1970, Wellck et al., 1971). Manabe et al. explain their results as due to a shift of the scale at which absorption occurs. Wellck et al. explain their results in terms of the improved eddy meridional momentum transports and show basic agreement of the fine grid transports with observational data. Since K_E is still low, one additional process may be operating incorrectly.

The integrated conversion, $C(K_E,K_M)$, appears basically accurate in the GISS model energetics. When

presented on a pressure versus latitude display, we find that large cancellations are occurring on either side of the jet stream in two sets of observational data, Figs. 1(b) and 1(c). The model's failure to reproduce this pattern is very strikingly shown in Fig. 1(a) using data from January 1973. Bearing in mind

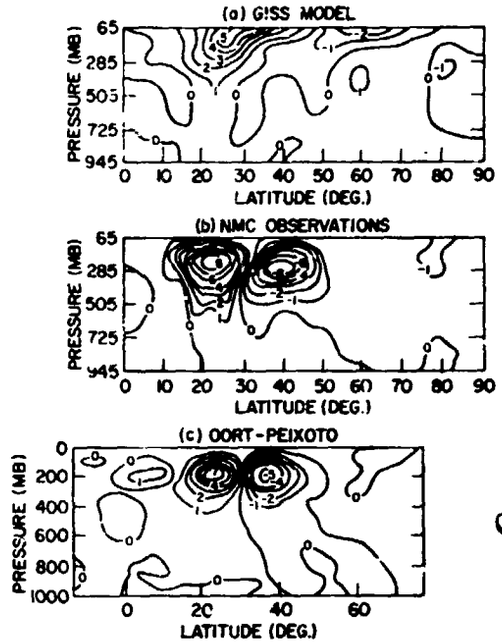

Fig. 1. Northern hemisphere conversion from K_E to K_M. Units: $W/(m^2\ bar)$.

that positive values correspond to conversion from K_E to K_M, there is clearly a large deficit of energy going from K_M to K_E. New GISS results for January 1974 and new NCAR results show similar patterns.

The deficit of conversions to K_E is also shown strikingly in a K_E versus time display for three Januaries in Fig. 2. The model easily follows decreases in K_E (1973, 1975) but is unable to follow an initial increase in K_E (1974). When the conversion term is spectrally analyzed all observational wave numbers show the positive and negative peaks of Fig. 1(c). All model wave numbers lack the negative peak except for wave number 6, the wavelength of maximum baro-

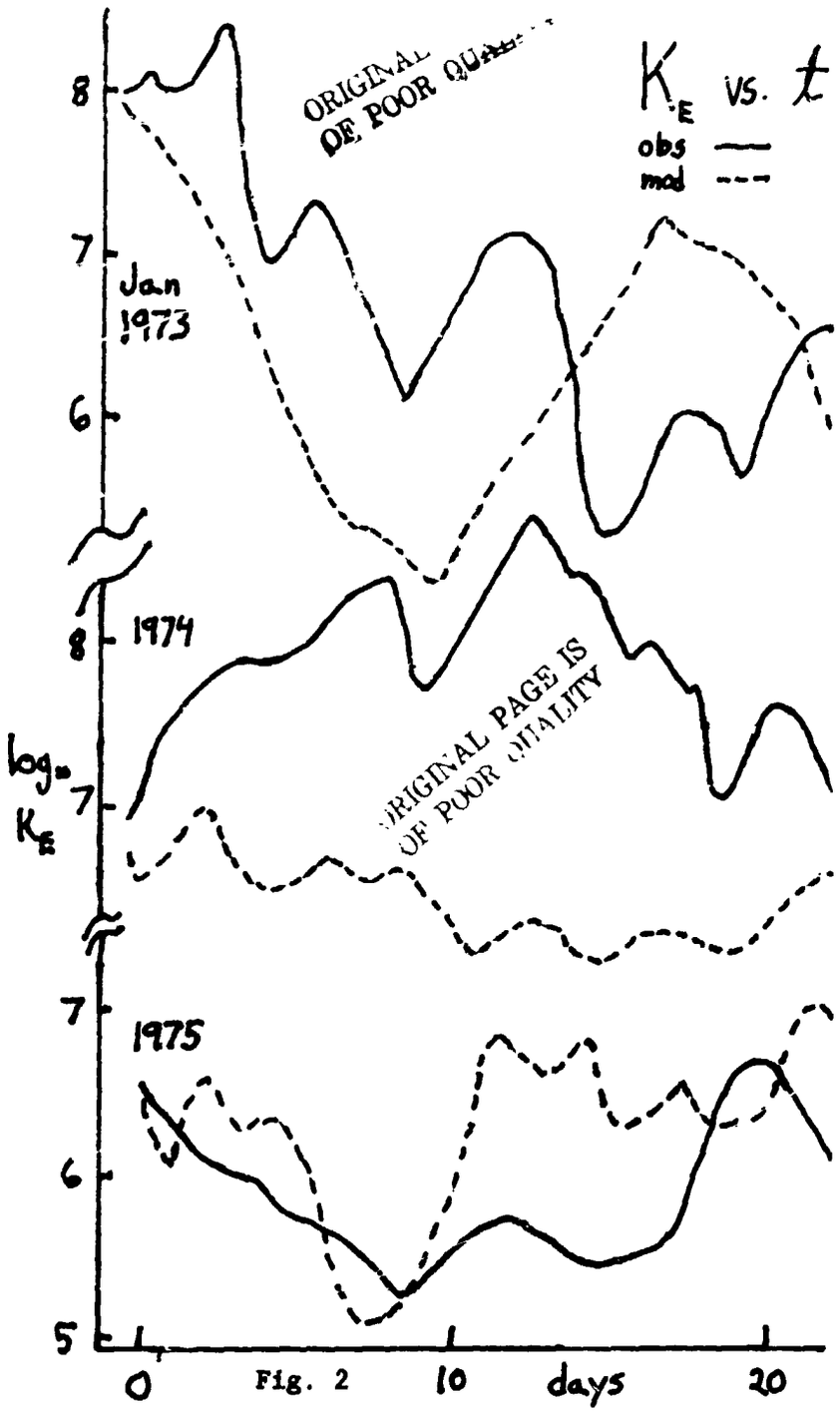
ORIGINAL
OF POOR QUA
K_E vs. t
obs
mod
8
7
6
Jan
1973
1974
8
7
$\log_{10}$
K_E
ORIGINAL PAGE IS
OF POOR QUALITY
7
6
5
1975
0
10
days
20

Fig. 2

clinicity. Some error is occurring in the non-baroclinic conversions from K_M to K_E.

The formulas for such conversions contain factors proportional to the latitudinal and vertical gradient of the mean zonal wind, $[u]$. We conclude that the dominant cause of low K_E values is the lack of sufficient $[u]$ gradients near the jet stream resulting in erroneously low values of $C(K_E,K_M)$. The agreement with integrated hemispheric means implies that the model atmosphere will produce the conversion at some minimum level of K_E as shown in Fig. 2. Such conversions will not, however, necessarily occur at the right time or place.

Spectral Predictability

We have calculated the two-dimensional error spectrum of the 500 mb height fields for the 3 Januaries given above, and correlated them with the rms errors as a function of time. The error spectra are calculated using the methods of Baer (1972), and represent rms over longitudinal wave number where the distinction between triangular and rhomboidal truncation does not enter.

Two significant results emerge. First, the low wave number error coefficients approach their asymptotic values more slowly than high wave numbers. Second, and perhaps most significant, the initial spectral coefficients of the observed 500 mb field show a suggestive correlation with the rate of rise of the rms errors. This relationship is shown in Table 1.

Table 1. Correlation of 500 mb rms error rise with low wave number region of observed spectrum.

	days to 50% of asymptotic limit	wave number coefficients of initial data 1	2	3	4	5
Jan 73	8	308	2534	93	394	177
74	5	235	2476	187	512	240
75	10	337	2605	66	502	101

Underscored values deviate by more than 20% from mean.

While additional cases must be studied, the possibility of predicting the rate of rise of the rms error would be quite significant. The correlation with the time behavior of K_E is intriguing here. Clearly, only in January 1974 did the energy initially rise and this is just the case with the fastest rate of rise of rms error.

Each of these conclusions go to the heart of the GISS satellite data impact studies. Our results suggest that improved model resolution would improve the eddy kinetic energy situation, and probably improve the absolute predictability beyond 48 h. The spectral results suggest a technique for identifying synoptic situations where good predictability is likely.

REFERENCES

Baer, F., 1972: An alternate scale representation of atmospheric energy spectra. J. Atmos. Sci., 29, 649-664.

Manabe,S., J. Smagorinsky, J.L. Holloway, Jr. and H.M Stone, 1970: Simulated climatology of a general circulation model with a hydrologic cycle. III. Effects of increased horizontal computational resolution. Mon. Wea. Rev., 98, 175-212.

Wellck,R.E., A. Kasahara, W. . Washington and G. De Santo, 1971: Effect of horizontal resolution in a finite difference model of the general circulation. on. Wea. Rev., 99, 673-683.

NASA WEATHER AND CLIMATE PROGRAM
SCIENCE REVIEW

ATTENDEES

Robert F. Adler
Goddard Space Flight Center
Code 914
Greenbelt, MD 20771
(301) 982-2885

M. A. Alaka
NOAA/NWS
8060 13th Street
Silver Spring, MD 20910
427-7773

L. J. Allison
Goddard Space Flight Center
Code 915
Greenbelt, MD 20771
982-5056

Akio Arakawa
UCLA
Department Atmospheric Sciences
Los Angeles, CA 90024
(213) 825-1852

Albert Arking
Goddard Space Flight Center
Code 915
Greenbelt, MD 20771
(301) 982-2208

David Atlas
Goddard Space Flight Center
Code 910
Greenbelt, MD 20771
(301) 982-2626

Om P. Bahethi
Science Systems & Appl., Inc.
8804 Cipriano Court
Lanham, MD 20801
(301) 552-1975

W. R. Bandeen
Goddard Space Flight Center
Code 910
Greenbelt, MD 20771
(301) 982-4406

W. L. Barnes
Goddard Space Flight Center
Code 941
Greenbelt, MD 20771
(301) 982-4117

Jon F. Bartholic
Univ. of Florida
1172 McCarty Hall
Fruit Crops Dept. (IFAS)
Gainesville, FL 32611

Eugene Bierly
National Science Foundation
Climate Dynamics RSCH Section
Washington, DC 20550
634-1543

Fred E. Bittner
NOAA/NESS Analysis & Evaluation
Branch, S1111 WWB Room 510
Stop G, Washington, DC 20233
(301) 763-8414, 6515

Dean Bowman
USAF ETAC
634 E 5th Street
Trenton, IL 62293

Kenneth L. Brinkman
Hughes Aircraft Co., (S&CG)
Bldg. 373
El Segundo, CA 90245
(213) 648-3329

Norman L. Canfield
NOAA, OA2
6010 Executive Blvd.
Rockville, MD 20852
443-8241

A. J. Cervenka
NASA HQS
Code ERO
Washington DC 20546

M. T. Chahine
Jet Propulsion Laboratory
Bldg. 183-301
4800 Oak Grove Drive
Pasadena, CA 91103

Ming-Dah Chow
SAI Comsystems Corporation
Mandex, Inc.
6215 Greenbelt Rd., Suite 301
College Park, MD 20740
(301) 474-7772

Lee Cisney
Goddard Space Flight Center
Code 914
Greenbelt, MD 20771
982-2624

Frank Coneybear
Ball Brothers
1411 Jefferson Davis Highway
Arlington, VA 22202
(703) 521-1150

Duane S. Cooley, W111
National Weather Service, NOAA
8060 13th Street
Silver Spring, MD 20910

Harold A. Corzine
NOAA
6010 Executive Blvd.
Rockville, MD 20852
443-8108

R. C. Costen
Langley Research Center
Code 423
Hampton, VA 23666
(804) 827-3431
FTS: 982-3431

N. L. Crabill
Langley Research Center
Code 247
Hampton, VA 23666
928-3274

Paul Dalrymple
Corps of Engineers
Engineer Topographic Labs.
Ft. Belvoir, VA 22060
664-1561

Bernard C. Diesen, AFGWC/NASA
Liaison
Goddard Space Flight Center
Code 601
Greenbelt, MD 20771
082-4556

Maurizio Di Ruscio
Goddard Space Flight Center
Code 620
Greenbelt, MD 20771
982-6194

James C. Dodge
NASA HQS
Code ERD
Washington, DC 20546
755-8617

L. L. Dubach
Goddard Space Flight Center
Code 601
Greenbelt, MD 20771
982-4556

I. J. Eberstein
Goddard Space Flight Center
Code 912
Greenbelt, MD 20771
982-4538

D. A. Flower
Jet Propulsion Laboratory,
Code 168-327
4800 Oak Grove Drive
Pasadena, CA 91103
792-4151

William W. Fowlis
ES 82, Marshall Space Flight Center
AL 35803
(205) 453-0875

Allen L. Franta
GE/MATSCO
5050 Powder Mill Road
Beltsville, MD 20705
932-3500 X250

Robert S. Fraser
GSFC
Code 915

T. T. Fujita
Dept. of Geophysical Sciences
Univ. of Chicago
5734 S. Ellis Ave.
Chicago, IL 60637

Inez Fung
Goddard Space Flight Center
Code 911
Greenbelt, MD 20771
982-2373

David M. Garrison,
AFGWC-TDL Liaison
Gramax Building, W423, Room 811
8060 13th Street
Silver Spring, MD 20910
427-7639

J. Patrick Gary
Goddard Space Flight Center
Code 933
Greenbelt, MD 20771
982-6079

Cecil Gentry
GE/MATSCO
5050 Powder Mill Road
Beltsville, MD 20705
937-8848

David H. George
NOAA/National Weather Service
W112x3
8060 13th Street
Silver Spring, MD 20910
427-7677

Michael Ghil
Courant Institute, NYU
251 Mercer Street
New York, NY 10012

Dalu Giuseppe
Goddard Space Flight Center
Code 915
Greenbelt, MD 20771
982-6369

Brent B. Goddard
NOAA/NESS
FB-4, Room 3051
Suitland, MD 20233
763-2506

R. A. Goldberg
Goddard Space Flight Center
Code 912
Greenbelt, MD 20771
982-4603

L. R. Greenwood
Langley Research Center, Code 10
Hampton, VA 23665
827-2893

Edwin F. Harrison
Langley Research Center
Code 271
Hampton, VA 23665
827-2977

Harshvardhan
Goddard Space Flight Center
Code 915
Greenbelt, MD 20771
982-6360

Kenneth D. Hadeen
NOAA/EDS/CEDDA
3300 Whitehaven St. N. W.
Washington, DC 20235

M. Halem
Goddard Space Flight Center
Code 911
Greenbelt, MD 20771
982-2482

James Hansen
NASA Goddard Institute for
Space Studies
2880 Broadway
New York, NY 10025

A. F. Hasler
Goddard Space Flight Center
Code 914
Greenbelt, MD 20771
982-2885

D. F. Heath
Goddard Space Flight Center
Code 912
Greenbelt, MD 20771
982-6421

Richard C. Herfurth
Goddard Space Flight Center
Code 901
Greenbelt, MD 20771

Gerald F. Herman
University of Wisconsin
Dept. of Meteorology
1225 w. Dayton St.
Madison, WI 53711

E. Hilsenrath
Goddard Space Flight Center
Code 912
Greenbelt, MD 20771

A. C. Holland
Wallops Flight Center
DAS/E106
Wallops Island, VA 23337
8-928-5328

Joshua Z. Holland
NOAA/EDS/CEDDA
3300 Whitehaven St. N. W.
Washington, DC 20235
634-7251

Donald H. Hunt
NOAA RD1
5010 Executive Blvd.
Rockville, MD 20852
443-8971

Herbert E. Hunter
Adapt Service Corp.
Box 58
Reading, MA 01867
(617) 657-2245

Eugene Isaacson
Courant Institute, NYU
251 Mercer Street
New York, NY 10012

Karl R. Johannessen
NOAA/NWS, Room 1410
8060 13th Street
Silver Spring, MD
427-7700

Winthrop T. Johnson
Sigma Data Services
Goddard Space Flight Center
Code 911
982-2438

James B. Jones
NOAA/NWS
Code W12
Silver Spring, MD 20910
427-7704

Michael L. Kaplan
George Washington Univ.
Langley Research Center
MS 423
Hampton, VA 23665
(804) 827-2335

Major James Kerlin
USAF
World Weather Bldg, W32
Washington, DC 20233
(301) 763-8058

David B. King, Jr.
Jet Propulsion Laboratory
MS 183-501
4800 Oak Grove Drive
Pasadena, CA 91103

William H. Klein
NOAA-National Weather Service
Systems Devel. Office, W4.
Room 1216
8060 13th Street
Silver Spring, MD 20910
427-7747

Earl R. Kreins
Goddard Space Flight Center
Code 901

H. Lee Kyle
Goddard Space Flight Center
Code 931
982-5940

Charles Laughlin
Goddard Space Flight Center
Code 901

Ronald L. Lavoie
Science & Academic Affairs
NOAA
6010 Executive Blvd.
Rockville, MD 20852
443-8721

In Lee
Ames Research Center
MS 245-3
Moffett Field, CA 94035

J. D. Lin
Univ. of Connecticut
Box U-37
Storrs, CT 06268
(203) 486-4017

L. Meredith
Goddard Space Flight Center
Code 900
982-5003

Yale Mintz
Goddard Space Flight Center
Code 911
982-2371

Raymond A. Minzner
Goddard Space Flight Center
Code 914
982-5786

Richard B. Morrison
Ball Brothers
1411 Jefferson Davis Highway
Arlington, VA 22202
(703) 521-1150

Burt Morse
NOAA, NESS, SEL
6621 Wakefield Drive #910
Alexandria, VA 22307
763-2597

John F. Moses
NOAA/NESS
3110 Trinty Drive
Bowie, MD 20715
763-2506

Frederick R. Mosher
Space Science and Engineering Center
Univ. of Wisconsin
1225 W. Dayton Street
Madison, WI 53706
(608) 882-5446

John P. Mugler, Jr.
Langley Research Center
MS 422
Hampton, VA 23665
928-2717

Thomas D. Murphy
2nd Weather Squadron, USAF
Andrews AFB, MD 20331
981-6929

Wayne McGovern
NOAA (RD-4)
6010 Executive Blvd.
Rockville, MD 20852
443-8841

Major William McKechney
AF Office of Scientific Research (AFOSR/NP)
Bolling AFB, DC 20332
767-4906

Myron Nack
Computer Sciences Corp.
8728 Colesville Road
Silver Spring MD 20910
589-1545

E. A. Neil
Goddard Space Flight Center
Code 901
982-6291

L. V. Novak
Goddard Space Flight Center
Code 912
982-5940

Thomas H. R. O'Neill
5926 Merritt Place (HOME)
Falls Church, VA 22041
755-8620

William A. Pearce
EG&G/Washington Analytical Services Center
6801 Kenilworth Ave.
Riverdale, MD 20840
(301) 779-2800 x247

Tom Perry
Wallops Flight Center
Bldg. N-159
Wallops Island, VA 23337
928-5518

Cindy Peslen
Goddard Space Flight Center
Code 914
982-6360

Majorie D. Petty
VIMS
P. O. Box 784
Gloveester Pt. VA 23062
642-2111 x147

James B. Pollack
Code SST
NASA Ames Research Center
Moffett Field, CA 94035

C. Dale Pope
Kennedy Space Center
SA-APP
Florida 32899
(305) 867-3017

Karen Posey
Goddard Space Flight Center
Code 933
982-6997

C. Prabhakara
Goddard Space Flight Center
Code 915

R. Rados
Goddard Space Flight Center
Code 901
982-2624

David Randall
MIT
Rm. 54-1522
Cambridge, MA 02139
(617) 253-5431

Mirle Rao
Goddard Space Flight Center
Code 915
982-4724

Eugene M. Rasmusson
NOAA/EDS/CEDDA
Page Bldg No. 2
3300 Witehaven St.
Washington, DC 20235
634-7288

Elmar R. Reiter
Dept. of Atmospheric Science
Colorado St. Univ.
Ft. Collins, CO 80523
(303) 401-8555

Alan Robock
Meteorology Program
Univ. of Maryland
College Park, MD 20742
(301) 454-5087

Edward Rodgers
Goddard Space Flight Center
Code 914

Robert Schiffer
NASA HQS
Code ERD
Washington, DC 20546

Mark R. Schoeberl
Naval Research Laboratory
Code 7750
Washington, DC
(202) 767-2401

James R. Scoggins
Texas A&M Univ.
Department of Meteorology
College Station, TX 77843
(713) 845-7671

O. H. Shemdin
Jet Propulsion Laboratory
MS 183-501
4800 Oak Grove Drive
Pasadena, CA 91103
792-2447

William E. Shenk
Goddard Space Flight Center
Code 914
982-5948

Jagadish Shukla
Dept. of Meteorology
MIT
54-1724
Cambridge, MA 02139
(617) 253-6208

R. E. Smith
Marshall Space Flight Center
Code ES81
Alabama 35812
(205) 453-3101

W. G. Stroud
Goddard Space Flight Center
Code 900
982-4400

Yogesh C. Sud
Sigma Data Services
Goddard Space Flight Center
Code 911
982-4610

John T. Suttles
Langley Research Center
Code 423
Hampton, VA 23665
(804) 827-3431

Paul Swan
Ames Research Center
245-3
Moffett Field, CA 94035
(415) 965-6489

Dan Tarpley
NOAA/NESS
Stop E
FB 4 S1124
Washington, DC 20233
763-2700

J. Teleford
Desert Research Institute
Univ. Nevada
Reno, Nevada 89507
(702) 972-1676

Joel Tenenbaum
SUNY
Division of Natural Sciences
Purchase, NY 10577
(914) 253-5156

Sidney Teweles
GS/MATSCO
7811 Birnam Wood Drive
McLean, VA 22101
937-8848

J. S. Theon
Goddard Space Flight Center
Code 910
982-5249

Robert W. L. Thomas
EG&G Washington Analytical
Services Center
6801 Kenilworth Ave.
Riverdale, MD 20840
779-2800 x202

Pitt G. Thome
NASA HQS
Code ERD
Washington, DC 20546

Owen E. Thompson
Univ. of Md.
Meteorology Program
College Park, MD 20742
454-5090

S. G. Tilford
NASA HQS
Code ST
Washington, DC 20546
755-3766

Arnold L. Torres
Drexel University
Chemistry Dept.
Philadelphia, PA 19104
(215) 895-2640

M. Steven Tracton
NOAA/NMC
W 324
Washington, DC 20023
763-8164

Carlo Ulivieri
Univ. of Rome (NASA Contractor)
Goddard Space Flight Center
Code 620
982-6194

Mark Waters
NOAA/NESS, Stop E
FB 4, S1124, Room 3065
Washington, DC 20233
763-2700

Tom Wilheit
Goddard Space Flight Center
Code 953
982-5105

Charles V. Woerner
Langley Research Center
Code 271
Hampton, VA 23665
827-2977